

Dissertation
submitted to the
Combined Faculty of Natural Sciences and Mathematics
of Heidelberg University, Germany
for the degree of
Doctor of Natural Sciences

Put forward by

Torsten Victor Zache

born in: *Berlin*

Oral examination: *June 17, 2020*

Quantum simulation of high-energy physics with ultracold atoms

Referees:

Prof. Dr. Jürgen Berges
Priv.-Doz. Dr. Martin Gärtner

HEIDELBERG UNIVERSITY

DOCTORAL THESIS

**Quantum simulation of high-energy
physics with ultracold atoms**

Author: *Torsten Victor Zache*

Supervisor: *Prof. Dr. Jürgen Berges*

Dissertation

submitted to the

Combined Faculty of Natural Sciences and Mathematics

of Heidelberg University, Germany

for the degree of

Doctor of Natural Sciences

April 4, 2020

“And I’m not happy with all the analyses that go with just the classical theory, because nature isn’t classical, dammit, and if you want to make a simulation of nature, you’d better make it quantum mechanical, and by golly it’s a wonderful problem, because it doesn’t look so easy.”

R. P. Feynman [1]

Zusammenfassung

Quantensimulation der Hochenergiephysik mit ultrakalten Atomen

Die Vorhersage der Quantendynamik von geladener Materie, die mit dynamischen Eichfeldern interagiert, ist eine außerordentliche Herausforderung in der theoretischen Physik. In Ermangelung einer allgemein anwendbaren Berechnungsmethode bieten Quantensimulatoren eine vielversprechende Alternative.

Die vorliegende Arbeit leistet einen Beitrag zur Quantensimulation der Hochenergiephysik, wobei wir uns auf die Plattform ultrakalter Atome konzentrieren. Mittels Wilson-Fermionen schlagen wir vor die Implementierung von Gittereichtheorien basierend auf Gemischen kalter Atome in einem optischen Gitter zu verbessern. Numerische Simulationen zeigen, dass dies die Realisierung der Schwinger-Paar-Produktion mit aktueller Technologie möglich macht. Unsere vorgeschlagene Implementierung ist modular und ein elementarer Baustein wird experimentell demonstriert. Darüber hinaus identifizieren wir dynamische topologische Übergänge, die wir im massiven Schwinger-Modell entdeckt haben, als geeignetes Ziel für die Anwendung von Quantensimulatoren. Durch die Definition eines eichinvarianten Ordnungsparameter können wir zeigen, dass diese Übergänge jenseits schwacher Wechselwirkungen bestehen bleiben.

Im zweiten Teil dieser Arbeit entwickeln wir einen Formalismus für die Analyse von Quantensimulatoren mittels experimentell zugänglicher irreduzibler Korrelationsfunktionen zu gleichen Zeiten. Wir verifizieren diesen Ansatz numerisch für das Sine-Gordon-Modell im thermischen Gleichgewicht, das durch zwei tunnelgekoppelte Superfluide quantensimuliert wird. Schließlich wenden wir unsere Analyse auf die Nichtgleichgewichtsdynamik eines Spinor-Bose-Gases an und finden eine unterdrückte effektive Wechselwirkung in einem stark korrelierten Infrarotbereich.

Abstract

Quantum simulation of high-energy physics with ultracold atoms

Predicting the quantum dynamics of charged matter interacting with dynamical gauge fields poses an outstanding challenge in theoretical physics. Lacking a generally applicable computational method, quantum simulators offer a promising alternative.

In this thesis, we contribute to the quantum simulation of high-energy physics, focusing on the platform of ultracold atoms. Using Wilson fermions, we propose to improve implementations of lattice gauge theories based on mixtures of cold atoms in optical lattices. Numerical benchmarks indicate that this makes the realization of Schwinger pair production feasible with current technology. Our proposal is modular and an elementary building is demonstrated experimentally. We further identify dynamical topological transitions, which we discovered in the massive Schwinger model, as a suitable target for quantum simulators. Defining a gauge-invariant order parameter, these transitions are shown to persist beyond weak coupling.

In the second part of this thesis, we develop a framework for analyzing quantum simulators in terms of experimentally accessible irreducible correlation functions at equal times. We verify this approach numerically for the sine-Gordon model in thermal equilibrium, quantum simulated by two tunnel-coupled superfluids. Finally, we apply our analysis to the non-equilibrium dynamics of a spinor Bose gas, revealing suppressed effective interactions in a strongly-correlated infrared regime.

Acknowledgments

First of all, I want to express my gratitude towards my supervisor Jürgen Berges for his guidance through my doctoral studies. Our discussions shaped my view on physics in general and his support enabled the success of my projects. Second, I thank Philipp Hauke, whose time in Heidelberg luckily fell into the years of my doctoral studies. I profited a lot from his open-mindedness in discussions, where many new ideas were generated. Further, I am indebted to Fred Jendrzejewski, Jörg Schmiedmayer and Markus Oberthaler for exciting collaborations on their amazing experiments, which were of paramount importance for my work. I also want to take this opportunity to thank the administration at our institute, in particular Tina Kuka. The relevance of their work for the ITP can not be underestimated.

Thanks to all the past and present members of our research group: Valentin Kasper for his mentoring during my time as a master student, Asier Piñeiro Orioli for listening to crazy Friday's ideas, Niklas Müller for not taking things too seriously and Aleksas Mazeliauskas for always bringing in new ideas. Oscar Garcia-Montero for providing the most enjoyable coffee and the experience of sharing an office for what felt like a life-time, Robert Ott for endless discussions and coffee breaks, Linda Shen for perfecting the construction of doctoral hats, Aleksandr Chatrchyan for being humorously himself and Alexander Lehmann for being honest. Also Kirill Boguslavski, Alexander Schuckert, Roland Walz, Daniel Spitz, Malo Tarpin, Michael Heinrich, Gregor Fauth, Ignacio Aliaga Sirvent, Jan Schneider, Erekle Arshilava, Lasse Gresista, Daniel Kirchhoff, Frederick del Pozo, Dustin Peschke and everyone else for making the time in Phil'weg 12 so enjoyable. I am also very thankful for my part-time membership of SynQS, whose members treated me as one of their own. A second desk in the NaLi office was extremely valuable for our collaborations and I specifically thank Alexander Mil, also for the walrus. Thanks to Sebastian Erne and Thomas Schweigler for a great collaboration, and to the whole Vienna group for their hospitality. Special thanks to Maximilian Prüfer, for maintaining our friendship through weekly physics lunches that turned into great research.

In the life beyond physics, there could not be better friends than Florian Andreas, Jens Puschhof and Micha Wijesingha and I am looking forward to extend our traditions forever. I further want to thank Raissa Meurer and Franz Liewald for every single board game evening and a fun festival, David Becker-Koch for the shared attempt to learn the Russian language and Fabian Krajewski for Doppelkopflers bootcamp and the advice when my motorbike got lost.

Finally, I am grateful for my family, in particular my parents who supported me in every decision of my life leading to the person I am today, and Lars for being the best brother I can imagine. And Isabella, for everything else.

Thanks again to Linda, Max, Robert, David, Jürgen and Isa for valuable comments and proof-reading parts of this thesis.

Contents

Zusammenfassung	iii
Abstract	v
Acknowledgments	vii
1 Introduction	1
1.1 Motivation	1
1.2 Key concepts	2
1.3 Overview	5
I Quantum simulation of gauge theories	9
2 Implementation of lattice gauge theories with Wilson fermions	11
2.1 Introduction	11
2.2 Wilson fermions	13
2.3 Cold-atom QED	19
2.4 Details of the experimental implementation	25
2.5 Choice of experimental parameters	31
2.6 Benchmark: Onset of Schwinger pair production	34
2.7 Details of the numerical simulation	39
2.8 Summary	45
2.A The Wannier-Stark system	47
2.B Derivation of the Landau-Zener formula	51
3 Realization of a scalable building block for U(1) gauge theories	55
3.1 Proposed implementation	55
3.2 Experimental realization of the building block	58
3.3 Effective description of the building block dynamics	61
3.4 Summary	64
3.A Experimental details	65
3.B Details of the implementation	66
3.C Numerical simulation of the trapped mixture	71
3.D Spin-changing collisions as an anharmonic oscillator	77

4	Dynamical topological transitions in the massive Schwinger model	81
4.1	Motivation and setup	81
4.2	Non-interacting limit	83
4.3	Towards strong coupling	86
4.4	Summary	90
4.A	Free fermion calculations	91
4.B	Solving Gauss' law on a ring	95
II	Analyzing quantum simulators with quantum field theory	101
5	Extraction of the instantaneous effective action in equilibrium	103
5.1	Introduction	103
5.2	Extracting the irreducible vertices from equal-time correlations . . .	105
5.3	Example: Sine-Gordon model	114
5.4	Experimental results: Proof of principle	120
5.5	Summary	124
5.A	Technical details	126
5.B	Quantum thermal equilibrium	135
6	Extraction of the instantaneous effective action out of equilibrium	139
6.1	Introduction	139
6.2	Extraction of the effective action	140
6.3	Momentum and time dependence	143
6.4	Summary	145
6.A	Experimental details	147
6.B	Data analysis of correlation functions	148
6.C	Quantum field dynamics with equal-time correlations	149
7	Conclusion	159
7.1	Discussion	159
7.2	Outlook	160
	Declaration of authorship and publications	163
	Bibliography	165

List of figures and tables

2.1	Sketch of the proposed implementation of lattice QED in one spatial dimension	12
2.2	Comparison of the continuum and lattice dispersion relations	14
2.3	Sketch of a cold-atom implementation of lattice fermions in one spatial dimension	16
2.4	Sketch of the proposed implementation based on Wilson fermions . .	21
2.5	The limiting time-scales	33
2.6	Dimensionless parameters entering the lattice QED simulation	33
2.7	Benchmarking simulations	37
2.8	Particle-production rate	38
2.9	Benchmarking simulations for the second parameter set	43
2.10	Fits of the particle production rate	43
2.11	Mass-quenched simulation	45
3.1	Engineering a gauge theory	56
3.2	Tunability of the initial conditions	59
3.3	Dynamics of particle production	60
3.4	Resonant particle production	62
3.5	Integrated two-dimensional density profiles of the two-species BEC .	73
3.6	Integrated one-dimensional density profiles of the two-species BEC .	74
3.7	Illustration of a single GPE simulation with experimental imperfections	75
3.8	Particle production dynamics from averaged GPE simulations	76
3.9	Resonance shape	78
3.10	Asymmetry of the resonance and the anharmonic potential	79
4.1	Phase of the time-ordered correlator	83
4.2	Dynamical topological transitions at vanishing gauge coupling . . .	84
4.3	Dynamical topological transitions beyond weak coupling	86
4.4	Finite-size dependence of the critical times	89
5.1	Feynman diagrams relating full and connected correlation functions	109
5.2	Feynman diagrams relating connected and 1PI correlation functions	111
5.3	1PI vertices in the weak coupling regime	116
5.4	Loop corrections to the 1PI two-point function	117
5.5	Loop corrections to the 1PI four-vertex	118
5.6	1PI four-vertex as a function of Q	119

5.7	Schematics of the experimental setup	120
5.8	Cosine transformed second-order connected correlation function . .	121
5.9	Experimental 1PI two-point function	122
5.10	Experimental four-vertex	123
5.11	Running coupling	125
5.12	The different generating functionals	126
6.1	Experimental platform and extraction of correlation functions	141
6.2	Statistical significance of the four-point 1PI correlator in momentum space	142
6.3	Momentum conserving diagonals of the 1PI correlators	144
6.4	Observation of scaling in time of the distribution function and the four-vertex	146
6.5	Number of experimental realizations	148

List of abbreviations

BCH	Baker-Campbell-Hausdorff
BEC	Bose-Einstein Condensate
CP	Charge conjugation (and) Parity
DQPT	Dynamical Quantum Phase Transition
ED	Exact Diagonalization
GPE	Gross-Pitaevskii Equation
HEP	High-Energy Physics
IR	InfraRed
LGT	Lattice Gauge Theory
LZ	Landau Zener
1PI	One(1)-Particle Irreducible
(P)BC	(Periodic) Boundary Conditions
PDE	Partial Differential Equation
QCD	Quantum ChromoDynamics
QED	Quantum ElectroDynamics
QFT	Quantum Field Theory
SCC	Spin-Changing Collisions
SG	Sine-Gordon
TF	Thomas-Fermi
UV	UltraViolet
WS	Wannier-Stark

Chapter 1

Introduction

1.1 Motivation

Since quantum computers were first envisioned in the early 1980's [1, 2] the microscopic control of quantum systems has reached an unprecedented level. This progress paved the way for the fast-growing field of quantum simulation [3, 4]. By quantum simulation we understand the controlled manipulation of a physical quantum system with the purpose of emulating another quantum system [4]. While quantum simulators found their first application in condensed matter physics [5, 6], the interest in quantum simulations of high-energy physics (HEP) started growing in the last decade [7–9]. Physical phenomena arising in this context include fermion pair production [10] or string breaking [11], both occurring in the real-time dynamics of gauge theories such as quantum electrodynamics (QED) or quantum chromodynamics (QCD). Difficulties in simulating the quantum dynamics of these theories motivate the use of quantum devices, which promise to overcome the limitations of classical computational resources [3, 12]. In recent years, several theoretical proposals have been put forward, resulting in the first experimental realizations [13–16] of quantum simulators for simple small-scale model systems motivated by HEP.

Along the way towards the long-time goal of quantum simulating QCD [17], a number of open problems need to be resolved. The first theoretical task in any quantum simulation is the identification of an appropriate experimental platform, together with a mapping of the target model onto the experimental system. In this context, the improvement and extension of existing proposals to higher spatial dimensions and non-abelian gauge groups (see [7–10, 18–30] and references therein), while retaining experimental feasibility together with the possibility to reach large system sizes [31], is the key challenge. At the same time, it is necessary to identify relevant physical scenarios [32, 33] that can be addressed by a quantum simulator, taking into account experimental limitations and imperfections. Related questions are how to verify a quantum simulation [34, 35], and in particular, to what extent does the simulator respect gauge invariance [36, 37]? These questions lead to the read-out of quantum simulators in general. What observables are accessible and how to sort the relevant information [38, 39]? This thesis presents our recent contributions towards resolving these open questions. Specifically, we address the

quantum simulation of $U(1)$ gauge theories and the analysis of quantum simulators from a quantum field theory perspective.

1.2 Key concepts

The quantum simulation of HEP is an interdisciplinary field of research, bringing together different disciplines within physics. In order to bridge this gap, we give a brief introduction into key concepts relevant for this thesis: *quantum simulation*, *quantum field theory*, and *gauge theories*.

1.2.1 Quantum simulation

In a *digital* quantum computation, described by the circuit model [40], one encodes information in the quantum state of a collection of quantum bits (qubits) as a superposition of binary bit strings. An arbitrary unitary transformation of this state may then be realized in terms of elementary operations (universal quantum gates) acting on a few qubits. While it is indeed possible to simulate any local quantum system in this way [41], digital quantum simulators are not the main topic of this work.

Instead, we focus on *analog* quantum simulators. The basic idea of an analog quantum simulation is to engineer a synthetic quantum system in a highly controlled fashion in order to emulate the physics of a target model. This approach is usually formulated in the Hamiltonian picture as follows [4]. The task is to control an experimental system described by H_{sim} such that its Hamiltonian can be directly mapped to a desired model H_{target} ,

$$H_{\text{target}} \leftrightarrow H_{\text{sim}} . \quad (1.1)$$

Ideally, Eq. (1.1) should be understood as a one-to-one map¹ that identifies suitable degrees of freedom, Hilbert spaces, and the structure of the Hamiltonians on both sides. In this way, the experimental system describes the same physical content as the target model. In practice, the mapping (1.1) between target model and simulator is of course not exact, but relies on approximations. Nevertheless, an analog quantum simulation can provide important qualitative or even quantitative predictions [34].

The potential of quantum simulators is based on the structure of quantum many-body systems. In general, the Hilbert space dimension grows exponentially with the number of degrees of freedom. This fact impedes solutions using an exact diagonalization of the Hamiltonian for large systems, for instance in the thermodynamic limit. Sometimes this curse of dimensionality can be circumvented by quantum Monte-Carlo methods [42, 43] that solve the quantum many-body problem by efficient sampling from a statistical ensemble. However, these statistical approaches

¹Crucially, only relative (energy) scales matter for this mapping such that the huge difference in absolute scales between, e.g., a high-energy collision and an ultracold atom experiment is unimportant.

can break down due to so-called sign problems [44, 45], which can occur for instance in the presence of fermions or in real-time dynamics. Quantum simulators, being intrinsically of quantum nature, are a priori free of these complications and thus offer a promising alternative [3].

The platforms employed for quantum simulations range from arrays of trapped ions [46] over photons [47] and superconducting circuits [48] to ultracold atomic gases [49]. The choice of platform depends on the desired target model and the details of its implementation. In this thesis, we focus on quantum simulations based on ultracold atoms.

1.2.2 Quantum field theory

Quantum field theory (QFT) describes quantum many-body systems in the limit of infinitely many degrees of freedom. The most profound difference between (few-body) quantum mechanics and QFT is the concept of *renormalization*. In a generic QFT, quantum fluctuations introduce a dependence of coupling parameters g on the energy scale μ at which the system is observed. This scale-dependence is described within the renormalization group by beta-functions [50],

$$\beta(g) = \frac{dg}{d \log \mu}. \quad (1.2)$$

If $\beta(g) > 0$, the coupling increases with increasing energy scale. Conversely, it decreases with decreasing energy scale and therefore does not affect the low-energy physics. Consequently, the coupling is called irrelevant. The situation is reversed for $\beta(g) < 0$ and the coupling is called relevant.

Due to this behavior, the renormalization group provides the modern interpretation of QFT: A (renormalizable) QFT is determined by a finite number of relevant couplings (and the corresponding terms in the action or Hamiltonian) whose values at a given energy scale have to be fixed by an experimental measurement. At the same time, QFT can be seen as a low-energy effective theory which describes the universal long-distance behavior (determined by the relevant couplings) that is independent of the microscopic details (the irrelevant couplings) [51].

The observables of QFT are correlation functions $C^{(n)}(x_1, \dots, x_n)$, i.e., quantum expectation values of field operators at different points x_1, \dots, x_n in space-time. The way in which these correlators change at large distances between points encodes the scale-dependence of the QFT. Thus, by measuring correlation functions in a quantum simulator, it is in principle possible to access this information and to identify the relevant couplings.

For numerical calculations², a QFT can be formulated by specifying an action S with coupling parameters g on a space-time lattice with finite spacing a . Formally, a provides an ultraviolet (UV) regulator and sets the energy scale $\mu \sim 1/a$ at which

²In fact, this is more than a practicality: The lattice approach provides a *definition* of QFTs beyond perturbation theory.

S with its parameters g is defined. One then calculates correlators according to a functional integral with a weight determined by S . Finally, one has to reduce a while keeping certain values of (renormalized) correlators fixed, such as a physical mass m [52]. The existence of a continuum limit with finite m means that it is possible to approach the limit $a \rightarrow 0$ with fixed m by appropriately adjusting the parameters g according to $\beta(g)$. In this limit, the correlation length $\xi = (ma)^{-1}$, which controls the exponential decay of the correlator $C^{(2)}(x, 0) \sim e^{-|x|/\xi}$ at large distances, diverges. In practice, this allows to extract the physical behavior at small but finite a from a suitable scaling analysis [52].

Throughout this thesis, we employ a Hamiltonian formulation of QFT. While this choice is less common in the HEP context, it is most convenient for quantum simulations because we aim to identify an experimental setup with a target model according to Eq. (1.1). Within this approach, it is also useful to employ a Hamiltonian lattice regularization where space is discretized but time is kept continuous.

1.2.3 Gauge theories

The concept of symmetries is ubiquitous in theoretical physics. It describes that certain aspects of a physical model are preserved under transformations described by a corresponding symmetry group. Most prominent examples include the invariance of the laws of classical mechanics under spatial translations and rotations. These *global* symmetries imply, via Noether's theorem [53], the conservation of linear and angular momentum.

A symmetry is called *local* if the corresponding transformation can act differently at every point in space-time. Loosely speaking, gauge theories are physical models with such local symmetries. More precisely, a gauge theory can be defined as a field theory whose action is gauge invariant, i.e., it remains unchanged under local transformations specified the gauge group [50]. Among the simplest examples are $U(1)$ gauge theories, such as QED. Here, a global $U(1)$ symmetry implies the conservation of an associated charge Q . Gauge invariance further ties local changes of this charge to the surrounding gauge fields. For example, in electrodynamics the electric charge density ρ and the corresponding current \mathbf{j} are coupled to electric \mathbf{E} and magnetic fields \mathbf{B} according to Maxwell's equations [54].

The framework of lattice gauge theories (LGT) implements the lattice formulation of QFT while retaining gauge invariance exactly [52, 55]. This formulation provides a non-perturbative definition of quantum gauge field theories and has proven to be invaluable for numerical simulations. It is also perfectly suited for quantum simulators as discussed in this thesis.

In the Hamiltonian formulation of LGTs [56], gauge invariance implies an extensive³ number of conserved quantities described by operators G_n that commute with

³Here we mean extensive in the thermodynamic sense: There exist constraints at every lattice point n and thus the number of constraints increases linearly with the system size.

the Hamiltonian H ,

$$[G_n, H] = 0. \quad (1.3)$$

Additionally, the allowed states $|\text{phys}\rangle$ are restricted to be eigenstates of G_n . These constraints make a prediction of the resulting dynamics extremely challenging.

1.3 Overview

In this work, we specifically address the quantum simulation of gauge theories and the analysis of quantum simulators from a QFT perspective. Accordingly, this thesis is structured in two parts. In the remainder of this introduction, we give a brief overview over our contributions to the quantum simulation of HEP.

1.3.1 Quantum simulation of gauge theories

The main target model of part I is QED in one spatial dimension, also known as the massive Schwinger model. This model is one of the simplest theories to describe charged matter interacting with gauge fields, here electrons and positrons interacting with an electric field. Sharing certain features with QCD, the massive Schwinger model has proven to be a valuable toy model for HEP [57].

Implementation of lattice gauge theories with Wilson fermions. In chapter 2, we describe a detailed proposal [29] to implement the massive Schwinger model with a mixture of ultracold bosons and fermions trapped in an optical lattice potential. Here, two hyperfine states of the bosonic and fermionic species are used to implement the gauge and matter fields, respectively. Following earlier proposals [10, 18], we realize the gauge-invariant interaction with hetero-nuclear collisions that exchange angular momentum between the two species. Crucially, these spin-changing collisions (SCC) conserve the global magnetization, which – by careful engineering of the trapped mixture – is turned into a local symmetry that furnishes the required $U(1)$ gauge invariance of QED.

In contrast to earlier proposals, we exploit the possibility to use different lattice formulations leading to the same continuum theory to improve our setup by using Wilson fermions. With numerical benchmark simulations, we show that an optimized set of experimental parameters allows to observe the process of Schwinger pair production, i.e., the creation of electron-positron pairs from the fermionic vacuum due to a strong electric field. In particular, we show that the non-perturbative nature of this effect can be extracted quantitatively from a quantum simulation with currently available technology.

Realization of a scalable building block for $U(1)$ gauge theories. The following chapter 3 extends our proposal by giving up the direct correspondence between

the lattice sites of the target model and the lattice wells of the simulator. In this way, the gauge-invariant interaction is isolated in an elementary building block, which simplifies the experimental realization. An extended $U(1)$ gauge theory can be realized by connecting multiple building blocks via laser-assisted tunneling, demonstrating the potential scalability of our approach.

We further describe our recent experiment [16] that realizes a single building block with bosonic instead of fermionic matter. The faithful representation of this minimal $U(1)$ gauge theory and its full tunability is demonstrated experimentally, which we verify by comparison to numerical simulations of the target model including experimental imperfections.

Dynamical topological transitions in the massive Schwinger model. The first part closes with chapter 4, which focuses on an extension of the massive Schwinger model that includes a so-called topological θ -term. This term originates in the vacuum structure of the theory and analogous terms also appear for other gauge theories, in particular QCD in three spatial dimensions. In both cases, the topological term breaks combined charge conjugation and parity (CP) symmetry, i.e., the invariance of the model under a simultaneous reflection of space and the exchange of positively and negatively charged excitations. Experimental observations indicate that QCD conserves CP [58], which implies the absence of a θ -term. This puzzle has been coined the strong CP problem. Its most common resolution [59] involves an additional hypothetical field (the axion) that leads to a dynamical relaxation of the θ -term.

Motivated by this solution to the strong CP problem, we study the dynamics of the massive Schwinger model after a quench of its θ -term [33]. We discover dynamical topological transitions, which are signaled by an order parameter that we construct from gauge-invariant time-ordered two-point correlation functions of the matter fields. These transitions are related to dynamical quantum phase transitions (DQPT), which have been observed previously in condensed matter lattice models [60]. Our results show that DQPTs also exist in the continuum limit. Moreover, our numerical simulations indicate that the transitions persist in the presence of interactions. Furthermore, these transition can robustly be identified on small lattices due to their topological origin. Together with their occurrence on short time-scales, the dynamical topological transitions constitute an ideal target for quantum simulations of QED.

1.3.2 Analyzing quantum simulators with quantum field theory

The focus of part II lies on the read-out of quantum simulators. We address the question of how to sort the information that can be extracted by measuring higher-order correlation functions. To this end, we apply the concept of one-particle irreducible (1PI) correlators [50], which constitute the building blocks of every QFT.

Extraction of the instantaneous effective action in equilibrium. In chapter 5, we first give a detailed review of the different types of correlation functions and the associated generating functionals which occur in the construction of QFTs. In contrast to the standard approach, we employ a formulation [61] based on correlation functions at equal times, which have become accessible in recent quantum simulation experiments [38]. We show that the measurement of equal-time 1PI correlators, which are generated by the instantaneous effective action, allows to extract the momentum-dependence of effective interaction vertices, thereby providing important information about the scale-dependence of the underlying QFT.

In thermal equilibrium, we test our approach [39] for the example of the Sine-Gordon model, a paradigmatic QFT in one spatial dimension. Numerical simulations exhibit excellent agreement with qualitative and quantitative analytical expectations, which verifies our method. Additionally, the model is quantum simulated by two tunnel-coupled superfluids in a proof-of-principle experiment that confirms the possibility to extract the field theory description of a quantum many-body system from experimental data.

Extraction of the instantaneous effective action out of equilibrium. The chapter 6 extends the approach developed in the previous chapter and contains a first application out of equilibrium. Here, the experimental platform is a spin-1 Bose gas that has recently been employed to quantum simulate the physics of non-thermal fixed points [62]. The latter are characterized by a self-similar evolution of an emergent (particle number) distribution function in momentum and time. The theoretical description of non-thermal fixed points remains challenging as it requires non-perturbative methods due to strong correlations (large occupations) in the infrared (IR) regime. Approximate kinetic descriptions [63, 64] suggest that the dynamics is driven by an effective momentum-dependent interaction vertex.

Our analysis [65] of the non-equilibrium dynamics in terms of equal-time 1PI correlators indeed reveals a similar qualitative behavior. We find a strong suppression of the 1PI four-vertex in a strongly-correlated IR regime. Additionally, the structure of this vertex indicates momentum conservation, which signals spatial translation invariance of the quantum simulation. These results demonstrate the capabilities of quantum simulators to provide input for improving QFT descriptions of challenging non-equilibrium situations.

Conclusion. We discuss our results and their relevance for the quantum simulation of HEP in the concluding chapter 7. In the final section, we give an outlook for future research directions.

1.3.3 Statement of contribution

The five main chapters of this thesis are based on research articles [16, 29, 33, 39, 65] that are either published or being considered in peer-reviewed journals. Since

modern physics is a collaborative research effort, I am not the single author of any of these articles. While none of the discussed experiments were carried out by myself, I performed most of the theoretical calculations. My personal contributions to the articles [16, 29, 33, 39, 65] are clearly indicated in the beginning of the corresponding chapters where I list the contributions of all authors and mark the inclusion of additional material.

Part I

Quantum simulation of gauge theories

Chapter 2

Implementation of lattice gauge theories with Wilson fermions

This chapter is based on the article [29] with the figures and large parts of the text taken from it. The improved implementation based on Wilson fermions was developed in discussions among all authors (F. Hebenstreit, F. Jendrzejewski, M. Oberthaler, J. Berges, P. Hauke and myself). While all authors participated in the writing of the manuscript [29], I made significant contributions to the wording and structuring of the text. The explicit calculations, i.e., the parameter estimates and the numerical simulation, were performed by me. In the appendices 2.A and 2.B, I include additional related material that was not printed in [29].

2.1 Introduction

Even though many proposals to quantum simulate gauge theories exist, there is yet no experimental realization capable of simulating relevant physical processes, such as Schwinger pair production of fermions and anti-fermions in the presence of strong electric fields [66, 67] or string breaking due to confinement [68–70]. Further progress hinges crucially on efficient implementations, such that present state-of-the-art experimental resources become sufficient to achieve this goal. In view of finding optimal implementations, the Nielsen-Ninomiya no-go-theorem [71] becomes particularly important: it states that it is not possible to discretize relativistic fermions while retaining the relevant symmetries of the continuum theory. Being forced to make a choice between discretizations with different symmetry properties, one should be guided by the requirements of the task at hand, e.g, by conceptual advantages, numerical efficiency, or – as discussed here – ease of experimental implementation. So far, however, most proposals for the engineering of quantum simulators for lattice gauge theories employ one specific discretization procedure via the so-called staggered fermion formulation [72].

In this chapter, we propose the use of an alternative discretization based on Wilson fermions [73]. As discussed below, Wilson fermions have conceptual advantages over staggered fermions when going to higher dimensions. Moreover, we show that Wilson fermions can provide a very efficient framework for the experimental

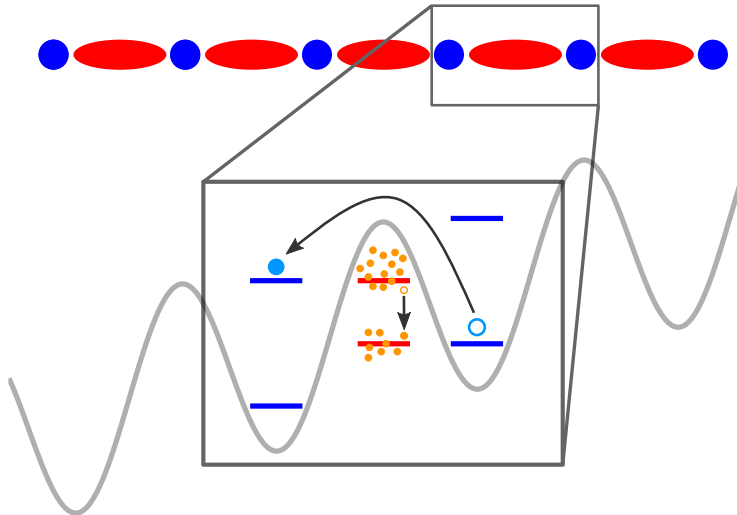


FIGURE 2.1: Sketch of the proposed implementation of lattice QED in one spatial dimension. Fermions trapped on the lattice sites (blue circles) are coupled via a correlated interaction with the Bose condensates residing on the links (red ellipses). The zoom schematically shows how the gauge-invariant coupling can be realized via spin-changing collisions between the fermions (blue) and bosons (orange) in a tilted optical lattice. This process involves two internal states per species as indicated by the blue and red bars.

implementation of gauge theories using ultracold atoms in optical lattices. As an example, we discuss QED in $1 + 1$ space-time dimensions implemented with a two-species mixture. Radiofrequency-dressed ${}^6\text{Li}$ atoms act as the fermionic matter, while small condensates of bosonic ${}^{23}\text{Na}$ atoms represent the dynamical gauge fields. Inter-species spin-changing collisions generate the dynamics of an interacting gauge theory, where local gauge invariance is ensured by angular momentum and energy conservation, see Fig. 2.1. Strikingly, the use of Wilson fermions enables an implementation through tilted optical lattices, instead of the more involved superlattices employed for staggered fermions [11]. We benchmark our proposal by a theoretical analysis, and show that the non-perturbative onset of Schwinger pair production may be observed in realistic experimental settings.

Wilson fermions have been considered previously in a cold-atom context for the quantum simulation of topological insulators [74–76]. In contrast, we are interested here in the full, interacting quantum theory with dynamical gauge fields.

This chapter is organized as follows. In Sec. 2.2, we present the lattice Hamiltonian of Wilson fermions. We show that an optimal choice of parameters significantly simplifies the resulting setup, and we compare it to the staggered-fermion formulation. In Sec. 2.3, we discuss how the theory is promoted to a gauge theory by the introduction of dynamical gauge fields. Moreover, we reformulate the gauge theory to match it with the degrees of freedom available in cold atomic gases and propose a possible implementation in a Bose-Fermi mixture in an optical lattice. We give an intuitive interpretation of various processes appearing in the proposed experimental setup, describe the envisioned experimental protocol, and discuss possible

limitations. Sections 2.4 and 2.5 give details on the experimental implementation and the choice of parameters, respectively. In Sec. 2.6, we benchmark the proposed experiment with the example of the Schwinger mechanism. In particular, we show that an experiment with realistic parameters may extract the rate of particle–anti-particle production. Details of the numerical simulation are discussed in Sec. 2.7. Section 2.8 presents our conclusions.

2.2 Wilson fermions

Before turning to dynamical gauge theories describing the Lorentz-invariant interaction of fermionic matter with gauge bosons, we momentarily drop the gauge degrees of freedom for clarity. The non-interacting fermion part of the theory is described in the continuum in d spatial dimensions by the Dirac Hamiltonian

$$H_D = \int d^d \mathbf{x} \psi^\dagger(\mathbf{x}) \gamma^0 [i\gamma^j \partial_j + m] \psi(\mathbf{x}), \quad (2.1)$$

where $\psi(\mathbf{x})$ is a fermionic Dirac spinor with $2^{d/2}$ components for d even and $2^{(d+1)/2}$ components for d odd. The γ^0 and γ^j denote the gamma matrices in $d+1$ space-time dimensions [77] and ∂_j is a partial derivative in the spatial direction $j = 1, \dots, d$. This Hamiltonian describes the kinetic energy and rest mass m of Dirac fermions and leads to the dispersion relation of relativistic particles with energy $\sqrt{m^2 + \mathbf{p}^2}$.

2.2.1 The doubling problem

For simulations on classical computers as well as on quantum devices consisting of sites in optical lattices or arrays of qubits, the continuum theory has to be discretized on a lattice. In view of quantum simulation, we work here in the Hamiltonian lattice formalism, with spatial lattice spacing a and continuous *real* time t .

The simplest discretization of fermions replaces the kinetic energy in Eq. (2.1) with a nearest-neighbor hopping term. This naive procedure, however, leads to a discretized model with an additional “doubling symmetry” [78]. Its physical consequence is the appearance of spurious states, where each fermion in the continuum theory leads to 2^d fermion species for d discretized dimensions, see Fig. 2.2. These additional degrees of freedom affect the extrapolation to the continuum limit such that the correct continuum results are not recovered.

The Nielsen–Ninomiya no-go-theorem [71] implies that, in order to remove these doublers, one has to sacrifice at least one of several fundamental characteristics of the continuum derivative: hermiticity, locality, discrete translational symmetry or chiral symmetry. The choice which of these characteristics to sacrifice gives room for various strategies [79], with the staggered fermion [72] and Wilson fermion [80] prescriptions being among the ones most commonly known.

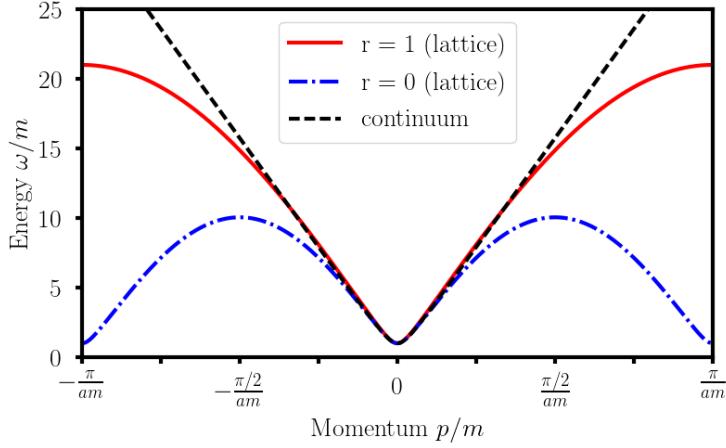


FIGURE 2.2: Comparison of the continuum and lattice dispersion relations, plotted within the first lattice Brillouin zone for lattice spacing $a = 0.1/m$ and $d = 1$ spatial dimension. The black, dashed line is the continuum result given by the Dirac Hamiltonian (2.1), the low-energy behavior of which we aim at reproducing. Discretizing the continuum kinetic energy by a nearest-neighbor hopping yields the blue, dashed-dotted dispersion relation, which has spurious low-energy states. The addition of a Wilson term, see Eq. (2.3), removes the minima at the edge of the Brillouin zone, and thus effectively eliminates the fermion doublers (red, solid line; plotted here for $r = 1$).

2.2.2 Non-interacting Wilson fermions

Wilson fermions sacrifice chiral symmetry to decouple the doublers from the low-energy degrees of freedom that describe the continuum theory. Despite the lack of chiral symmetry, relevant real-time phenomena can be efficiently simulated with Wilson fermions, with accuracy comparable to alternative implementations that respect chiral symmetry [81].

Wilson fermions can be understood as the addition of a second-order derivative, which is discretized as

$$-\frac{a}{2} \int d^d \mathbf{x} \sum_j \psi^\dagger(\mathbf{x}) \gamma^0 \partial_j^2 \psi(\mathbf{x}) \rightarrow -\frac{a}{2} \sum_{\mathbf{n}} a^d \left(\psi_{\mathbf{n}}^\dagger \gamma^0 \sum_j \frac{\psi_{\mathbf{n}+\mathbf{e}_j} - 2\psi_{\mathbf{n}} + \psi_{\mathbf{n}-\mathbf{e}_j}}{a^2} \right). \quad (2.2)$$

Here and in the following, the fermionic Dirac spinor $\psi_{\mathbf{n}}$ is located at lattice site $\mathbf{n} = (n_j)_{j=1,\dots,d}$ and \mathbf{e}_j denotes a translation by a single site along the spatial direction j . This so-called Wilson term together with a hermitian discretization of the Dirac Hamiltonian (2.1) yields the lattice Hamiltonian of Wilson fermions,

$$H_W = \sum_{\mathbf{n}} a^d \psi_{\mathbf{n}}^\dagger \gamma^0 \left(m + \frac{dr}{a} \right) \psi_{\mathbf{n}} - \frac{a^{d-1}}{2} \sum_{\mathbf{n}} \left(\psi_{\mathbf{n}}^\dagger \gamma^0 \sum_j [i\gamma^j + r] \psi_{\mathbf{n}+\mathbf{e}_j} + \text{h.c.} \right). \quad (2.3)$$

The Wilson term is proportional to the lattice spacing a and thus does not contribute

in the continuum limit $a \rightarrow 0$. Nevertheless, for any $a > 0$ it suppresses the fermion doublers as low-energy degrees of freedom, which is illustrated in Fig. 2.2. This assures the recovery of the relevant continuum theory in the limit $a \rightarrow 0$. The strength of the Wilson term, given by the Wilson parameter r , can be adjusted in the range $0 < |r| \leq 1$ while still describing the same continuum theory [52]. In the following, we will exploit this freedom to optimize the implementation in a cold-atom quantum simulator.

2.2.3 Optimized Hamiltonian

In principle, the matrices $i\gamma^0\gamma^j + r\gamma^0$ in Eq. (2.3) couple all components of the spinors on neighboring lattice sites. In an optical-lattice implementation, each of these couplings needs to be realized by a separate hopping process, which in the full gauge theory discussed below will moreover require the correct interactions with the gauge fields. With regard to experimental feasibility, it is thus highly desirable to minimize the number of coupling terms. In view of our application to Schwinger pair production below, we consider the case of one spatial dimension, $d = 1$, where the gamma matrices can be represented with the three Pauli matrices σ^α , $\alpha = x, y, z$,

$$\gamma^0 = \sigma^\alpha, \quad \gamma^1 = i\sigma^\beta, \quad (\alpha \neq \beta). \quad (2.4)$$

In the following, we choose $\alpha = x$ and $\beta = z$. In the Hamiltonian (2.3), the second term then takes a particularly simple form by adjusting the Wilson parameter to $r = 1$, such that

$$\gamma^0 = \begin{pmatrix} 0 & 1 \\ 1 & 0 \end{pmatrix}, \quad \gamma^1 = \begin{pmatrix} i & 0 \\ 0 & -i \end{pmatrix}, \quad i\gamma^0\gamma^1 + r\gamma^0 = \begin{pmatrix} 0 & 2 \\ 0 & 0 \end{pmatrix} \quad (2.5)$$

These choices lead to the Hamiltonian

$$H_W = \left(m + \frac{1}{a}\right) \sum_n \left(\psi_{n,1}^\dagger \psi_{n,2} + \text{h.c.}\right) + \frac{1}{a} \sum_n \left(\psi_{n,1}^\dagger \psi_{n+1,2} + \text{h.c.}\right), \quad (2.6)$$

where we have substituted $\psi_n \rightarrow \sqrt{a}(-1)^n \psi_n$ and written out the components, $\psi_n = (\psi_{n,1}, \psi_{n,2})$, which fulfill the anti-commutation relations

$$\{\psi_{n,\alpha}, \psi_{n',\beta}^\dagger\} = \delta_{\alpha\beta} \delta_{nn'}. \quad (2.7)$$

The above choice of the γ -matrix representation and Wilson parameter is optimal in the sense that only one out of four possible terms that couple neighboring lattice sites remains.

Though the striking simplicity of (2.6) is special for one spatial dimension, in higher dimensions one can apply the same strategy of choosing different values of r , representations of γ^μ , and canonical transformations to $\psi_{\mathbf{n}} \rightarrow C_{\mathbf{n}}\psi_{\mathbf{n}}$ to optimize for experimental needs.

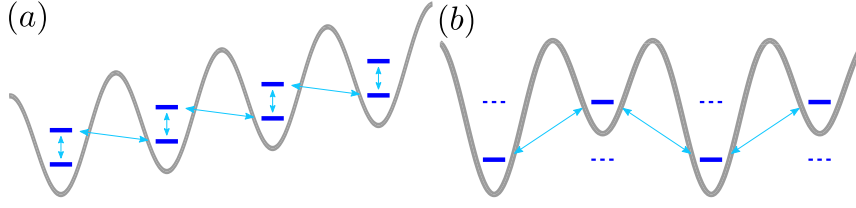


FIGURE 2.3: Sketch of a cold-atom implementation of lattice fermions in one spatial dimension. (a) Optimized Wilson formulation; (b) staggered formulation. The levels (blue) representing fermionic atoms are coupled as indicated with arrows. The gray curves represent optical potentials. The Hamiltonian of Wilson fermions (2.6) has a ladder-like structure, which suggests that it can be implemented in a tilted lattice, while proposals with staggered fermions based on (2.8) typically require an optical superlattice [11].

2.2.4 Comparison to staggered fermions

It is instructive to compare the above Wilson Hamiltonian to the lattice Hamiltonian of staggered fermions as it has been used in previous proposals for quantum simulators of lattice gauge theories. Staggered fermions sacrifice the discrete translational invariance on the lattice. They give a particularly simple formulation in one spatial dimension, where they enable one to analytically remove the fermion doublers [82]. The Hamiltonian for non-interacting fermions reads in this case

$$H_{\text{st}} = \sum_n \left\{ m (-1)^n c_n^\dagger c_n - \frac{i}{2a} [c_n^\dagger c_{n+1} - \text{h.c.}] \right\}. \quad (2.8)$$

Here, the Dirac spinor is decomposed onto neighboring lattice sites such that there is only one fermionic degree of freedom c_n living on each site.

In contrast, the Wilson formulation contains two components $\psi_{n,1}$ and $\psi_{n,2}$ at each lattice site, and thus realizes the same number of degrees of freedom in only half the space. Moreover, as discussed in the next section, gauge fields enter only on links connecting different lattice sites, such that Wilson fermions require only about half the gauge degrees of freedom.

A prominent difference of Eq. (2.8) with respect to the optimized Wilson formulation (2.6) concerns the sign factors appearing in the staggered mass term, which are also present in the interacting Hamiltonian that takes gauge fields into account. The experimental realization of the alternating on-site energy typically requires an optical superlattice [11], while the Wilson formulation suggests a tilted potential as illustrated in Fig. 2.3. The tilted potential could be less demanding experimentally and can be used to suppress unwanted tunneling processes as discussed in detail in Section 2.3.

Moreover, the decoupling of fermion doublers in the staggered formulation is special to $1 + 1$ space-time dimensions [52]. The theory becomes considerably more involved in higher dimensions where multiple, coupled fermion species have to be simulated. The resulting theory involves several coupled fermion species called “tastes”, and the computation of physical observables requires a correction scheme by

taking roots of the staggered fermion determinant. This “rooting procedure” is sometimes discussed controversially, but in practice many complications come from the multi-parameter fitting procedures that are required because of (“taste”) symmetry violations involving the spurious degrees of freedom in staggered formulations [52].

In comparison, the Wilson decoupling of spurious doublers proceeds along the same lines in one or more spatial dimensions. On the other hand, while the low-energy sector of staggered fermions produces the correct dispersion relation up to order a^2 , the usual Wilson Hamiltonian is only accurate to first order in the lattice spacing a . Nevertheless, as it has been recently shown, relatively simple (“tree-level”) improvements enable a remarkably good scaling towards the continuum limit of relevant real-time processes of QED and QCD in three spatial dimensions [83–85]. These include not only Schwinger pair production but also, e.g., the important phenomenon of anomalous currents due to the presence of quantum anomalies in QED and QCD. The latter depend crucially on the chiral characteristics of the system, showing that the explicit breaking of chiral symmetry by Wilson fermions is no fundamental roadblock.

2.2.5 Coupling to gauge fields

The strong potential of Wilson fermions for atomic quantum simulations becomes fully apparent when considering interacting gauge theories, as we will discuss now. Prominent examples for interacting gauge theories include QED based on the Abelian $U(1)$ gauge group, and QCD with underlying non-Abelian $SU(3)$ gauge group [52].

To illustrate the use of Wilson fermions, we proceed by focusing on the relatively simple example of the gauge group $\mathcal{G} = U(1)$ as realized in QED, where the fermionic matter fields $\psi_{\mathbf{n}}$ represent single-flavor Dirac spinors. In this case, since the $U(1)$ gauge group is local, gauge transformations amount to multiplication of the fermion fields with a potentially site-dependent phase $\alpha_{\mathbf{n}}$,

$$\psi_{\mathbf{n}} \rightarrow \psi'_{\mathbf{n}} = e^{i\alpha_{\mathbf{n}}} \psi_{\mathbf{n}} . \quad (2.9)$$

Hopping terms such as $\psi_{\mathbf{n}}^\dagger \psi_{\mathbf{n}+\mathbf{e}_j}$ appearing in the non-interacting fermion Hamiltonian (2.3) are not invariant under this local gauge transformation for arbitrary non-constant $\alpha_{\mathbf{n}} \neq \alpha_{\mathbf{n}+\mathbf{e}_j}$.

In the interacting gauge theory, gauge invariance is obtained by coupling to operators $U_{\mathbf{n},j}$, which reside on the links between two neighboring lattice sites \mathbf{n} and $\mathbf{n} + \mathbf{e}_j$, and which transform as

$$U_{\mathbf{n},j} \rightarrow U'_{\mathbf{n},j} = e^{i\alpha_{\mathbf{n}}} U_{\mathbf{n},j} e^{-i\alpha_{\mathbf{n}+\mathbf{e}_j}} . \quad (2.10)$$

The transformations (2.9) and (2.10) can be realized as $\psi'_{\mathbf{n}} = V^\dagger \psi_{\mathbf{n}} V$ and $U'_{\mathbf{n},j} =$

$V^\dagger U_{\mathbf{n},j} V$ via the unitary operator $V = \exp[-i/e \sum_{\mathbf{n}} \alpha_{\mathbf{n}} G_{\mathbf{n}}]$ with the hermitian generator $G_{\mathbf{n}} = \sum_j (E_{\mathbf{n},j} - E_{\mathbf{n}-\mathbf{e}_j,j}) - e\psi_{\mathbf{n}}^\dagger \psi_{\mathbf{n}}$ ¹. Here, $E_{\mathbf{n},j}$ is the conjugate field to $U_{\mathbf{n},j}$, which fulfills the commutation relation

$$[E_{\mathbf{n},j}, U_{\mathbf{m},k}] = e\delta_{jk}\delta_{\mathbf{n},\mathbf{m}}U_{\mathbf{m},k}. \quad (2.11)$$

Gauge invariance corresponds to $[G_{\mathbf{n}}, H] = 0$. Thus, the full Hilbert space can be decomposed into sectors corresponding to different eigenvalues $q_{\mathbf{n}}$ of $G_{\mathbf{n}}$, and the physical Hilbert space is defined by picking a suitable subspace. Physically, the $q_{\mathbf{n}}$ are interpreted as the conserved charges of the group $\mathcal{G} = U(1)$, i.e., the electric charge. The restriction of the accessible Hilbert space to a single eigensector of the generator $G_{\mathbf{n}}$ is the lattice analogue of the familiar Gauss' law, which states that the electric charge is locally conserved, i.e., $\nabla E = \rho$. To fulfill the requirement of gauge invariance, in the interacting theory the hopping terms in the lattice Hamiltonian (2.3) are replaced by the combination $\psi_{\mathbf{n}}^\dagger U_{\mathbf{n},j} \psi_{\mathbf{n}+\mathbf{e}_j}$, which couples the dynamics of the fermions to that of the gauge fields.

The presence of the gauge fields is associated to an energy cost, governed by the electric Hamiltonian²

$$H_E = \frac{a^{2-d}}{2} \sum_{\mathbf{n},j} E_{\mathbf{n},j}^2. \quad (2.12)$$

This Hamiltonian is gauge invariant and implements the equations of motion for U that give rise to the correct continuum limit as $a \rightarrow 0$ [56]. In spatial dimensions higher than $d = 1$, the gauge fields also have a magnetic contribution H_B , for details on which we refer to Refs. [56]. In total, we end up with the lattice Hamiltonian of QED with Wilson fermions as

$$H_{\text{QED}} = H_E + H_B + \sum_{\mathbf{n}} \psi_{\mathbf{n}}^\dagger \gamma^0 \left(m + \frac{r}{a} \right) \psi_{\mathbf{n}} \quad (2.13)$$

$$- \frac{1}{2a} \sum_{\mathbf{n}} \left(\psi_{\mathbf{n}}^\dagger \gamma^0 \sum_j [i\gamma^j + r] U_{\mathbf{n},j} \psi_{\mathbf{n}+\mathbf{e}_j} + \text{h.c.} \right).$$

As far as the fermion sector is concerned, it is straightforward to generalize the above construction also to non-Abelian gauge theories. In the fundamental representation of $SU(N)$, the fermion spinors carry an additional group index and the link variables require a different formulation, but the structure of the gauge-matter interactions as given by Eqs. (2.9) and (2.10) remains the same [52]. For

¹The definition of $G_{\mathbf{n}}$ is not unique. The sign of e and a possible constant shift are conventions depending on the definition of the fermionic charge operator (see Eq.s (2.15) and (2.24)).

²The power of a arises from our choice of dimensions, where $[E] = [e] = (3-d)/2$ in units where $[m] = 1$, in contrast to $[\tilde{E}] = (d+1)/2$ in the continuum. While both choices agree for $d = 1$, in our convention the phase α is dimensionless for all d . Similarly, we rescaled ψ to be dimensionless in contrast to $[\tilde{\psi}] = d/2$ in the continuum.

staggered fermions, implementations of non-Abelian gauge theories with cold atoms have been discussed in Refs. [19, 23, 24].

2.3 Cold-atom QED

The lattice gauge theory written in Eq. (2.13) consists of fermions interacting with gauge fields. We now reformulate the theory in a way that matches the degrees of freedom available in cold atomic gases, using the simplest case of QED in one spatial dimension, also known as the massive Schwinger model [86]. In this case, Eq. (2.13) simplifies due to the absence of the magnetic field term H_B and we can adopt the compact form of Eq. (2.6).

2.3.1 Optimized cold-atom Wilson Hamiltonian

Using the same optimization choices as led to Eq. (2.6), Eq. (2.13) yields the quantum many-body Hamiltonian

$$H_{\text{QED}} = \sum_n \left\{ \frac{a}{2} E_n^2 + \left(m + \frac{1}{a} \right) \psi_n^\dagger \begin{pmatrix} 0 & 1 \\ 1 & 0 \end{pmatrix} \psi_n \right\} + \frac{1}{a} \sum_n \left\{ \psi_n^\dagger \begin{pmatrix} 0 & 1 \\ 0 & 0 \end{pmatrix} U_n \psi_{n+1} + \text{h.c.} \right\}. \quad (2.14)$$

To alleviate notation, we label the gauge fields for $d = 1$ only with the site to the left, i.e., $E_n = E_{n,j=1}$ and analogously for U . Here, $n = 1 \dots N$ is the number of lattice sites. Thanks to the choices of the previous section, the number of links carrying the gauge–matter interactions is only half that of staggered fermions for the same number of quantum simulated fermionic degrees of freedom.

The generators of the gauge transformations are now given by

$$G_n = E_n - E_{n-1} + e \left(1 - \sum_{\alpha=1,2} \psi_{n,\alpha}^\dagger \psi_{n,\alpha} \right). \quad (2.15)$$

We choose our physical states from the zero-charge sector $G_n |\text{phys}\rangle = 0$.

The remaining procedure is similar to previous implementations with staggered fermions [10, 87]. The commutation relation (2.11), together with the requirements of E being hermitian and U being unitary, can only be fulfilled in an infinite-dimensional Hilbert space. Since the quantum control of infinitely many degrees of freedom is in practice impossible, we adopt the so-called quantum link [88] formalism as a regularization, which replaces the gauge operators on each link by spin operators,

$$E_n \rightarrow e L_{z,n}, \quad U_n \rightarrow [\ell(\ell + 1)]^{-1/2} L_{+,n}, \quad (2.16)$$

with $[L_{n,\alpha}, L_{m,\beta}] = i\delta_{nm}\epsilon_{\alpha\beta\gamma}L_{m,\gamma}$, $\alpha, \beta, \gamma \in \{x, y, z\}$ and $L_{\pm,n} = L_{x,n} \pm iL_{y,n}$. This regularization leaves gauge invariance and the commutation relation (2.11) intact, but sacrifices unitarity of the link operators, which now fulfill the commutation relation $[U_n, U_m^\dagger] = 2\delta_{nm}E_m/[c\ell(\ell+1)]$. Already for small representations of the quantum spin [89], quantum link models share salient features with QED, such as confinement and string breaking [23]. Moreover, in the limit of large spins ($\ell \rightarrow \infty$), which we are focusing on, one recovers full QED [10]. Finally, we represent the spin operators with two Schwinger bosons,

$$L_{z,n} = \frac{1}{2} \left(b_n^\dagger b_n - d_n^\dagger d_n \right), \quad L_{+,n} = b_n^\dagger d_n, \quad (2.17)$$

which fulfill the constraint

$$2\ell = b_n^\dagger b_n + d_n^\dagger d_n. \quad (2.18)$$

This yields the final Hamiltonian that may be realized with cold atoms in an optical lattice,

$$\begin{aligned} H_{\text{CA}} = & \frac{ae^2}{4} \sum_n \left(b_n^\dagger b_n^\dagger b_n b_n + d_n^\dagger d_n^\dagger d_n d_n \right) + \left(m + \frac{1}{a} \right) \sum_n \left(\psi_{n,1}^\dagger \psi_{n,2} + \text{h.c.} \right) \\ & + \frac{1}{a\sqrt{\ell(\ell+1)}} \sum_n \left(\psi_{n,1}^\dagger b_n^\dagger d_n \psi_{n+1,2} + \text{h.c.} \right), \end{aligned} \quad (2.19)$$

where we used that $L_{z,n}^2 = (b_n^\dagger b_n - \ell)^2/2 + (\ell - d_n^\dagger d_n)^2/2$ and dropped an irrelevant constant. As it becomes apparent in this formulation, gauge degrees of freedom only enter in couplings between matter fields at different sites, but not in the on-site terms $\sim \psi_{n,1}^\dagger \psi_{n,2}$.

2.3.2 Experimental implementation

We propose to realize the Hamiltonian (2.19) with a Bose-Fermi mixture in a tilted optical lattice as sketched in Fig. 2.4. Transverse motion is frozen out by a strong radial confinement, rendering the system effectively one-dimensional. The mixture is additionally subjected to an optical lattice potential that is attractive (repulsive) for the fermions (bosons), such that the atomic species are allocated in an alternating fashion. In the following, we will refer to the positions of the fermions (bosons) as sites (links). For a sufficiently deep lattice, the atoms will occupy localized Wannier states, such that tunneling beyond neighboring sites (links) can be neglected. Tilting the optical potential suppresses this direct tunneling and effectively localizes the atoms on single sites (links). Moreover, the species are prepared in two selected hyperfine states each (denoted by annihilation operators $\psi_{1,n}, \psi_{2,n}$ respectively b_n, d_n). The desired dynamics governed by Eq. (2.19) can now be realized by implementing the following three interactions among these states (angular momentum and energy conservation ensure that the dynamics accesses no other states [18, 87]).

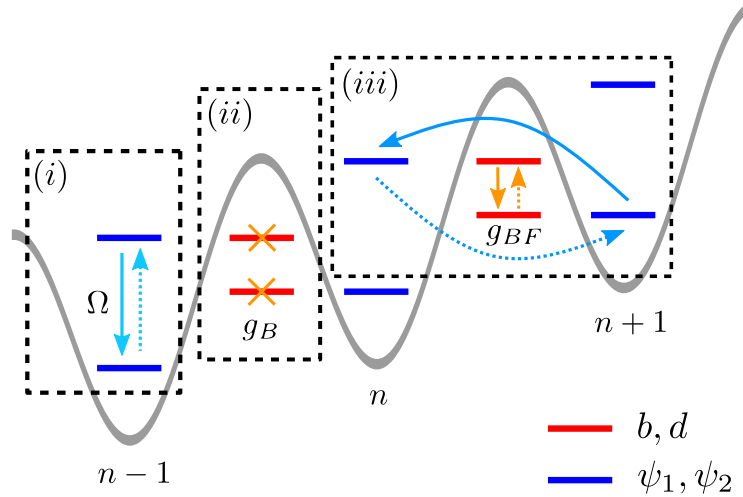


FIGURE 2.4: Sketch of the proposed implementation. Fermions and bosons (blue and red bars, respectively) can occupy two hyperfine states each and are trapped in a tilted optical lattice potential (gray line). The gauge-invariant dynamics of 1+1D QED is realized by three processes: (i) local oscillation between the fermionic species [see Eq. (2.20)]; (ii) local bosonic self-interaction [see Eq. (2.21)]; (iii) correlated hopping of both species due to spin-changing collisions [see Eq. (2.22)].

- (i) We propose to drive resonant oscillations with Rabi frequency Ω between the two fermionic states on each site using radiofrequency radiation. This realizes the second line of Hamiltonian (2.19), i.e., the electron mass plus the on-site part of the Wilson term,

$$\Omega \leftrightarrow m + \frac{1}{a}. \quad (2.20)$$

- (ii) We assume 2ℓ Bose condensed atoms on each link. In the trapping potential, the atomic cloud feels an effective interaction constant g_B given by the scattering length, the boson mass, and overlap integrals over localized Wannier functions, see Eq. (2.48). These interactions set the energy scale for the simulated electric field, the first line of Hamiltonian (2.19),

$$g_B \leftrightarrow \frac{a\epsilon^2}{2}. \quad (2.21)$$

- (iii) The gauge-invariant interactions in the third line of Hamiltonian (2.19) are implemented using spin-changing collisions (SCC) between the fermions and bosons [18, 22, 87]. For this purpose, one has to choose appropriate hyperfine states to ensure angular momentum conservation and then apply an external magnetic field in order to tune the SCC into resonance. These lead to a correlated hopping of the bosons and fermions with an effective interaction g_{BF} , see Eq. (2.46). These interactions set the lattice-spacing parameter of the

quantum-simulated gauge theory,

$$g_{BF} \leftrightarrow \frac{1}{a\sqrt{\ell(\ell+1)}}. \quad (2.22)$$

Further details on a possible realization will be discussed in the following section 2.4. Equations (2.20-2.22) define the two relevant dimensionless parameters of the simulated theory, am and e/m . Note that the value of a is not equivalent to the optical-lattice spacing a_{lat} imposed in the quantum simulator [see Eq. (2.27)].

2.3.3 Interpretation of the cold atom Hamiltonian

The individual processes contributing to Eq. (2.19) permit of physical interpretations in simplified limits, which are useful to gain some intuition.

Free fermion Hamiltonian

The fermionic part of Hamiltonian (2.19) becomes particularly simple in the absence of interactions with the gauge fields. Referring to the single-particle states of $\psi_{n,1}$ and $\psi_{n,2}$ as $|\uparrow\rangle_n$ and $|\downarrow\rangle_n$, respectively, we start by considering the local, purely fermionic part in the second line of (2.19), which dominates in the heavy-mass limit $m \rightarrow \infty$. It is diagonal in the basis $|\leftarrow\rangle_n = \frac{1}{\sqrt{2}}(|\uparrow\rangle_n - |\downarrow\rangle_n)$ and $|\rightarrow\rangle_n = \frac{1}{\sqrt{2}}(|\uparrow\rangle_n + |\downarrow\rangle_n)$, with eigenvalues $-m$ and $+m$, respectively. In this basis the local fermionic Hilbert space is given by

$$\mathcal{H}_n = \{|0_{\leftarrow}0_{\rightarrow}\rangle_n, |1_{\leftarrow}0_{\rightarrow}\rangle_n, |0_{\leftarrow}1_{\rightarrow}\rangle_n, |1_{\leftarrow}1_{\rightarrow}\rangle_n\}, \quad (2.23)$$

where $|j_{\rightarrow}k_{\leftarrow}\rangle_n$ denotes a state with j fermions in the state $|\rightarrow\rangle_n$ and k fermions in $|\leftarrow\rangle_n$. We can therefore identify the fermionic vacuum and electron/positron states according to

$$\text{vacuum ("Dirac sea") : } \quad |\Omega\rangle_n \leftrightarrow |1_{\leftarrow}0_{\rightarrow}\rangle_n, \quad (2.24a)$$

$$\text{electron : } \quad |e^-\rangle_n \leftrightarrow |1_{\leftarrow}1_{\rightarrow}\rangle_n, \quad (2.24b)$$

$$\text{positron : } \quad |e^+\rangle_n \leftrightarrow |0_{\leftarrow}0_{\rightarrow}\rangle_n, \quad (2.24c)$$

$$\text{electron + positron : } \quad |e^-e^+\rangle_n \leftrightarrow |0_{\leftarrow}1_{\rightarrow}\rangle_n. \quad (2.24d)$$

Intuitively, an electron corresponds to the presence of a fermion in $|\rightarrow\rangle_n$, while a positron corresponds to the absence of a fermion in $|\leftarrow\rangle_n$.

For a finite fermion mass m , we have to take into account the fermionic hopping terms in (2.19). The decomposition of the vacuum state into the local fermionic states is then formally given by a Slater determinant involving all lattice sites. In this case, it is more convenient to describe the quantum system in terms of correlation functions. In absence of interactions with the gauge field, the matter fields form a free theory. An initial vacuum of non-interacting fermions can thus

be completely described in terms of the equal-time statistical propagators $F_{mn}^{\alpha\beta} = \frac{1}{2} \left\langle \left[\psi_{m,\alpha}, \psi_{n,\beta}^\dagger \right] \right\rangle$. In momentum space, this non-interacting vacuum is characterized by the correlations (cf. section 2.7)

$$F_{kk}^{11} = 0, \quad F_{kk}^{22} = 0, \quad F_{kk}^{21} = \frac{\omega_k}{2z_k} \quad (2.25)$$

and $F_{kk'}^{\alpha\beta} = 0$ for $k \neq k'$. Here, $z_k = m + \frac{1}{a} \left(1 + \exp\left(\frac{2\pi ik}{N}\right) \right)$ and the dispersion $\omega_k = |z_k|$, $k = 0, 1, \dots, N-1$.

Gauge-field energy

In the experiment, the gauge part corresponds to an array of trapped spinor BECs in two hyperfine states. For the semi-classical limit of large occupation numbers, every local BEC can be pictured by a collective spin Bloch sphere. According to the replacements (2.16) and (2.17) the simulated electric field corresponds to an occupation imbalance between the two states, i.e., $E_n/e \leftrightarrow 1/2 \left(b_n^\dagger b_n - d_n^\dagger d_n \right)$. Consequently it can be associated with the azimuthal angle measuring the distance from the equator of the Bloch sphere. Thus, the electric energy, which arises from the bosonic self-interactions in Eq. (2.19) corresponds to the so-called one-axis twisting Hamiltonian [90]. This clarifies the contribution from (2.21): It generates a rotation of the polar angle, whose frequency depends on the azimuthal angle. This corresponds to a phase rotation of $U_n \leftrightarrow [\ell(\ell+1)]^{-1/2} b_n^\dagger d_n$ in the gauge theory. However, this simple dynamics that happens locally on every link is modified by the correlated hopping of bosons and fermions.

Correlated hopping

In the heavy-mass limit underlying the identifications of equation (2.24), one can also easily visualize the effect of the correlated hopping (2.22). For example, the elementary process for the local production of a single e^+e^- pair is composed of the hopping and simultaneous flipping of a single (fermionic) spin from one site to the next, while decreasing the (bosonic) imbalance on the link joining the two sites.

As for the free-fermion part discussed above, the simplified interpretation in terms of local single-particle states is convenient to gain a basic understanding of the cold-atom system, but in order to describe the full complexity of the many-particle quantum dynamics it becomes necessary to consider many-body correlation functions. Indeed, for a finite fermion mass, pair production happens non-locally and can only be detected by measuring correlation functions. In fact, even the concept of a particle is ill-defined in the generic interacting non-equilibrium situation [91]. As a measure for the total fermion particle number density $n = \frac{1}{L} \sum_k \tilde{n}_k$, we employ a typical definition following from the instantaneous diagonalization of the purely fermionic contribution to the full Hamiltonian. Then, n can be expressed in terms of the energy density $\tilde{\epsilon}_k$, which is a function of the statistical propagator, and

the dispersion $\tilde{\omega}_k$,

$$\tilde{n}_k = \frac{\tilde{\epsilon}_k}{\tilde{\omega}_k} + 1, \quad \tilde{\epsilon}_k = - \left(\tilde{z}_k F_{kk}^{21} + [\tilde{z}_k F_{kk}^{21}]^* \right), \quad (2.26)$$

where the tilde indicates that all quantities have to be calculated on the background of the gauge fields.

2.3.4 Experimental limitations

There are a number of experimental limitations that set bounds on the implementation of (2.19). In realistic conditions, the number of bosons on each link will fluctuate around the target value 2ℓ in a range in the order of $\sqrt{2\ell}/(2\ell)$. One may interpret this as disorder on the hopping terms between sites. In the weak-coupling regimes accessible to our benchmarking calculations, one may estimate the resulting localization lengths by diagonalizing the free-fermion Hamiltonian. For the occupation numbers that we aim at, the relative disorder strength will be on the percent level, resulting in localization lengths that are purely finite-size limited for realistic system sizes of few tens of sites. Thus, while it is an interesting perspective to study the effect of this disorder in large systems and strong coupling, for early experiments it is negligible compared to other error sources. Another error source derives from nearest-neighbor elastic scattering between the species. As we argue below in section 2.4, for weak coupling its effect on the dynamics is negligible, though it may have a quantitative influence at strong coupling. Nevertheless, these terms are gauge invariant, so that the result will remain a valid U(1) gauge theory.

Stronger restrictions come from several experimental imperfections. The most important ones limit the accessible time-scales in the experiment as summarized in the following, and discussed in detail in the sections 2.4 and 2.5.

First of all, we have replaced the gauge fields by finite spin operators (2.16). To quantitatively approach QED predictions, we would thus like to employ BECs with large atom numbers corresponding to $\ell \rightarrow \infty$. The large boson density will lead to considerable three-body losses [92], which depend on the precise lattice structure. These losses set a limiting time T_3 for the validity of the quantum simulation.

A second restriction comes from the need to suppress direct hopping terms of the two species and to conserve the boson number locally on each link to ensure the constraint (2.18). Wilson fermions naturally favor a tilted lattice, which conveniently suppresses direct tunneling. On the downside, the tilt renders states localized on single lattice sites unstable [93]. After a time T_{LZ} , they decay due to Landau-Zener transitions, which is the second main limitation of our proposed setup.

Finally, experiments will implement a set of lattice QED parameters a, m, e with a resulting Brillouin zone of finite size $\sim 1/a$. Since we are interested in Schwinger pair production in strong electric fields, the creation and subsequent acceleration of particles becomes unphysical when the energy of these particles reaches the cutoff $\sim 1/a$. This gives a third time-scale T_{lat} that limits the accessible dynamics.

An experimental implementation will have to carefully balance between these different imperfections. Nevertheless, as we will show in the remainder of this chapter, the observation of relevant phenomena is achievable in state-of-the-art experiments. Moreover, T_3 and T_{lat} can be mitigated if we do not require quantitative agreement with continuum QED. For any finite a , the experiment will implement a valid lattice gauge theory. Similarly, by settling for finite representations $l < \infty$, one implements quantum links models, which are valid gauge theories in their own right. Already for extremely small representations, these share the most salient qualitative features with usual QED, such as string-breaking dynamics [11].

2.4 Details of the experimental implementation

As outlined above, we propose to implement (2.19) with a mixture of fermions and bosons trapped in an optical lattice. In the following, we discuss some details and subtleties that arise in this implementation. Though we keep the discussion general, when giving numerical estimates we assume a mixture of fermionic ${}^6\text{Li}$ and bosonic ${}^{23}\text{Na}$. For the most part, we assume transverse degrees of freedom to be frozen out and consider the mixture to be effectively one-dimensional.

2.4.1 Single-particle Hamiltonian

In accordance with the structure of Wilson fermions (see Fig. 2.3), we propose to employ a tilted optical lattice of the form

$$V_{\chi}^{(\text{lat})}(x) = \mathcal{F}_{\chi}x + \begin{cases} V_{\chi} \cos^2\left(\frac{\pi x}{a_{\text{lat}}}\right), & \chi = B \\ V_{\chi} \sin^2\left(\frac{\pi x}{a_{\text{lat}}}\right), & \chi = F \end{cases}, \quad (2.27)$$

where the species index $\chi = F, B$ refers to either fermions on the lattice sites or bosons on the links. The depth V_{χ} , the spacing a_{lat} , and the tilt strength \mathcal{F}_{χ} of the optical lattice may be tuned independently. Additionally, we apply a constant magnetic field \mathcal{B} perpendicular to the x -direction, which we assume to give rise to a linear Zeeman shift,

$$V_{\chi,s}^{(\mathcal{Z})} = -m_{\chi,s} g_{\chi,s}^{(\mathcal{B})} \mu_{\mathcal{B}} \mathcal{B}. \quad (2.28)$$

Here, $s = \uparrow, \downarrow$ denotes the selected two hyperfine states for each species to which the relevant dynamics of the system is restricted; $m_{\chi,s}$ is the corresponding magnetic quantum number, $\mu_{\mathcal{B}}$ denotes the Bohr magneton, and $g_{\chi,s}^{(\mathcal{B})}$ is the Landé g-factor. Neglecting interactions for a moment, the quadratic part of the full Hamiltonian is

given by

$$H_0 = \sum_{\chi, s} \int dx \chi_s^\dagger(x) \mathcal{H}_0(\chi, s) \chi_s(x) \quad (2.29)$$

$$\mathcal{H}_0(\chi, s) = -\frac{\hbar^2 \partial_x^2}{2M_\chi} + V_\chi^{(\text{lat})}(x) + V_{\chi, s}^{(Z)}, \quad (2.30)$$

where M_χ is the atomic mass and we assumed the lattice potential to be species-dependent, but the same for different hyperfine states. The fields, which we denote by χ_s , obey canonical commutation or anti-commutation relations according to their statistics, i.e.,

$$\left[\chi_s(x), \chi_r^\dagger(y) \right]_{\zeta(\chi)} = \delta(x - y), \quad (2.31)$$

where we abbreviate $[X, Y]_{\pm} = XY \pm YX$ with $\zeta(B) = -$ and $\zeta(F) = +$.

2.4.2 Suppression of direct tunneling in a tilted lattice

Additionally to its matching the natural structure of Wilson fermions, we employ the tilt to suppress direct tunneling of the fermions. This is crucial to ensure gauge invariance, because the fermions must only hop between different lattice sites due to interactions with the bosons. In the untilted case ($\mathcal{F}_\chi = 0$), the one-particle Bloch waves for the potential in Eq. (2.30) without external magnetic field ($\mathcal{B} = 0$) are Mathieu functions. In this case, the ground band has the dispersion relation

$$\epsilon_\chi(k) = \frac{\omega_\chi}{2} - 2J_\chi \cos(ka_{\text{lat}}), \quad k \in \left[-\frac{\pi}{a_{\text{lat}}}, \frac{\pi}{a_{\text{lat}}} \right), \quad (2.32)$$

with the mean energy $\omega_\chi = 2\sqrt{V_\chi E_{\text{rec}, \chi}}$. Here $E_{\text{rec}, \chi} = \hbar^2 / [2M_\chi (a_{\text{lat}}/\pi)^2]$ is the recoil energy and the ratio $\xi_\chi = 2\sqrt{V_\chi}/E_{\text{rec}, \chi}$ controls the lattice depth. In the limit of a deep lattice ($\xi_\chi \gg 1$) the hopping element is given by

$$J_\chi = \sqrt{\frac{2}{\pi}} E_{\text{rec}, \chi} (\xi_\chi)^{3/2} e^{-\xi_\chi} [1 + \mathcal{O}(1/\xi_\chi)], \quad (2.33)$$

which can be obtained exactly from analytic properties of the Mathieu functions.

We can suppress direct tunneling for both species by choosing a sufficiently strong tilt, i.e.,

$$a_{\text{lat}} \mathcal{F}_\chi \gg J_\chi. \quad (2.34)$$

In the presence of the tilt, the states in the ground band are modified into resonances

of a Wannier-Stark ladder (for more details see the appendix 2.A). Including non-vanishing $\mathcal{B} \neq 0$, the energy levels are

$$\mathcal{E}_{F,s}(l) = \frac{1}{2}\omega_F + la_{\text{lat}}\mathcal{F}_F - m_{F,s}g_{F,s}^{(\mathcal{B})}\mu\mathcal{B}, \quad (2.35)$$

$$\mathcal{E}_{B,s}(l) = \frac{1}{2}\omega_B + \left(l + \frac{1}{2}\right)a_{\text{lat}}\mathcal{F}_B - m_{B,s}g_{B,s}^{(\mathcal{B})}\mu\mathcal{B}. \quad (2.36)$$

The states of the Wannier-Stark ladder have a finite lifetime which can be estimated from the decay rate Γ_χ due to Landau-Zener transitions (for more details see the appendices 2.A and 2.B).

$$\Gamma_\chi = \frac{a_{\text{lat}}\mathcal{F}_\chi}{2\pi\hbar} \exp\left(-\frac{\pi^2\Delta_\chi^2}{8E_\chi a_{\text{lat}}\mathcal{F}_\chi}\right) \leq \frac{a_{\text{lat}}\mathcal{F}_\chi}{2\pi\hbar}, \quad (2.37)$$

where $\Delta_\chi \approx \omega_\chi$ is the gap between the ground band and the first excited band. This lifetime is one of the relevant experimental restrictions.

2.4.3 Choice of the magnetic field

Under the above condition (2.34), we may neglect direct tunneling. The quadratic part (2.29) of the full Hamiltonian then amounts to a Wannier-Stark ladder of long-lived resonances. These are coupled by a correlated hopping of the fermions and bosons as in Ref. [87], which induces the gauge-invariant matter–gauge-field interaction. For this purpose, the spin-changing collisions for the chosen hyperfine levels $s = \uparrow, \downarrow$ need to be tuned into resonance, i.e., we demand

$$\mathcal{E}_{F\uparrow}(l) - \mathcal{E}_{F\downarrow}(l+1) \stackrel{!}{=} \mathcal{E}_{B\uparrow}(l) - \mathcal{E}_{B\downarrow}(l) \quad \forall l. \quad (2.38)$$

If the two components \uparrow, \downarrow are chosen from the same hyperfine manifold for each species, the g-factors are spin-independent, $g_{\chi,s}^{(\mathcal{B})} = g_\chi^{(\mathcal{B})}$. Then the resonance conditions can be rewritten as

$$\frac{a_{\text{lat}}\mathcal{F}_F}{\mu\mathcal{B}} \stackrel{!}{=} g_B^{(\mathcal{B})}\Delta_B^{(\mathcal{B})} - g_F^{(\mathcal{B})}\Delta_F^{(\mathcal{B})}, \quad (2.39)$$

where we introduced the abbreviation $\Delta_\chi^{(\mathcal{B})} = m_{\chi\uparrow} - m_{\chi\downarrow}$.

For a mixture of bosonic ^{23}Na and fermionic ^6Li , respectively, we choose the following levels from the ground hyperfine manifold:

$$m_{B\uparrow} = 0, \quad m_{B\downarrow} = -1, \quad m_{F\uparrow} = \frac{1}{2}, \quad m_{F\downarrow} = -\frac{1}{2}. \quad (2.40)$$

The corresponding Landé factors are $g_F^{(\mathcal{B})} = -\frac{2}{3}$ and $g_B^{(\mathcal{B})} = -\frac{1}{2}$.

2.4.4 Effective interaction constants from overlap integrals in the tilted lattice

In order to match the coefficients of Hamiltonian (2.19) with experimental parameters, we need to calculate overlap integrals involving Wannier-Stark functions $\Psi_{l,\chi}(x)$. In our case, they are built from the Wannier functions $\psi_{l,\chi}(x)$ located at lattice sites (respectively links) $l = 1 \dots N$ of the untilted lattice. The Wannier-Stark functions can be written as superpositions (see the appendix 2.A)

$$\Psi_{l,\chi}(x) = \sum_m \mathcal{J}_{m-l} \left(\frac{2J_\chi}{a_{\text{lat}} F_\chi} \right) \psi_{m,\chi}(x), \quad (2.41)$$

where $\mathcal{J}_m(\dots)$ denote Bessel functions of the first kind. We only consider the ground band here. For sufficiently deep lattices, to estimate the relevant overlap integrals, we may approximate the Wannier functions appearing in the series (2.41) as harmonic oscillator eigenfunctions,

$$\psi_{l,\chi}(x) = \left(\pi a_\chi^{\text{HO}} \right)^{-1/4} \exp \left[-\frac{1}{2} \left(\frac{x - x_{l,\chi}}{a_\chi^{\text{HO}}} \right)^2 \right], \quad (2.42)$$

where $x_{l,\chi}$ denote the minima of the tilted potentials and the harmonic oscillator lengths should be determined from a Taylor expansion of the tilted potentials around their minima. The minima are shifted from the untilted case to the positions

$$x_{l,B} = \left(l + \frac{1}{2} \right) a_{\text{lat}} - \delta_B, \quad x_{l,F} = l a_{\text{lat}} - \delta_F, \quad (2.43)$$

$$\delta_\chi = \frac{a_{\text{lat}}}{2\pi} \arcsin \left(\frac{a_{\text{lat}} \mathcal{F}_\chi}{\pi V_\chi} \right) \approx \frac{a_{\text{lat}}}{2\pi} \frac{a_{\text{lat}} \mathcal{F}_\chi}{\pi V_\chi}. \quad (2.44)$$

The oscillator length, $a_\chi^{\text{HO}} = \sqrt{\hbar / (m_\chi \omega_\chi^{\text{HO}})}$, is determined from the condition

$$m_\chi \left(\omega_\chi^{\text{HO}} \right)^2 \stackrel{!}{=} 2V_\chi \left(\frac{\pi}{a_{\text{lat}}} \right)^2 \sqrt{1 - \left(\frac{a_{\text{lat}} \mathcal{F}_\chi}{\pi V_\chi} \right)^2}. \quad (2.45)$$

Using the approximation (2.42), we can calculate the effective interaction constants that enter the quantum simulation. For clarity, we first present estimates based on single-particle wavefunctions. For the bosonic condensates, we subsequently use a more appropriate estimate to take their high occupation into account.

The effective boson-fermion inter-species interaction generating the matter-field hopping is given by the 3D overlap integral

$$g_{BF} = \frac{g_{BF}^{(3D)}}{2} \int dx dy dz |\Phi_B(y, z)|^2 |\Phi_F(y, z)|^2 (\Psi_{l+1,F}(x))^* |\Psi_{l,B}(x)|^2 \Psi_{l,F}(x), \quad (2.46)$$

where $g_{BF}^{(3D)} = (\sqrt{2}/3) 2\pi\hbar^2 a_{BF}/M_{\text{red}}$ is the relevant three-dimensional interaction constant with scattering length $a_{BF} \approx 0.9a_0$ and the reduced mass $M_{\text{red}} = M_F M_B / (M_F + M_B)$. The Clebsch-Gordon coefficient $\sqrt{2}/3$ is the same as for the previous proposal [87]. For simplicity, we assume a symmetrically harmonic transverse confinement with the same trapping frequency ω_{\perp} for B and F , i.e.,

$$\Phi_{\chi}(y, z) = (\pi a_{\perp, \chi}^2)^{-1/2} \exp\left(-\frac{y^2 + z^2}{2a_{\perp, \chi}^2}\right) \quad (2.47)$$

and $a_{\perp, \chi} = \sqrt{\hbar / (M_{\chi} \omega_{\perp})}$.

Furthermore, we need to calculate the effective bosonic intra-species interaction

$$g_B = \frac{g_B^{(3D)}}{2} \int dx dy dz |\Phi_B(y, z)|^4 |\Psi_{l, B}(x)|^4, \quad (2.48)$$

where $g_B^{(3D)} = (1/6) 4\pi\hbar^2 a_B/M_B$ is the relevant interaction strength with $a_B \approx 5a_0$. For the Clebsch-Gordon coefficient, we again refer to [87]. At the large boson occupation numbers that we are interested in, the effective interaction constant is modified due to deviations of the bosonic wave-function from the harmonic-oscillator shape. In a first approximation, we may treat this effect in a Thomas-Fermi (TF) limit, i.e., we consider the bosonic mean-field wavefunction as

$$\Phi_{\text{TF}}(x) = \sqrt{\frac{\tilde{\mu}}{\tilde{g}}} \left[1 - \frac{x^2}{x_{\text{TF}}^2}\right] \Theta(|x| - x_{\text{TF}}) \quad (2.49)$$

with the TF radius $x_{\text{TF}} = \sqrt{2\tilde{\mu} / [M_B (\omega_B^{\text{HO}})^2]}$ and the effective chemical potential $\tilde{\mu}$ is determined by the number of bosons on each link as $N_B = 4x_{\text{TF}}\tilde{\mu} / (3\tilde{g})$. Thus, in terms of the experimental parameters,

$$x_{\text{TF}} = \left\{ \frac{4V_B}{3\tilde{g}N_B} \left(\frac{\pi}{a}\right)^2 \sqrt{1 - \left(\frac{a_{\text{lat}}\mathcal{F}_B}{\pi V_B}\right)^2} \right\}^{-1/3}, \quad (2.50)$$

where \tilde{g} is the effective 1D inter-bosonic coupling given by

$$\tilde{g} = \frac{g_B^{(3D)}}{2} \int dy dz |\Phi_B(y, z)|^4. \quad (2.51)$$

Due to the vastly different trapping frequencies (few Hz compared to several kHz, see below), it is justified to treat the bosons in the radial direction in the harmonic approximation, while taking into account the TF profile in the longitudinal direction. The results of the following sections are obtained with the effective interaction constants calculated within this approximation.

2.4.5 Other scattering processes

So far, we have only related the effective interaction constants of the desired interactions to the microscopic properties of the Bose-Fermi mixture. In this subsection, we briefly discuss possible other scattering processes.

In general, all on-site or nearest-neighbor, both of density-density and spin-spin type, inter- and intra-species interactions could be as relevant as the desired spin-changing collision (2.22). Due to a judicious choice of the magnetic field together with the tilted lattice as described above only the SCCs are resonant and all other inelastic processes are presumably suppressed. We therefore restrict ourselves to elastic collisions. Since these do not change the local occupation numbers of either species, the corresponding contributions all commute with the Gauss' law operator and hence do not spoil gauge-invariance of the quantum simulator. The leading purely bosonic contribution comes from on-site interactions that have already been taken into account and set the energy scale for the simulated electric field (2.21).

In addition, density-density interactions between the two species on neighboring sites give rise to a term like

$$\sim \sum_n \left[\left(b_n^\dagger b_n + d_n^\dagger d_n \right) \sum_{\alpha=1,2} \left(\psi_{n,\alpha}^\dagger \psi_{n,\alpha} + \psi_{n+1,\alpha}^\dagger \psi_{n+1,\alpha} \right) \right]. \quad (2.52)$$

For an appropriate initial state preparation that respects the constraint (2.18), the above term reduces to the total fermion particle number (which is conserved) and thus does not affect the dynamics.

Nearest-neighbor spin-spin interactions on the other hand lead to the contribution

$$\sim \sum_n \left(d_{n-1}^\dagger d_{n-1} + d_n^\dagger d_n \right) \left(\psi_{n,1}^\dagger \psi_{n,1} - \psi_{n,2}^\dagger \psi_{n,2} \right) \quad (2.53)$$

$$= \sum_n \left(2\ell - \frac{E_{n-1} + E_n}{e} \right) \left(\psi_{n,1}^\dagger \psi_{n,1} - \psi_{n,2}^\dagger \psi_{n,2} \right), \quad (2.54)$$

where we used the definitions (2.16) & (2.17), as well as the constraint (2.18). The term proportional to ℓ only affects the resonance condition (2.39) and can be absorbed into a redefinition of the energy levels (2.38). For the real-time dynamics considered in this work, it is useful to further define $E_n \equiv E_n^{(0)} + \delta E_n$, where $E_n^{(0)} = \langle E_n(t=0) \rangle \gtrsim \frac{m^2}{e}$ is the initial value of the electric field. Absorbing also $E_n^{(0)}$ into the energy levels (2.38), we parametrically estimate that the above contribution does not alter the dynamics as long as $\langle \delta E_n \rangle \ll \frac{m^2}{e}$. This argument is most accurate in the weak-coupling limit, where $(\frac{m}{e})^2 \gg 1$. In fact, for our benchmarking simulations the condition is fulfilled for all times shown below in figures 2.9 & 2.7. We can therefore neglect it for the proposed experiment that may extract the Schwinger pair production rate as shown in figure 2.8. For the case of strong coupling, which we are ultimately interested in, these elastic inter-species spin-spin interactions

will however quantitatively change the behavior in general. We want to stress that the resulting theory will nevertheless be a fully interacting dynamical $U(1)$ gauge theory.

Finally, we note that for a general choice of fermion species, purely fermionic on-site interactions can yield unwanted effects. However, for the present choice of Lithium, these are absent due to a zero of the relevant scattering length at low magnetic fields [94].

2.4.6 Three-body losses

One of the leading limitations of our proposal is the instability of the local BECs due to three-body collisions. On a mean-field level, these three-body losses may be modeled as

$$\frac{\dot{N}_B}{N_B} = -\frac{K_3}{N_B} \int dx dy dz |\psi_B(x, y, z)|^6, \quad (2.55)$$

with the total particle number per link $N_B = \int dx dy dz |\psi_B(x, y, z)|^2$ and the species-dependent constant K_3 , commonly referred to as the three-body loss rate coefficient. We estimate the typical time-scale for three-body losses, T_3 , as the inverse of the right-hand side of equation (2.55). Demanding this time to be much larger than any other time scale in the experiment sets a limit on the boson particle number N_B per link.

2.5 Choice of experimental parameters

In the implementation proposed above, several imperfections arise that limit accessible time scales. In this section, we discuss the main limitations and an optimization procedure to maximize the time simulatable in the experiment.

2.5.1 Experimental limitations

A first limitation appears through the three-body loss time of the bosonic condensates, T_3 . Second, the localized Wannier-Stark states in the tilted periodic potential have a finite life-time. For the choice of a mixture between ${}^6\text{Li}$ and ${}^{23}\text{Na}$, due to the smaller mass of the fermionic atoms the limiting factor will be the fermion life time, which we denote by T_{LZ} . Third, the proposed lattice QED implementation will have a finite lattice spacing a . Deviations from the continuum limit will appear at a time scale T_{lat} , which is defined below.

One can balance between these three effects by adapting the following experimental parameters:

1. The number of bosons per link N_B ,
2. the number of lattice sites N ,

3. the optical lattice spacing a_{lat} ,
4. the lattice depth V_{χ} ,
5. the radial confinement $\omega_{\perp, \chi}$,
6. the tilt of the lattice $a_{\text{lat}} \mathcal{F}_{\chi}$.

Allowing different parameters for the bosons and fermions, the three time-scales depend on 9 different experimental parameters. We are looking for a set of parameters for which the minimum of $(T_3, T_{LZ}, T_{\text{lat}})$ becomes maximal. This optimization is constrained by experimental restrictions, for instance the achievable number of lattice sites.

In addition, each parameter set corresponds to two dimensionless parameters on the lattice QED side, namely the lattice spacing am and the coupling constant e/m in units of the fermion mass m . We wish to obtain relevant results for continuum QED and thus seek small values of $am \lesssim 1$. On the other hand, we want to perform benchmarking simulations employing an approximation which relies on $e/m < 1$. These different desiderata generate a rather complicated optimization problem.

2.5.2 Simplified optimization procedure

Relying on physical intuition, we simplify the problem by considering the limiting time-scales as a function of a_{lat} in the range $5 - 10 \mu\text{m}$. Since one of the main complications consists of realizing strong spin-changing collisions, we choose rather shallow lattices, $V_B = 2E_{\text{rec}, B}$ and $V_F = E_{\text{rec}, F}$ and fix the tilts $a_{\text{lat}} \mathcal{F}_{\chi} = 10J_{\chi}$ such that direct tunneling in the shallow lattice is suppressed. We further fix a strong radial confinement $\omega_{\perp, \chi} = 2\pi \times 10 \text{ kHz}$ that renders the system effectively one-dimensional. Now we can tune N_B , such that T_3 and T_{LZ} lie approximately in the same range. We choose $N_B = 3000$, i.e., $\ell = 1500$, which is sufficiently large for the quantum link regularization to approximate QED. Finally, the total number of lattice sites is irrelevant for the determination of three time-scales, but enters as the IR-cutoff after having determined the simulation parameter am . We will come back to this point later.

We can now calculate the effective bosonic interaction constant (g_B) and the effective interaction constant for correlated hopping between the fermions and bosons (g_{BF}) as functions of a_{lat} . Finally, we may adjust the local oscillation frequency between the two fermionic states (Ω). Then, we can make the connection to lattice QED according to Eqs. (2.20), (2.21), and (2.22). On the QED side, we choose to measure energies and times in units of m , which in experimental parameters corresponds to $m \leftrightarrow \Omega - 2\sqrt{\ell(\ell+1)}g_B$. As a bound for the validity of the lattice simulation, we take $T_{\text{lat}}m = 2\pi/(am)$, which is the time when the momentum $p_{\text{lat}} = eET_{\text{lat}}$ of particles accelerated by a constant electric field $E = m^2/e$ reaches the cutoff $\sim 2\pi/a$. Within this framework, we consider a two-step procedure choosing first a_{lat} and

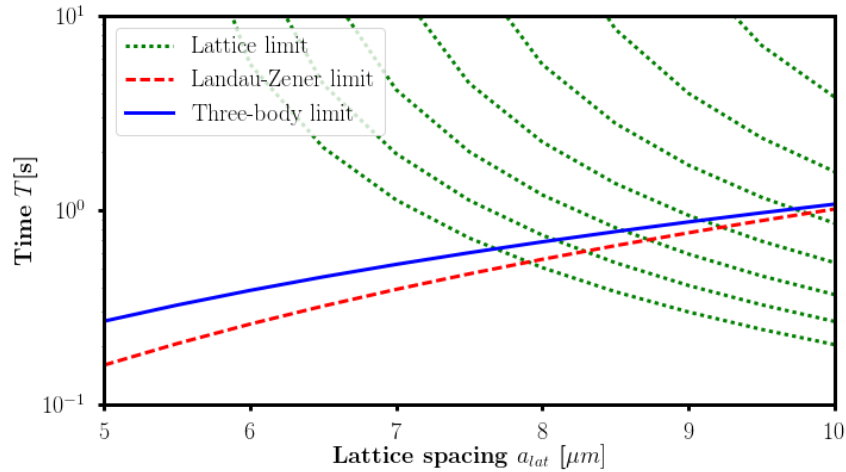


FIGURE 2.5: The limiting time-scales $T_3(a_{\text{lat}})$ (blue, solid), $T_{LZ}(a_{\text{lat}})$ (red, dashed), and $T_{\text{lat}}(a_{\text{lat}}, \Omega)$ (green, dotted; top to bottom for $\Omega = 2\pi \times 4 - 7$ Hz in steps of 0.5 Hz). An optimal choice of experimental parameters maximizes the minimum of these three time scales, conditioned on the desired set of simulation parameters, see 2.6. Note the logarithmic scale of the ordinate.

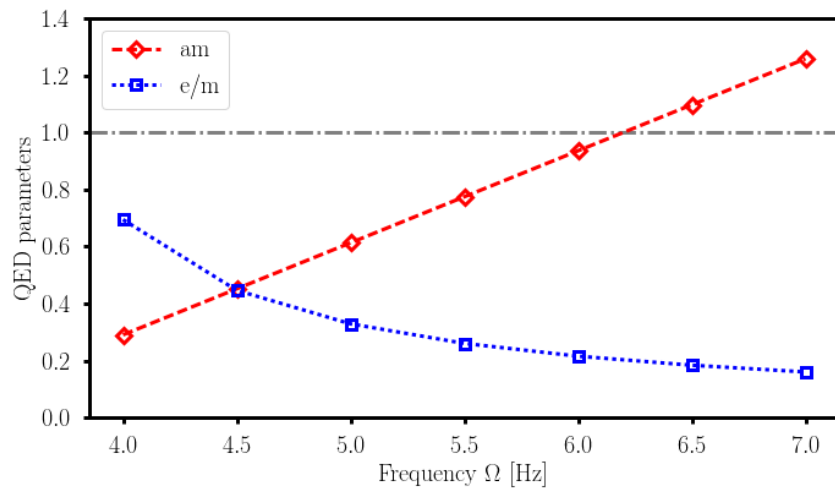


FIGURE 2.6: Dimensionless parameters entering the lattice QED simulation, $am(\Omega)$ (red diamonds, dashed), and $e/m(\Omega)$ (blue squares, dotted). The horizontal gray dashed-dotted line indicates the limiting unity. The inverse behavior favors strong coupling at small lattice spacing.

subsequently Ω in order to optimize the functions $T_3(a_{\text{lat}})$, $T_{LZ}(a_{\text{lat}})$ and $T_{\text{lat}}(a_{\text{lat}}, \Omega)$, $am(a_{\text{lat}}, \Omega)$, $e/m(a_{\text{lat}}, \Omega)$.

Figure 2.5 shows the limiting time-scales for different values of Ω in the range of $2\pi \times (4 - 7)$ Hz. As this plot shows, large values of a_{lat} are favorable if we adjust Ω accordingly. Consequently, we choose a rather large $a_{\text{lat}} = 10 \mu\text{m}$ and plot the remaining Ω dependence of the lattice QED parameters in Fig. 2.6. The observed converse behavior of am and e/m restrains us from choosing an arbitrarily small lattice spacing a for the benchmarking simulations. Note that this should not be seen as a problem of the implementation, but rather getting close to the

continuum limit means studying the strong-coupling regime of QED³. This regime is notoriously difficult for numerical simulations and thus a non-trivial target for quantum simulation. For benchmarking, however, we choose the following two possibilities:

$$\Omega = 2\pi \times 4.5 \text{ Hz} : \quad am = 0.45, \quad e/m = 0.45 \quad (2.56)$$

$$\Omega = 2\pi \times 6 \text{ Hz} : \quad am = 0.94, \quad e/m = 0.22 \quad (2.57)$$

Finally, we choose the number of lattice sites to be $N = 20$, which corresponds to a reasonable size of the optical lattice. The corresponding IR-cutoff on the QED side in units of the fermion mass is given by $1/(N \times am) \sim \mathcal{O}(0.1)$. Thus, we should be able to resolve sufficiently many modes at small momenta to observe the phenomenon of Schwinger pair production.

2.6 Benchmark: Onset of Schwinger pair production

Having shown how to use Wilson fermions in order to realize a particularly compact formulation of 1+1D QED in optical lattices, we now turn to making quantitative predictions for the proposed experimental realization. To this end, we perform numerical simulations of an important effect that occurs in 1+1D QED: pair production via the Schwinger mechanism [66, 67]. The mechanism describes how a strong external electric field transfers energy to vacuum fluctuations and turns them into pairs of real particles and anti-particles. In the present case of 1+1 dimensions, one can analytically compute the particle-production rate in the continuum

$$\frac{\dot{n}}{m^2} = \frac{E}{\pi E_c} \exp\left(-\frac{\pi E_c}{E}\right), \quad (2.58)$$

which is valid for a constant background field that was turned on in the infinite past [67] (see appendix 2.B for a heuristic derivation). Most importantly, the exponential factor induces a dramatic increase of particle production above a critical field $E_c = m^2/e$. In this regime, the particle production is non-perturbative and thus constitutes an excellent non-trivial target for quantum simulation. Moreover, there is no known analytic prediction for the fully interacting theory including the back-reaction of the produced particles onto the gauge fields [91].

In the following, we show that the proposed implementation strategy, using a mixture of fermionic ⁶Li and bosonic ²³Na based on current technology, allows one to simulate the Schwinger mechanism and the non-perturbative particle-production rate. For benchmarking purposes, we consider the limit of weak gauge coupling, where powerful functional-integral methods provide quantitatively reliable results [95, 96]. Beyond this weak-coupling benchmark regime, the experiment should

³Here, we are referring to the bare parameters am and e/m . Approaching the correct continuum limit is more subtle in general since it requires to adjust the bare coupling parameters as briefly discussed in the introduction.

be able to proceed also into the regime of strong coupling, where these functional-integral methods are expected to fail. Details of the simulation procedure are summarized in the following section 2.7.

2.6.1 Proposed experimental protocol

To quantum simulate the Schwinger mechanism, we propose the following experimental protocol. First, the bosonic and fermionic atoms are loaded into the tilted optical lattice structure. At sufficiently low temperatures, we will have single fermions per lattice site in the state $|\downarrow\rangle_n$ and single-component condensates with average particle number $\langle d_n^\dagger d_n \rangle$ on the links. Initially, the imbalance $\delta N_n = \langle b_n^\dagger b_n - d_n^\dagger d_n \rangle$ of the two hyperfine states, which defines the electric field as discussed in section 2.3.3, is tuned to $\delta N_n = 0$. This can be achieved with a linear coupling between the two states, e.g., via radiofrequency radiation. This initial state, where the electric field is prepared in a product of coherent states, is only approximately restricted to a single gauge sector. However, as it has been shown numerically [95], in the limit of large boson number and for the present scenario the small fluctuations of the electric field are too insignificant to compromise the gauge-invariant dynamics.

As described in the previous section, in the heavy-mass limit, the fermionic vacuum is given by the local superpositions $|\leftarrow\rangle_n = \frac{1}{\sqrt{2}}(|\uparrow\rangle_n - |\downarrow\rangle_n)$. This state can be easily generated from a polarized gas by a $\pi/2$ radiofrequency pulse (with a phase shift of $\pi/2$ with respect to the radiofrequency pulse $\propto \Omega$ that drives the dynamics). Together with the gauge fields, this realizes the ground state at infinite fermion mass. Alternatively, one may adiabatically prepare the ground state at a finite value of the fermion rest mass, e.g., by adiabatically ramping down the optical lattice such that the correlated hopping is gradually turned on.

With either choice of the fermion initial state, the dynamics can be started by quenching the bosonic imbalance δN_n from zero to a desired initial electric field. For the experimentally less demanding case of the infinite-mass ground state, this will realize a combination of the targeted Schwinger mechanism with a mass quench from infinity to a desired, finite value. Below, we demonstrate that both initialization procedures yield comparable results for the particle production rate, at least for the parameter regimes studied in this work (i.e., weak coupling and relatively coarse lattices).

After the initialization procedure, the system evolves for a desired time under Hamiltonian (2.19), after which we extract the relevant observables. In particular, we are interested in the volume-averaged electric field and the total fermion particle number. The first is easily achieved by reading out the bosonic imbalance via standard absorption imaging. Current experimental techniques allow for single-site resolution, such that one can also access the local electric fields and their spatial correlations.

The total fermion particle number can be measured in a number of ways. First, the definition of the particle number given in Eq. (2.26) can be measured by adiabatically transferring the system to the limit of infinite mass by increasing Ω , see Eq. (2.20). A subsequent $\pi/2$ radiofrequency pulse around the y axis on the fermion Bloch sphere maps fermions in the upper (lower) band onto the pseudo-spin state $|\uparrow\rangle$ ($|\downarrow\rangle$). Through a Stern-Gerlach measurement, one can thus detect the produced particle–anti-particle pairs. In addition, their momentum dependence can be resolved by time-of-flight imaging. Since the increase of m amounts to an increase of the critical field $E_c = m^2/e$, this scheme effectively turns the Schwinger mechanism off smoothly, in a similar spirit as for the so-called Sauter pulses that are often used to model the Schwinger mechanism in time-dependent (classical) background fields [91]. Second, one can map out the full band structure by adapting the tomography scheme developed in Ref. [97] and first demonstrated experimentally in Ref. [98]. The particle number is obtained by comparison to the tomography for the ground state at the mass parameter targeted in the dynamics. Third, the full information about the fermionic part of the theory can be reconstructed by measuring spin-dependent and spatially resolved fermion correlation functions, either via quantum-gas microscopy [99–101] or, since we are interested in the spatial continuum limit, on coarse grained length scales larger than the lattice spacing.

2.6.2 Simulated real-time dynamics of fermion density and electric field

While lattice-QED has only two free parameters am and e/m , one can change various ingredients on the experimental side. Different choices can drastically affect the various time scales governing the quantum simulator. Following the simple optimization procedure discussed in 2.5, we focus on two examples of realistic parameter sets, which translate to

$$\begin{aligned} \text{(i):} \quad & am = 0.45, & e/m = 0.45, & E_0/E_c = 7. \\ \text{(ii):} \quad & am = 0.94, & e/m = 0.22, & E_0/E_c = 3, \end{aligned}$$

As these values illustrate, if working at finer lattice spacing am , experimental restrictions of the present proposal require an increase of the coupling e/m . This combination limits the numerical technique employed here to coarse lattices, as it is quantitatively reliable only at small e/m . However, in the experiment it will allow one to reach exactly the most interesting regime, namely close to the continuum limit and with strong coupling.

Since the results for these parameter sets are qualitatively very similar, we discuss in the following only the set (i) (Fig. 2.7) and delegate the results of set (ii) to the next section (Fig. 2.9). For both choices, the initial electric field E_0 exceeds the critical value in Eq. (2.58), and thus we expect an enhanced production of electron-positron pairs. We simulate the real-time evolution of the particle number

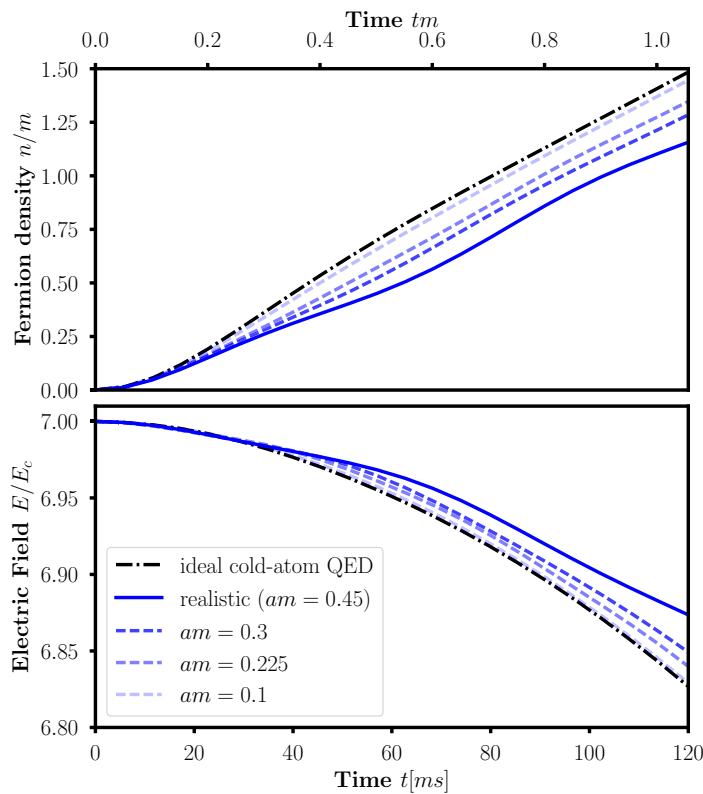


FIGURE 2.7: Benchmarking simulations ($e/m = 0.45$, $am = 0.45$, $N = 20$, and $\ell = 1500$; blue solid line) qualitatively recover the ideal continuum Schwinger rate (the limit of small am as well as large N and ℓ ; black dash-dotted). As the interpolating lines for different am at fixed volume $L = aN = 9/m$ show, the benchmark simulations are converged with respect to ℓ and smoothly approach the continuum prediction (dashed lines from dark to light blue $am = 0.3, 0.225$, and 0.1).

as well as the decay of the initial electric field employing a semi-classical functional-integral method [10, 87, 95] summarized in the next section 2.7 and compare them to an idealized implementation with $\ell, N \rightarrow \infty$ and $a \rightarrow 0$. The latter is obtained numerically by increasing ℓ and approaching the spatial continuum limit ($a \rightarrow 0$ with $aN = \text{const}$) until convergence of the fermion density and the electric field is observed. For the presented realistic parameter sets, though quantitative deviations from the expected QED behavior occur, the observed particle production shows good qualitative agreement. It is also possible to observe the onset of the decay of the electric field due to the backreaction of the fermions. Observed deviations are mainly due to the large lattice spacings and do not result from the finite $\ell < \infty$, which we conclude from the interpolating curves that approach the continuum limit with decreasing a , while keeping ℓ constant. The quantum simulator will thus be capable of simulating a dynamical lattice gauge theory, though the realistically reachable lattice parameters a still lead to quantitative deviations from the spatial continuum limit, at least for the weak coupling regime.

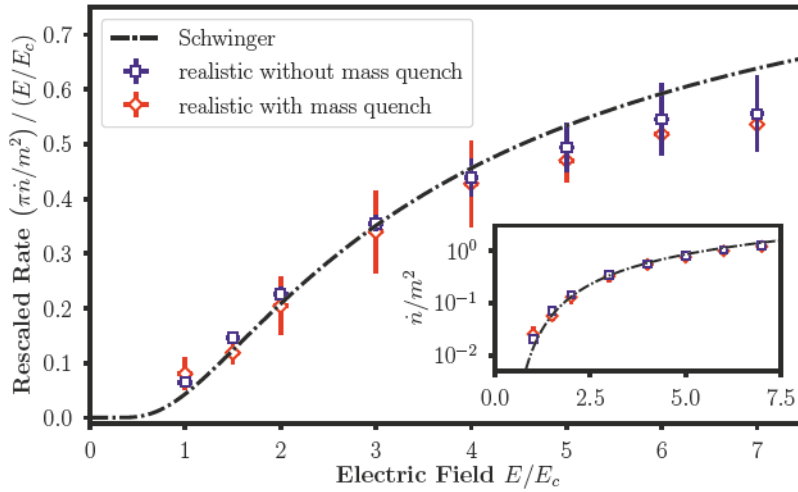


FIGURE 2.8: The proposed quantum simulator can quantitatively predict the non-perturbative behavior of the particle-production rate due to the Schwinger effect[67]. Blue squares (red diamonds) are extracted from linear fits to results of our benchmark simulations without (with) initial mass quench. The right-most squares corresponds to the set of realistic parameters used in Fig. 2.7 (and 2.11) and the others only differ in the initial electric field. The black dashed-dotted line is the analytic prediction. For the parameters chosen in this work, the results for both initialization procedures agree within the estimated experimental accuracy (cf. section 2.7). Main panel: particle-production rate, rescaled by the linear factor $E/(\pi E_c)$. Inset: full rate in logarithmic scale.

2.6.3 Non-perturbative particle production rate

Even with lattice artifacts, the dependence of the particle production rate on the initial value of the electric field is highly non-trivial. In Fig. 2.8, we present the numerically extracted particle production rate after dividing out the “trivial” linear dependence on E , for both initialization procedures outlined above and compare it to the analytical prediction (2.58). Our simulations indicate that the proposed implementation can reproduce quantitatively the non-perturbative suppression of particle production for weak fields $E < \pi E_c$. For larger fields $E > \pi E_c$, we furthermore observe the expected saturation of the rescaled rate, though quantitative agreement is not achieved due to deviations from the continuum limit. Nevertheless, the full rate, plotted in the inset of Fig. 2.8 is remarkably close to the analytic prediction over two orders of magnitude for our simulations both with and without initial mass quench. (The excellent agreement for weak fields should be taken with a grain of salt since the rate will be very challenging to extract in a realistic experiment in this region.) As these results indicate, non-trivial effects of lattice gauge theories are within reach of current optical-lattice technology.

2.7 Details of the numerical simulation

For our numerical simulations, we employ a functional-integral approach that was also used to benchmark a previous implementation with staggered fermions [10, 87]. The main idea of this method is to map the full quantum theory onto a classical-statistical ensemble, which is achieved by a semi-classical expansion around the initial state. Observables are then obtained by solving classical equations of motion and sampling over fluctuating initial values. This results in a non-perturbative approximation of the quantum dynamics, which is valid for sufficiently large electric fields E and weak coupling e/m . In the context of cold atomic gases, the method is related to the well-known truncated Wigner approximation and can be derived by integrating out the fermionic degrees of freedom. The validity to benchmark the proposed quantum simulator relies on the fact that the dynamics is dominated by the Bose condensates and that direct interactions between the fermions are absent.

2.7.1 Classical equations of motion

In order to calculate the equations of motions for the classical-statistical approach to Bose-Fermi mixtures, we consider the Weyl symbol of the cold atom Hamiltonian (2.19), which is given by

$$H = \frac{ae^2}{4} \sum_n (|b_n|^4 + |d_n|^4) + \left(m + \frac{1}{a}\right) \sum_n \left(\psi_{n,1}^\dagger \psi_{n,2} + \psi_{n,2}^\dagger \psi_{n,1}\right) \quad (2.59)$$

$$+ \frac{1}{a\sqrt{\ell(\ell+1)}} \sum_n \left(\psi_{n-1,1}^\dagger b_{n-1}^* d_{n-1} \psi_{n,2} + \text{h.c.}\right) .$$

In this expression, b_n, d_n are c-numbers and $\psi_{n,\alpha}$ are fermionic operators at site n and hyperfine state α . Thus, we can decompose the Hamiltonian to $H = H_B + H_F$, with the pure c-number part $H_B = \frac{ae^2}{4} \sum_n (|b_n|^4 + |d_n|^4)$ and the fermionic part $H_F = \sum_{mn,\alpha\beta} \psi_{m,\alpha}^\dagger (h_F)_{mn}^{\alpha\beta} \psi_{n,\beta}$, where we abbreviated

$$(h_F)_{mn}^{\alpha\beta} = \left(m + \frac{1}{a}\right) \delta_{mn} \sigma_x^{\alpha\beta} + \frac{1}{a\sqrt{\ell(\ell+1)}} \left(b_m^* d_m \delta_{m,n-1} \sigma_+^{\alpha\beta} + d_{m-1}^* b_{m-1} \delta_{m-1,n} \sigma_-^{\alpha\beta}\right) \quad (2.60)$$

with the Pauli matrices

$$\sigma_x = \begin{pmatrix} 0 & 1 \\ 1 & 0 \end{pmatrix}, \quad \sigma_y = \begin{pmatrix} 0 & -i \\ i & 0 \end{pmatrix}, \quad \sigma_\pm = \frac{1}{2} (\sigma_x \pm i\sigma_y) . \quad (2.61)$$

In terms of the equal-time two-point function $D_{mn}^{\alpha\beta} = \langle \psi_{m,\alpha}^\dagger \psi_{n,\beta} \rangle$, where $\langle \dots \rangle$ denotes a quantum expectation value, the explicit equations of motion for the

classical-statistical theory are derived from

$$i\partial_t c_n = \frac{\partial H_A}{\partial c_n^*} + \text{Tr} \left[\frac{\partial (h_F)}{\partial c_n^*} D \right], \quad i\partial_t D_{mn}^{\alpha\beta} = [h_F, D]_{mn}^{\alpha\beta}, \quad (2.62)$$

where $c \in \{b, d\}$ and the trace runs over spatial and fermionic species indices m, n and α, β , respectively. Rewriting $D_{mn}^{\alpha\beta} = \frac{1}{2}\delta_{mn}\delta^{\alpha\beta} - F_{nm}^{\beta\alpha}$ with the statistical propagator $F_{mn}^{\alpha\beta} = \frac{1}{2} \langle [\psi_{m,\alpha}, \psi_{n,\beta}^\dagger] \rangle$, the full set of equations of motion can be reduced to

$$i\partial_t b_n = \frac{ae^2}{2} |b_n|^2 b_n - \frac{d_n}{a\sqrt{\ell(\ell+1)}} [F_{n+1,n}^{21}]^*, \quad (2.63a)$$

$$i\partial_t d_n = \frac{ae^2}{2} |d_n|^2 d_n - \frac{b_n}{a\sqrt{\ell(\ell+1)}} F_{n+1,n}^{21}, \quad (2.63b)$$

$$i\partial_t F_{nm}^{21} = \left(m + \frac{1}{a}\right) (F_{nm}^{22} - F_{nm}^{11}) + \frac{1}{a\sqrt{\ell(\ell+1)}} (b_m^* d_m F_{n,m+1}^{22} - b_{n-1}^* d_{n-1} F_{n-1,m}^{11}), \quad (2.63c)$$

$$i\partial_t F_{nm}^{11} = \left(m + \frac{1}{a}\right) ([F_{mn}^{21}]^* - F_{nm}^{21}) + \frac{1}{a\sqrt{\ell(\ell+1)}} (b_m^* d_m [F_{m+1,n}^{21}]^* - d_n^* b_n F_{n+1,m}^{21}), \quad (2.63d)$$

$$i\partial_t F_{nm}^{22} = \left(m + \frac{1}{a}\right) (F_{nm}^{21} - [F_{mn}^{21}]^*) + \frac{1}{a\sqrt{\ell(\ell+1)}} (d_{m-1}^* b_{m-1} F_{n,m-1}^{21} - b_{n-1}^* d_{n-1} [F_{m,n-1}^{21}]^*). \quad (2.63e)$$

Solving these equations numerically for the initial values specified in the next subsection allows us to benchmark our proposed implementation with Wilson fermions. Since the dynamics is dominated by the coherent electric field, a single run with given initial conditions already gives a good approximation. For the purpose of the present work, we therefore omit the statistical sampling of fluctuating initial values, similar to what was done in Refs. [10, 87].

2.7.2 Initial values

As discussed above, we consider Schwinger pair production as a test of the proposed implementation of cold-atom QED. Accordingly, we initialize a fermionic vacuum state in the presence of a strong electric field that exceeds the critical value $E_c = m^2/e$.

Gauge sector

In the gauge sector, we initialize a coherent electric field as a coherent spin state with expectation value $L_{z,n}^{(0)}$. The constraint $2\ell = b_n^\dagger b_n + d_n^\dagger d_n$ is Wigner transformed to the c-number expression $2\ell = |b_n|^2 + |d_n|^2 - 1$, which allows for solving the

Weyl symbol of the spin operator, $L_{z,n} = \frac{1}{2} (|b_n|^2 - |d_n|^2)$, for b or d as $|b_n|^2 = (\ell + \frac{1}{2}) + (L_{z,n})_W$, $|d_n|^2 = (\ell + \frac{1}{2}) - (L_{z,n})_W$. Thus, we choose the initial values

$$b_n(t_0) = \sqrt{\left(\ell + \frac{1}{2}\right) + L_{z,n}^{(0)}}, \quad (2.64)$$

$$d_n(t_0) = \sqrt{\left(\ell + \frac{1}{2}\right) - L_{z,n}^{(0)}}, \quad (2.65)$$

where $L_{z,n}^{(0)} \in [-\ell, \ell]$. We choose a homogeneous initial value $L_{z,n}^{(0)} = E_0/e$ with electric field $E_0 = 7E_c$ and $E_0 = 3E_c$, respectively, for the two sets of optimized experimental parameters. These values are related to the initial bosonic imbalance as $\Delta N = 2E_0/e \sim \mathcal{O}(100) \ll \ell$. To ensure that three-particle losses are not only irrelevant for the absolute number of N_B atoms but also for their relative distribution among the two hyperfine states, we stop the simulations at $\mathcal{O}(100 \text{ ms})$ instead of $\mathcal{O}(1 \text{ s})$.

Fermion sector

We want to initialize the fermion sector in a vacuum state, i.e., a ground state of the fermionic part H_ψ without electric fields. To this end, we diagonalize $H_\psi = \sum_k \omega_k (a_k^\dagger a_k + c_k^\dagger c_k - 1)$, by the canonical transformation

$$\begin{pmatrix} a_k \\ c_k^\dagger \end{pmatrix} = \frac{1}{\sqrt{2}} \begin{pmatrix} \psi_{k,1} + \frac{z_k}{\omega_k} \psi_{k,2} \\ \psi_{k,1} - \frac{z_k}{\omega_k} \psi_{k,2} \end{pmatrix} \quad (2.66)$$

in Fourier space, $\psi_{k,\alpha} = \frac{1}{\sqrt{N}} \sum_{n=0}^{N-1} e^{-2\pi i n k / N} \psi_{n,\alpha}$, with the dispersion relation $\omega_k = |z_k|$, where $z_k = m + \frac{1}{a} (1 + \exp(\frac{2\pi i k}{N}))$. The ground state $|\Omega\rangle$ is defined by $a_k|\Omega\rangle = c_k|\Omega\rangle = 0$, which translates into the following initial conditions for the fermionic propagator in momentum space,

$$F_{kk}^{11}(t_0) = 0, \quad F_{kk}^{22}(t_0) = 0, \quad F_{kk}^{21}(t_0) = \frac{\omega_k}{2z_k}, \quad (2.67)$$

and $F_{kk'}^{\alpha\beta}(t_0) = 0$ for $k \neq k'$. These correlators are related to position space via $F_{kk'}^{\alpha\beta} = \frac{1}{N} \sum_{nm} e^{-\frac{2\pi i}{N}(mk' - nk)} F_{mn}^{\alpha\beta}$.

Gauge invariance

The chosen initial conditions fulfill the (mean) Gauss' law

$$\langle G_n \rangle = \frac{1}{2} (|b_n|^2 - |d_n|^2) - \frac{1}{2} (|b_{n-1}|^2 - |d_{n-1}|^2) + F_{nn}^{11} + F_{nn}^{22} = 0. \quad (2.68)$$

This constraint is satisfied during the time evolution by construction, which can also be verified explicitly by applying the equations of motion.

2.7.3 Observables

We extract the total electric field as

$$\frac{E}{E_c} = \frac{e^2}{m^2} \frac{1}{2N} \sum_n \left(|b_n|^2 - |d_n|^2 \right). \quad (2.69)$$

The total fermionic particle number density is

$$n = \frac{1}{L} \sum_k \tilde{n}_k, \quad (2.70)$$

where $\tilde{n}_k = \langle \tilde{a}_k^\dagger \tilde{a}_k + \tilde{c}_k^\dagger \tilde{c}_k \rangle = \frac{\tilde{\epsilon}_k}{\tilde{\omega}_k} + 1$ and the tilde denotes quantities derived from the instantaneous diagonalization of the fermionic part of the Hamiltonian in the homogeneous background of b, d . Then

$$\tilde{\epsilon}_k = - \left(\tilde{z}_k F_{kk}^{21} + [\tilde{z}_k F_{kk}^{21}]^* \right) \quad (2.71)$$

with $\tilde{z}_k(b, d) = M + \frac{1}{a} \left(1 + d^* b \exp \left(\frac{2\pi i k}{N} \right) \right)$ and $\tilde{\omega}_k = |\tilde{z}_k|$.

2.7.4 Numerical results for an alternative parameter set

For comparison with Fig. 2.7, we show in Fig. 2.9 the results for the second parameter set

$$am = 0.94, \quad e/m = 0.22, \quad E_0/E_c = 3,$$

Qualitatively, the behavior is very similar to what we found in Fig. 2.7, indicating that in this regime of weak coupling the slightly different values of e/m do not qualitatively affect the physics of the Schwinger mechanism. However, due to the relatively large lattice spacing, the electric field and the fermion density start to deviate more strongly from the expected continuum behavior at about $t \approx 70$ ms.

2.7.5 Details concerning Fig. 2.8, particle production rate

We extract the particle production rate by fitting a linear function with an offset to the simulated particle number. The final and initial points for this fit have to be adjusted due to the following two reasons. First, the initial value problem considered here can be understood as a quench of the electric field. Therefore, the very early time dynamics is dominated by this quench and not by the Schwinger mechanism, which is a many-body phenomenon appearing in the long-time limit. Second, the simulation is limited by lattice artifacts as discussed in section 2.5. The reason is that the produced particles are accelerated and invalidate the simulation as soon as they reach the boundary of the Brillouin zone. We empirically find that we can avoid both complications if we take $\delta t = 1/m$ as a constant window length for the fit and

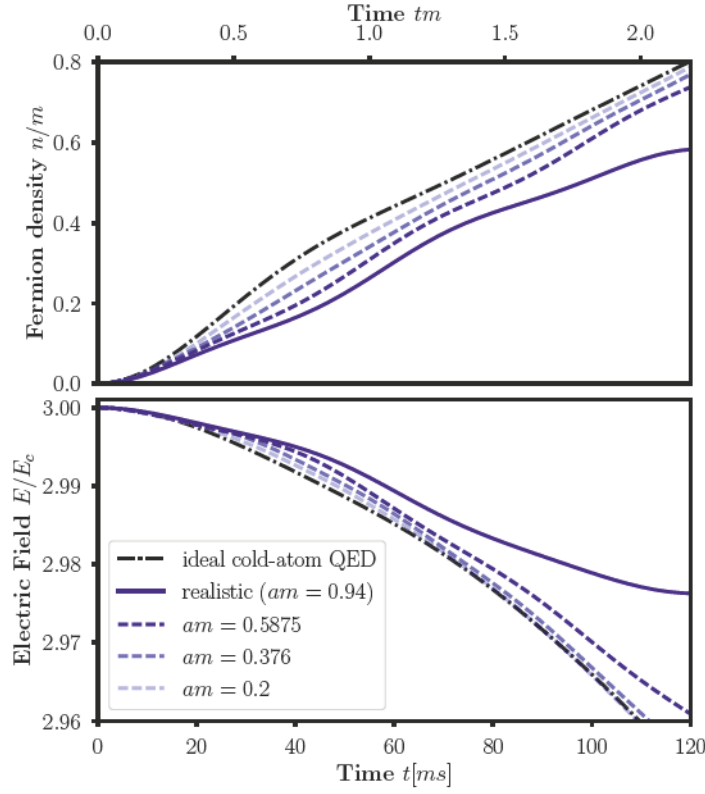


FIGURE 2.9: Benchmarking simulations at $e/m = 0.22$. For the experimentally relevant value of $am = 0.94$, stronger deviations from the continuum limit can be observed than in Fig. 2.7. Nevertheless, the results connect smoothly to the spatial continuum limit, as it can be seen by varying a for fixed volume $L = aN = 18.8/m$ (from dark to light blue $\{am, N\} = \{0.94, 20\}, \{0.5875, 32\}, \{0.376, 50\}, \{0.2, 94\}$; each with $\ell = 1500$). Cold-atom QED stands for the idealized parameters $am = 0.05$ with $N = 376$ and $\ell = 5000$, for which the data are converged to $\ell \rightarrow \infty$ and the spatial continuum limit.

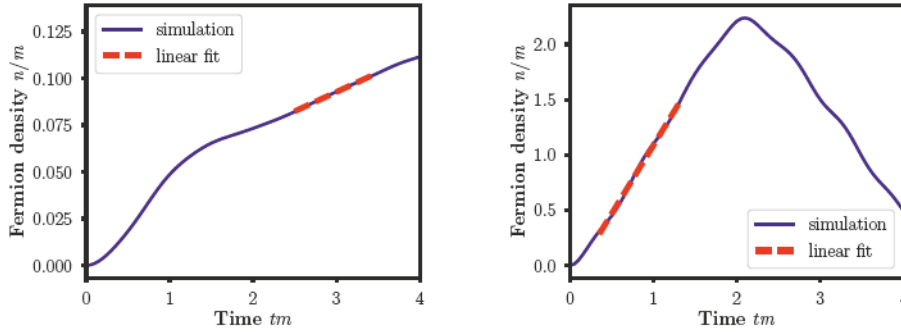


FIGURE 2.10: Examples of two linear fits underlying Fig. 2.8. Left: $E_0/E_c = 1$ with the fit in the linear regime after the initial quench. Right: $E_0/E_c = 7$ with the fit at early times before the occurrence of lattice artifacts. The time interval for the fit is fixed to the constant value of $\delta t = 1/m$.

adjust the initial point accordingly. In Fig. 2.10, we show the fits for the largest and smallest values of E_0 that we considered.

In order to estimate the experimental error of the rescaled rate, we tentatively assume that the bosonic particle number imbalance $\langle b_n^\dagger b_n - d_n^\dagger d_n \rangle$ can be measured with an absolute accuracy of 10 particles on each site. Then the electric field E/E_c has an uncertainty of $\Delta(E/E_c) \approx 0.07$, see Eq. (2.69). We have further included the standard deviation of the fits in the calculation of the errors, although it is negligibly small compared to the uncertainty of the electric field. Though both errors are barely visible in total rate (inset of Fig. 2.8), they lead to significant uncertainties of the rescaled rate for larger fields (main panel of Fig. 2.8). Nevertheless, the non-perturbative behavior of the Schwinger rate can be clearly seen, and the qualitative agreement with the analytical predictions is satisfactory, in particular in light of the fact that the latter are derived for the limit of infinitely large times.

To close this section, let us comment on the experimental challenges to extract the rate. The total particle number corresponding to the density $n/m = 1$ is $n/m \times L = 9$, thus on average $\mathcal{O}(10)$ respectively $\mathcal{O}(0.1)$ particles are produced over the whole lattice for the initial value $E = 7E_c$ respectively $E = 1E_c$. Consequently, while the large-field case seems reasonably accessible, in the weak-field case the precise detection of the produced particles is very challenging with current technology. Moreover, the measurement of the rate requires an even higher accuracy as compared to the total particle number. This is more relevant for the weak-field regime, where the initial quench dynamics dominates the total particle number production at the short times accessible in the experiment. Concerning the time-scales, we finally note that the fits for $E < 7E_c$ require an observation time of up to ~ 400 ms. This may limit the observability of rates at small fields, since then three body losses become increasingly important, see Sec. 2.5.1.

2.7.6 Results for the initial infinite-mass vacuum

In this subsection, we present results for the experimentally more feasible initialization of the free fermion vacuum for infinite mass m . Therefore we initialize the numerical simulation according to the fermion correlators (2.67) with $m \rightarrow \infty$ and solve the same equations of motions as before (with finite m). This corresponds to an additional quench of the fermion mass that is absent in the adiabatic preparation of the fermion vacuum. Figure 2.11 compares the extracted particle number density and the electric field for this initial condition to the data already shown in the main part. Due to the additional mass quench, the initial state is not the true vacuum of free fermions and thus the system starts at non-vanishing fermion density. Even though the quantitative behavior of the particle-production is quite different, the production *rate* is very similar to the previously shown result. At the short times presented here, the electric field also shows qualitatively the same behavior as for

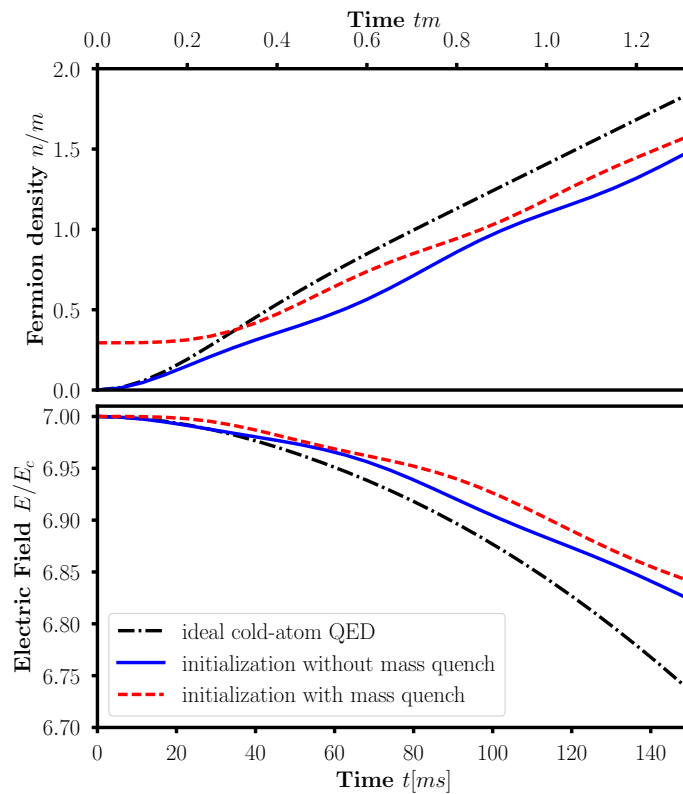


FIGURE 2.11: The mass-quenched simulation ($e/m = 0.45$, $am = 0.45$, $N = 20$, and $\ell = 1500$; red dashed line) shows a similar growth of the fermion density as the simulation without an initial mass quench (same lattice parameters; blue solid line). The main qualitative difference for this parameter regime is the non-vanishing initial fermion density, which is due to the mass quench not realizing the vacuum of the free fermions. Both experimentally relevant simulations yield a growth rate comparable to the ideal continuum result (the limit of small am as well as large N and ℓ ; black dash-dotted).

the simulations without mass quench. For comparison, we have included the simulations with mass quench in the analysis of the production rate of electron-positron pairs shown in figure 2.8.

The consistence of the results leads us to conclude that the quantum simulator could also be benchmarked following the experimentally simpler initialization procedure, at least for the experimental and resulting lattice parameters that we have chosen in this work.

2.8 Summary

To summarize, exploiting the freedom in discretizing relativistic fermions on a lattice opens up a hitherto unexplored possibility for optimizing quantum simulators in view of experimental implementations. We have exemplified this for the Wilson formulation of lattice fermions, where it enables an elegant implementation of 1+1D QED. Our numerical benchmark calculations indicate that available experimental

resources may access the Schwinger mechanism of particle-anti-particle production, and in particular extract the non-perturbative onset of the production rate. The performance of the quantum simulator may even be further improved by resorting to mixtures with enhanced spin-changing collisions, such as sodium–potassium.

As a final aim of a cold-atom quantum simulator, it stands to advance into parameter regimes that are not accessible to computer simulations. For the optimized parameters in the experimental implementation proposed in this work, the dimensionless coupling e/m and the lattice spacing am cannot be tuned independently. Rather, as one is increased, the other one has to be decreased and vice versa, which can be exploited as follows. First, one can use the particle-production rate in the regime of small e/m (and thus large am) to benchmark the quantum simulator using numerical methods. The experiment may then proceed into the relevant regime of strong coupling, which for the optimized parameters permits us also to reduce the lattice spacing. This regime of strong coupling is not accessible within current numerical simulations such as the functional integral method employed here. The proposed experiment involves $20 \times 2 = 40$ fermionic degrees of freedom interacting with 20 BECs of $\mathcal{O}(1000)$ atoms each, resulting in a Hilbert space size that is also beyond the capability of exact diagonalization methods. While the specific case of 1+1D gauge theories can also be treated efficiently using methods based on the density matrix renormalization group [96, 102–104], these approaches are typically limited to low dimensions and equilibrium properties or short time dynamics. Since a quantum simulation of lattice gauge theories may in principle be free of such limitations, a generalization of our present work using Wilson fermions to, e.g., higher dimensions will be extremely interesting.

Our work also opens an interesting pathway for future theoretical investigations. By casting Wilson fermions in the compact form of the Hamiltonian in Eq. (2.6), the free lattice theory becomes manifestly equivalent to the Su-Schrieffer-Heeger model, one of the simplest models displaying non-trivial topological properties [105]. Indeed, the topological properties of free Wilson fermions have been considered in Ref. [74] and, very recently, in Ref. [76]. Such topological properties in the context of interacting gauge theories are the subject of the final chapter 4 of the first part of this thesis.

Appendix: Cold atoms in a tilted optical lattice and Landau-Zener tunneling

In this appendix, we give more details about the description of cold atoms a tilted optical lattice. In section 2.A, we discuss the energy levels of the Wannier-Stark ladder, their wavefunctions and estimated lifetime. In section 2.B, we present a simple derivation of the Landau-Zener formula, from which we deduce the Schwinger pair production rate.

2.A The Wannier-Stark system

In this section, we summarize some important aspects of the Wannier-Stark problem following the detailed review [93]. Consider a quantum-mechanical particle of mass m moving in a one-dimensional periodic potential $V(x+a) = V(x)$ with lattice spacing a , subject to a constant force F . For later purposes, we also assume a reflection invariant potential $V(-x) = V(x)$. The corresponding Hamiltonian reads

$$H_W = H_0 + Fx, \quad H_0 = \frac{p^2}{2m} + V(x), \quad (2.72)$$

where H_0 denotes the unperturbed Hamiltonian ($F = 0$). Most importantly, the linear term breaks the discrete symmetry $x \rightarrow x+a$. Thus for an eigenstate $H_W \Psi = E_0 \Psi$, we can generate a ladder of new eigenstates with different energies

$$E_l = E_0 + laF, \quad l \in \mathbb{Z}, \quad (2.73)$$

by translation over l periods. This is the so-called Wannier-Stark (WS) ladder. We expect any superposition of these states to show oscillations with the Bloch period $T_B = \frac{2\pi}{aF}$. However, the tilt leaves the full Hamiltonian ($F \neq 0$) unbounded from below, such that H_W has a continuous spectrum. In fact, the states of the WS ladder are merely resonances,

$$\mathcal{E}_{\alpha,l} = E_\alpha + laF - \frac{i}{2}\Gamma_\alpha, \quad (2.74)$$

with a finite lifetime $\tau = \frac{1}{\Gamma_\alpha}$ and band index α . There exist powerful methods to determine the precise value of $\mathcal{E}_{\alpha,l}$ and the corresponding eigenfunctions, see [93]. For our purposes, it suffices to treat the eigenfunctions and the real part of $\mathcal{E}_{\alpha,l}$ within a tight-binding approximation and determine the imaginary part of $\mathcal{E}_{\alpha,l}$ from a Landau-Zener tunneling estimate.

2.A.1 Tight-binding model

It is well known that the eigenfunctions of the $F = 0$ case are Bloch waves,

$$H_0 \phi_{\alpha,k} = \epsilon_\alpha(k) \phi_{\alpha,k}, \quad \phi_{\alpha,k}(x) = e^{ikx} u_{\alpha,k}(x), \quad u_{\alpha,k}(x+a) = u_{\alpha,k}(x), \quad (2.75)$$

where the quasi-momentum k is restricted to the first Brillouin zone $-\frac{\pi}{a} \leq k < \frac{\pi}{a}$ because of the periodicity of the Bloch bands, $\epsilon_\alpha(k) = \epsilon_\alpha(k + \frac{2\pi}{a})$. We may choose the phase of the complex Bloch functions $\phi_{\alpha,k}(x)$ to make them periodic and analytic functions of k , such that we can expand them in a Fourier series with coefficients

$$\psi_{\alpha,l}(x) = \int_{-\pi/a}^{\pi/a} dk e^{-ikla} \phi_{\alpha,k}(x) \quad (2.76)$$

known as Wannier functions. They are exponentially localized in the l -th cell of the potential and form a complete set w.r.t. both indices, α and l . The tight-binding approximation is derived by calculating matrix elements in the Wannier basis, keeping only the diagonal elements of Fx , as well as diagonal and secondary diagonal elements of H_0 w.r.t. l , i.e.,

$$\begin{aligned} H_{\text{TB}} &= \sum_{\alpha,l} \langle \psi_{\alpha,l} | H_0 + Fx | \psi_{\alpha,l} \rangle | \psi_{\alpha,l} \rangle \langle \psi_{\alpha,l} | \\ &+ \sum_{\alpha,l} \{ \langle \psi_{\alpha,l} | H_0 | \psi_{\alpha,l+1} \rangle | \psi_{\alpha,l} \rangle \langle \psi_{\alpha,l+1} | + \langle \psi_{\alpha,l+1} | H_0 | \psi_{\alpha,l} \rangle | \psi_{\alpha,l+1} \rangle \langle \psi_{\alpha,l} | \} . \end{aligned} \quad (2.77)$$

In particular, H_0 gives the energy contribution

$$\begin{aligned} \langle \psi_{\alpha,l} | H_0 | \psi_{\alpha,l} \rangle &= \int dx \psi_{\alpha,l}^*(x) H_0 \psi_{\alpha,l}(x) = \int dx dk dq \phi_{\alpha,q}(x) e^{iqla} H_0 e^{-ikla} \phi_{\alpha,k}(x) \\ &= \frac{a}{2\pi} \int dk dq e^{i(q-k)la} \delta_{\alpha\alpha} \delta_{kq} \epsilon_\alpha(k) = \frac{a}{2\pi} \int dk \epsilon_\alpha(k) \equiv \bar{\epsilon}_\alpha \end{aligned} \quad (2.78)$$

and similarly the hopping element

$$\langle \psi_{\alpha,l} | H_0 | \psi_{\alpha,l+1} \rangle = \int dx \psi_{\alpha,l+1}^*(x) H_0 \psi_{\alpha,l}(x) = \frac{a}{2\pi} \int dk e^{-ika} \epsilon_\alpha(k) \equiv J_\alpha, \quad (2.79)$$

where every momentum integration is restricted to the first Brillouin zone. Since Bloch waves are eigenfunctions of the translation operator $T_a x = x + a$, the Wannier functions obey $\psi_{\alpha,l+1}(x) = \psi_{\alpha,l}(x - a)$ from which we find

$$\langle \psi_{\alpha,l+n} | Fx | \psi_{\alpha,l+n} \rangle - \langle \psi_{\alpha,l} | Fx | \psi_{\alpha,l} \rangle = naF, \quad n \in \mathbb{N}. \quad (2.80)$$

Dropping an irrelevant constant, the tight-binding Hamiltonian becomes

$$H_{\text{TB}} = \sum_{\alpha,l} \{ (\bar{\epsilon}_\alpha + laF) | \psi_{\alpha,l} \rangle \langle \psi_{\alpha,l} | + J_\alpha [| \psi_{\alpha,l} \rangle \langle \psi_{\alpha,l+1} | + \text{h.c.}] \}, \quad (2.81)$$

where we have used $J_\alpha = J_\alpha^*$ due to the symmetry $\epsilon_\alpha(-k) = \epsilon_\alpha(k)$. To diagonalize H_{TB} , we make the ansatz $|\Psi_{\alpha,l}\rangle = \sum_m c_m(\alpha, l) |\psi_{\alpha,l}\rangle$. The eigenvalue equation $H_{TB}|\psi_{\alpha,l}\rangle = E_{\alpha,l}|\psi_{\alpha,l}\rangle$ implies

$$c_{m+1}(\alpha, l) + c_{m-1}(\alpha, l) = \frac{E_{\alpha,l} - (\bar{\epsilon}_\alpha + maF)}{J_\alpha} c_m(\alpha, l), \quad (2.82)$$

i.e., the expansion coefficients obey the same recurrence relation as solutions to the Bessel equation

$$z^2 B_\nu''(z) + z B_\nu'(z) + (z^2 - \nu^2) B_\nu(z) = 0, \quad \frac{2\nu}{z} B_\nu(z) = B_{\nu+1}(z) + B_{\nu-1}(z). \quad (2.83)$$

Normalizability in the infinitely large system determines the coefficients to be Bessel functions of the first kind⁴,

$$c_m(\alpha, l) = J_{m-l} \left(\frac{2J_\alpha}{aF} \right), \quad (2.84)$$

and determines the spectrum to be the WS ladder, $E_{\alpha,l} = \bar{\epsilon}_\alpha + laF$. The physical interpretation is the following:

- For $F = 0$, the energy levels of the Wannier states $|\psi_{\alpha,l}\rangle$ coincide for every l and the tunneling J_α couples them into Bloch states $|\phi_{\alpha,k}\rangle = \sum_l e^{ikl} |\psi_{\alpha,l}\rangle$, which produces the Bloch bands $\epsilon_\alpha(k) = \bar{\epsilon}_\alpha + 2J_\alpha \cos(ak)$.
- For $F \neq 0$, the degeneracy is lifted and tunneling is suppressed, such that we find the *Wannier-Stark functions* $|\Psi_{\alpha,l}\rangle = \sum_m J_{m-l} \left(\frac{2J_\alpha}{aF} \right) |\psi_{\alpha,l}\rangle$ as eigenfunctions corresponding to the discrete WS ladder, which are effectively localized on a few lattice sites.

2.A.2 Landau-Zener tunneling

Since the tight-binding approximation is unable to determine the lifetime of the WS resonances, we make a semi-classical estimate using the Landau-Zener (LZ) formula,

$$P_{LZ} = \exp \left(-\frac{\pi \Delta^2}{4 |\dot{\epsilon}(\Delta = 0)|} \right), \quad (2.85)$$

which yields the asymptotic probability for a transition between two energy eigenstates at an avoided crossing. Here, Δ denotes the energy gap between the two states and $|\dot{\epsilon}(\Delta = 0)|$ is the “velocity” of the crossing at vanishing gap. We restrict ourselves to the lowest band in the tight-binding model described above. Δ is then just given by the band gap between the ground band and the first excited band and it remains to determine the “velocity” $|\dot{\epsilon}(\Delta = 0)|$.

⁴There should be no danger of confusing the tunneling elements J_α with the Bessel functions J_{m-l} .

The gauge transformation $\psi(t, x) \rightarrow \psi(t, x)e^{-iFxt}$ brings the Hamiltonian (2.72) into the form

$$H' = \frac{(p - Ft)^2}{2m} + V(x). \quad (2.86)$$

This observation demonstrates that any Bloch state (semi-classically) has a time-dependent momentum $k(t) = k_0 - Ft$, which explores the first Brillouin zone and gets periodically reflected at its boundaries, $|k| = \frac{\pi}{a}$. For simplicity, we consider a single LZ transition at the position of the avoided crossing between the ground band and the first excited band, i.e., at $|k_{\text{avoided}}| = \frac{\pi}{a}$, for each Bloch period T_B . In the limit of vanishing gap, the dispersion relation becomes the one of a free particle, $\epsilon(k) = \frac{k^2}{2m}$, such that we can calculate the “velocity”

$$|\dot{\epsilon}(\Delta = 0)| = \left| \frac{d\epsilon(k)}{dk} \frac{dk(t)}{dt} \right|_{\Delta=0, k=\frac{\pi}{a}} = \frac{\pi}{ma} F = \frac{2a}{\pi} E_r F, \quad (2.87)$$

where we have introduced the recoil energy $E_r = \frac{\pi^2}{2ma^2}$. Thus we approximate the decay rate of the ground band as

$$\Gamma \approx \frac{1}{T_B} P_{\text{LZ}} = \frac{aF}{2\pi} \exp\left(-\frac{\pi^2 \Delta^2}{8E_r a F}\right). \quad (2.88)$$

Note that we have implicitly assumed that the system is “off resonance”, in the sense that no two states of WS ladders from different bands are degenerate. We should keep in mind that such a degeneracy may drastically decrease the lifetime due to resonant LZ tunneling.

2.A.3 Cold atoms in a tilted lattice

For the relevant case of cold quantum gases in an optical lattice, we consider the potential

$$V(x) = V_0 \sin^2\left(\frac{\pi x}{a}\right). \quad (2.89)$$

The case of $F = 0$ is well-known [106] and the corresponding eigenvalue problem can be brought into the form of a Mathieu equation,

$$\left[\partial_y^2 + \left(\frac{E}{V_0} - s \right) + s \cos(2y) \right] \psi_E(y) = 0, \quad (2.90)$$

where $y = \frac{\pi x}{a}$ and the parameter $s = 2\sqrt{\frac{V_0}{E_r}}$ controls the lattice depth. The dispersion relation for the ground band is given by

$$\epsilon(k) = \frac{\omega_0}{2} - 2\tilde{J} \cos(ka), \quad (2.91)$$

where $\omega_0 = sE_r$. The width \tilde{J} of the band can be expressed with the help of Mathieu functions. In the limit of a deep lattice, $s \gg 1$, one finds

$$\tilde{J} \approx \omega_0 \left(\frac{8s}{\pi^2} \right)^{1/4} e^{-s} + \dots \quad (2.92)$$

Consequently, the tilted lattice ($F \neq 0$) features the WS ladder

$$E_l = \frac{\omega_0}{2} + laF, \quad l \in \mathbb{Z} \quad (2.93)$$

and nearest-neighbor hopping is suppressed for

$$aF \gg |J| = 2\tilde{J}. \quad (2.94)$$

Additionally, experiments are limited by the lifetime

$$\tau = \frac{1}{\Gamma} = \frac{2\pi}{aF} \exp\left(\frac{\pi^2 \Delta^2}{8E_r aF}\right) \approx \frac{2\pi}{aF} \exp\left(\frac{\pi^2 s^2 E_r}{8aF}\right), \quad (2.95)$$

where the band gap can be calculated from Mathieu eigenvalues as $\Delta \approx \omega_0$ in the limit $s \gg 1$. In this limit, we may further approximate the Wannier functions of the ground band at site l as harmonic oscillator eigenfunctions

$$\psi_l(x) = (\pi a_{\text{HO}}^2)^{-1/4} \exp\left(-\frac{(x - x_l)^2}{2a_{\text{HO}}^2}\right), \quad (2.96)$$

where x_l denotes the l -th minimum of $V(x)$ and the harmonic oscillator length $a_{\text{HO}} = (m\omega_{\text{HO}})^{-1/2}$ is obtained by matching the trapping frequencies with the curvature of the potential around the minima, i.e., $m\omega_{\text{HO}}^2 = V''(x_l)$. For the calculation of overlap integrals involving Wannier-Stark functions we use the next-to-leading order in their expansion as

$$\Psi_l(x) = \sum_m J_{m-l} \left(-\frac{4\tilde{J}}{aF} \right) \psi_m(x) \approx \psi_l(x) - \frac{2\tilde{J}}{aF} [\psi_{l+1}(x) - \psi_{l-1}(x)], \quad (2.97)$$

where we made use of the series expansion of Bessel's functions as

$$J_n(z) = \sum_{j=0}^{\infty} \frac{(-1)^j}{j! \Gamma(n+j+1)} \left(\frac{z}{2} \right)^{2j+n}. \quad (2.98)$$

2.B Derivation of the Landau-Zener formula

Consider a two-level system described by the Hamiltonian

$$H_{\text{LZ}} = \frac{1}{2} \begin{pmatrix} vt & \Delta \\ \Delta & -vt \end{pmatrix}. \quad (2.99)$$

It has the eigenvalues $\lambda_{\pm}(t) = \pm \frac{1}{2} \sqrt{\Delta^2 + (vt)^2}$, i.e., for $\Delta \neq 0$ the system exhibits an avoided crossing. Let us assume that we prepare the ground state in the infinite past. What is the probability to find the system in the excited state in the infinite future? The answer is given by the Landau-Zener (LZ) as discussed below.

We give a convenient solution of the problem [107] that does not rely on the explicit solution of the Schrödinger equation. Writing the general wavefunction $\psi(t) = (\alpha(t), \beta(t))^T$ with the initial condition $|\psi(t)|^2 \rightarrow (1, 0)^T$ ($t \rightarrow -\infty$), it is our task to calculate $|\alpha(t)|^2$ at $t \rightarrow \infty$. Applying the Schrödinger equation $i\partial_t \psi(t) = H\psi(t)$ twice, the components decouple and we find

$$-\ddot{\alpha}(t) = \left[\frac{iv}{2} + \left(\frac{\Delta}{2}\right)^2 + \left(\frac{vt}{2}\right)^2 \right] \alpha(t). \quad (2.100)$$

Instead of solving this equation explicitly, we use the fact that

$$\int_{-\infty}^{\infty} dt \frac{\dot{\alpha}(t)}{\alpha(t)} = \log \left[\frac{\alpha(\infty)}{\alpha(-\infty)} \right] \quad (2.101)$$

and evaluate the left-hand side as follows. If the problem has a convergent solution, then

$$\alpha(t) \simeq |\alpha| e^{-i\varphi_{\alpha}(t)} \quad (2.102)$$

as an asymptotic expansion at $t \rightarrow \pm\infty$ with a time-dependent phase $\varphi_{\alpha}(t)$ and a time-independent amplitude $|\alpha|$. Then the e.o.m. becomes

$$\left\{ \ddot{\varphi}_{\alpha}^2(t) - \left[\left(\frac{\Delta}{2}\right)^2 + \left(\frac{vt}{2}\right)^2 \right] + i \left[\ddot{\varphi}_{\alpha}(t) - \frac{v}{2} \right] \right\} \alpha(t) = 0, \quad (2.103)$$

which is solved by

$$\ddot{\varphi}_{\alpha}(t) = \frac{v}{2}, \quad \dot{\varphi}_{\alpha}(t) = \pm \frac{v|t|}{2} \sqrt{1 + \left(\frac{\Delta}{vt}\right)^2} = \frac{vt}{2} \left\{ 1 + \frac{1}{2} \left(\frac{\Delta}{vt}\right)^2 + \mathcal{O} \left[\left(\frac{\Delta}{vt}\right)^4 \right] \right\}. \quad (2.104)$$

Consequently, we approximate

$$\frac{\dot{\alpha}(t)}{\alpha(t)} \simeq -i\dot{\varphi}_{\alpha}(t) \approx -i \left(\frac{vt}{2} + \frac{\Delta^2}{4vt} \right) + \dots \quad (2.105)$$

and solve the integral by extending it to the complex plane and applying Cauchy's theorem,

$$\int_{-\infty}^{\infty} dt \frac{\dot{\alpha}(t)}{\alpha(t)} = - \int_{\mathcal{C}_{\pm}} dz \frac{\dot{\alpha}(z)}{\alpha(z)}, \quad (2.106)$$

where C_{\pm} denotes an upper resp. lower infinite half-circle given by $z = Re^{\pm i\theta}$ with $\theta \in [0, \pi]$ and $R \rightarrow \infty$. Therefore

$$\log \left[\frac{\alpha(\infty)}{\alpha(-\infty)} \right] = \pm \int_0^{\pi} d\theta \left(\frac{vR^2}{2} e^{\pm 2i\theta} + \frac{\Delta^2}{4v} \right) = \pm \frac{\pi\Delta^2}{4v}. \quad (2.107)$$

Normalizability requires the negative sign, such that

$$\alpha(\infty) = \alpha(-\infty) \exp \left(-\frac{\pi\Delta^2}{4v} \right). \quad (2.108)$$

Using the initial value $|\alpha(-\infty)|^2 = 1$, we arrive at the celebrated LZ formula for the probability to find the system in the excited state,

$$P \equiv |\alpha(\infty)|^2 = \exp \left(-\frac{\pi\Delta^2}{2v} \right). \quad (2.109)$$

The final result depends on the energy gap Δ between the two states. We want to emphasize that the second parameter v can be obtained as

$$\frac{v}{2} = \left| \frac{d\lambda_{\pm}(t)}{dt} \right|_{\Delta=0}, \quad (2.110)$$

i.e., it describes the ‘‘slope’’ of the energy levels at the avoided crossing in the limit $\Delta \rightarrow 0$.

2.B.1 Schwinger pair production from Landau-Zener tunneling

Using the Landau-Zener formula, we also provide a heuristic derivation of the Schwinger pair production, Eq. (2.58), in the following. The bare fermion vacuum of QED can be seen as an insulator with mass gap $2m$. Applying a constant external electric field modifies the momentum as $p \rightarrow p + eEt$. Focusing first on $p = 0$, the probability of exciting a fermion-antifermion pair is equivalent to the Landau-Zener problem with $v = eE$ and $\Delta = 2m$. This observation immediately implies that the electric field results in an occupation of

$$n_0 = \exp \left(-\frac{\pi m^2}{eE} \right). \quad (2.111)$$

Due to the dispersion $\omega(p) = \sqrt{p^2 + m^2}$, the pair production is exponentially suppressed for any $p \neq 0$. Neglecting any backreaction of the produced fermions on the electric field, the former will simply shift through momentum space with $p(t) = p + eEt$. We thus expect the particle number distribution $n(p, t) = n_0 \Theta(p) \Theta(eEt - p)$ for an external field turned on at $t = 0$. Then the total particle number density is

$$n(t) = 2 \int_{-\infty}^{\infty} \frac{dp}{2\pi} n(p, t) = \frac{eEt}{\pi} \exp \left(-\frac{\pi m^2}{eE} \right), \quad (2.112)$$

where we included a factor of 2 to account for fermions and anti-fermions. Taking a time derivative, we reproduce Eq. (2.58). This argument also gives another point of view on the validity of the Schwinger rate. It neglects any switch-on effect of the electric field and can therefore only be valid at sufficiently late times when the Landau-Zener formula becomes accurate. At the same time, the backreaction of the produced fermions on the electric field is neglected, which invalidates the rate in fully dynamical QED at late times. Moreover, the whole argument is based on a tunneling process across the mass gap. Hence, we can expect the pair production rate to be correct in an intermediate regime of not too early and not too late times, parametrically $1/m \lesssim t \lesssim 1/e$, in a weak-coupling regime $e \ll m$ with strong fields $E \gtrsim m^2/e$.

Chapter 3

Realization of a scalable building block for U(1) gauge theories

This chapter and its appendices 3.A and 3.B are based on the article [16] with the figures and large parts of the text taken from it. The authors of [16] contributed as follows: A. Mil, A. Hegde, A. Xia and R. P. Bhatt set up the experiment and performed the measurements; A. Mil and myself performed the data analysis; P. Hauke, J. Berges and myself developed the theory; P. Hauke, J. Berges, M. K. Oberthaler and F. Jendrzejewski supervised the project. All authors participated in the writing of the manuscript [16] and I made significant contributions to the wording and structuring of the text. In the appendices 3.C and 3.D, I include additional related material that was not printed in [16]. The article [16] is also covered in the experimental doctoral thesis by A. Mil [108].

3.1 Proposed implementation

Our aim is the development of a scalable and highly tunable platform for a continuous U(1) gauge theory, such as realized in QED. Here we enforce the defining local U(1) symmetry through spin-changing collisions in atomic mixtures, as discussed in the previous chapter. This promising mechanism to protect gauge-invariance has been put forward in various proposals [10, 18, 22, 29] but so far it was not demonstrated experimentally. In this chapter we demonstrate the engineering of an elementary building block in a mixture of bosonic atoms, demonstrate its high tunability, and verify its faithful representation of the desired model.

Building on the results of the previous chapter, we further propose an extended implementation scheme in an optical lattice, where each lattice well constitutes an elementary building block that contains both matter and gauge fields. Repetitions of this elementary unit can be connected using laser-assisted tunneling. Importantly, gauge and matter fields are spatially arranged in such a way that the spin-changing collisions occur within single lattice wells, in contrast to previous proposals [10, 18, 22, 29] where the gauge and matter fields were spatially separated and spin-changing collisions had to be accompanied by hopping across different sites of the optical lattice.

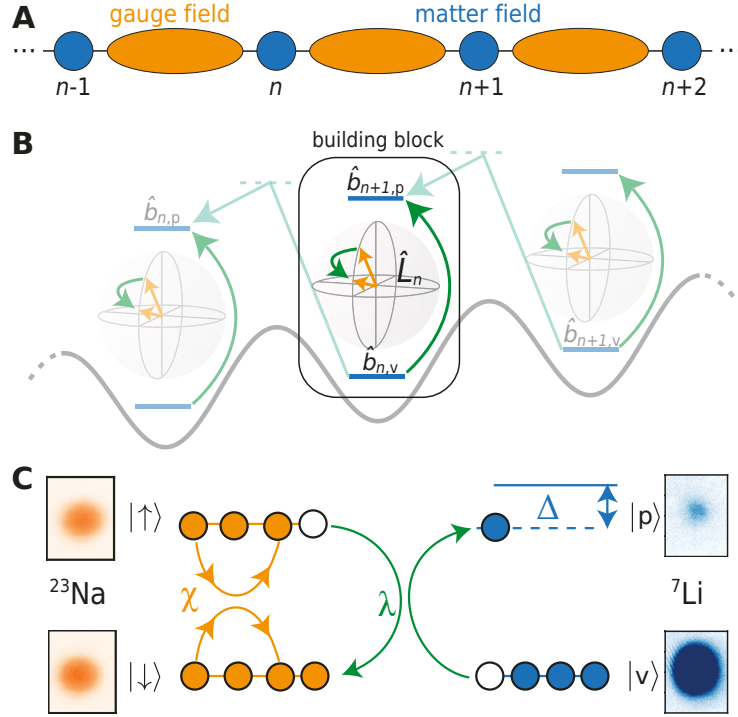


FIGURE 3.1: Engineering a gauge theory. (A) Structure of a lattice gauge theory. Matter fields reside on sites, gauge fields on the links in-between. (B) Proposed implementation of the extended system. Individual building blocks consist of long spins (representing gauge fields) and matter states, which are confined within the same well and whose interaction constitutes a local $U(1)$ symmetry. An array of building blocks in an optical lattice is connected via laser-assisted tunneling. (C) Experimental realization of the elementary building block with bosonic gauge (sodium) and matter (lithium) fields. The gauge-invariant interaction is realized by hetero-nuclear spin-changing collisions.

We specify our proposal for a one-dimensional gauge theory on a spatial lattice, as visualized in Fig. 3.1A. Charged matter fields reside on the lattice sites n , with gauge fields on the links in-between the sites [109]. We consider two-component matter fields labeled “p” and “v”, which are described by the operators $(\hat{b}_{n,p}, \hat{b}_{n,v})$. To realize the gauge fields with the atomic system, we employ the quantum link formulation [11, 88, 110], where the gauge fields are replaced by quantum mechanical spins \hat{L}_n , labeling link operators by the index of the site to the left. In this formulation, the spin z -component $\hat{L}_{n,z}$ can be identified with a discrete “electric” field. We recover the continuous gauge fields of the original quantum field theory in a controlled way by working in the limit of long spins [10].

Physically, this system of charged matter and gauge fields can be realized in a mixture of two atomic Bose–Einstein condensates (BECs) with two internal components each (in our experiment, we use ^7Li and ^{23}Na). An extended system can be obtained by use of an optical lattice. In our scheme, we abandon the one-to-one correspondence between the sites of the simulated lattice gauge theory and the sites of the optical-lattice simulator. This correspondence characterized previous

proposals and necessitated physically placing the gauge fields in-between matter sites [10, 18, 22, 29]. Instead, as illustrated in Fig. 3.1B, here one site of the physical lattice hosts two matter components, each taken from one adjacent site ($\hat{b}_{n+1,p}$ and $\hat{b}_{n,v}$), as well as the link ($\hat{\mathbf{L}}_n$).

The enhanced physical overlap in this configuration decisively improves time scales of the spin-changing collisions, which up to now was a major limiting factor for experimental implementations. Moreover, a single well of the optical lattice already contains the essential processes between matter and gauge fields, and thus represents an elementary building block of the lattice gauge theory. These building blocks can be coupled by Raman-assisted tunneling of the matter fields [111, 112].

The Hamiltonian $\hat{H} = \sum_n [\hat{H}_n + \hbar\Omega(\hat{b}_{n,p}^\dagger \hat{b}_{n,v} + \text{h.c.})]$ of the extended system can thus be decomposed into the elementary building-block Hamiltonian \hat{H}_n and the laser-assisted tunneling (with Raman frequency $\sim \Omega$). Here, \hat{H}_n reads (writing $\hat{b}_p \equiv \hat{b}_{n+1,p}$, $\hat{b}_v \equiv \hat{b}_{n,v}$, and $\hat{\mathbf{L}} \equiv \hat{\mathbf{L}}_n$)

$$\hat{H}_n/\hbar = \chi \hat{L}_z^2 + \frac{\Delta}{2} (\hat{b}_p^\dagger \hat{b}_p - \hat{b}_v^\dagger \hat{b}_v) + \lambda (\hat{b}_p^\dagger \hat{L}_- \hat{b}_v + \hat{b}_v^\dagger \hat{L}_+ \hat{b}_p). \quad (3.1)$$

The first term on the right-hand side of Eq. (3.1), which is proportional to the parameter χ , describes the energy of the gauge field, while the second term $\sim \Delta$ sets the energy difference between the two matter components. The last term $\sim \lambda$ describes the $U(1)$ invariant coupling between matter and gauge fields, which is essential to retain the local $U(1)$ gauge symmetry of the Hamiltonian \hat{H} .

3.1.1 Bosonic U(1) lattice gauge theory

Our experiment aims at implementing a $U(1)$ lattice gauge theory with bosonic matter. Since this is non-standard, we briefly discuss the target model and its relation to QED in this section. The theory is described by the Hamiltonian

$$\hat{H} = \sum_n \left\{ \frac{a}{2} \hat{E}_n^2 + \left(m + \frac{1}{a} \right) [\hat{b}_{n,1}^\dagger \hat{b}_{n,2} + \text{h.c.}] \right\} + \frac{1}{a} \sum_n [\hat{b}_{n,1}^\dagger \hat{U}_n \hat{b}_{n+1,2} + \text{h.c.}] . \quad (3.2)$$

Here, the gauge fields \hat{E}_n, \hat{U}_n live on links n that connect two neighboring lattice sites n and $n - 1$ where the two-component matter fields $\hat{b}_{n,i}$ with $i = 1, 2$ are situated. The gauge fields obey the standard commutation relations

$$[\hat{E}_n, \hat{U}_m] = e \delta_{nm} \hat{U}_m , \quad (3.3)$$

where e is the electric charge. In contrast to QED, we consider bosonic operators for the matter fields, obeying

$$[\hat{b}_{n,i}, \hat{b}_{m,j}^\dagger] = \delta_{nm} \delta_{ij} . \quad (3.4)$$

Nevertheless, the Hamiltonian is gauge-invariant, $[\hat{H}, \hat{G}_n] = 0$, with the Gauss' law operator

$$\hat{G}_n = \hat{E}_n - \hat{E}_{n-1} - e \sum_i \hat{b}_{n,i}^\dagger \hat{b}_{n,i} \quad (3.5)$$

that generates $U(1)$ gauge transformation. Consequently, the model is a proper $U(1)$ lattice gauge theory.

The Hamiltonian in the form (3.2) is motivated by our previous proposal, discussed in chapter 2, to implement QED with Wilson fermions with mass m and lattice spacing a . With the identifications

$$\chi \leftrightarrow \frac{ae^2}{2}, \quad \lambda \leftrightarrow \frac{1}{a\sqrt{L(L+1)}}, \quad \Omega \leftrightarrow m + \frac{1}{a}, \quad (3.6)$$

our proposed extended implementation realizes the target model in the limit of large spin length L of the "gauge" bosons when tuning $\Delta \rightarrow 0$. When bosonic matter is used instead of fermionic matter, for QED in three spatial dimensions it is known that Lorentz invariance remains broken even in the continuum limit, which prohibits an interpretation as a relativistic quantum field theory. Similarly, in one spatial dimension, we expect that the theory with bosonic matter will not lead to a relativistic continuum theory. Thus, to obtain a well-behaved continuum limit, we intend to replace the bosons by fermions in future experiments. Following Ref. [29], after replacing the bosons in the experiment by fermions, the above Hamiltonian will describe a standard lattice discretization of QED. In particular, the fermionic version of the model has a well-behaved continuum limit where Lorentz invariance, which is explicitly broken by the lattice discretization, is recovered.

3.2 Experimental realization of the building block

We implement the elementary building block Hamiltonian \hat{H}_n with a mixture of 300×10^3 sodium and 50×10^3 lithium atoms as sketched in Fig. 3.1C (see appendices 3.A and 3.B for details). Both species are kept in an optical dipole trap such that the external trapping potential is spin-insensitive for both species. An external magnetic bias field of $B \approx 2$ G suppresses any spin change energetically, such that only the two Zeeman levels, $m_F = 0$ and 1, of the $F = 1$ hyperfine ground state manifolds are populated during the experiment. The ^{23}Na states are labeled as $|\uparrow\rangle = |m_F = 0\rangle$ and $|\downarrow\rangle = |m_F = 1\rangle$, on which the spin operator $\hat{\mathbf{L}}$ associated to the gauge field acts. The first term of (3.1) is then identified with the one-axis twisting Hamiltonian [113, 114]. We label the ^7Li states as "particle" $|\text{p}\rangle = |m_F = 0\rangle$ and "vacuum" $|\text{v}\rangle = |m_F = 1\rangle$, in accordance with the matter field operators \hat{b}_p and \hat{b}_v . With this identification, the second term arises from energy shifts due to the external magnetic field and density interactions. Finally, the term $\sim \lambda$ is physically implemented by hetero-nuclear spin-changing interactions [115].

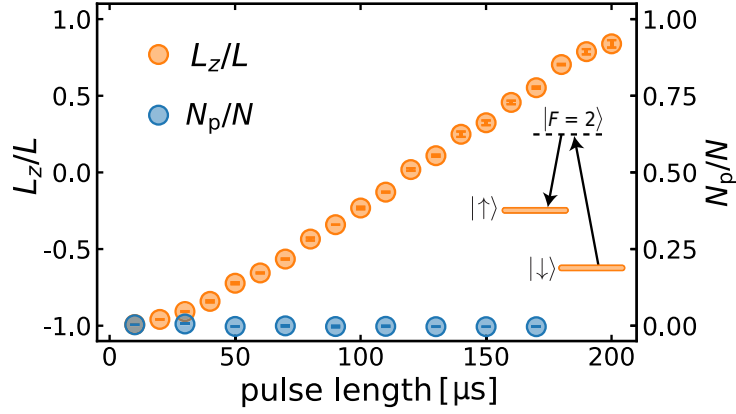


FIGURE 3.2: Tunability of the initial conditions. The normalized spin z -component L_z/L of ^{23}Na atoms as a function of the preparation pulse length, which shows that the gauge field can be tuned experimentally over the entire possible range. Simultaneously, the particle number N_p/N of ^7Li is kept in the vacuum state. The inset shows a sketch of the experimental protocol used for tuning the initial conditions.

3.2.1 Initialization

The resulting setup is highly tunable, as we now demonstrate experimentally on the building block. We achieve tunability of the gauge field through a two-pulse Rabi coupling of the Na atoms between $|\downarrow\rangle$ and $|\uparrow\rangle$ using an intermediate $|F=2\rangle$ state, which yields a desired value of $L_z/L = (N_\uparrow - N_\downarrow)/(N_\uparrow + N_\downarrow)$ (Fig. 3.2). At the same time, we keep the ^7Li atoms in $|v\rangle$, corresponding to the initial vacuum of the matter sector at $\Delta \rightarrow \infty$, with $\lesssim 1\%$ detected in $|p\rangle$ (see Fig. 3.2).

3.2.2 Dynamics of spin-changing collisions

If the gauge invariant coupling is turned off by removing the Na atoms from the trap, we observe no dynamics in the matter sector beyond the detection noise. On the other hand, once the gauge field is present, the matter sector clearly undergoes a transfer from $|v\rangle$ to $|p\rangle$ for proper initial conditions, as illustrated in Fig. 3.3A for an initialization to $\tilde{N}_G = -0.188$ at a magnetic field of $B_A = 2.118(2) \text{ G}$ ¹. This observation demonstrates the controlled operation of hetero-nuclear spin-changing collisions implementing the gauge-invariant dynamics in the experiment.

To quantify our observations, we extract the ratio N_P , with $N = N_p + N_v$, as a function of time as presented in Fig. 3.3B. We observe non-zero N_P , describing “particle production”, on a timescale of few tens of ms, with up to 6% of the total N being transferred to $|p\rangle$. This value is consistent with our expectations from conservation of the initial energy $E_0/\hbar = \chi L_z^2 - \Delta N_v/2$, from which we estimate a maximum amplitude on the order of a few percent (see appendix 3.D for a simple explanation of the maximum amplitude in terms of a particle oscillating in an anharmonic potential). Due to the much larger ^{23}Na condensate, the expected

¹All uncertainties given in this chapter correspond to a 68% confidence interval.

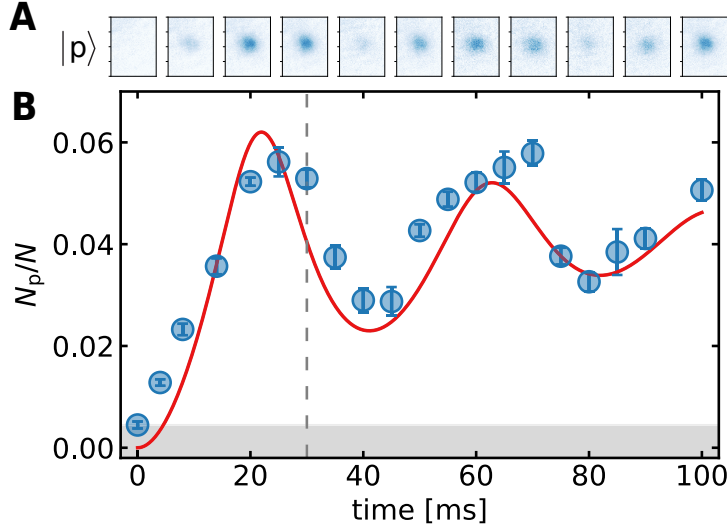


FIGURE 3.3: Dynamics of particle production. (A) The number density distribution in state $|p\rangle$ as a function of time for $\tilde{N}_G = -0.188$. (B) The corresponding particle number N_p/N . The blue circles give the experimental values with bars indicating the statistical error on the mean. The red curve is the theoretical mean-field prediction of Hamiltonian (3.1) with parameters determined from a fit of the data in Fig. 3.4A and phenomenological damping. The shaded area indicates the experimental noise floor. The dashed line marks the time of 30ms as it is used for the experimental sequence generating the data in Fig. 3.4.

corresponding change in \tilde{N}_G is $\sim 2\%$, which is currently not detectable with our imaging routine (see appendix 3.A). Coherent oscillations in N_p are seen to persist for about 100 ms.

3.2.3 Tunability of the model parameters

We display N_p/N over the entire range of initial L_z in Fig. 3.4, keeping a fixed time of 30 ms. The upper panel A corresponds to the same experimental setting as in Fig. 3.3. A clear resonance for particle production can be seen around $L_z/L \simeq -0.5$, approximately captured by the resonance condition $2\chi L_z \sim \Delta$ (see section 3.3 below). The asymmetry of the resonance is a clear manifestation of the non-linearity of the dynamics (see appendix 3.D for a detailed discussion of the non-linearity). As we reduce the magnetic field B , presented in Fig. 3.4B-D, we observe a shift of the resonant particle production together with a reduction in amplitude, which continues to be qualitatively captured by the resonance condition $2\chi L_z \sim \Delta$. The maximal amplitude of the particle production is necessarily reduced by the conservation of total magnetization as the resonant peak is pushed closer to $L_z/L = -1$. For fields that are smaller than $B_{\min} \approx 1.96$ G, the matter field and gauge field dynamics become too off-resonant and particle production can no longer be observed.

We compare the experimental results to the mean-field predictions of Hamiltonian (3.1) for chosen χ , λ and $\Delta(L_z, B) = \Delta_0 + \Delta_L L_z/L + \Delta_B(B - B_A)/B_A$ (see 3.B

for the origin of the dependence on the magnetic field B and the initial spin L_z). A first-principle calculation of these model parameters, using only experimental input of our setup, yields $\chi^{\text{th}}/2\pi \approx 14.92$ mHz, $\lambda^{\text{th}}/2\pi \approx 42.3$ μ Hz, $\Delta_0^{\text{th}}/2\pi \approx -77$ Hz, $\Delta_L^{\text{th}}/2\pi \approx 4.474$ kHz and $\Delta_B^{\text{th}}/2\pi \approx -1.669$ kHz. These values are obtained by neglecting any residual spatial dynamics [116] of the atomic clouds within the trapping potential, which renormalizes the model parameters. Moreover, the mean-field approximation cannot capture the decoherence observed in Fig. 3.3 at later times. However, the features of the resonance data in Fig. 3.4 are more robust against the decoherence as it probes the initial rise of particle production.

We include the decoherence into the model phenomenologically by implementing a damping term characterized by $\gamma/2\pi = 3.54(94)$ Hz, which is determined by an exponential envelope fit to the data of Fig. 3.3B. Physically, the damping has several origins: Quantum fluctuations; fluctuations of initial state preparation as well as values of parameters; atom loss; the spatial dynamics of the two species within the building block. Importantly, the first two do not compromise gauge invariance. The last two sources of dissipation can be controlled by reducing the particle density and by implementing a deep optical lattice that freezes out the spatial dynamics within individual wells. Fixing γ , the best agreement (solid red line) with the data in Fig. 3.4A is obtained for $\chi/2\pi = 8.802(8)$ mHz, $\lambda/2\pi = 16.4(6)$ μ Hz, $\Delta_0/2\pi = -4.8(16)$ Hz and $\Delta_L/2\pi = 2.681(1)$ kHz. The prediction with these model parameters shows excellent agreement with the data in Fig. 3.3B (red line) for all times observed. Remarkably, our established model also describes the data in Fig. 3.4B-D by including $\Delta_B/2\pi = -519.3(3)$ Hz. In the next section, we discuss this effective model in more detail.

3.3 Effective description of the building block dynamics

We find that all experimental data is well described by the building block Hamiltonian in the mean-field approximation with a phenomenological damping term. The deviation from the mean-field building block can be understood from considering experimental imperfections, such as fluctuating initial conditions and spatial inhomogeneities, or quantum fluctuations. These lead to a decoherence of the observed oscillations and renormalize the building block parameters. The damping is characterized by a decoherence time scale $1/\gamma$, which is determined by fitting the envelope of the oscillation in Fig. 3.3B1 with an exponential decay, yielding $1/\gamma = 46(12)$ ms, i.e., $\gamma/2\pi = 3.54(94)$ Hz.

In practice, we solve the dynamics arising from the Hamiltonian in Eq. (3.1) in the mean-field approximation. For convenience, we rewrite it in terms of two coupled effective spins of length $L_N = N_N/2$ and $L_L = N_L/2$ by using the Schwinger representation also for Li. Then the Hamiltonian becomes $H/\hbar = \chi L_{z,N}^2 + \Delta L_{z,L} + 2\lambda (L_{x,N}L_{x,L} + L_{y,N}L_{y,L})$. We can take the damping into account by formally coupling the system to a bath (consisting, e.g., of the spatial modes

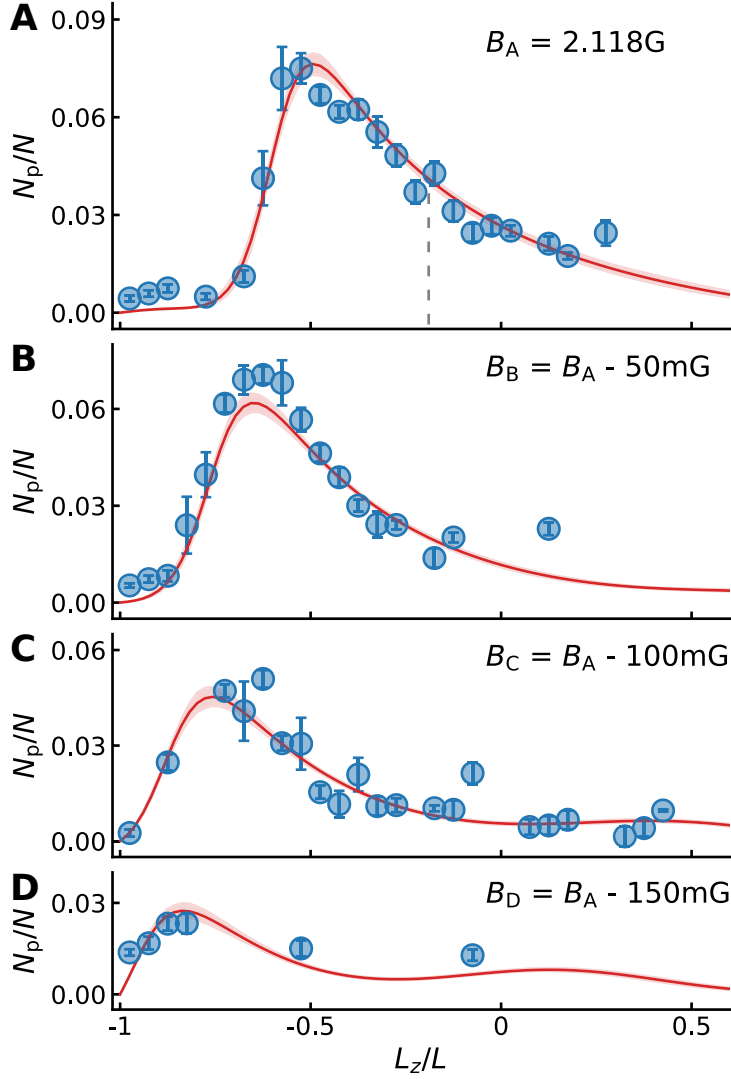


FIGURE 3.4: Resonant particle production. (A-D) The number of produced particles as a function of initially prepared L_z/L after 30ms for different bias magnetic fields. Blue circles are experimental values with bars indicating the error on the mean. The red curve in (A) arises from the theoretical model using the best estimate values of χ , λ , Δ_0 and Δ_L . The remaining curves in (B-D) are computed using the same parameters including Δ_B . The shaded area indicates confidence intervals of the fit from bootstrap resampling. The dashed line in (A) indicates the L_z/L value corresponding to the time evolution shown in Fig. 3.3.

that we neglected). Assuming dephasing of the spin components orthogonal to the magnetization $M = L_{z,N} + L_{z,L}$, we employ the Lindblad-type Heisenberg equation of motion (as discussed, e.g., in [117]) for an observable \mathcal{O} ,

$$\partial_t \mathcal{O} = i[H, \mathcal{O}] + \gamma \left(L^\dagger \mathcal{O} L - \frac{1}{2} \{L^\dagger L, \mathcal{O}\} \right) \quad (3.7)$$

with a single jump operator $L = M$ with the decay rate γ . The resulting (mean-field) equations of motion for the spin components are

$$\partial_t L_{x,N} = -2\chi L_{z,N} L_{y,N} + 2\lambda L_{z,N} L_{y,L} - \frac{\gamma}{2} L_{x,N} , \quad (3.8a)$$

$$\partial_t L_{y,N} = 2\chi L_{z,N} L_{x,N} - 2\lambda L_{z,N} L_{x,L} - \frac{\gamma}{2} L_{y,N} , \quad (3.8b)$$

$$\partial_t L_{z,N} = 2\lambda(L_{y,N} L_{x,L} - L_{x,N} L_{y,L}) , \quad (3.8c)$$

$$\partial_t L_{x,L} = -\Delta L_{y,L} + 2\lambda L_{z,L} L_{y,N} - \frac{\gamma}{2} L_{x,L} , \quad (3.8d)$$

$$\partial_t L_{y,L} = \Delta L_{x,L} - 2\lambda L_{z,L} L_{x,N} - \frac{\gamma}{2} L_{y,L} , \quad (3.8e)$$

$$\partial_t L_{z,L} = 2\lambda(L_{y,L} L_{x,N} - L_{x,L} L_{y,N}) , \quad (3.8f)$$

with initial conditions $\mathbf{L}_L(0) = (0, 0, -1) \times L_L$ and $\mathbf{L}_N(0) = (\cos \theta, 0, \sin \theta) \times L_N$. Here, $\theta \in [-\pi, \pi]$ is chosen in accordance to the quench that initiates the dynamics. We fit the numerical solution to the resonance data via the observable $N_p = L_{z,L} + L_L$. To this end, we assume that $\Delta = \Delta_0 + \Delta_L L_{z,N}(0)/L_N + \Delta_B(B - B_A)/B_A$. This dependence of Δ on the initial spin $L_{z,N}(0)$ (for fixed $\mathbf{L}_L(0)$) and the magnetic field B is analogous to the functional form derived in appendix 3.B for an ideal building block. We obtain the effective model parameters χ , λ , Δ_0 and Δ_L from a single fit to the data shown in Fig. 3.4A with given γ . Fixing these parameters, Δ_B is determined by a second fit to the data of Fig. 3.4B-D. Explicitly, the fits yield the following set of model parameters describing all experimental data:

$$\frac{\chi}{2\pi} = 8.802(8) \text{ mHz} , \quad (3.9a)$$

$$\frac{\lambda}{2\pi} = 16.4(6) \text{ } \mu\text{Hz} , \quad (3.9b)$$

$$\frac{\Delta_0}{2\pi} = -4.8(16) \text{ Hz} , \quad (3.9c)$$

$$\frac{\Delta_L}{2\pi} = 2.681(1) \text{ kHz} , \quad (3.9d)$$

$$\frac{\Delta_B}{2\pi} = -519.3(3) \text{ Hz} . \quad (3.9e)$$

Comparing to the microscopic ab-initio estimates (see appendices 3.B and 3.C) gives

$$\chi^{\text{th}}/\chi \approx 1.7 , \quad (3.10a)$$

$$\lambda^{\text{th}}/\lambda \approx 2.6 , \quad (3.10b)$$

$$\Delta_0^{\text{th}}/\Delta_0 \approx 16 , \quad (3.10c)$$

$$\Delta_L^{\text{th}}/\Delta_L \approx 1.7 , \quad (3.10d)$$

$$\Delta_B^{\text{th}}/\Delta_B \approx 3.2 . \quad (3.10e)$$

The estimates are typically larger than the measured values by factors of about 2 to 3, which hints at a systematic uncertainty in the microscopic parameters that enter the

ab-initio calculation. Nevertheless, most values lie in the right order of magnitude. Importantly, the signs agree, such that the qualitative nature of the shift due to B and $L_{z,N}$ is predicted in agreement with the experiment. The precise value of Δ_0 is less important to fit the experimental data (essentially because of the large value of Δ_L), which is also apparent from its larger uncertainty. This observation makes the larger deviation between the fitted value Δ_0 and the estimate Δ_0^{th} plausible.

In terms of the two coupled spins, the resonance can also be understood more intuitively as follows. In our case, $L_N \approx 6L_L$ and thus by angular momentum conservation the component $L_{z,N}$ can not change much (at most $\sim 17\%$) in the course of the dynamics. Now, if the spins were not coupled, they would rotate in the (x, y) -plane with frequencies given by $2\chi L_{z,N}$ and Δ . If the two frequencies were very different, the coupling $\propto \lambda$ would average out. Therefore $2\chi L_{z,N} \sim \Delta$ gives an approximate condition for the resonance (assuming approximately constant $L_{z,N}$). Solving this condition for $L_{z,N}$ with the fitted experimental parameters gives the following resonance estimates for the four magnetic fields employed in the experiment:

$$\left. \frac{L_{z,N}}{L_N} \right|_{\text{resonance}} = \frac{\Delta_0 + \Delta_B (B - B_A) / B_A}{\chi N_N - \Delta_L} \in \{0.12(4), -0.18(4), -0.47(5), -0.78(6)\} ,$$

$$B \in \{B_A, B_B, B_C, B_D\} . \quad (3.11)$$

The actual peak position is not accurately reproduced because the naive resonance condition is not quantitative for the employed particle numbers, and non-linearities and damping of the equations of motion modify the resonance. Nevertheless, the qualitative shift of the resonance peak is well captured.

3.4 Summary

Our results demonstrate the controlled operation of an elementary building block of a $U(1)$ gauge theory, and thus open the door for large-scale implementations of lattice gauge theories in atomic mixtures. The potential for scalability is an important ingredient for realistic applications to gauge field theory problems. Digital quantum simulations of gauge theories on universal quantum computers [13, 14] are challenging to scale up. This difficulty makes analog quantum simulators, as treated here, highly attractive, since they can be scaled up while still maintaining excellent quantum coherence [3, 25, 31, 35, 118, 119]. Proceeding to the extended system requires to combine the current experiment with the established tools of an optical lattice and laser-assisted tunneling (see appendix 3.B). The resulting extended gauge theory will enable the observation of relevant phenomena such as plasma oscillations or resonant particle production in strong-field QED [95]. Along the path to the relativistic gauge theories realized in nature, we will replace bosonic ${}^7\text{Li}$ with fermionic ${}^6\text{Li}$, which will allow for the recovery of Lorentz-invariance in the continuum limit.

Appendix: More details about the spinor Bose-Bose mixture

In this appendix, we give more details about the experiment (section 3.A) and about the implementation of the $U(1)$ gauge theory (section 3.B). In section 3.C, we discuss how to simulate the experiment in three spatial dimensions, which demonstrates how spatial dynamics affects the evolution. Finally, we give another explanation for the observed resonance by rewriting the dynamics of spin-changing collisions as an anharmonic oscillator in section 3.D.

3.A Experimental details

We prepare a mixture of bosonic ^{23}Na and ^7Li in a single crossed optical dipole trap from a far red detuned laser with 1064 nm wavelength. The atoms experience trapping frequencies of $(\omega_x, \omega_y, \omega_z)_{\text{Na}} \approx 2\pi \times (243, 180, 410)\text{Hz}$ for sodium and $(\omega_x, \omega_y, \omega_z)_{\text{Li}} = 2.08 \times (\omega_x, \omega_y, \omega_z)_{\text{Na}}$ for lithium. To maximize the spatial overlap of the two individual clouds, we align the direction of strongest confinement in gravity direction whereby reducing the differential gravitational sag to approximately $1.1\mu\text{m}$. The atomic clouds are evaporatively cooled to Bose Einstein condensation and contain about 300×10^3 ^{23}Na atoms and 50×10^3 ^7Li atoms respectively.

For the spin-exchange dynamics we take into account the following sublevels of the Hyperfine ground state: $|\downarrow\rangle = |F = 1, m_F = 1\rangle$, $|\uparrow\rangle = |F = 1, m_F = 0\rangle$ for sodium, as well as $|\text{v}\rangle = |F = 1, m_F = 1\rangle$, $|\text{p}\rangle = |F = 1, m_F = 0\rangle$ for lithium. We apply an offset magnetic field of $B_A = 2.118(2)\text{G}$, which lifts the degeneracy of the magnetically sensitive states. Moreover around B_0 the level spacing of both species approach each other at $(E_{|\uparrow\rangle} - E_{|\downarrow\rangle})/\hbar \approx (E_{|\text{p}\rangle} - E_{|\text{v}\rangle})/\hbar \sim 1.45\text{MHz}$, energetically allowing hetero-nuclear spin transfer. Detailed information about the scattering lengths in our system is given in section 3.B.

At the beginning of the experimental sequence the atoms are prepared in $|\downarrow\rangle$ and $|\text{v}\rangle$ respectively, suppressing any spin exchange due to conservation of magnetization. We initiate the spin dynamics by quenching sodium into a desired superposition of $|\uparrow\rangle$ and $|\downarrow\rangle$. To ensure that lithium stays spin polarized during the quench, instead of direct radiofrequency transfer we couple the sodium states with a two pulse microwave transition sequence using the sodium $|F = 2, m_F = 0\rangle$ state as an intermediate state. The first pulse is of variable length, driving population from $|\downarrow\rangle$ to the intermediate state with a Rabi frequency of $2\pi \times 2.5\text{kHz}$. The second pulse is fixed to $100\mu\text{s}$ (corresponding to a π -pulse) and subsequently drives the population from the intermediate state to $|\uparrow\rangle$. The total length of the pulse sequence is at most $300\mu\text{s}$, which is at least one order of magnitude faster than the spin dynamics we observe in our experiment. The initial superposition quench causes undesired external dynamics of the sodium cloud due to the two states $|\uparrow\rangle$ and $|\downarrow\rangle$ being immiscible [116]. This leads to relative motion of the two sodium spin components within the trap after the superposition quench (see section 3.C for

more details). Our observation time is limited by losses in the $|\uparrow\rangle$ state, leading to a lifetime of the $|\uparrow\rangle$ population of about 560 ms for the data shown in Fig. 3.4.

After an evolution time of up to 100 ms we switch off the trapping potential and perform a Stern-Gerlach sequence, where a magnetic field gradient is applied across the atoms' position for 1.5 ms that separates the magnetic substates spatially. After a free expansion time of 3 ms (sodium) and 2 ms (lithium) the two spin states of each species are separated by approximately 130 μm . Then we use absorption imaging to detect the spatial distribution of both species on two individual CCD cameras. The information about the population of substates is then extracted from the images by integrating the density distribution of the individual spin components.

The observable in the experiment is the relative lithium atom number population N_p/N . For lithium being initially spin polarized in $|\downarrow\rangle$, atoms transferred to $|\uparrow\rangle$ are the signature of spin-changing collisions. The main source of detection noise for this observable are fringe patterns on the images which are resulting from diffraction and interference in the imaging path. To account for those we post-process the lithium absorption images by applying a fringe removal algorithm [120], which reduces the experimental noise floor below 1% (see Fig. 3.3B).

Due to the 6 times higher sodium atom number the relative change between the population of $|\uparrow\rangle$ and $|\downarrow\rangle$ resulting from spin-changing collisions is expected to be at most 1%. This change can currently not be detected with our imaging routine. Main limitation are the external dynamics of the sodium spin components in the trap after the initial quench. This results in strong variation of the density distribution of the individual sodium components which our imaging calibration is systematically sensitive to [121].

The observable N_p/N is obtained as an average from a statistical ensemble of multiple experimental realizations. Each data point shown in Figs. 3.3 and 3.4 corresponds to at least three and ten measurements, respectively. The data displayed in Fig. 3.4 is binned in 5% intervals of L_z/L . As the curve in Fig. 3.4D becomes comparably featureless, we used our resources to more accurately resolve the other sets for Fig. 3.4A-C.

For more details about the experiment, we refer to the doctoral thesis of A. Mil [108].

3.B Details of the implementation

3.B.1 Microscopic Hamiltonian

In our experiments, we work with two internal spin states, $m_F = 0, 1$, each from the spin $F_s = 1$ manifold of the two Bose gases, $s = N, L$ (^{23}Na and ^7Li in our case). The total Hamiltonian, $H = H_0 + H_1$, of the combined system splits into free, $H_0 = H_N + H_L$, and interaction, $H_1 = H_{NN} + H_{LL} + H_{NL}$, parts [122, 123]. The free

parts have the form

$$\hat{H}_s = \int d^3\mathbf{x} \sum_{\alpha} \hat{\psi}_{s,\alpha}^{\dagger}(\mathbf{x}) \hat{\mathcal{H}}_{s,\alpha}(\mathbf{x}) \hat{\psi}_{s,\alpha}(\mathbf{x}) , \quad (3.12a)$$

$$\hat{\mathcal{H}}_{s,\alpha}(\mathbf{x}) = \frac{-\nabla_{\mathbf{x}}^2}{2m_s} + V_s(\mathbf{x}) + E_{s,\alpha}(B) . \quad (3.12b)$$

Here, m_s denotes the atomic masses, V_s is the trapping potential and $E_{s,\alpha}(B)$ is the Zeeman shift in the presence of an external magnetic field B , given by the Breit-Rabi formula. The field operators $\hat{\psi}_{s,\alpha}(\mathbf{x})$ fulfill bosonic commutation relations $[\hat{\psi}_{s,\alpha}(\mathbf{x}), \hat{\psi}_{s',\beta}^{\dagger}(\mathbf{y})] = \delta_{ss'} \delta_{\alpha\beta} \delta(\mathbf{x} - \mathbf{y})$, where $\alpha, \beta \in \{0, 1\}$ denote the m_F states.

The intra-species and inter-species interactions which are spin-conserving are described by

$$\hat{H}_{ss} = \frac{1}{2} \int d^3\mathbf{x} \sum_{\alpha,\beta} g_{\alpha\beta}^s \hat{\psi}_{s,\alpha}^{\dagger}(\mathbf{x}) \hat{\psi}_{s,\beta}^{\dagger}(\mathbf{x}) \hat{\psi}_{s,\beta}(\mathbf{x}) \hat{\psi}_{s,\alpha}(\mathbf{x}) , \quad (3.13a)$$

$$\hat{H}_{NL} = \int d^3\mathbf{x} \sum_{\alpha,\beta} g_{\alpha\beta}^{Mix} \hat{\psi}_{N,\alpha}^{\dagger}(\mathbf{x}) \hat{\psi}_{L,\beta}^{\dagger}(\mathbf{x}) \hat{\psi}_{L,\beta}(\mathbf{x}) \hat{\psi}_{N,\alpha}(\mathbf{x}) , \quad (3.13b)$$

where the interaction constants $g_{\alpha\beta}^s = \frac{4\pi\hbar^2}{m_s} a_{\alpha\beta}^s$ and $g_{\alpha\beta}^{Mix} = \frac{2\pi\hbar^2}{\mu} a_{\alpha\beta}^{Mix}$ are determined by the following scattering lengths: $a_{11}^N = a_{10}^N = a_{01}^N = 55a_B$, $a_{00}^N = 53a_B$, $a_{11}^L = a_{10}^L = a_{01}^L = 6.8a_B$, $a_{00}^L = 12.5a_B$ [122] and $a_{00}^{Mix} = a_{10}^{Mix} = a_{01}^{Mix} = 19.65a_B$, $a_{11}^{Mix} = 20a_B$ [124]. The hetero-nuclear spin-changing collisions are described by

$$\hat{H}_{SCC} = g^{SCC} \int d^3\mathbf{x} \psi_{N,0}^{\dagger}(\mathbf{x}) \psi_{L,1}^{\dagger}(\mathbf{x}) \psi_{N,1}(\mathbf{x}) \psi_{L,0}(\mathbf{x}) + \text{h.c.} \quad (3.14)$$

with the interaction strength $g^{SCC} = \frac{2\pi\hbar^2}{\mu} a_{SCC}$ and the scattering length $a_{SCC} = 0.35a_B$ [124].

3.B.2 Proposed extended implementation

We propose to implement the extended $U(1)$ gauge theory described in section 3.1 as follows. Starting from the microscopic Hamiltonian, a deep optical lattice localizes the atomic clouds on individual lattice wells n . Expanding the field operators into localized Wannier functions, $\hat{\psi}_{s,\alpha} = \sum_n \hat{b}_{s,\alpha,n} \Phi_{s,\alpha,n}(\mathbf{x})$, we first perform the spatial integration to obtain a tight-binding Hamiltonian. For a sufficiently deep potential, all tunneling and interaction terms between neighboring wells are negligible, resulting in an array of elementary building blocks n , each containing both species. The Hamiltonian has the form $\hat{H} = \sum_n \hat{H}_n$ with $\hat{H}_n = \sum_{s,n} \left(\hat{H}_{s,n} + \hat{H}_{ss,n} \right) + \hat{H}_{NL,n} + \hat{H}_{SCC,n}$

and

$$\hat{H}_{s,n} = \sum_{\alpha} E_{s,\alpha}(B) \hat{b}_{s,\alpha,n}^{\dagger} \hat{b}_{s,\alpha,n} , \quad (3.15a)$$

$$\begin{aligned} \hat{H}_{ss,n} &= X_{11}^s \hat{b}_{s,1,n}^{\dagger} \hat{b}_{s,1,n}^{\dagger} \hat{b}_{s,1,n} \hat{b}_{s,1,n} + X_{00}^s \hat{b}_{s,0,n}^{\dagger} \hat{b}_{s,0,n}^{\dagger} \hat{b}_{s,0,n} \hat{b}_{s,0,n} \\ &\quad + 2X_{10}^s \hat{b}_{s,1,n}^{\dagger} \hat{b}_{s,0,n}^{\dagger} \hat{b}_{s,1,n} \hat{b}_{s,0,n} , \end{aligned} \quad (3.15b)$$

$$\begin{aligned} \hat{H}_{NL,n} &= X_{11}^{Mix} \hat{b}_{N,1,n}^{\dagger} \hat{b}_{N,1,n} \hat{b}_{L,1,n}^{\dagger} \hat{b}_{L,1,n} + X_{00}^{Mix} \hat{b}_{N,0,n}^{\dagger} \hat{b}_{N,0,n} \hat{b}_{L,0,n}^{\dagger} \hat{b}_{L,0,n} \\ &\quad + X_{10}^{Mix} \hat{b}_{N,1,n}^{\dagger} \hat{b}_{N,1,n} \hat{b}_{L,0,n}^{\dagger} \hat{b}_{L,0,n} + X_{10}^{Mix} \hat{b}_{N,0,n}^{\dagger} \hat{b}_{N,0,n} \hat{b}_{L,1,n}^{\dagger} \hat{b}_{L,1,n} , \end{aligned} \quad (3.15c)$$

$$\hat{H}_{SCC,n} = X^{SCC} \left[\hat{b}_{N,0,n}^{\dagger} \hat{b}_{L,1,n}^{\dagger} \hat{b}_{N,1,n} \hat{b}_{L,0,n} + \hat{b}_{N,1,n}^{\dagger} \hat{b}_{L,0,n}^{\dagger} \hat{b}_{N,0,n} \hat{b}_{L,1,n} \right] . \quad (3.15d)$$

The precise values of the energy levels E and interaction constants X depend on the details of the optical lattice and the corresponding Wannier functions $\Phi_{s,\alpha,n}(\mathbf{x})$.

We then identify the gauge fields on the building block via the Schwinger representation of angular momentum operators,

$$\hat{L}_{+,n} = \hat{b}_{N,0,n}^{\dagger} \hat{b}_{N,1,n} , \quad \hat{L}_{-,n} = \hat{b}_{N,1,n}^{\dagger} \hat{b}_{N,0,n} , \quad \hat{L}_{z,n} = \frac{1}{2} \left(\hat{b}_{N,0,n}^{\dagger} \hat{b}_{N,0,n} - \hat{b}_{N,1,n}^{\dagger} \hat{b}_{N,1,n} \right) . \quad (3.16)$$

The matter fields on a building block, however, are partially associated with the two neighboring internal degrees of freedom according to

$$\hat{b}_n = \begin{pmatrix} \hat{b}_{n,p} \\ \hat{b}_{n,v} \end{pmatrix} , \quad \hat{b}_{n,p} = \hat{b}_{L,n-1,0} , \quad \hat{b}_{n,v} = \hat{b}_{L,n,1} . \quad (3.17)$$

The matter fields carry a $U(1)$ charge \hat{Q}_n , which enters the Gauss' law operators \hat{G}_n as

$$\hat{Q}_n = \hat{b}_n \hat{b}_n = \hat{b}_{n,p}^{\dagger} \hat{b}_{n,p} + \hat{b}_{n,v}^{\dagger} \hat{b}_{n,v} , \quad \hat{G}_n = \hat{L}_{z,n} - \hat{L}_{z,n-1} - \hat{Q}_n . \quad (3.18)$$

This construction ensures Gauss' law, $[\hat{G}_n, \hat{H}] = [\hat{G}_n, \hat{H}_{SCC,n} + \hat{H}_{SCC,n-1}] = 0$, because $[\hat{L}_{z,n}, \hat{H}_{SCC,n}] - [\hat{L}_{z,n-1}, \hat{H}_{SCC,n-1}] = [\hat{Q}_n, \hat{H}_{SCC,n} + \hat{H}_{SCC,n-1}]$. Physically, a global $U(1)$ symmetry due to the conservation of the total magnetization, which arises from angular momentum conservation, is localized on each building block. This localization, which is achieved by associating a building block n with a link n and components of the matter fields on the neighboring lattice sites n and $n+1$, is the key to the scalability of our proposal.

Finally, we connect the building blocks to an extended one-dimensional system by the term

$$H_{\Omega} = \hbar\Omega \sum_n \left(\hat{b}_{L,n,1}^{\dagger} \hat{b}_{L,n-1,0} + \text{h.c.} \right) = \hbar\Omega \sum_n \left(\hat{b}_{n,v}^{\dagger} \hat{b}_{n,p} + \text{h.c.} \right) , \quad (3.19)$$

which can be realized with, e.g., laser-assisted tunneling. Crucially, this connection

respects Gauss' law, $[H_\Omega, \hat{G}_n] = [H_\Omega, \hat{Q}_n] = 0$. The resulting lattice model is similar to our previous proposal [29] with Dirac fermions replaced by two-component bosons,

$$\begin{aligned} \hat{H}/\hbar = \sum_n \left\{ \chi \hat{L}_{z,n}^2 + \Omega \hat{b}_n^\dagger \sigma_x \hat{b}_n + \lambda \left[\hat{b}_{n,v}^\dagger L_{-,n} \hat{b}_{n+1,p} + \text{h.c.} \right] \right\} \\ + (\text{other gauge-invariant terms}) , \end{aligned} \quad (3.20)$$

as discussed in section 3.1.

3.B.3 The building block

In the following, we focus on a single building block n of the extended proposal, as realized in the present experiment. To this end, we consider only two matter field components, $\hat{b}_p = \hat{b}_{L,n,0}$ and $\hat{b}_v = \hat{b}_{L,n,1}$, together with a single spin $\hat{\mathbf{L}} = \hat{\mathbf{L}}_n$. The microscopic Hamiltonian conserves the total magnetization \hat{M} and the total particle numbers \hat{N}_L, \hat{N}_N . To simplify the Hamiltonian of a single building block, we assume an initial state with fixed magnetization M and particle numbers N_N, N_L^2 . After some algebra, we obtain the building block Hamiltonian given in Eq. (3.1), up to constants involving only the conserved numbers N_N, N_L and M . The Hamiltonian is gauge invariant because it commutes with the two reduced Gauss' law operators associated with neighboring lattice sites,

$$\hat{G}'_n = \hat{L}_z + \hat{b}_p^\dagger \hat{b}_p , \quad \hat{G}'_{n+1} = -\hat{L}_z + \hat{b}_v^\dagger \hat{b}_v . \quad (3.21)$$

The parameters are given by

$$\Delta = - \left[\delta_{ext}^L - \delta_{ext}^N + \delta_{int}^L - \delta_{int}^N + \frac{\chi_{NL}}{2} (N_N - N_L) + 2M \left\{ -\chi_L - \frac{\chi_{NL}}{2} \right\} \right] , \quad (3.22a)$$

$$\chi = -\chi_N - \chi_L - \chi_{NL} , \quad (3.22b)$$

$$\lambda = X^{SCC} , \quad (3.22c)$$

where we abbreviated the effective interaction constants

$$\chi_s = - [X_{00}^s + X_{11}^s - 2X_{10}^s] = [X_{11}^s - X_{00}^s] , \quad (3.23)$$

the mean-field energy shifts

$$\delta_{int}^s = [X_{11}^s - X_{00}^s] (N_s - 1) = \chi_s (N_s - 1) , \quad (3.24)$$

²It is questionable whether this condition can be realized by preparing a corresponding eigenstate in the experiment. The fact that we can describe the experiment on the mean-field level shows that this subtlety is not relevant at the moment. However, it can be crucial for investigating quantum effects after preparing a gauge-invariant state in future experiments.

and the single-particle energy level differences $\delta_{ext}^s = E_{s,1} - E_{s,0}$. The interaction constants are calculated from the relevant overlap integrals by rescaling the microscopic parameters as $X_{\alpha\beta}^s = I_{\alpha\beta}^s \frac{g_{\alpha\beta}^s}{2}$, $X_{\alpha\beta}^{Mis} = I_{\alpha\beta}^{Mix} g_{\alpha\beta}^{Mix}$ and $X^{SCC} = I_{10}^{Mix} g^{SCC}$ with

$$I_{\alpha\beta}^s = \int d^3\mathbf{x} \Phi_{s,\alpha,n}^2(\mathbf{x}) \Phi_{s,\beta,n}^2(\mathbf{x}), \quad I_{\alpha\beta}^{Mix} = \int d^3\mathbf{x} \Phi_{N,\alpha,n}^2(\mathbf{x}) \Phi_{L,\beta,n}^2(\mathbf{x}), \quad (3.25)$$

where we have chosen real basis functions Φ . From the known experimental parameters, we estimate the overlap integrals from the initial mean-field BEC wave-function $\Phi_{s,1,n}$ with all atoms of both species in the $m_F = 1$ state by setting $\Phi_{s,1,n} = \Phi_{s,0,n}$. We have calculated the necessary wave-functions by imaginary-time propagation of the Gross-Pitaevskii equation corresponding to full microscopic Hamiltonian (for more details see the section 3.C). In the experiment, we tune the magnetization M through the initial value of the spin $L_z(0)$ and the magnetic field B . To quantify this dependence, we split $\Delta = \Delta_0 + \Delta_L L_{z,N}(0)/L_N + \Delta_B(B - B_A)/B_A$, which holds for $(B - B_A) \ll B_A$ and fixed initial condition for the Li atoms. With the given experimental and microscopic parameters, we obtain the following estimates:

$$\frac{\chi}{2\pi} \approx 14.92 \text{ mHz}, \quad (3.26a)$$

$$\frac{\lambda}{2\pi} \approx 42.3 \text{ } \mu\text{Hz}, \quad (3.26b)$$

$$\frac{\Delta_0}{2\pi} \approx -77 \text{ Hz}, \quad (3.26c)$$

$$\frac{\Delta_L}{2\pi} \approx 4.474 \text{ kHz}, \quad (3.26d)$$

$$\frac{\Delta_B}{2\pi} \approx -1.669 \text{ kHz}. \quad (3.26e)$$

3.B.4 Estimates for the extended system

For scaling up our system to an extended lattice gauge theory, we propose to use a one-dimensional optical lattice array created by a laser of 532nm wavelength, which is blue detuned for both species. The connecting term, Eq. (3.19), can be realized by laser-assisted tunneling between neighboring lattice sites. Former proposals required a species selective lattice, where different species reside on alternating lattice sites whereas in this implementation both atomic species reside on the same sites. This arrangement greatly improves the feasibility of an experimental realization. First, an alternating lattice is technically more demanding. Second, in an alternating lattice tight confinement is necessary to avoid undesired direct tunneling between lattice sites. This confinement, however, diminishes also the spin-changing collisions dynamics, which involve spatial hopping across lattice sites. In our implementation, each site already contains the gauge-invariant interaction via on-site spin-changing collisions. Therefore, tight confinement on individual lattice wells that suppresses direct tunneling at the same time increases the gauge-invariant coupling.

For the laser-assisted tunneling, we consider two laser beams, each having a large detuning Δ from the lithium D1 line. We describe the two beams by $\mathbf{E}_{1,2} = E_{1,2} \mathbf{u}_{1,2} \cos(\mathbf{k}_{1,2} \mathbf{x} - \omega_{1,2} t)$, with $\mathbf{k}_{1,2}$ and $\omega_{1,2}$ being the wave vector and frequency of each laser beam, respectively. The frequency difference of the lasers is tuned to match the transition frequency between the states $\psi_p = \psi_{L,0}$ and $\psi_v = \psi_{L,1}$. As discussed, e.g., in [125] this leads to the following contribution to the Hamiltonian,

$$\hat{V} = \int d^3 \mathbf{x} \Omega_e \hat{\psi}_p^\dagger(\mathbf{x}) \hat{\psi}_v(\mathbf{x}) e^{i\mathbf{q}\mathbf{x}} + \text{h.c.} , \quad (3.27)$$

where $\mathbf{q} = \mathbf{k}_1 - \mathbf{k}_2$, and Ω_e being the effective coupling strength. To estimate the effective tunneling strength, we use similar parameters as in the previous proposal [29]. For the lattice this results in a lattice spacing of $a_L = 2 \mu\text{m}$ and a lattice depth of $15E_R$ for lithium, and $115E_R$ for sodium, such that tunneling is even more strongly suppressed for sodium. In this configuration, we obtain a direct tunneling element on the order of a few Hz. We then estimate the tunneling strength in the presence of Eq. (3.27). A lower limit for the estimate is given when considering the Wannier functions within the lattice sites to be harmonic oscillator ground states. Further assuming a detuning of $\Delta = 1\text{nm}$, we estimate a laser-assisted tunneling strength on the order of a few kHz. Considering spin-changing collisions dynamics, which may also happen on the scale of hundreds of Hz, we expect the overall dynamics of the extended system to be at least ten times faster than in previous proposals [10, 29].

3.C Numerical simulation of the trapped mixture

To get a better understanding of the experimental setup we need to go beyond an ideal setup and take into account experimental imperfections. Here, we focus on the spatial structure and residual dynamics of the atomic clouds within the trapping potential. As a first approximation, we describe the BECs in a mean-field approximation which means that we solve the Gross-Pitaevskii equation (GPE) derived from the microscopic Hamiltonian described in section 3.B.1 numerically. The numerical solution is based on a pseudo-spectral method, called ‘‘split-step’’, where we refer to [126, 127] for more details. In the following we briefly summarize the main idea and point out necessary modifications to simulate the present model.

Consider a partial differential equation (PDE) of the form

$$i\partial_t \psi(t, x) = (T + V) \psi(t, x) , \quad (3.28)$$

where T and V are (not necessarily linear) differential operators, for which the corresponding PDE is exactly solvable, i.e., we have explicit expressions for the formal solutions $\psi(t, x) = e^{-iDt} \psi(0, x)$ with $D = T, V$. Then the solution for a short

time Δt may be written as

$$\psi(t, x) = e^{-i(T+V)\Delta t}\psi(0, x) \approx e^{-iT\Delta t}e^{-iV\Delta t}\psi(0, x), \quad (3.29)$$

where the error goes to zero as $\Delta t \rightarrow 0$ according to the BCH formula. For the GPE of a one-component BEC, $T = -\nabla^2/(2m)$ is the kinetic energy term, which is diagonal in Fourier space, and $V = V_{\text{trap}} + g|\psi|^2$ is the potential energy term, which is diagonal in position space. By evolving $\psi(t, x)$ in alternating steps according to T and V one obtains an approximation to the exact solution of the full PDE. In practice, space is discretized on a periodic lattice with spacing a and spatial extent L and one can efficiently switch between position and momentum space using the fast Fourier transform algorithm. The resulting numerical implementation scales as $\sim N_t N_x \log N_x$, where N_t is the number of time steps and $N_x = (L/a)^d$ is the total number of lattice sites for spatial dimension d . The parameters have to be tuned such that convergence with respect to decreasing the time step Δt , increasing the system size L and decreasing the lattice spacing a (for fixed L) is achieved to a desired precision. Crucially, the split-step method is symplectic, which ensures that certain symmetries of the system are preserved [127, 128]. For the case of a GPE, this includes the conservation of total particle number and total energy.

In contrast to the standard GPE, the Bose-Bose mixture involves four hyperfine components, described by $\psi_{N/L,1/0}$. As a consequence, the GPE includes not only kinetic energy terms T and potential energy terms V , which are both diagonal in the hyperfine index. There is a third type of terms, due to the spin-changing collisions, that mix the different hyperfine components. This part of the evolution equation is local in position space and takes the form

$$i\partial_t\psi_{N,1} = g\psi_{L,1}^*\psi_{L,0}\psi_{N,0}, \quad i\partial_t\psi_{N,0} = g\psi_{L,0}^*\psi_{L,1}\psi_{N,1}, \quad (3.30a)$$

$$i\partial_t\psi_{L,1} = g\psi_{N,1}^*\psi_{N,0}\psi_{L,0}, \quad i\partial_t\psi_{L,0} = g\psi_{N,0}^*\psi_{N,1}\psi_{L,1}. \quad (3.30b)$$

We have not found a simple analytic solution to these equations. To be able to include the spin-changing collision in the simulation, we instead consider

$$i\partial\psi_1 = \tilde{g}\psi_0, \quad i\partial\psi_0 = \tilde{g}^*\psi_1, \quad (3.31)$$

which can be seen as “half” of the previous equations for, e.g., fixed $\tilde{g} = g\psi_{L,1}^*\psi_{L,0}$. With initial conditions $\psi_1(0)$ and $\psi_0(0)$, the solution is

$$\psi_1(t) = \psi_1(0) \cos(\omega t) - i\psi_0(0) \frac{\omega}{\tilde{g}} \sin(\omega t), \quad (3.32a)$$

$$\psi_0(t) = \psi_0(0) \cos(\omega t) - i\psi_1(0) \frac{\omega}{\tilde{g}^*} \sin(\omega t), \quad (3.32b)$$

with $\omega = |\tilde{g}|$. We can thus approximate the solution to Eq. (3.30) by solving alternately for $\psi_{N,1/0}$ with $\tilde{g} = g\psi_{L,1}^*\psi_{L,0}$ and for $\psi_{L,1/0}$ with $\tilde{g} = g\psi_{N,1}^*\psi_{N,0}$. Specifically, we evolve $\psi_{N,1/0}$ for a short time $\Delta t/2$, then $\psi_{L,1/0}$ for Δt and again $\psi_{N,1/0}$ for $\Delta t/2$.

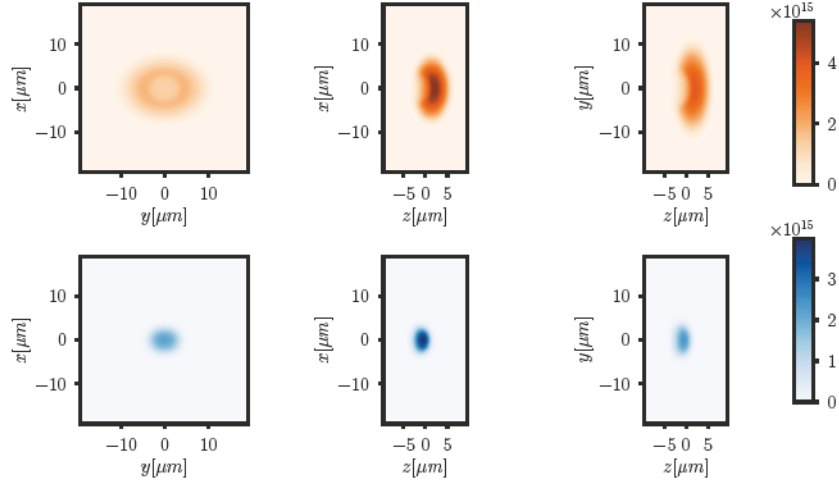


FIGURE 3.5: The plots show the integrated (over z, y, x from left to right) two-dimensional density profiles in units of $1/\text{m}^2$ of sodium (in $m_F = 1$, top row) and lithium (in $m_F = 1$, top row), obtained from imaginary time propagation of the corresponding GPE. We observe a clear change of the atomic clouds due to their interaction: the smaller and lighter lithium cloud “sits” on top of a distorted ellipsoidal sodium cloud (gravity acts in z -direction). The simulation was done on a three-dimensional lattice with $N_x = N_y = 256$ and $N_z = 128$ grid points and lattice spacing $a = 0.15\mu\text{m}$.

This (so-called Strang) splitting is accurate to second order [127]. In this way we include the spin-changing collisions into the numerical split-step integration of the combined GPE. As a result, the final integrator is again symplectic and also approximately conserves the total magnetization (up to bounded oscillations that go to zero as $\Delta t \rightarrow 0$).

Solving the imaginary time version for the GPE (together with appropriate normalization steps, see [129] for more details) we have calculated the initial mean-field wavefunctions $\psi_{N/L,1}^{(0)}(x, y, z)$ of the BEC mixture in the $m_F = 1$ states. The resulting density profiles $n_{N/L,1}^{(0)}(x, y, z) = |\psi_{N/L,1}^{(0)}(x, y, z)|^2$ are shown in the figures 3.5 and 3.6. The obtained solutions are then used as an initial state for simulating the real-time dynamics following the quench of the experiment, which we realize by initializing a desired imbalance between the two sodium components, i.e., $\psi_{N,m_F}(x, y, z)(t = 0) = \alpha_{m_F} \psi_{N,1}^{(0)}(x, y, z)$ with $|\alpha_1|^2 + |\alpha_0|^2 = 1$.

In order to describe the experiment in more detail, we take into account several imperfections that are neglected in the ideal GPE simulation. In particular, we have observed loss in the $m_F = 0$ density of sodium. An exponential fit of the experimental data revealed a finite life-time τ , which we take into account by adding a term, $i/(2\tau)\psi_{N,0}$, to the corresponding component of the GPE. Furthermore, we have observed a strong dependence of the simulation results on the initial particle numbers N_N and N_L . Consequently, we extracted the fluctuations from experiment

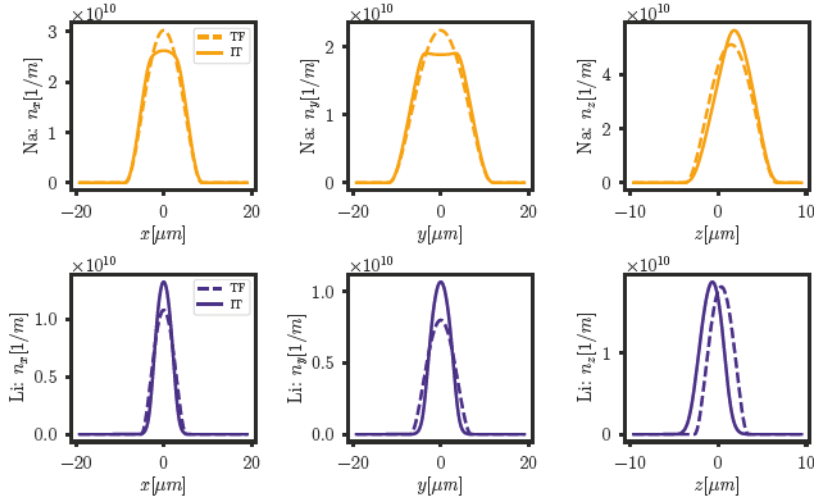


FIGURE 3.6: The plots show the integrated (over z and y , z and x , y and x from left to right) one-dimensional density profiles of sodium (in $m_F = 1$, top row) and lithium (in $m_F = 1$, top row) for the parameters as in figure 3.5. We compare the result from imaginary time propagation (solid lines, “IT”) to a Thomas-Fermi prediction that neglects the interaction between sodium and lithium (dashed lines, “TF”), which shows that the density-density interactions significantly modify the shape of the two-species condensate.

and calculated their mean values and empirical standard deviations,

$$\bar{N}_N \approx 295.8 \times 10^3, \quad \sigma_{N_N} \approx 7.2 \times 10^3, \quad (3.33a)$$

$$\bar{N}_L \approx 55.6 \times 10^3, \quad \sigma_{N_L} \approx 3.9 \times 10^3, \quad (3.33b)$$

$$\bar{\tau} \approx 505.7 \text{ms}, \quad \sigma_{\tau} \approx 24.0 \text{ms}. \quad (3.33c)$$

We include these fluctuations into our simulation by sampling the corresponding parameters from independent Gaussian distributions with expectation value and variance estimated from the experimental data. The results of a single simulation are illustrated in figure 3.7.

The simulation demonstrates that the sodium clouds change their spatial shape in the course of the dynamics. In particular, the two components $m_F = 1, 0$ tend to “avoid each other”, i.e., regions of large density in one component typically correspond to low densities in the other component. This behavior is expected because the hyperfine states are immiscible [130]. As a direct consequence of this observation, we do not expect to be able to describe the experiment in a single-mode approximation with the naive microscopic parameters given in Eq. (3.26). However, the fit shown in figures 3.3 and 3.4 demonstrates that a single mode description is sufficient to describe the experimental observations. This fact fortifies our statement that the spatial dynamics essentially “renormalizes” the model parameters, which in turn enables a simple description of the global observable N_p/N .

By averaging multiple GPE simulations, we obtain a prediction for the experimental observable, shown in figure 3.8. Even though the predicted curve does not

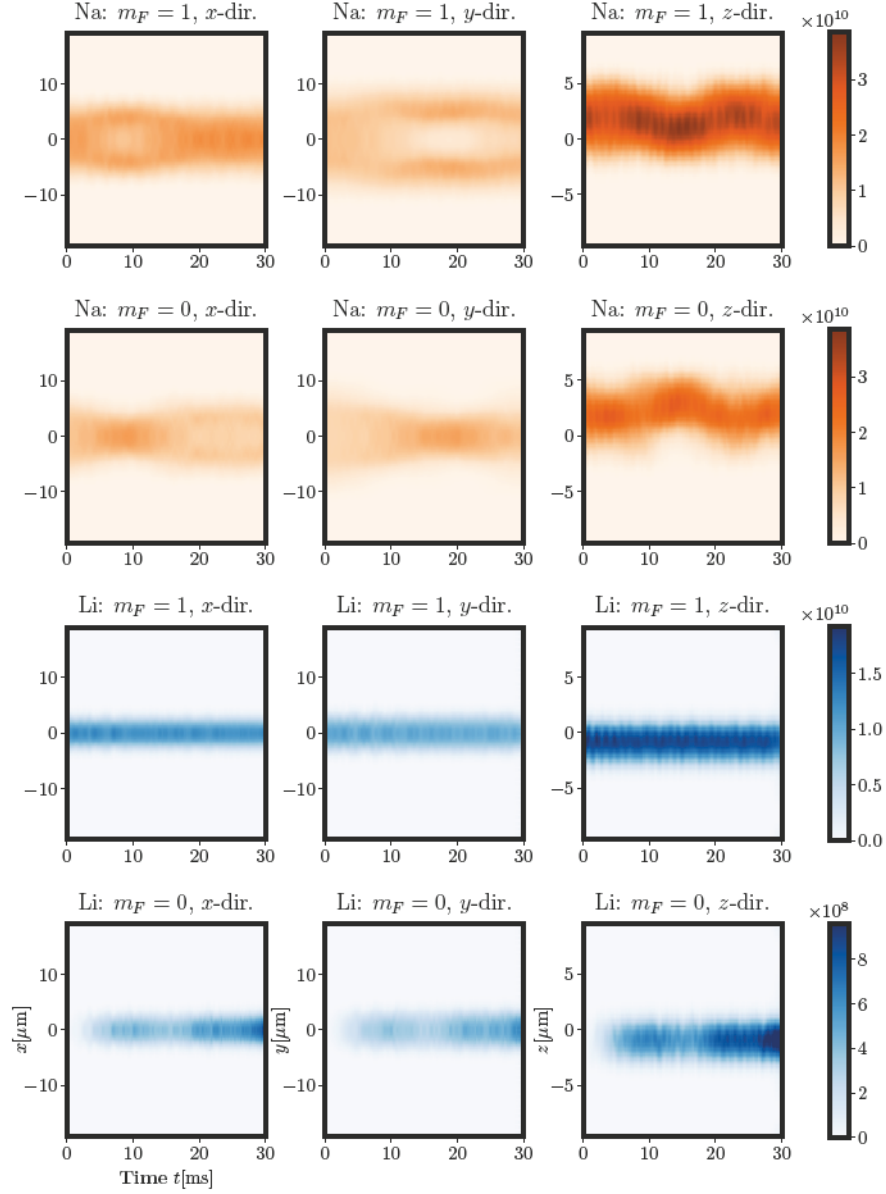


FIGURE 3.7: We plot the evolution of one-dimensional integrated densities (rows: $m_F = 1, 0$ components for sodium and lithium, columns: profiles in x, y, z -directions) extracted from a single GPE simulation in units of $1/\text{m}$. The simulation predicts spin-exchange dynamics that increases the density of lithium in $m_F = 0$. However, we also observe substantial spatial dynamics that “demixes” the sodium clouds. Note the increased color scale of the lithium $m_F = 0$ state by a factor of 20 compared to $m_F = 1$ for better visibility

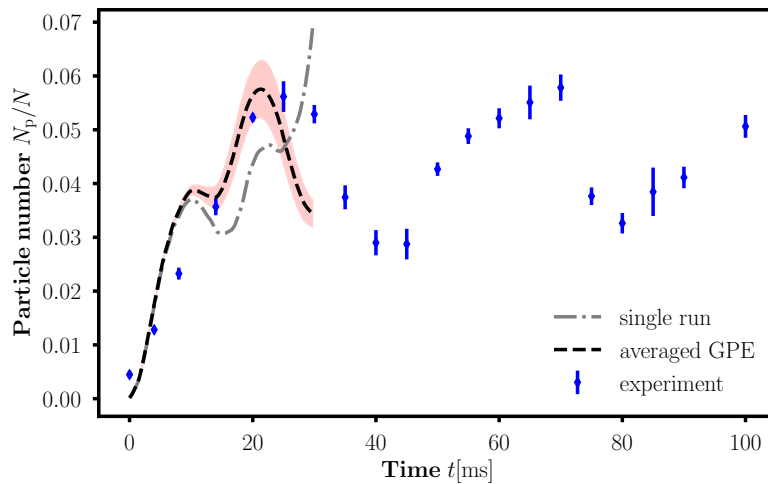


FIGURE 3.8: We show the average evolution of the particle number (black dashed line) obtained from 100 GPE simulations with fluctuating experimental parameters. The red band indicates the error on the mean and the gray dashed-dotted line corresponds to the specific realization shown in figure 3.7. The initial rise is in reasonable agreement with the experimental data (blue symbols).

quantitatively agree with the experimental data, the amplitude of the initial rise agrees well³. However, due to lattice artifacts at $t \gtrsim 30$ ms (not shown) the present lattice sizes prohibit long simulation times, which would be necessary to make a quantitative prediction of, e.g., an oscillation frequency. Additionally, the individual runs start to differ strongly after ~ 20 ms, such that also the required statistics increases with the evolution time. As a consequence, we have no quantitative ab-initio prediction of the experiment for the full observation time at the moment.

There is a number of possible reasons for the deviations between the simulation and the experiment. First, the GPE simulation is a mean-field approximation that neglects quantum-statistical fluctuations. Second, the approximation also assumes perfect condensates and neglects any thermal fraction of the Bose gases. Third, any experimental input parameter is not perfectly fixed; moreover, their fluctuations are neither Gaussian nor independent. Finally, after the presented simulations were completed, the particle number measurements were re-calibrated, which revealed substantially lower particle numbers for lithium (see [108] for new parameter estimates). We expect that a repetition of the simulation, including for instance more appropriate fluctuations and refined parameters, would lead to a better agreement. Nevertheless, the results presented in this section already provide a qualitative picture of the real-space dynamics of spin-changing collisions and indicate that the experiment indeed follows the expected dynamics.

³We have chosen to display a specific realization in figure 3.7 that is close to this mean evolution.

3.D Spin-changing collisions as an anharmonic oscillator

Let us reconsider the mean-field single mode evolution equations of the two coupled spins, Eq. (3.8). Without the phenomenological damping, this set of equations can be written as

$$i\partial_t L_{z,N} = \lambda (L_{+,N} L_{-,L} - L_{-,N} L_{+,L}) , \quad (3.34a)$$

$$i\partial_t L_{\pm,N} = \mp 2\chi L_{z,N} L_{\pm,N} \pm 2\lambda L_{z,N} L_{\pm,L} , \quad (3.34b)$$

$$i\partial_t L_{z,L} = \lambda (L_{+,L} L_{-,N} - L_{-,L} L_{+,N}) , \quad (3.34c)$$

$$i\partial_t L_{\pm,L} = \mp \Delta L_{\pm,L} \pm 2\lambda L_{z,L} L_{\pm,N} , \quad (3.34d)$$

where $L_{\pm} = L_x \pm iL_y$, which arise from the classical Hamiltonian

$$H = \chi L_{z,N}^2 + \Delta L_{z,L} + \lambda (L_{+,N} L_{-,L} + L_{-,N} L_{+,L}) . \quad (3.35)$$

The evolution can be simplified by considering the conservation of the total energy $E = H$, the magnetization $M = L_{z,N} + L_{z,L}$, as well as the spin lengths $\ell_s = \sqrt{L_{z,s}^2 + L_{+,s} L_{-,s}} = \frac{N_s}{2}$ for both species $s = N, L$. With

$$L_{z,N} = M - L_{z,L} , \quad (3.36a)$$

$$L_{+,L} L_{-,L} = \ell_L^2 - L_{z,L}^2 , \quad (3.36b)$$

$$L_{+,N} L_{-,N} = \ell_L^2 - (M - L_{z,L})^2 , \quad (3.36c)$$

$$\lambda (L_{+,N} L_{-,L} + L_{-,N} L_{+,L}) = E - \chi (M - L_{z,L})^2 - \Delta L_{z,L} , \quad (3.36d)$$

we can exploit the conservation laws to derive a closed equation for $L_{z,N}$. Explicitly, we calculate

$$\begin{aligned} -\partial_t^2 L_{z,L} &= \lambda [(-\Delta L_{+,L} + 2\lambda L_{z,L} L_{+,N}) L_{-,N} - (\Delta L_{-,L} - 2\lambda L_{z,L} L_{-,N}) L_{+,N}] \\ &\quad + \lambda [(2\chi L_{z,N} L_{-,N} - 2\lambda L_{z,N} L_{-,L}) L_{+,L} \\ &\quad - (-2\chi L_{z,N} L_{+,N} + 2\lambda L_{z,N} L_{+,L}) L_{-,L}] \end{aligned} \quad (3.37a)$$

$$\begin{aligned} &= g (L_{+,N} L_{-,L} + L_{-,N} L_{+,L}) (-\Delta + 2\chi L_{z,N}) \\ &\quad + 4\lambda^2 [L_{z,L} L_{+,N} L_{-,N} - L_{z,N} L_{+,L} L_{-,L}] \end{aligned} \quad (3.37b)$$

$$\begin{aligned} &= \lambda \left(E - \chi (M - L_{z,L})^2 - \Delta L_{z,L} \right) [-\Delta + 2\chi (M - L_{z,L})] \\ &\quad + 4\lambda^2 \left\{ L_{z,L} \left[\ell_N^2 - (M - L_{z,L})^2 \right] - (M - L_{z,L}) (\ell_L^2 - L_{z,L}^2) \right\} . \end{aligned} \quad (3.37c)$$

This equation has the form of a particle oscillating in an anharmonic potential, i.e.,

$$\partial_t^2 L_{z,L} = -V'(L_{z,L}) , \quad V(L_z) = c_1 L_z + \frac{c_2}{2} L_z^2 + \frac{c_3}{3} L_z^3 + \frac{c_4}{4} L_z^4 \quad (3.38)$$

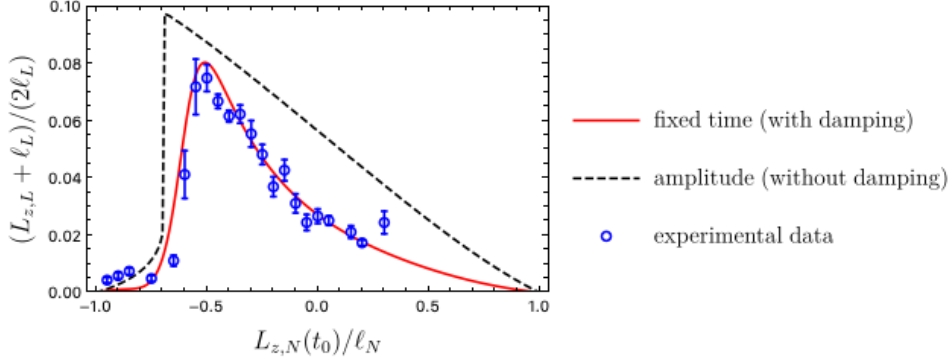


FIGURE 3.9: The plot shows the resonance of figure 3.4A with the same experimental data (blue symbols), together with numerical simulations of the anharmonic oscillator, Eq. (3.38), with fit parameters given in Eq. (3.9). While the damped simulation (red curve, evaluated at fixed time $t = 30\text{ms}$) fits the experimental data, the pure anharmonic oscillator (black dashed curved, evaluated is the oscillation amplitude) clearly shows the characteristic triangular shape (cf. figure 3.10.)

with the coefficients

$$c_1 = -\Delta m + 2\chi EM - 4\lambda^2 \ell_L^2 M + \chi \Delta M - 2\chi^2 M^3, \quad (3.39a)$$

$$c_2 = -2\chi E + 4\lambda^2 \ell_L^2 + 4\lambda^2 \ell_N^2 + \Delta^2 - 4\chi \Delta M + 6\chi^2 M^2 - 4\lambda^2 M^2, \quad (3.39b)$$

$$c_3 = 3\chi \Delta - 6\chi^2 M + 12\lambda^2 M, \quad (3.39c)$$

$$c_4 = 2\chi^2 - 8\lambda^2. \quad (3.39d)$$

For our usual initial conditions, Li is fully polarized. This implies the initial values

$$L_{z,L}(t_0) = -\ell_L, \quad \partial_t L_{z,L}(t_0) = 0. \quad (3.40)$$

The resulting oscillation of $L_{z,L}$ can therefore be pictured by the potential V , which is set by the initial condition of Na. In our case, the total energy is then fixed to be

$$E = \chi (M - \ell_L)^2 + \Delta \ell_L \quad (3.41)$$

and the behavior of the system is dictated by the initial Na imbalance, which sets the magnetization in the range

$$-\ell_L - \ell_N \leq M \leq -\ell_L + \ell_N. \quad (3.42)$$

In figure 3.9, we show the resulting resonance obtained from a numerical solution with the parameters given in Eq. (3.9) that we used to fit the experiment at the magnetic field B_A . The plot shows the amplitude of the oscillation of $L_{z,L}$ (i.e., the maximum value) together with the value at fixed time $t = 30\text{ms}$ for a simulation where we include a friction term $2\gamma \partial_t L_{z,L}$ with the same damping constant as before. Although the dynamics of this damping is not identical with the one introduced in Eq. (3.8), the obtained resonance again fits the experimental data. Both the damped

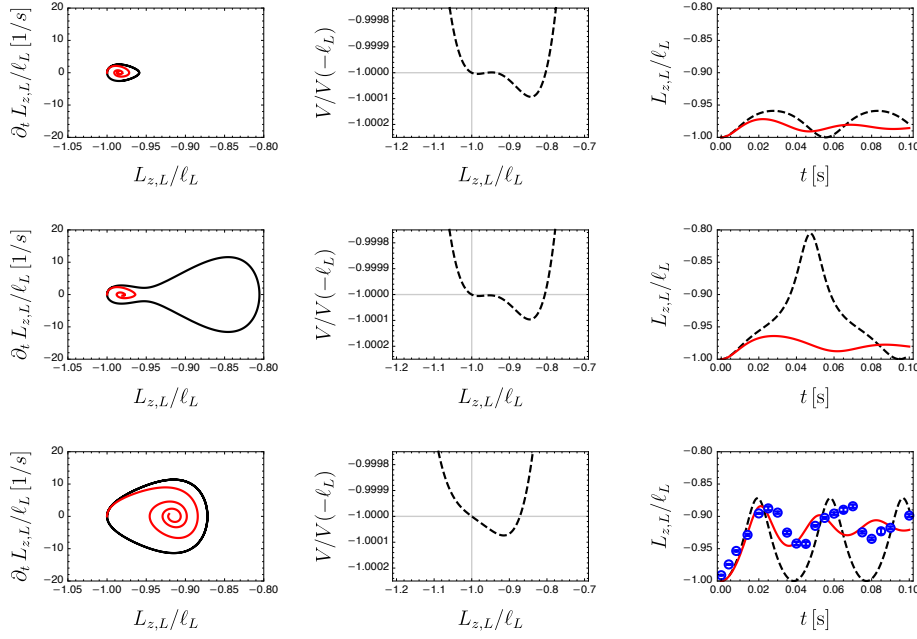


FIGURE 3.10: The three rows show simulation results for different values of $L_{z,N}/\ell_N = -0.7, -0.68, -0.118$ (top to bottom). The middle panel shows the potential V with the initial condition $L_{z,L} = -\ell_L$ indicated by the gray lines. The right panel shows the following dynamics of $L_{z,L}$ for undamped (gray dashed line) and damped (red solid line) oscillators. The left panel shows a phase space picture of the evolution. The change of the shape of the potential is responsible for the shape of the resonance shown in figure 3.9. In particular, the (dis)appearance of a local minimum close to the initial state is responsible for the non-analytic change of the amplitude of $L_{z,L}$ as a function of the initial $L_{z,N}$.

and undamped results show a characteristic asymmetric shape with a very steep slope around $L_{z,N} \approx -0.7\ell_N$.

The origin of this shape is a direct consequence of the anharmonic potential $V(L_z)$. This is illustrated in figure 3.10. Depending on the initial value of $L_{z,N}$, the potential $V(L_{z,L})$ changes its shape and the spin $L_{z,L}$ is either “trapped” in a local minimum or can “escape” to the global minimum, resulting in much larger oscillation amplitudes.

The plot in the bottom right of figure 3.10, which includes the experimental data, shows that the phenomenological friction term describes the experiment less accurately than the damping introduced in Eq. (3.8). However, the resonance shown in figure 3.9 is not affected because it only probes the early-time dynamics where this difference is insignificant. In conclusion, the qualitative features of the spin-changing collisions observed in the experiment are well captured by a anharmonic oscillator. This observation may provide important physical intuition for future experiments on hetero-nuclear spin-changing collisions.

Chapter 4

Dynamical topological transitions in the massive Schwinger model

This chapter is based on the article [33] with the figures and large parts of the text taken from it. This project was initiated by discussions among F. Jendrzejewski, P. Hauke and myself during our combined work on the projects discussed in the previous two chapters. I performed the analytic and numerical calculations presented here. The numerical simulations were supported by J. T. Schneider. The interpretation in terms of correlation functions was developed in discussions among N. Müller, J. Berges, P. Hauke and myself. While all authors participated in the writing of the manuscript [33], I made significant contributions to the wording and structuring of the text. In the appendices 4.A and 4.B, I include additional related material that was not printed in [33].

4.1 Motivation and setup

The topological structure of gauge theories has many important manifestations [131–135]. In quantum chromodynamics (QCD), e.g., it allows for an additional term in the action that explicitly breaks charge conjugation parity (CP) symmetry [136–138]. Though the angle θ that parametrizes this term is in principle unconstrained, experiments have found very strong bounds on CP violation, consistent with $\theta = 0$ [58]. In one elegant explanation, θ is described as a dynamical field that undergoes a phase transition, the “axion” [59, 139, 140], which is currently sought after in experiments [141]. However, the controlled study of topological effects far from equilibrium remains highly challenging [142]. Here, quantum simulators, as discussed in the previous chapters, offer an attractive alternative approach. While theories of the standard model, such as QCD, are beyond the current abilities of quantum simulators, existing technology [13, 14] can already simulate simpler models, which puts insights into the topological properties of gauge theories within reach. In this respect, the massive Schwinger model [86], describing quantum electrodynamics (QED) in 1+1 dimensions, is particularly interesting because it allows for a CP-violating θ -term similar to QCD. However, while ground state and thermal properties of QCD

and of the Schwinger model have been extensively studied [57, 143], much less is known about their topological structure out of equilibrium.

In this chapter, we investigate the non-equilibrium real-time evolution of the massive Schwinger model after a quench of the topological θ angle. We find topological transitions in the fermion sector, which appear as vortices in the single-particle propagator when θ changes by more than a critical value. In the limit of vanishing gauge coupling, we rigorously connect this phenomenon to dynamical quantum phase transitions (DQPTs), which in condensed-matter lattice models are currently receiving considerable attention [60, 144–146]. A topological nature of DQPTs has previously been revealed in non-interacting theories [147–149]. Here, we demonstrate how to construct a general dynamical topological invariant that is valid in the continuum and, most importantly, also in interacting theories. Moreover, our topological invariant provides a physical interpretation of DQPTs in terms of fermionic correlation functions. Enabled by this result, we use non-perturbative real-time lattice calculations at intermediate to strong coupling to show that the topological transition persists up to $e/m \lesssim 1$. Already for lattices as small as 8 sites, we obtain good infrared convergence. Moreover, the relevant phenomena occur on time scales that have already been accessed in proof-of-principle quantum simulations of gauge theories [13, 14]. These features will enable near-future experiments based on trapped ions [13], superconducting qubits [14], and cold neutral atoms [29] to probe this dynamical topological transition.

4.1.1 θ -quenches in the massive Schwinger model

The massive Schwinger model is a prototype model for 3+1D QCD since both share important features such as a non-trivial topological vacuum structure and a chiral anomaly [57, 86]. CP violation can be studied by adding a so-called topological θ -term, $(e\theta/2\pi) E_x$, to the Hamiltonian density, where E is the electric field and e the dimensionful gauge coupling. In temporal axial gauge, and by making a chiral transformation, the θ -term can be absorbed into the fermion mass term to give the following Hamiltonian [86],

$$H_\theta = \int dx \left[\frac{1}{2} E_x^2 + \psi_x^\dagger \gamma^0 \left(i\gamma^1 D_x + m e^{i\theta\gamma^5} \right) \psi_x \right]. \quad (4.1)$$

Here, ψ are two-component fermion operators, $\gamma^{0/1}$ constitute the Clifford algebra in two space-time dimensions, and $\gamma^5 \equiv \gamma^0\gamma^1$. The Hamiltonian contains the energy of the electric field, the kinetic term of the fermions, which are coupled to the gauge sector via the covariant derivative $D_x = \partial_x + ieA_x$, where e is the electric coupling, and the fermion rest mass m . While the addition of the θ -term is an imaginary contribution to the action (see [150]), we emphasize that the Hamiltonian (4.1) remains hermitian. In particular, its spectrum is real and θ does not introduce any instability.

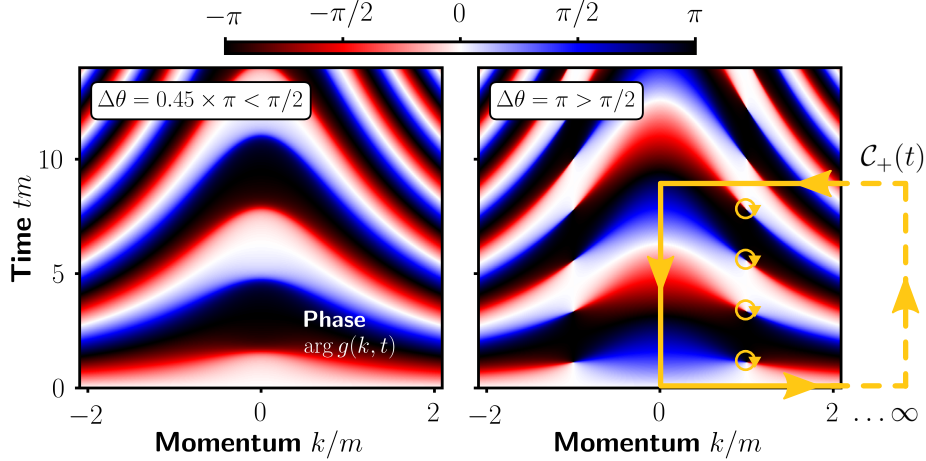


FIGURE 4.1: Phase of the time-ordered correlator [Eq. (4.2)] after θ quenches at vanishing gauge coupling. The real-time evolution of the phase exhibits qualitative differences when the quench is weaker/stronger than the critical value $\Delta\theta_c = \pi/2$, exemplified here for $\Delta\theta = 0.45\pi$ (left) and $\Delta\theta = \pi$ (right). The phase is analytic for small quenches ($|\Delta\theta| < \Delta\theta_c$), while for large quenches ($|\Delta\theta| > \Delta\theta_c$) vortices form at $(\pm k_c, t_c^{(n)})$. The integration path $\mathcal{C}_+(t)$, here shown for $tm \approx 9$, encloses a discrete number of vortices (marked by yellow circles), leading to integer increments of the topological invariant ν as time progresses (see Fig. 4.2).

Here, we wish to study how topological properties appearing through the CP-violating θ -term become manifest in the real-time dynamics of the theory. To this end, we prepare the system in the ground-state $|\Omega(\theta)\rangle$ of H_θ and switch abruptly to another value θ' , thereby quenching the system out of equilibrium. Since the θ -angle in the massive Schwinger model has the same topological origin as its counterpart in 3+1D QCD, we can interpret the studied quench as a classical, external axion field. In the following, we will show that this quench generates topological transitions, which appear as momentum–time vortices in the phase of the gauge-invariant time-ordered Green’s function,

$$g_{\theta \rightarrow \theta'}(k, t) = \int dx e^{-ikx} \langle \psi^\dagger(x, t) e^{-ie \int_0^x dx' A(x', t)} \psi(0, 0) \rangle. \quad (4.2)$$

Here, we abbreviated $\langle \dots \rangle = \langle \Omega(\theta) | \dots | \Omega(\theta) \rangle$ and $O(x, t) = e^{iH_\theta t} O(x) e^{-iH_\theta t}$ with $O \in \{\psi, \psi^\dagger, A\}$, which encodes the dependence on the quench parameters. We will first discuss these topological transitions in the continuum theory at weak coupling, where we show analytically their direct correspondence to DQPTs. These results will motivate the definition of a general topological invariant, which will enable us to study also the interacting theory, discussed further below.

4.2 Non-interacting limit

In the limit of vanishing coupling, $e/m \rightarrow 0$, the massive Schwinger model is reduced to a free fermionic theory that can be solved analytically (see appendix

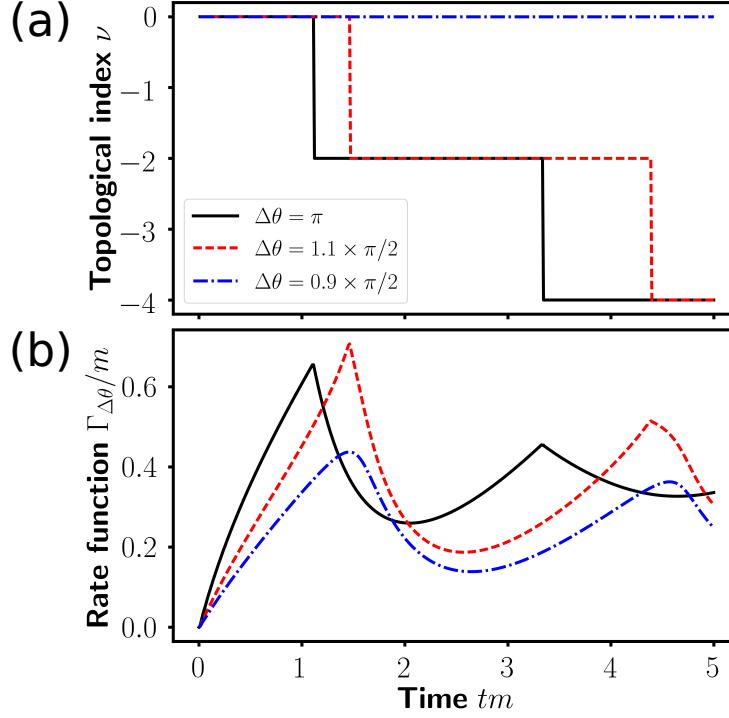


FIGURE 4.2: Dynamical topological transitions at vanishing gauge coupling. (a) The topological invariant exhibits jumps at critical times $t_c^{(n)} = (2n - 1)\pi / [2\omega(k_c)]$ with $n \in \mathbb{N}$, if $|\Delta\theta| > \pi/2$, while the dynamics is topologically trivial for $|\Delta\theta| < \pi/2$. (b) For $|\Delta\theta| > \pi/2$, the rate function [Eq. (4.5)] shows non-analytic kinks at times $t_c^{(n)}$.

4.A for detailed calculations) by diagonalizing $H_\theta = \int dk H_\theta(k)$, with $H_\theta(k) = \psi_k^\dagger \gamma^0 (k\gamma^1 + m e^{i\theta\gamma^5}) \psi_k$. Figure 4.1 displays the phase of $g_{\theta \rightarrow \theta'}$ as a function of (k, t) for two exemplary quenches with $\Delta\theta = 0.45\pi, \pi$ (our results here depend only on $\Delta\theta = (\theta - \theta') \in (-\pi, \pi]$). Strong quenches in the range $|\Delta\theta| > \frac{\pi}{2}$ are accompanied by the formation of vortices at critical times $t_c^{(n)} = (2n - 1)t_c$, with $t_c = \pi / [2\omega(k_c)]$, $n \in \mathbb{N}$ and $\omega(k) = \sqrt{k^2 + m^2}$. These appear in pairs of opposite winding at critical modes $\pm k_c = \pm m\sqrt{-\cos(\Delta\theta)}$.

4.2.1 An order parameter for dynamical topological transitions

This observation suggests to define a dynamical topological order parameter that counts the difference of vortices contained in left (-) versus right (+) moving modes, $\nu \equiv n_+ - n_-$, with

$$n_\pm(t) \equiv \frac{1}{2\pi} \oint_{\mathcal{C}_\pm(t)} dz \left\{ \tilde{g}^\dagger(\mathbf{z}) \nabla_{\mathbf{z}} \tilde{g}(\mathbf{z}) \right\}. \quad (4.3)$$

Here, $\tilde{g}(\mathbf{z}) \equiv g_{\theta \rightarrow \theta'}(k, t') / |g_{\theta \rightarrow \theta'}(k, t')|$ and $\mathcal{C}_\pm(t)$ is a rectangular path enclosing the left/right half of the $\mathbf{z} = (k, t')$ -plane up to the present time t , i.e., it runs (counter-clockwise) along $(0, 0) \leftrightarrow (0, t) \leftrightarrow (\pm\infty, t) \leftrightarrow (\pm\infty, 0) \leftrightarrow (0, 0)$ as visualized in

Fig. 4.1. As exemplified in Fig. 4.2(a), the topological invariant remains trivial for $|\Delta\theta| < \pi/2$, while for $|\Delta\theta| > \pi/2$ it changes abruptly at critical times $t_c^{(n)}$.

These critical times coincide with fundamental changes in the properties of the real-time evolution, coined DQPTs [60]. DQPTs are revealed in the so-called Loschmidt amplitude, which is related to the vacuum persistence amplitude [91] and which is a common measure, e.g., in the field of quantum chaos [151]. The Loschmidt amplitude quantifies the overlap of the time-evolved state with its initial condition,

$$L_{\theta \rightarrow \theta'}(t) \equiv \langle \Omega(\theta) | e^{-iH_{\theta'} t} | \Omega(\theta) \rangle . \quad (4.4)$$

It is convenient to further define an intensive “rate function”

$$\Gamma_{\theta \rightarrow \theta'}^{(L)}(t) \equiv - \lim_{V \rightarrow \infty} \frac{1}{V} \log |L_{\theta \rightarrow \theta'}(t)| . \quad (4.5)$$

DQPTs appear as non-analyticities of Eq. (4.5) [zeros of Eq. (4.4)].

In the limit $e/m \rightarrow 0$, where the system is in a product state $|\Omega(\theta)\rangle = \bigotimes_k |\Omega_k(\theta)\rangle$, the Loschmidt amplitude can be decomposed into Fourier modes,

$$L_{\theta \rightarrow \theta'}(t) = \prod_k \langle \Omega_k(\theta) | e^{-iH_{\theta'}(k)t} | \Omega_k(\theta) \rangle . \quad (4.6)$$

At $e/m \rightarrow 0$, we have the additional identity $\langle \Omega_k(\theta) | e^{-iH_{\theta'}(k)t} | \Omega_k(\theta) \rangle = g_{\theta \rightarrow \theta'}(k, t)$ (see 4.A for a proof). Thus, zeros of the Loschmidt amplitude imply that the phase of the Green’s function becomes undefined for a critical mode, enabling the appearance of the vortices seen in Fig. 4.1. As a consequence, at zero coupling the topological transitions and non-analyticities of the rate function in Eq. (4.5) strictly coincide [see Fig. 4.2(b)].

For non-interacting lattice theories, a topological nature of DQPTs has previously been revealed through the phase of the Fourier-decomposed Loschmidt amplitude, $\arg [\langle \Omega_k(\theta) | \exp[-iH_{\theta'}(k)t] | \Omega_k(\theta) \rangle] = \phi_{\text{geom}} + \phi_{\text{dyn}}$ [147]. Here, the total phase has been divided into a trivial dynamical phase $\phi_{\text{dyn}}(k, t)$ and the so-called Pancharatnam geometric phase, $\phi_{\text{geom}}(k, t)$. At a DQPT, the winding number of ϕ_{geom} changes by an integer. This change can be computed by integration across (half) the Brillouin zone at fixed time t [147], which has been used in the recent experiments of Refs. [148, 149]. For this prescription to work, however, one needs to subtract the trivial dynamical phase ϕ_{dyn} , which can reasonably be obtained only perturbatively close to the non-interacting case. Compared to this standard prescription, our construction in Eq. (4.3) has a number of advantages. First, the prescription of Ref. [147] fails for $\theta \neq 0, \pi$, where the absence of a particle–hole symmetry makes modes at $k = 0, \pm\infty$ inequivalent. Second, and more importantly, by using a closed path in the (k, t) plane (cf. Fig. 4.1) only the singular geometric part contributes to the integral in Eq. (4.3), irrespective of the smooth dynamical phase. Thus, together with the definition through fermionic correlators, Eq. (4.2), instead of Fourier modes

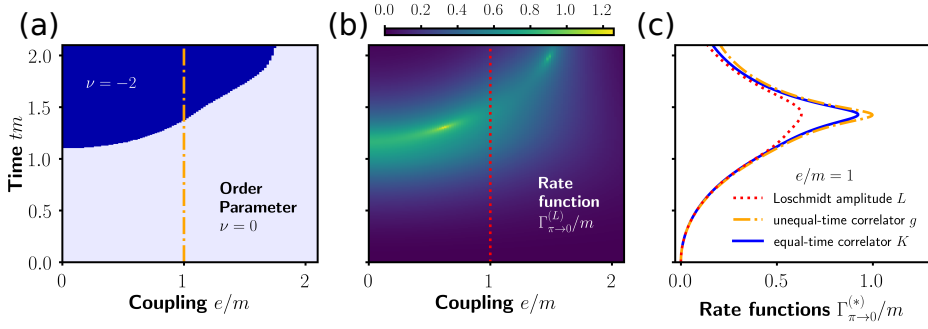


FIGURE 4.3: Dynamical topological transitions beyond weak coupling. (a) The integer-valued topological invariant ν clearly distinguishes different “phases” in the (t, e) -plane. The topological transition persists at larger coupling, but shifts towards later times and appears at sufficiently large coupling. (b) The maxima of the rate function obtained from the many-body overlap agree qualitatively with the transitions in ν , but are blurred by the finite lattice size. (c) Rate functions computed from the full wave-function overlap [red dotted; c.f. panel (b) and Eq. (4.5)], from fermionic two-time correlators [orange dot-dashed; c.f. panel (a) and Eq. (4.2)], and equal-time correlators [blue solid line; c.f. Eq. (4.8)], all indicate the same time of the first topological transition, here illustrated for $e/m = 1$. Simulations are for a small lattice of $N = 8$ sites as relevant for first quantum-simulator experiments, and with lattice spacing $am = 0.8$.

of the wave-function overlap, Eq. (4.6), our formulation enables us to tackle also the interacting theory.

4.3 Towards strong coupling

To investigate if the topological transitions persist at non-vanishing coupling, $e/m > 0$, we perform non-perturbative real-time lattice simulations based on Exact Diagonalization (ED), using the Python package QuSpin [152]. We focus on the strongest quench $\Delta\theta = \pi$ (or $-m \rightarrow m$), using staggered fermions with lattice Hamiltonian [82]

$$H = \sum_{n=0}^{N-1} \left[\frac{a}{2} E_n^2 + m (-1)^n \phi_n^\dagger \phi_n - \frac{i}{2a} \left(\phi_n^\dagger U_n \phi_{n+1} - \text{h.c.} \right) \right]. \quad (4.7)$$

Here, ϕ_n are one-component fermion operators on an even number of lattice sites N , E_n and U_n are electric fields and links, and a is the lattice spacing. To apply ED, we restrict the simulation to the physical Hilbert space by solving the Gauss’ law constraint $G_n|\text{phys}\rangle = 0$ with $G_n = E_n - E_{n-1} - e \left[\phi_n^\dagger \phi_n + \frac{(-1)^{n-1}}{2} \right]$. In contrast to previous works [13, 153], we use periodic boundary conditions (PBC)¹, see the appendix 4.B for more details. To efficiently compute the topological invariant ν in our numerics, we adapt a formalism that has originally been developed for computing Chern numbers in momentum space [154]. The possibility to adapt

¹To obtain a finite-dimensional Hilbert space, we drop the single remaining bosonic mode describing a homogeneous background electric field.

this formalism to our case is another feature of our definition in Eq. (4.3) since it is enabled by the use of a closed integration path in the (k, t) plane. This adaption forces ν to remain integer-valued even when evaluated on coarse grids, thus leading to convergence already for small lattices ².

As can be expected from the above discussions, at small e/m transitions in the topological invariant coincide with maxima in the rate function, see Fig. 4.3. Further, both structures congruently persists at larger values of e/m . Importantly, however, while the system sizes accessible for ED do not allow one to discern clear kinks in the rate function, the non-equilibrium topological invariant ν sharply distinguishes between topologically inequivalent phases, revealing a shift of the transitions towards larger t_c as e/m is increased. While the results for $e/m \lesssim 1$ are already reasonably finite-volume converged for the small system size plotted, at $e/m \gtrsim 1$ finite-volume effects persist up to $N = 20$ (see section 4.3.2 below). Nevertheless, the topological transition must vanish at sufficiently large coupling e_c because θ becomes an irrelevant parameter in the limit $m \rightarrow 0$ [155]. Finite size effects in our numerical results hinder a quantitative determination of e_c . Motivated by these limitations, we propose to quantum simulate of the present setup.

4.3.1 Quantum simulation

Importantly, the first topological transition happens on times of order $t_c m \sim 1 - 2$, which lies within coherence times that are accessible with existing and proposed quantum simulators [13, 14, 29]. A straightforward realization of the scenario discussed in this chapter may be achieved with a quantum computer based on trapped-ions or superconducting qubits, where quench dynamics has been studied recently [13, 14]. Though these experiments used only four lattice sites of staggered fermions, larger lattices are within reach of current technology [156–159]. Very recently, it has been shown that variational algorithms can prepare the ground state of the lattice Schwinger model with 8 to 20 sites with high fidelity [35, 160]. The relevant dynamics can be implemented by discretizing the unitary evolution operator into a sequence of quantum gates [13, 161]. For staggered fermions, the mass term is realized by local rotations and can be quenched by inverting the direction of rotation. All observables studied in this chapter can then be accessed by an appropriate sequence of unitary operators intermitted by spin flips. Alternatively, various works have proposed analog quantum simulators of the massive Schwinger model [7, 8, 26, 162]. In the implementations proposed in the previous chapters, which are based on mixtures of cold atoms in a tilted optical lattice, the fermion mass corresponds to Rabi oscillations between two hyperfine states driven by radiofrequency radiation or is set by the laser-assisted tunneling. In these setups, a mass quench may be

²In the non-interacting limit the topological invariant is not affected by the choice of lattice regularization, which we have explicitly checked at the example of staggered and Wilson fermions. Here, we restrict the simulations in the interacting case to staggered fermions, which are closer to the continuum limit given the limited resources.

simply implemented by abruptly adjusting the corresponding parameters, e.g., the Rabi frequency.

These experiments may unveil the topological transitions through different observables: First, a digital quantum computer could in principle work with the many-body wavefunctions to directly calculate the order parameter ν [Eq. (4.3)] and the rate function $\Gamma_{\theta \rightarrow \theta'}(t)$ [Eq. (4.5)]. Second, one could measure the two-time correlator $g_{\theta \rightarrow \theta'}(k, t)$ [Eq. (4.2)] [163, 164] and thereby avoid the study of many-body overlaps. Third, the discrete transition points of the order parameter are indicated also in experimentally more accessible equal-time correlation functions, $[\underline{F}(t)]_{xy}^{\alpha\beta} \equiv \langle [\psi^\alpha(t, x), \bar{\psi}^\beta(t, y)] \rangle$. Namely, let us define

$$K_{\theta \rightarrow \theta'}(t) \equiv \prod_k [\mathbf{F}(k, t) + \mathbf{F}(k, 0)]^2, \quad (4.8)$$

where $\mathbf{F} = (F_s, F_1, F_5)$ are Lorentz components³ of the correlator, $\underline{F}(t) = F_s(t)\mathbf{1} + F_\mu(t)\gamma^\mu + iF_5(t)\gamma^5$. One has $K_{\theta \rightarrow \theta'}(t) = \prod_k |g_{\theta \rightarrow \theta'}(k, t)|^2 = |L_{\theta \rightarrow \theta'}(t)|^2$ in the non-interacting limit (for details, see the appendix 4.A). This motivates to define the rate functions $\Gamma^{(g)}(t)$ and $\Gamma^{(K)}(t)$ analogously to $\Gamma^{(L)}(t)$ by replacing $|L(t)|$ in Eq. (4.5) with $\prod_k |g(k, t)|$ and $\sqrt{K(t)}$, respectively. We thus have three complementary definitions that coincide for $e/m \rightarrow 0$, obtained from equal-time correlators, Eq. (4.8), two-time correlators, Eq. (4.2), and the full many-body Loschmidt amplitude, Eq. (4.4). Remarkably, as illustrated in Fig. 4.3(c) for $e/m = 1$, even at intermediate couplings the maxima of all three rate functions indicate the same critical times with relative deviation less than about 8%. Below we show a quantitative comparison, which demonstrates that the three rate functions show comparable finite size deviations, which for the topological order parameter are significantly smaller.

Besides its experimental simplicity, Eq. (4.8) also gives an interesting interpretation of the dynamical topological transition in terms of a dephasing effect. Namely, Eq. (4.8) has zeros if and only if the mode k_c at time t_c exhibits perfect anti-correlation with the initial state, $\mathbf{F}(k_c, t_c) = -\mathbf{F}(k_c, 0)$. This anti-correlation is responsible for the non-analytic behavior of the associated rate function.

4.3.2 Finite size dependence of the transition times

We have extracted the critical times of the first topological transition $t_c^{(1)}$ as indicated by the rate functions of the Loschmidt amplitude L , the equal-time correlator K , the two-time correlator g , and the dynamical topological order parameter ν . While ν unambiguously determines a critical time by its discontinuous jump between two integer values, we have chosen the maxima of the three different rate functions as an indicator of $t_c^{(1)}$ for a quantitative comparison. This comparison is shown in Fig. 4.4 for weak ($e/m = 0.5$) and intermediate ($e/m = 1.0$) coupling strength as a function of lattice sites N . Remarkably, all three rate functions indicate similar

³We exclude F_0 in \mathbf{F} because mode-wise charge conservation implies $F_0(k, t) = 0$ at $e/m = 0$.

transition times for all investigated parameters. Nevertheless, the rate functions exhibit strong finite-size fluctuations, as expected for the small lattice sizes accessible with exact diagonalization, which become more pronounced at stronger coupling. In comparison, the transition times indicated by the dynamical topological order parameter show a smoother N -dependence with reduced finite-size deviations. We attribute this to the topological robustness of ν , which makes it a more suitable observable for finite lattices.

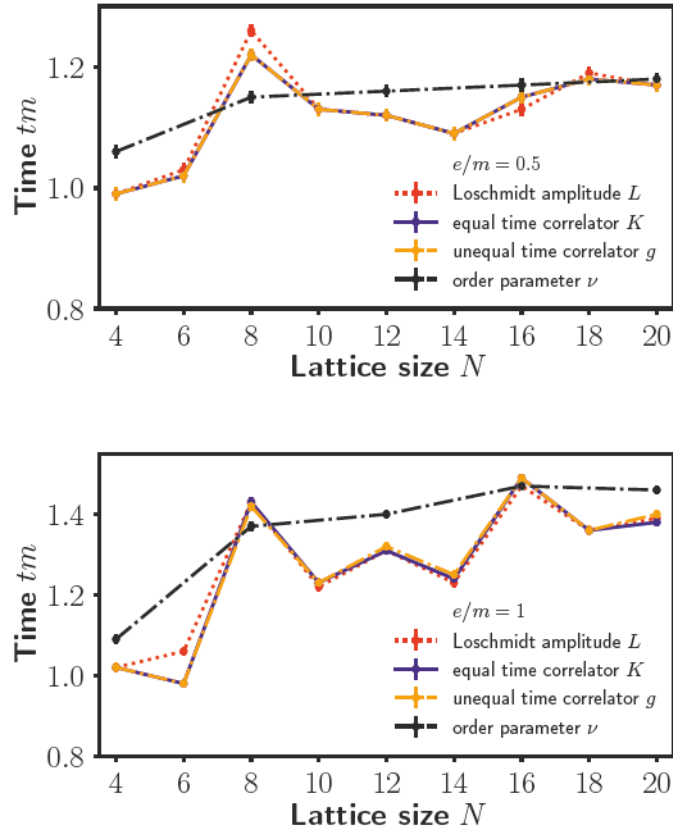


FIGURE 4.4: The critical times $t_c^{(1)}$ of the first topological transition as indicated by the first maxima of the three different rate functions - extracted from the Loschmidt amplitude L (red, dotted), the equal-time correlator K (blue, solid) and the two-time correlator g (orange, dashed) - are shown in comparison to the time indicated by the dynamical topological order parameter ν (black, dashed-dotted). In general, finite-size deviations are more pronounced for intermediate coupling ($e/m = 1.0$, right) than for weak coupling ($e/m = 0.5$, left), and are stronger for the rate functions than for the order parameter. Note that we only show data for ν for $N/2$ even because our definition is ambiguous for $N/2$ odd. The lattice spacing is $am = 0.8$ for all simulations. The error bars arise from a finite time step $dt/a = 0.01$ for saving the data.

4.4 Summary

In this chapter, we have studied the real-time dynamics of massive 1+1D QED with a θ -term, as a prototype model for topological effects in gauge theories. By establishing a general dynamical topological order parameter, which can be obtained from fermionic correlators and is valid in interacting theories, we have identified the appearance of dynamical topological transitions after changes in the external “axion” field. A connection between the topological transitions to DQPTs, which is rigorous at zero coupling, persists in our numerics of the interacting theory, thus providing a physical interpretation of DQPTs in terms of fermionic correlators. Finally, our topological order parameter can directly be applied also in the study of condensed-matter models, where the construction of topological invariants for interacting systems is a major outstanding challenge [165–167].

In this study, we have identified a relevant problem for state-of-the-art quantum simulation. The described dynamical transitions constitute an ideal first step because the relevant dynamics appears at short time scales and small system sizes. We expect the topological nature to provide robustness against experimental imperfections, which may provide a starting point to tackle the question of certifiability of quantum simulation.

Despite the simplicity of the considered model, our study shows that quantum simulators provide a unique perspective to the topological structure of QCD out of equilibrium. Phenomena closely related to the physics studied in this chapter are the conjectured Chiral Magnetic and similar effects [168–171], which remain challenging in and out of equilibrium for theoretical studies [81, 84, 142, 172–178]. Here, a simple next step for future quantum simulators is to model these effects by spatial domains of the θ -parameter [179].

Appendix: Even more about the massive Schwinger model

In the first section 4.A of this appendix, we give a detailed summary of analytic predictions for the quench dynamics, which are based on non-interacting fermions. In the second section 4.B, we prove a general solution of Gauss' law on a periodic one-dimensional lattice for arbitrary fermion discretizations, which we used for the numerical ED simulations.

4.A Free fermion calculations

4.A.1 Diagonalization

Consider the free fermion Hamiltonian $H = \int_0^L dx \psi_x^\dagger \gamma^0 (i\gamma^1 \partial_x + m e^{i\theta\gamma^5}) \psi_x$ on a circle of length L . The spatial structure of the Hamiltonian becomes diagonal in Fourier space,

$$\psi_x = \frac{1}{\sqrt{L}} \sum_p \psi_p e^{ipx}, \quad \psi_p = \frac{1}{\sqrt{L}} \int_0^L dx \psi_x e^{-ipx}, \quad (4.9)$$

where the sum runs over all $p = 2\pi n/L$ with $n \in \mathbb{Z}$. Choosing

$$\gamma^0 = \begin{pmatrix} 1 & 0 \\ 0 & -1 \end{pmatrix}, \quad \gamma^1 = \begin{pmatrix} 0 & 1 \\ -1 & 0 \end{pmatrix}, \quad \gamma^5 = \begin{pmatrix} 0 & 1 \\ 1 & 0 \end{pmatrix}, \quad (4.10)$$

as a specific representation of the Clifford algebra, the Hamiltonian reads

$$H = \sum_p \psi_p^\dagger H_p \psi_p, \quad H_p(\theta, m) = \begin{pmatrix} m \cos \theta & -p + im \sin \theta \\ -p - im \sin \theta & -m \cos \theta \end{pmatrix}, \quad (4.11)$$

which leads to the eigenvalues and -vectors $\pm\omega_p = \pm\sqrt{p^2 + m^2}$ and u_p^\pm . Defining quasi-particle operators by

$$\begin{pmatrix} a_p \\ b_{-p}^\dagger \end{pmatrix} = U_p^\dagger \psi_p, \quad (4.12)$$

where $U_p = (u_p^+, u_p^-)$ is the unitary with $U_p^\dagger H_p U_p = \text{diag}(\omega_p, -\omega_p)$, this yields

$$H = \sum_p \omega_p (a_p^\dagger a_p + b_p^\dagger b_p - 1). \quad (4.13)$$

The explicit expressions for the eigenvectors are

$$u_p^+ = [2\omega_p(\omega_p - m \cos \theta)]^{-1/2} \begin{pmatrix} p - im \sin \theta \\ m \cos \theta - \omega_p \end{pmatrix}, \quad (4.14a)$$

$$u_p^- = [2\omega_p(\omega_p - m \cos \theta)]^{-1/2} \begin{pmatrix} -m \cos \theta + \omega_p \\ p + im \sin \theta \end{pmatrix}, \quad (4.14b)$$

such that the commutation relations are preserved, $\{a_p, a_q^\dagger\} = \delta_{pq} = \{b_p, b_q^\dagger\}$. The vacuum $|\Omega\rangle$ is the ground state of H and fulfills $a_p|\Omega\rangle = 0 = b_{-p}|\Omega\rangle$.

Two sets of quasi-particle operators corresponding to $H(\theta, m)$ and $H(\theta', m')$ are directly related by

$$\begin{pmatrix} a_p(\theta, m) \\ b_{-p}^\dagger(\theta, m) \end{pmatrix} = U_p^\dagger(\theta, m) U_p(\theta', m') \begin{pmatrix} a_p(\theta', m') \\ b_{-p}^\dagger(\theta', m') \end{pmatrix}. \quad (4.15)$$

The two corresponding vacua can be related by

$$|\Omega(\theta, m)\rangle = \prod_p N_p^{-1} \left[A_p + B_p a_p^\dagger(\theta', m') b_{-p}^\dagger(\theta', m') \right] |\Omega(\theta', m')\rangle \quad (4.16)$$

with the coefficients

$$A_p(\theta, m; \theta', m') = (u_p^-)^\dagger(\theta', m') u_p^-(\theta, m), \quad (4.17a)$$

$$B_p(\theta, m; \theta', m') = (u_p^-)^\dagger(\theta', m') u_p^+(\theta, m) \quad (4.17b)$$

and $|N_p|^2 = |A_p|^2 + |B_p|^2 = 1$ is fixed by the normalization $\langle \Omega | \Omega \rangle = 1$ and the orthonormality of the eigenvectors u_p^\pm .

4.A.2 Quench dynamics and DQPT

The dynamics following a quench from $H(\theta, m)$ to $H(\theta', m')$ is described by

$$\begin{aligned} |\psi_{\theta, m \rightarrow \theta', m'}(t)\rangle &= e^{-iH(\theta', m')t} |\Omega(\theta, m)\rangle \quad (4.18) \\ &= \prod_p N_p^{-1} \left[A_p e^{i\omega_p(m')t} + B_p a_p^\dagger(\theta', m') b_{-p}^\dagger(\theta', m') e^{-i\omega_p(m')t} \right] |\Omega(\theta', m')\rangle. \end{aligned}$$

Thus, the Loschmidt amplitude follows as

$$\begin{aligned} L_{\theta, m \rightarrow \theta', m'}(t) &= \langle \psi_{\theta, m \rightarrow \theta', m'}(0) | \psi_{\theta, m \rightarrow \theta', m'}(t) \rangle \quad (4.19) \\ &= \prod_p \left[\cos(\omega_p t) + i \frac{|B_p|^2 - |A_p|^2}{|A_p|^2 + |B_p|^2} \sin(\omega_p t) \right]. \end{aligned}$$

Focusing on θ -quenches with $m' = m$, we explicitly obtain after some algebra,

$$|A_p|^2 = \frac{\omega_p^2 + p^2 + m^2 \cos(\theta - \theta')}{2\omega_p^2}, \quad |B_p|^2 = \frac{m^2 \sin^2\left(\frac{\theta' - \theta}{2}\right)}{\omega_p^2}. \quad (4.20)$$

Therefore the Loschmidt amplitude becomes

$$L_{\theta \rightarrow \theta'}(t) = \prod_p \ell_{\theta \rightarrow \theta'}(t, p), \quad \ell_{\theta \rightarrow \theta'}(t, p) = \cos(\omega_p t) - i \frac{p^2 + m^2 \cos(\theta' - \theta)}{\omega_p^2} \sin(\omega_p t), \quad (4.21)$$

and from the condition $\ell(p, t) = 0$ we can read off the zeros to occur at

$$t_c^{(n)} = \frac{\pi(2n+1)}{\omega_{p_c}}, \quad p_c^2 = -m^2 \cos(\theta - \theta'). \quad (4.22)$$

In the thermodynamic limit, these zeros cause non-analyticities in the rate function associated to the Loschmidt amplitude,

$$\Gamma_{\theta' \rightarrow \theta}(t) = - \lim_{V \rightarrow \infty} \frac{1}{V} \log |L_{\theta \rightarrow \theta'}(t)| = - \int_{-\infty}^{\infty} \frac{dp}{2\pi} \log \ell_{\theta \rightarrow \theta'}(t, p). \quad (4.23)$$

The final integral expression is evaluated numerically for the results plotted in figure 4.1.

4.A.3 Two-time correlation functions and the order parameter

To get a better understanding of the physics underlying the DQPT, we observe the following identity

$$\begin{aligned} \ell_{\theta \rightarrow \theta'}(t, p) &= \langle \Omega(\theta) | a_p^\dagger(\theta') a_p(\theta') e^{i\omega_p t} + b_{-p}(\theta') b_{-p}^\dagger(\theta') e^{-i\omega_p t} | \Omega(\theta) \rangle \\ &= \langle \Omega(\theta) | \psi_p^\dagger(t) \psi_p(0) | \Omega(\theta) \rangle = g(t, p), \end{aligned} \quad (4.24)$$

where $\psi(t) = e^{iH(\theta')t} \psi e^{-iH(\theta')t}$ denotes a Heisenberg field operator w.r.t. to the post-quench Hamiltonian. Consequently, the DQPTs occur at zeros of the time-ordered correlator $g(t, p)$. As a consequence, the phase of $g(t, p) = |g(t, p)| e^{i\varphi(t, p)}$ becomes ill-defined at the critical points $(t_c^{(n)}, p_c)$ and develops a winding. This observation underlies the order parameter introduced in this chapter. Crucially, we change the perspective from the Loschmidt amplitude to correlation functions, which in turn have a straightforward generalization and interpretation also in the interacting theory.

4.A.4 Interpretation with equal-time correlators

We can give yet another interpretation by considering the Loschmidt echo,

$$|L_{\theta \rightarrow \theta'}(t)|^2 = \text{Tr} [\rho_{\theta \rightarrow \theta'}(t) \rho_{\theta \rightarrow \theta'}(0)] , \quad (4.25)$$

where $\rho_{\theta \rightarrow \theta'}(t) = e^{-iH(\theta')t} |\Omega(\theta)\rangle \langle \Omega(\theta)| e^{iH(\theta)t}$ is the pure-state density operator. For two Gaussian states ρ_k , $k = 1, 2$, e.g., ground states of a non-interacting system and their time-evolution, the trace in (4.25) can be calculated (see [180]) as

$$\text{Tr} [\rho_1 \rho_2] = \det \left[G_1 G_2 + \tilde{G}_1 \tilde{G}_2 \right] , \quad (4.26)$$

with the correlators

$$(G_k)_{ij} = \text{Tr} \left[\rho_k \psi_i^\dagger \psi_j \right] , \quad \left(\tilde{G}_k \right)_{ij} = \delta_{ij} - (G_k)_{ij} . \quad (4.27)$$

In our case the indices i, j label both lattice sites and spinor components. Introducing the statistical propagator

$$(F_k)_{ij} = \frac{1}{2} \text{Tr} \left[\rho_k \left(\psi_i^\dagger \psi_j - \psi_j \psi_i^\dagger \right) \right] , \quad (4.28)$$

and using the commutation relations $\{ \psi_i^\dagger, \psi_j \} = \delta_{ij}$, we can rewrite the result (4.26) as

$$\text{Tr} [\rho_1 \rho_2] = \det \left[2F_1 F_2 + \frac{1}{2} \right] . \quad (4.29)$$

In the our case, this gives

$$|L_{\theta \rightarrow \theta'}(t)|^2 = \det \left[2F(t)F(0) + \frac{1}{2} \right] = \prod_p \det' \left[F(p, t)F(p, 0) + \frac{1}{2} \right] , \quad (4.30)$$

where the prime indicates the remaining determinant in spinor space after performing the spatial functional determinant in Fourier space where the correlators are diagonal,

$$F_{xy}(t) = \int \frac{dp}{2\pi} e^{ip(x-y)} F(p, t) . \quad (4.31)$$

We further decompose the correlator in its Lorentz components⁴, $\underline{F} = F\gamma^0 = F_s \mathbf{1} + F_0 \gamma^0 + F_1 \gamma^1 + iF_5 \gamma^5$. For brevity, we only state the explicit expressions for

⁴The additional matrix γ^0 corresponds to a change of variables from ψ^\dagger to $\bar{\psi} = \psi^\dagger \gamma^0$.

the simplest quench $-m \rightarrow m$ (or $\theta' = \pi \rightarrow \theta = 0$),

$$F_s(p, t) = \frac{1}{2} \text{Tr} [F(p, t) \gamma^0] = \frac{m}{\omega_p^3} \left[\frac{1}{2} (p^2 - m^2) + p^2 \cos(2\omega_p t) \right] \quad (4.32a)$$

$$F_0(p, t) = \frac{1}{2} \text{Tr} [\gamma^0 F(p, t) \gamma^0] = 0 \quad (4.32b)$$

$$F_1(p, t) = \frac{1}{2} \text{Tr} [\gamma^1 F(p, t) \gamma^0] = \frac{p}{\omega_p^3} \left[\frac{1}{2} (m^2 - p^2) + m^2 \cos(2\omega_p t) \right] \quad (4.32c)$$

$$F_5(p, t) = \frac{1}{2} \text{Tr} [-i\gamma^5 F(p, t) \gamma^0] = \frac{mp}{\omega_p^2} \sin(2\omega_p t) . \quad (4.32d)$$

At the critical momenta, where $p_c^2 = m^2$, these equations further simplify

$$F_s(p_c, t) = F_1(p_c, t) = \frac{1}{2\sqrt{2}} \cos(2\sqrt{2}mt) , \quad F_5(p_c, t) = \frac{1}{2} \sin(2\sqrt{2}mt) . \quad (4.33)$$

For a general θ -quench, the electric charge is conserved for each momentum mode separately, i.e., $F_0(p, t) = 0$, and the remaining components form a spin-1/2 vector $\mathbf{F}(p, t) = (F_s(p, t), F_1(p, t), F_5(p, t))$ with $\mathbf{F}^2(p, t) = 1/4$. Then a direct computation of the relevant determinant gives

$$\det' \left[F(p, t) \gamma_0 F(p, 0) \gamma_0 + \frac{1}{2} \right] = \frac{1}{2} + 2\mathbf{F}(p, t) \cdot \mathbf{F}(p, 0) \quad (4.34)$$

and therefore the Loschmidt can be written as

$$|L_{\theta \rightarrow \theta'}(t)|^2 = \prod_p [\mathbf{F}(p, t) + \mathbf{F}(p, 0)]^2 . \quad (4.35)$$

Thus a DQPT, determined by $|L_{\theta \rightarrow \theta'}(t)|^2 = 0$, occurs if $\mathbf{F}(p, t) = -\mathbf{F}(p, 0)$ (as already visible in Eq. (4.33)). This expression for the orthogonality of the time-evolved state and the initial state becomes particularly simple because the (non-interacting) system remains in a product state in momentum space, completely determined by the spin-1/2 vectors $\mathbf{F}(p, t)$, and may be pictured as a collection of Bloch spheres.

4.B Solving Gauss' law on a ring

In one spatial dimension, gauge invariance is very restrictive and prohibits propagating gauge degrees of freedom. As a consequence, the restriction to gauge-invariant states that fulfill Gauss' law allows us to rephrase the theory in terms of fermions only. While this procedure is well known in the continuum and straightforwardly generalizes to a lattice with open boundary conditions, we are not aware of a solution of Gauss' law with periodic boundary conditions (PBC). In this section we give a detailed solution of this problem with PBC.

4.B.1 Separating the background

We consider a general coupling between gauge and matter fields described by some fermion Hamiltonian H_ψ and focus on the electric energy part H_E . The full Hamiltonian reads

$$H = H_E + H_\psi, \quad H_E = \frac{a}{2} \sum_{n=0}^{N-1} E_n^2 \quad (4.36)$$

with a general Gauss' law operator

$$G_n = E_n - E_{n-1} - Q_n, \quad (4.37)$$

where H_ψ and Q_n depend on the fermion discretization. PBCs imply $E_0 = E_N$ and $Q_0 = Q_N$. We split

$$E_n = E + \delta E_n \quad (4.38)$$

with $E = \sum_n E_n$, such that we have the constraint

$$\sum_n \delta E_n = 0. \quad (4.39)$$

We can thus rewrite

$$\sum_n \frac{1}{2} \left[E^2 + 2E\delta E_n + (\delta E_n)^2 \right] = \frac{N}{2} E^2 + \frac{1}{2} \sum_n (\delta E_n)^2. \quad (4.40)$$

In the following we focus on the background-independent part and change notation $\delta E_n \rightarrow E_n$ and $H_E \rightarrow H_E - aNE^2/2$, i.e we restrict ourselves to

$$H_E = \frac{a}{2} \sum_{n=0}^{N-1} E_n^2, \quad \sum_{n=0}^{N-1} E_n = 0. \quad (4.41)$$

4.B.2 Solving Gauss' law

For simplicity, we assume N even. We will show that

$$H_E \simeq a \sum_{n=0}^{N-1} \sum_{d=0}^{N/2} f(d) Q_n (Q_{n+d} + Q_{n-d}) \quad (4.42)$$

for a suitably chosen function $f(d)$. Here, " \simeq " denotes equality on the physical subspace where $G_n = 0$. This result depends crucially on the periodic boundary conditions and the constraint (4.39) as will become clear in the following. Consider

the contribution

$$C_d = \sum_n Q_n (Q_{n+d} + Q_{n-d}) \quad (4.43)$$

$$\simeq \sum_n (E_n - E_{n-1}) (E_{n+d} - E_{n+d-1} + E_{n-d} - E_{n-d-1}) \quad (4.44)$$

$$= \sum_n E_n (2E_{n+d} + 2E_{n-d} - E_{n+d+1} - E_{n+d-1} - E_{n-d+1} - E_{n-d-1}) , \quad (4.45)$$

where we have first applied (4.37) for $G_n = 0$ and then shifted indices (which is possible due to the PBCs). It is helpful to picture the different contributions by a string of numbers specifying their coefficients as follows

$$C_0 \leftrightarrow \cdots - 2, + 4, - 2 \dots \quad (4.46a)$$

$$C_1 \leftrightarrow \cdots - 1, + 2, - 2, + 2, - 1 \dots \quad (4.46b)$$

$$C_2 \leftrightarrow \cdots - 1, + 2, - 1, + 0, - 1, + 2, - 1 \dots \quad (4.46c)$$

$$C_3 \leftrightarrow \cdots - 1, + 2, - 1, + 0, + 0, + 0, - 1, + 2, - 1 \dots \quad (4.46d)$$

Now, we want to choose $f(d)$, weighting the coefficients in the above diagram, such that every column-wise sum is canceled and only the middle one is non-vanishing. Special care needs to be taken about the boundary conditions. To this end, we replace the terms

$$E_n E_{n+N/2} = - \sum_{j \neq N/2} E_n E_{n+j} \quad (4.47)$$

according to the constraint (4.39). In this way, we arrive at the following conditions on $f(d)$ (the "obvious" conditions from the above diagram on the left-hand side, the "boundary" conditions on the right-hand side)

$$4f(0) - 2f(1) \neq 4f\left(\frac{N}{2}\right) - 2f\left(\frac{N}{2} - 1\right) \quad (4.48a)$$

$$2f(1) - 2f(0) - f(2) = 4f\left(\frac{N}{2}\right) - 2f\left(\frac{N}{2} - 1\right) \quad (4.48b)$$

$$2f(d) - f(d-1) - f(d+1) = 4f\left(\frac{N}{2}\right) - 2f\left(\frac{N}{2} - 1\right) \quad (4.48c)$$

$$2f\left(\frac{N}{2} - 1\right) - 2f\left(\frac{N}{2}\right) - f\left(\frac{N}{2} - 2\right) = 4f\left(\frac{N}{2}\right) - 2f\left(\frac{N}{2} - 1\right) . \quad (4.48d)$$

Here the first inequality insures that the coefficient in front of E_n^2 is non-zero, while the other coefficients ($E_n E_{n+d}$) are all vanishing. The d -dependent equation is only valid for $d \neq 0, 1, N/2-1, N/2$. In principle we thus have $2+(N/2+1)-4 = N/2-1$ equations and one inequality for $N/2+1$ unknown variables. The normalization (the overall factor) gives one more condition, such that we expect a one-dimensional solution space (without the inequality).

We will make the ansatz $f(0) = 0$ and $f(1) = 1$ and solve the system recursively. In the end, we will see that the solution satisfies the inequality

$$f\left(\frac{N}{2} - 1\right) - 2f\left(\frac{N}{2}\right) \neq 1 \quad (4.49)$$

and we adjust the overall factor. Note that there could be other solutions, but the following one leads to consistent physical interpretation as discussed further below. Our recursive ansatz yields

$$f(2) = 2 - 4f\left(\frac{N}{2}\right) + 2f\left(\frac{N}{2} - 1\right) \quad (4.50a)$$

$$f(d+1) = 2f(d) - f(d-1) - 4f\left(\frac{N}{2}\right) + 2f\left(\frac{N}{2} - 1\right), \quad 3 \leq d \leq \frac{N}{2} - 1 \quad (4.50b)$$

$$6f\left(\frac{N}{2}\right) = 4f\left(\frac{N}{2} - 1\right) - f\left(\frac{N}{2} - 2\right). \quad (4.50c)$$

The first two lines are solved as

$$f(d) = d - \left(\sum_{j=0}^{d-2} 4j\right) f\left(\frac{N}{2}\right) + \left(\sum_{j=0}^{d-2} 2j\right) f\left(\frac{N}{2} - 1\right), \quad 2 \leq d \leq \frac{N}{2} - 1 \quad (4.51)$$

$$= d + (d^2 - 3d + 2) \left[-2f\left(\frac{N}{2}\right) + f\left(\frac{N}{2} - 1\right)\right], \quad (4.52)$$

which can be used to obtain

$$f\left(\frac{N}{2} - 1\right) = \frac{-2N + 4 + 2f\left(\frac{N}{2}\right)(N^2 - 10N + 24)}{N^2 - 10N + 20} \quad (4.53)$$

$$f\left(\frac{N}{2} - 2\right) = \frac{N^2 - 8N + 8 + 2f\left(\frac{N}{2}\right)(N^2 - 14N + 48)}{N^2 - 10N + 20}, \quad (4.54)$$

from which one finds from the remaining equation

$$6f\left(\frac{N}{2}\right) = \frac{-N^2 + 8 + f\left(\frac{N}{2}\right)(6N^2 - 52N + 96)}{N^2 - 10N + 20} \quad (4.55)$$

with the solution

$$f\left(\frac{N}{2}\right) = \frac{N^2 - 8}{8(N - 3)}, \quad (4.56)$$

such that

$$f(d) = d + \frac{d^2 - 3d + 2}{3 - N}, \quad 2 \leq d \leq \frac{N}{2} - 1 \quad (4.57)$$

and the constraint

$$f\left(\frac{N}{2} - 1\right) - 2f\left(\frac{N}{2}\right) = \frac{1}{3-N} \neq 1 \quad (4.58)$$

is indeed satisfied if $N \neq 2$. The difference of the two sides of the equality $\frac{N-2}{N-3}$ sets the prefactor of E_n^2 .

In conclusion, we have found the identity

$$\begin{aligned} \sum_{n=0}^{N-1} E_n^2 \simeq & -\frac{N-3}{2(N-2)} \sum_{n=0}^{N-1} \left\{ Q_n (Q_{n+1} + Q_{n-1}) + \frac{N^2-8}{4(N-3)} Q_n Q_{n+N/2} \right. \\ & \left. + \sum_{d=2}^{N/2-1} \left[\left(d + \frac{d^2-3d+2}{N-3} \right) Q_n (Q_{n+d} + Q_{n-d}) \right] \right\}, \end{aligned} \quad (4.59)$$

on the physical Hilbert space, assuming $N \neq 2$, periodic boundary conditions and the separation of the background electric field.

4.B.3 Limits of the potential

In a more compact notation our result takes the form

$$H_E = \frac{a}{2} \sum_n E_n^2 = \sum_{nm} v(d_{nm}) Q_n Q_m, \quad (4.60)$$

where d_{nm} is the distance

$$d_{nm} = \min(|n-m|, N-|n-m|), \quad (4.61)$$

and the potential $v(d)$ is given by

$$v(d) = -\frac{a}{4} \left(\frac{N-3}{N-2} \right) \times \begin{cases} d, & d = 0, 1 \\ d + \frac{d^2-3d+2}{3-N}, & 2 \leq d \leq \frac{N}{2} - 1 \\ \frac{N^2-8}{4(N-3)}, & d = \frac{N}{2} \end{cases}. \quad (4.62)$$

If we take first the infinite volume limit $N \rightarrow \infty$, then

$$v(d) \rightarrow -\frac{ad}{4}, \quad d < \infty. \quad (4.63)$$

Taking first the continuum limit, we define $x = ad$ and $L = aN$. Keeping L fixed the asymptotic behavior is

$$d + \frac{d^2-3d+2}{3-N} = \frac{x^2 - Lx + 2a^2}{3a^2 - La} \rightarrow \frac{1}{a} \left(x - \frac{x^2}{L} \right), \quad (4.64)$$

such that

$$v(d) \rightarrow -\frac{1}{4} \left(x - \frac{x^2}{L} \right) . \quad (4.65)$$

In any case, the continuum limit in infinite volume gives

$$H_E \rightarrow -\frac{e^2}{4} \int dx dy |x - y| \rho(x) \rho(y) , \quad (4.66)$$

which is precisely the result one can obtain directly in the continuum theory (see [86]). For a finite system size with periodic boundary conditions, we have

$$H_E^{(L)} = -\frac{e^2}{4} \int dx dy V(r_{xy}) \rho(x) \rho(y) \quad (4.67)$$

with the potential

$$V(r) = r - \frac{r^2}{L} , \quad r_{xy} = \min(|x - y|, L - |x - y|) = \frac{1}{2} (L - |L - 2|x - y||) . \quad (4.68)$$

Note that this gives a correction to the (otherwise constant) force

$$F(r) = V'(r) = 1 - \frac{2r}{L} , \quad (4.69)$$

with minimum/maximum at $r = 0, L/2$.

In summary, we have obtained an explicit expression for the electric energy in terms of the fermionic charge. Our result agrees with the expectations from the continuum and provides a consistent correction for finite lattices.

Part II

Analyzing quantum simulators with quantum field theory

Chapter 5

Extraction of the instantaneous effective action in equilibrium

This chapter is based on the article [39] with the figures and large parts of the text taken from it. The contributions are the following. Foundational ideas for this project were defined in discussions among J. Schmiedmayer, J. Berges and S. Erne. I performed the analytical and numerical calculations for the theoretical part of this work. The code for extracting 1PI correlators was written by myself, while the code for generating thermal phase profiles was written by S. Erne. T. Schweigler performed the experiment and analyzed the experimental data, including the comparison to theory. J. Schmiedmayer and J. Berges supervised and guided the project. While all authors participated in the writing of the manuscript [39], I made significant contributions to the wording and structuring of the text. F. Cataldini, S. Ji, B. Rauer and M. Tajik helped conducting the experiment. In the appendix 5.B, I include additional related material that was not printed in [39].

5.1 Introduction

Quantum Field Theory (QFT) has a wide range of very successful applications from early-universe cosmology and high-energy physics to condensed matter physics. A central aspect of QFT is that it describes the many-body limit of complex interacting quantum systems, which is also relevant for quantum technology if devices become large. Present large-scale analog quantum simulators using ultra-cold atoms explore the many-body limit described by QFT [38, 62, 65, 99, 118, 119, 181–192]. Therefore, they may also be used to solve outstanding theoretical problems of QFT that are beyond classical computational techniques.

One of the big experimental challenges is probing the complex many-body states. One strategy is to detect every constituent (atom, superconducting qubit, quantum dot . . .) and its state. Such detections constitute a projective measurement of the many-body wave function in the constituent basis. For large systems such a measurement contains way too much information to be ever analyzed fully. This is reflected by the exponential complexity of “tomography” that prevents a complete characterization of the many-body quantum states [193].

By contrast, there are important simplifications occurring in the many-body limit described by QFT. In QFT, often only a small subset of the microscopic details of the underlying theory is relevant for the computation of measurable physical properties. This effective loss of details has its mathematical foundation in the renormalization program of QFT [50]. As a result, for a quantum simulation of such a theory, many of the detailed properties of the microscopic quantum device have no effect on the simulation outcome for quantities of interest [31].

This raises the important question of how to extract from experimental data the relevant information content of QFT. It is well known that an efficient description of QFT can be based on one-particle irreducible (1PI) correlation functions, called irreducible or proper vertices [50]. They represent the irreducible building blocks from which all physical observables may be constructed. This can be, e.g., the effective Hamiltonian determining the macroscopic dynamics, a possible spectrum of quasi-particles and their effective interaction strength. In a general setting, these vertices are functions of space and time or momentum and frequency, encoding the “running” of couplings prominently discussed in high-energy physics in the framework of the Standard Model of particle physics.

In principle, the irreducible vertices can be extracted from higher-order correlation functions [50]. The standard procedure employs correlation functions involving large time differences. While this is very suitable for high-energy collider experiments, where an analysis is based on the concept of asymptotic states in the infinite past and future, this is not adequate for many realizations of strongly interacting many-body systems where the notion of an initial state “long before” and a final state “long after” the collision is not physical. Moreover, often these systems are studied at a given snapshot in time, without any direct reference to states in the asymptotic past or future. This is especially true for cold-atom experiments where one takes pictures, for example measuring every atom either after time of flight [194] or in-situ [195, 196].

In this chapter, we develop a pathway to extract the irreducible vertices of a quantum many-body system from experimental measurements. Our approach employs a formulation of QFT based on equal-time correlation functions only [61, 197]. Equal-time correlation functions can be extracted from snapshot measurements [38, 190, 198] and, therefore, match well with experimental capabilities. We lay out the theoretical foundations of this approach, and illustrate the derivations using the sine-Gordon model. The irreducible vertices at equal times are estimated for this model both analytically and using numerical simulations. In particular, we show how to recover from the vertices the effective Hamiltonian underlying the dynamics. These theoretical results provide the basis for the benchmark verification of the QFT description extracted from experimental measurement. In the experiment, the sine-Gordon model is quantum simulated with two tunnel-coupled superfluids in thermal equilibrium [38]. We show how to extract the irreducible vertices from the experimental setup and compare the measurements to the theoretical estimates.

The agreement of the experimental results with the theoretical expectations within errors provides a proof-of-principle verification of the approach. This represents an important step towards quantum simulator applications that are beyond reach of classical computational techniques. A first example of such an application is the recent experimental extraction of the irreducible two- and four-vertices for a strongly correlated spin-1 Bose condensate far from equilibrium [65], where no theoretical solution is available and which has been performed in parallel to this work.

This chapter is organized as follows. We start in section 5.2 with a self-contained description of an equal-time formulation of quantum field theory and equal-time correlation functions as they arise naturally in experiments. In particular, we show how the instantaneous 1PI vertices, which constitute the fundamental building blocks of the QFT description of the many-body system, can be extracted from the measured equal-time correlation functions. In section 5.3, we illustrate these theoretical foundations for the sine-Gordon (SG) model [199–202] and calculate the 1PI correlation functions and the instantaneous effective action in the classical field theory limit in thermal equilibrium and compare it to numerical simulations. As a proof of principle, we show in section 5.4 an application to an experiment with two tunnel-coupled superfluids, which realizes the SG model [38, 203]. We conclude our work in section 5.5. The appendix 5.A contains detailed calculations.

5.2 **Extracting the irreducible vertices from equal-time correlations**

In a standard formulation of quantum field theory one starts from a typical scattering experiment which gives access to the transition amplitude between an initial state at times long before the collision and its final state at much later times. These transition amplitudes determine the S-matrix elements, which can be expressed in terms of time-ordered correlation functions of the underlying quantum field theory [50]. Knowledge of all time-ordered correlation functions is then equivalent to solving the quantum theory [204, 205].

However, time-ordered correlation functions and the description by an S-matrix formulation are conceptually less suitable in the analysis of strongly correlated complex quantum systems, which are often studied at a given snapshot in time. Such measurements at a given instant of time lead to the notion of equal-time correlation functions. In quantum field theory, these can be represented by expectation values of Weyl ordered products of field operators [61, 206]. Knowledge of all instantaneous (equal-time) correlation functions at a given time t contains all information about the many-body system at this instant of time. For example, the factorization properties of higher-order correlation functions directly reveal if the system is free (factorizing) or interacting (non factorizing) [38]. To extract the interaction constants of the underlying (effective) Hamiltonian one has to extract the so-called one-particle

irreducible (1PI) correlation functions [50] which represent the full non-perturbative interaction vertices of the quantum system.

While there are standard textbook concepts to extract the 1PI correlation functions from time-ordered correlation functions, the possibility to extract them from equal-time correlation functions is much less explored. Here we illustrate how to extract them from the equal-time correlations and thereby show how to determine the effective Hamiltonian from experiment at a snapshot in time.

We start in section 5.2.1 with an introduction to quantum field theory in an equal-time formalism. At the example of a scalar field theory, we show the relation to Wigner's phase-space formalism commonly used, e.g., in quantum optics. We further summarize how to extract connected correlation functions (5.2.2) and one-particle irreducible vertices (5.2.3) by introducing suitable generating functionals. Finally, we approximately calculate the instantaneous 1PI effective action in thermal equilibrium in section 5.2.4, which provides a direct connection to the parameters of the microscopic Hamiltonian, and give a recipe on how to proceed (5.2.5).

5.2.1 Equal-time formulation of quantum field theory

The use of equal-time correlations is motivated by the progress of cold atomic setups which nowadays allow to extract highly resolved images at a given instant in time. It has long been known that QFT can be set up by only employing such equal-time information, without relying on multi-time correlations [61, 197, 207]. This formulation has, however, never been widely used. Theoretical progress in solving the equal-time formalism is hampered by the lack of appropriate approximation schemes. Nevertheless, an equal-time formulation is perfectly suited to extract the irreducible vertices from experimental data representing a snapshot of the system at a fixed time.

Setting up an equal-time formulation relies on measurements of conjugate elementary operators that are non-commuting. As a consequence, one has to choose an ordering prescription [206]. Since correlations in cold atom systems are straightforwardly obtained by multiplying and averaging single shot results, the obtained correlations correspond to a fully symmetrized (so-called Weyl) ordering of the quantum operators. Moreover, as we show below, this choice of ordering leads to a definition of 1PI correlators that is directly related to Hamiltonian parameters. For the rest of this paper, we thus focus on Weyl-ordered correlation functions. A short discussion of other ordering prescriptions is given in the appendix 5.A.2.

For simplicity, we start with a real scalar field theory with Schrödinger field operators $\hat{\Phi}(\mathbf{x})$ and $\hat{\Pi}(\mathbf{x})$ that fulfill the canonical commutation relation

$$\left[\hat{\Phi}(\mathbf{x}), \hat{\Pi}(\mathbf{y}) \right] = i\hbar\delta(\mathbf{x} - \mathbf{y}) . \quad (5.1)$$

A general quantum state at time t is in the Schrödinger picture described by the density operator $\hat{\rho}_t$. Equivalently, knowing all correlations characterizes the state $\hat{\rho}_t$

(see appendix 5.A.3 for more details). Formally, all correlations can be conveniently summarized in the generating functional

$$Z_t[J] = \text{Tr} \left[\hat{\rho}_t \exp \left(J_{\mathbf{x}}^{\varphi} \hat{\Phi}_{\mathbf{x}} + J_{\mathbf{x}}^{\pi} \hat{\Pi}_{\mathbf{x}} \right) \right]. \quad (5.2)$$

Here we have introduced a notation where repeated indices are integrated over, e.g., $J_{\mathbf{x}}^{\varphi} \hat{\Phi}_{\mathbf{x}} = \int d^d x J^{\varphi}(\mathbf{x}) \hat{\Phi}(\mathbf{x})$. The J 's are so-called source fields, i.e., auxiliary variables that encode the dependence of $\hat{\rho}_t$ on $\hat{\Phi}$ and $\hat{\Pi}$, as indicated by φ and π . In the definition of Z_t , we have implemented the choice of ordering by treating the conjugate fields $\hat{\Phi}$ and $\hat{\Pi}$ symmetrically. The resulting correlation functions, which are obtained by taking functional derivatives are Weyl-ordered. For example at second order, we have

$$G_{\mathbf{x},\mathbf{y}}^{(2)}(t) = \begin{pmatrix} \langle \varphi_{\mathbf{x}} \varphi_{\mathbf{y}} \rangle_{W_t} & \langle \varphi_{\mathbf{x}} \pi_{\mathbf{y}} \rangle_{W_t} \\ \langle \pi_{\mathbf{x}} \varphi_{\mathbf{y}} \rangle_{W_t} & \langle \pi_{\mathbf{x}} \pi_{\mathbf{y}} \rangle_{W_t} \end{pmatrix}, \quad (5.3)$$

which consists of the three independent correlators

$$\langle \varphi_{\mathbf{x}} \varphi_{\mathbf{y}} \rangle_{W_t} = \left. \frac{\delta^2 Z_t[J]}{\delta J_{\mathbf{x}}^{\varphi} \delta J_{\mathbf{y}}^{\varphi}} \right|_{J=0} = \frac{1}{2} \text{Tr} \left[\hat{\rho}_t \left(\hat{\Phi}_{\mathbf{x}} \hat{\Phi}_{\mathbf{y}} + \hat{\Phi}_{\mathbf{y}} \hat{\Phi}_{\mathbf{x}} \right) \right], \quad (5.4a)$$

$$\langle \varphi_{\mathbf{x}} \pi_{\mathbf{y}} \rangle_{W_t} = \left. \frac{\delta^2 Z_t[J]}{\delta J_{\mathbf{x}}^{\varphi} \delta J_{\mathbf{y}}^{\pi}} \right|_{J=0} = \frac{1}{2} \text{Tr} \left[\hat{\rho}_t \left(\hat{\Phi}_{\mathbf{x}} \hat{\Pi}_{\mathbf{y}} + \hat{\Pi}_{\mathbf{y}} \hat{\Phi}_{\mathbf{x}} \right) \right], \quad (5.4b)$$

$$\langle \pi_{\mathbf{x}} \pi_{\mathbf{y}} \rangle_{W_t} = \left. \frac{\delta^2 Z_t[J]}{\delta J_{\mathbf{x}}^{\pi} \delta J_{\mathbf{y}}^{\pi}} \right|_{J=0} = \frac{1}{2} \text{Tr} \left[\hat{\rho}_t \left(\hat{\Pi}_{\mathbf{x}} \hat{\Pi}_{\mathbf{y}} + \hat{\Pi}_{\mathbf{y}} \hat{\Pi}_{\mathbf{x}} \right) \right]. \quad (5.4c)$$

This is explicitly verified in appendix 5.A.2, where also the higher-order case is discussed.

For a general quantum many-body system, $Z_t[J]$ may involve more than one pair of canonically conjugated fields. This possibility can be incorporated by adding appropriate sources J and essentially does not affect the general discussion.

In the following, we consider only correlators of φ to lighten the notation. Nevertheless, φ may stand for either of the two fields and π is only written explicitly when necessary to avoid confusion. In general, we then denote all Weyl-ordered correlators as

$$G_{\mathbf{x}_1, \dots, \mathbf{x}_n}^{(n)}(t) = \langle \varphi_{\mathbf{x}_1} \cdots \varphi_{\mathbf{x}_n} \rangle_{W_t} = \left. \frac{\delta^n Z_t[J]}{\delta J_{\mathbf{x}_1} \cdots \delta J_{\mathbf{x}_n}} \right|_{J=0}. \quad (5.5)$$

We refer to the appendix 5.A.1 for a summary of all notational conventions used throughout this paper. In Eq. (5.5), we have assumed a proper normalization, $\text{Tr} \hat{\rho}_t = 1$, which implies $Z_t[0] = 1$.

To make use of established, powerful QFT tools, we seek a representation of Z_t in terms of functional integrals. As shown in the appendix 5.A.4, the expression (5.2)

can be rewritten as a

$$Z_t[J] = \int \mathcal{D}\varphi \mathcal{D}\pi W_t[\varphi, \pi] \exp(J_{\mathbf{x}}^\varphi \varphi_{\mathbf{x}} + J_{\mathbf{x}}^\pi \pi_{\mathbf{x}}) . \quad (5.6)$$

The integration kernel W_t can be interpreted as a quasi-probability distribution,

$$W_t[\varphi, \pi] = \int \mathcal{D}\tilde{\varphi} \left\langle \varphi - \frac{\tilde{\varphi}}{2} \left| \hat{\rho}_t \right| \varphi + \frac{\tilde{\varphi}}{2} \right\rangle \exp\left(\frac{i}{\hbar} \tilde{\varphi}_{\mathbf{x}} \pi_{\mathbf{x}}\right) , \quad (5.7)$$

the so-called Wigner functional. Here $|\varphi\rangle$ denotes an eigenstate of the field operator $\hat{\Phi}$ with eigenvalue φ . The Wigner function itself has previously been applied successfully in the context of quantum optics [208] and also plays a prominent role in the semi-classical description of non-equilibrium quantum dynamics [209, 210]. Eq. (5.6) is the basis of the equal-time formulation of QFT and allows us to apply established procedures in the following.

5.2.2 Connected correlation functions

In QFT (and analogously in classical probability theory) it is well known that the correlations encoded in Z_t are largely redundant [50, 211]. The first step is the removal of additive redundancies, by the introduction of another generating functional,

$$E_t[J] = \log Z_t[J] . \quad (5.8)$$

We denote the corresponding correlations, called connected correlators, as

$$G_{c, \mathbf{x}_1, \dots, \mathbf{x}_n}^{(n)}(t) = \frac{\delta^n E_t[J]}{\delta J_{\mathbf{x}_1} \cdots \delta J_{\mathbf{x}_n}} \Big|_{J=0} . \quad (5.9)$$

Explicitly, as shown in the appendix 5.A.5, up to fourth order they are given by

$$G_{c, \mathbf{x}_1}^{(1)} = G_{\mathbf{x}_1}^{(1)} , \quad (5.10a)$$

$$G_{c, \mathbf{x}_1, \mathbf{x}_2}^{(2)} = G_{\mathbf{x}_1, \mathbf{x}_2}^{(2)} - G_{c, \mathbf{x}_1}^{(1)} G_{c, \mathbf{x}_2}^{(1)} , \quad (5.10b)$$

$$\begin{aligned} G_{c, \mathbf{x}_1, \mathbf{x}_2, \mathbf{x}_3}^{(3)} &= G_{\mathbf{x}_1, \mathbf{x}_2, \mathbf{x}_3}^{(3)} - \left(G_{c, \mathbf{x}_1, \mathbf{x}_2}^{(2)} G_{c, \mathbf{x}_3}^{(1)} + G_{c, \mathbf{x}_2, \mathbf{x}_3}^{(2)} G_{c, \mathbf{x}_1}^{(1)} + G_{c, \mathbf{x}_3, \mathbf{x}_1}^{(2)} G_{c, \mathbf{x}_2}^{(1)} \right) \\ &\quad - G_{c, \mathbf{x}_1}^{(1)} G_{c, \mathbf{x}_2}^{(1)} G_{c, \mathbf{x}_3}^{(1)} , \end{aligned} \quad (5.10c)$$

$$\begin{aligned} G_{c, \mathbf{x}_1, \mathbf{x}_2, \mathbf{x}_3, \mathbf{x}_4}^{(4)} &= G_{\mathbf{x}_1, \mathbf{x}_2, \mathbf{x}_3, \mathbf{x}_4}^{(4)} - \left(G_{c, \mathbf{x}_1, \mathbf{x}_2}^{(2)} G_{c, \mathbf{x}_3, \mathbf{x}_4}^{(2)} + G_{c, \mathbf{x}_1, \mathbf{x}_3}^{(2)} G_{c, \mathbf{x}_2, \mathbf{x}_4}^{(2)} + G_{c, \mathbf{x}_1, \mathbf{x}_4}^{(2)} G_{c, \mathbf{x}_2, \mathbf{x}_3}^{(2)} + \right) \\ &\quad - \left(G_{c, \mathbf{x}_1, \mathbf{x}_2, \mathbf{x}_3}^{(3)} G_{c, \mathbf{x}_4}^{(1)} + G_{c, \mathbf{x}_2, \mathbf{x}_3, \mathbf{x}_4}^{(3)} G_{c, \mathbf{x}_1}^{(1)} + G_{c, \mathbf{x}_3, \mathbf{x}_4, \mathbf{x}_1}^{(3)} G_{c, \mathbf{x}_2}^{(1)} + G_{c, \mathbf{x}_4, \mathbf{x}_1, \mathbf{x}_2}^{(3)} G_{c, \mathbf{x}_3}^{(1)} \right) \\ &\quad - \left(G_{c, \mathbf{x}_1, \mathbf{x}_2}^{(2)} G_{c, \mathbf{x}_3}^{(1)} G_{c, \mathbf{x}_4}^{(1)} + G_{c, \mathbf{x}_1, \mathbf{x}_3}^{(2)} G_{c, \mathbf{x}_2}^{(1)} G_{c, \mathbf{x}_4}^{(1)} + G_{c, \mathbf{x}_1, \mathbf{x}_4}^{(2)} G_{c, \mathbf{x}_2}^{(1)} G_{c, \mathbf{x}_3}^{(1)} \right. \\ &\quad \left. + G_{c, \mathbf{x}_2, \mathbf{x}_3}^{(2)} G_{c, \mathbf{x}_1}^{(1)} G_{c, \mathbf{x}_4}^{(1)} + G_{c, \mathbf{x}_2, \mathbf{x}_4}^{(2)} G_{c, \mathbf{x}_1}^{(1)} G_{c, \mathbf{x}_3}^{(1)} + G_{c, \mathbf{x}_3, \mathbf{x}_4}^{(2)} G_{c, \mathbf{x}_1}^{(1)} G_{c, \mathbf{x}_2}^{(1)} \right) \\ &\quad - G_{c, \mathbf{x}_1}^{(1)} G_{c, \mathbf{x}_2}^{(1)} G_{c, \mathbf{x}_3}^{(1)} G_{c, \mathbf{x}_4}^{(1)} , \end{aligned} \quad (5.10d)$$

where we suppressed the overall time-dependence for brevity. For every order n , the connected part $G_c^{(n)}$, is obtained by subtracting the information already given by lower-order functions $G_c^{(m < n)}$.

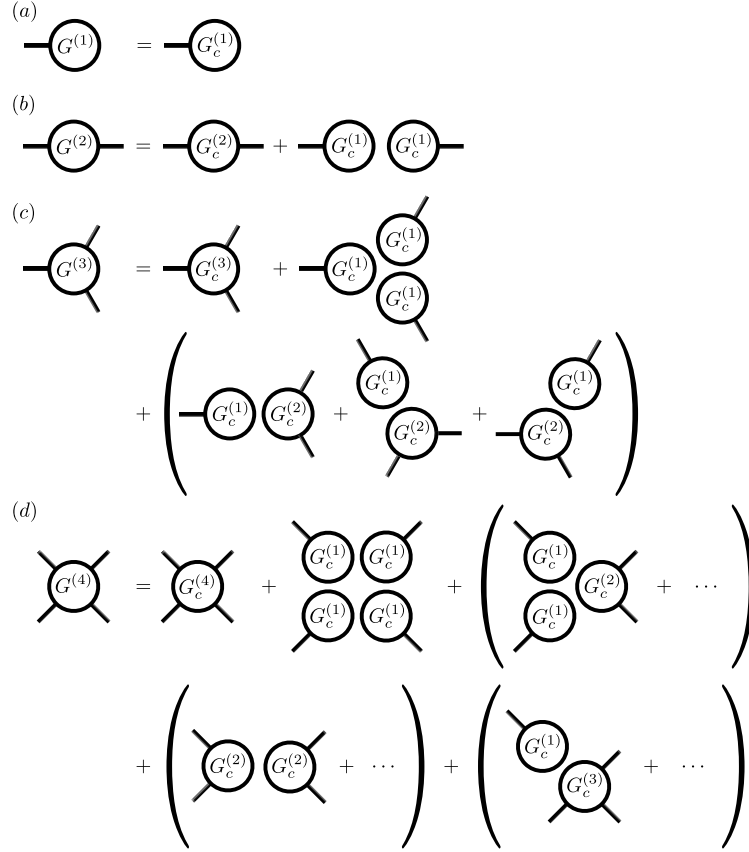


FIGURE 5.1: Feynman diagrams relating full and connected correlation functions. At first-order (a) the correlations are identical. At second-order (b) there is one disconnected diagram that contains redundant information. At higher orders an increasing number of disconnected diagrams need to be considered. We explicitly show the third-order (c) and fourth-order (d) correlations. The dots indicate permutations of the diagrammatic structure within the brackets, similar to (c).

This can be visualized by a graphical representation in terms of Feynman diagrams, which is very helpful to organize the underlying combinatorics. By careful examination of this reorganization, exemplified in Fig. 5.1, one learns that only connected graphs contribute to the correlators generated by E_t , hence the name connected correlations. In short, taking the logarithm of Z_t in Eq. (5.8) removes all disconnected diagrams.

Physically, this means that by inspecting the factorization of higher-order correlation functions, one can determine whether or not the quantum system is described by a Gaussian density operator $\hat{\rho}_t$. Since Gaussian distributions correspond to free (non-interacting) QFTs, this in principle allows to determine the basis of conjugate fields which diagonalizes the quantum many-body Hamiltonian that governs the system at hand.

5.2.3 One-particle irreducible vertices

The connected correlators of order higher than two still contain redundant information. In order to access the irreducible vertices, we define the instantaneous effective action

$$\Gamma_t[\Phi] = -E_t[J(\Phi)] + J_{\mathbf{x}}(\Phi)\Phi_{\mathbf{x}} \quad (5.11)$$

as a Legendre transform of E_t . In Eq. (5.11) the relation $\Phi_{\mathbf{x}}(J) = (\delta E_t[J]) / (\delta J_{\mathbf{x}})$ thus has to be inverted to obtain $J_{\mathbf{x}}(\Phi)$. We emphasize that the above notation is an abbreviation for a double Legendre transform in both of the conjugate fields Φ and Π . Accordingly, equations in this section implicitly include appropriate sums over the two fields.

Expanding the effective action in a functional Taylor series we have

$$\Gamma_t[\Phi] = \sum_{n=2}^{\infty} \frac{1}{n!} \Gamma_{\mathbf{x}_1, \dots, \mathbf{x}_n}^{(n)}(t) \prod_{j=1}^n (\Phi_{\mathbf{x}_j} - \bar{\Phi}_{\mathbf{x}_j}(t)) . \quad (5.12)$$

Here $\bar{\Phi}_{\mathbf{x}}(t) = \langle \varphi_{\mathbf{x}} \rangle_{W_t}$ is the mean value at time t , for which the effective action is stationary, i.e., $(\delta \Gamma_t[\Phi]) / (\delta \Phi) |_{\Phi=\bar{\Phi}} = 0$. The 1PI vertices,

$$\Gamma_{\mathbf{x}_1, \dots, \mathbf{x}_n}^{(n)}(t) = \left. \frac{\delta^n \Gamma_t[\Phi]}{\delta \Phi_{\mathbf{x}_1} \cdots \delta \Phi_{\mathbf{x}_n}} \right|_{\Phi=\bar{\Phi}} , \quad (5.13)$$

are the expansion coefficients in this series. In Eq. (5.12), the sum starts at $n = 2$ because we have omitted an irrelevant constant $\Gamma^{(0)1}$ and the first order, $\Gamma^{(1)}$, vanishes by construction due to the expansion around $\bar{\Phi}$. Physically, $\bar{\Phi}$ can take a non-vanishing value, which plays a crucial role, e.g., in the case of spontaneous symmetry breaking or the false vacuum decay [212].

As shown in the appendix 5.A.6, the 1PI vertices up to fourth order are related to the connected correlation functions as follows:

$$\Gamma_{\mathbf{x}_1}^{(1)} = 0 , \quad (5.14a)$$

$$\Gamma_{\mathbf{x}_1, \mathbf{x}_2}^{(2)} = \left[G_c^{(2)} \right]_{\mathbf{x}_1, \mathbf{x}_2}^{-1} , \quad (5.14b)$$

$$\Gamma_{\mathbf{x}_1, \mathbf{x}_2, \mathbf{x}_3}^{(3)} = -\Gamma_{\mathbf{x}_1, \mathbf{y}_1}^{(2)} \Gamma_{\mathbf{x}_2, \mathbf{y}_2}^{(2)} \Gamma_{\mathbf{x}_3, \mathbf{y}_3}^{(2)} G_{c, \mathbf{y}_1, \mathbf{y}_2, \mathbf{y}_3}^{(3)} , \quad (5.14c)$$

$$\begin{aligned} \Gamma_{\mathbf{x}_1, \mathbf{x}_2, \mathbf{x}_3, \mathbf{x}_4}^{(4)} = & -\Gamma_{\mathbf{x}_1, \mathbf{y}_1}^{(2)} \Gamma_{\mathbf{x}_2, \mathbf{y}_2}^{(2)} \Gamma_{\mathbf{x}_3, \mathbf{y}_3}^{(2)} \Gamma_{\mathbf{x}_4, \mathbf{y}_4}^{(2)} G_{c, \mathbf{y}_1, \mathbf{y}_2, \mathbf{y}_3, \mathbf{y}_4}^{(4)} + \Gamma_{\mathbf{x}_1, \mathbf{y}_1}^{(2)} \Gamma_{\mathbf{x}_2, \mathbf{y}_2}^{(2)} \Gamma_{\mathbf{x}_3, \mathbf{y}_3}^{(2)} \Gamma_{\mathbf{x}_4, \mathbf{y}_4}^{(2)} \Gamma_{\mathbf{z}_1, \mathbf{z}_2}^{(2)} \\ & \times \left(G_{c, \mathbf{y}_1, \mathbf{y}_2, \mathbf{z}_1}^{(3)} G_{c, \mathbf{z}_2, \mathbf{y}_3, \mathbf{y}_4}^{(3)} + G_{c, \mathbf{y}_1, \mathbf{y}_3, \mathbf{z}_1}^{(3)} G_{c, \mathbf{z}_2, \mathbf{y}_2, \mathbf{y}_4}^{(3)} + G_{c, \mathbf{y}_1, \mathbf{y}_4, \mathbf{z}_1}^{(3)} G_{c, \mathbf{z}_2, \mathbf{y}_2, \mathbf{y}_3}^{(3)} \right) . \end{aligned} \quad (5.14d)$$

We again emphasize that the explicit equations should be understood including appropriate sums over φ and π correlators (see appendix 5.A.6). For higher orders these relations become more complicated and calculations are conveniently performed with the graphical notation exemplified in Fig. 5.2. These diagrams also

¹In thermal equilibrium and for an unnormalized density operator, the constant $\Gamma^{(0)}$ plays the role of a thermodynamic potential, see appendix 5.B.

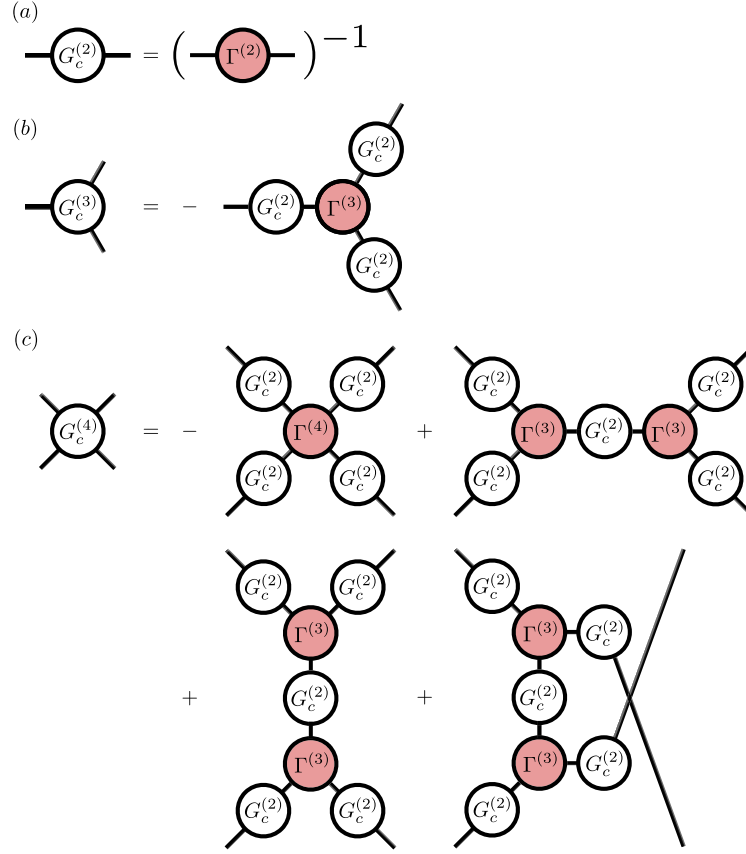


FIGURE 5.2: Feynman diagrams relating connected and 1PI correlation functions. At second order (a), the correlators are each others inverse. At third order (b), the connected correlator is “built” from connected two-point functions that are connected by the irreducible three-vertex. At fourth order (c), the structure is similar to (b) with contributions from the four- and three-vertices. Given the 1PI vertices $\Gamma^{(n)}$, all connected correlations can be calculated by summing so called tree-diagrams, which separate into two disconnected parts upon cutting a single line $G_c^{(2)}$ and hence do not contain any closed loops.

explain the attribute 1PI: The diagrams representing the vertices can not be disconnected by cutting a single line. In this sense they are the irreducible structures from which all correlation functions and thus all physical observables can be recovered.

This also justifies the name effective action: Γ_t is the quantum generalization of a classical action including all corrections due to quantum-statistical fluctuations. However, in contrast to the “standard” (unequal-time) action, there is one stationarity condition for each time t . Together, they do not give a time evolution equation for the one-point function in the usual sense² but one differential equation for each time t . In this way the time t is treated as a label in the equal-time formulation of QFT.

²The usual evolution equation for the (time-dependent) one-point function $\bar{\Phi}_x(t)$ can be obtained by taking another derivative of Eq. (5.14a) with respect to time t .

5.2.4 Measuring the effective Hamiltonian

So far, we have equivalently rewritten the quantum-statistical information of a system described by a density operator $\hat{\rho}_t$ in terms of generating functionals Z_t , E_t and Γ_t which encode full, connected and 1PI correlation functions, respectively. While the entries of the density matrix are typically inaccessible and less intuitive, the equal-time correlators can be measured in experiments and are directly related to relevant observables and structural information, such as occupation numbers and couplings. Next, we employ the equal-time formalism to relate parameters of an Hamiltonian to the 1PI correlators.

As a generic example we consider a relativistic scalar field theory with potential V described by the Hamiltonian

$$\hat{H} = \int_{\mathbf{x}} \left[\frac{1}{2} \hat{\Pi}_{\mathbf{x}}^2 + \frac{1}{2} (\nabla_{\mathbf{x}} \hat{\Phi}_{\mathbf{x}})^2 + V(\hat{\Phi}_{\mathbf{x}}) \right]. \quad (5.15)$$

Given the Hamiltonian \hat{H} , it is possible to derive an evolution equation for Γ_t [61] (see also the next chapter 6). For simplicity, we focus on the case of thermal equilibrium, which is a stationary solution Γ_{β} , described by the density operator $\hat{\rho}_{\beta} \sim \exp(-\beta \hat{H})$ with the prefactor fixed by normalization

In order to obtain the generating functional Eq. (5.6) we need to calculate the Wigner functional Eq. (5.7). In the interacting case, the involved functional integration can only be performed approximately. It is however possible to derive an exact equation for the thermal Wigner functional (see appendix 5.A.7). It takes the form of a functional flow equation, $\partial_{\beta} W_{\beta} = -(H_0 + \hbar^2 H_1 + \dots) W_{\beta}$, with

$$H_0 = \int_{\mathbf{x}} \left[\frac{1}{2} \pi_{\mathbf{x}}^2 + \frac{1}{2} (\nabla_{\mathbf{x}} \varphi_{\mathbf{x}})^2 + V_{\mathbf{x}}(\varphi) \right]. \quad (5.16)$$

It is straightforward to solve the equation for W_{β} perturbatively by a semi-classical expansion in powers of \hbar . An exact solution for $V = 0$ is discussed in appendix 5.B.

The leading order is the classical field theory limit, where we obtain $W_{\beta} \sim \exp(-\beta H_0)$ with the classical Hamiltonian H_0 . Then the generating functional Eq. (5.6) becomes

$$Z_{\beta}[J] \sim \int \mathcal{D}\pi \mathcal{D}\varphi e^{-\beta H_0 + J_{\mathbf{x}}^{\varphi} \varphi_{\mathbf{x}} + J_{\mathbf{x}}^{\pi} \pi_{\mathbf{x}}}. \quad (5.17)$$

Thus βH_0 plays the role of a classical action for the fluctuating fields φ and π . This allows us to calculate the effective action Γ_{β} in the equal-time formalism using established QFT methods, such as the background field method employed below.

We note that the two conjugate fields φ and π decouple in the present limit, which implies that the effective action separates as

$$\Gamma_{\beta}[\Phi, \Pi] = \Gamma_{\beta}[\Phi] + \Gamma_{\beta}[\Pi] \quad (5.18)$$

with $\Gamma_\beta[\Pi] = \frac{\beta}{2} \int_{\mathbf{x}} \Pi_{\mathbf{x}}^2 + \text{const.}$, as shown in appendix 5.A.8. The separation Eq. (5.18) is a property of the classical field approximation. In general, the quantum effective action of the full quantum theory requires knowledge of all equal-time correlators of φ and π , including mixed terms. However, symmetries such as time translation invariance simplify the discussion, see appendix 5.A.9.

By means of the background field method, we can calculate the effective action in a loop expansion. In the present formalism, we split

$$\Gamma_\beta[\Phi] = \beta H[\Phi] + \Gamma'_\beta[\Phi] , \quad (5.19)$$

where $H[\Phi] = H_0[\varphi = \Phi, \pi = 0]$. As shown in the appendix 5.A.10, the “rest” Γ'_β obeys the following functional integro-differential equation,

$$e^{-\Gamma'_\beta[\Phi]} = \int \mathcal{D}\varphi \exp \left(-\beta K[\varphi, \Phi] + \frac{\delta \Gamma'_\beta[\Phi]}{\delta \Phi_{\mathbf{x}}} \varphi_{\mathbf{x}} \right) , \quad (5.20)$$

where we abbreviated

$$K[\varphi, \Phi] = H[\Phi + \varphi] - H[\Phi] - \int_{\mathbf{x}} \frac{\delta H[\Phi]}{\delta \Phi_{\mathbf{x}}} \varphi_{\mathbf{x}} . \quad (5.21)$$

The solution of this equation is organized diagrammatically as an expansion in the number of loops (see [213] for a proof to all orders). At leading order (tree-level) in this expansion $\Gamma'_\beta = 0$ and thus the equal-time effective action is directly related to the microscopic Hamiltonian. Consequently, the 1PI vertices correspond to the interaction constants of the underlying system. Beyond the leading-order approximation, the notion of the microscopic Hamiltonian becomes a less useful concept. The effective action then plays the role of an “effective Hamiltonian”, with all corrections from quantum-statistical fluctuations taken into account.

Returning to the leading order approximation, which gives rise to the tree-level 1PI vertices, we explicitly have

$$\Gamma_{\mathbf{x},\mathbf{y}}^{(2)} = \nabla_{\mathbf{x}}^2 \delta(\mathbf{x} - \mathbf{y}) + \int_{\mathbf{z}} \frac{\delta^2 V_{\mathbf{z}}(\Phi)}{\delta \Phi_{\mathbf{x}} \delta \Phi_{\mathbf{y}}} \Big|_{\Phi=\bar{\Phi}} , \quad (5.22a)$$

$$\Gamma_{\mathbf{x}_1, \dots, \mathbf{x}_n}^{(n)} = \int_{\mathbf{z}} \frac{\delta^n V_{\mathbf{z}}(\Phi)}{\delta \Phi_{\mathbf{x}_1} \cdots \delta \Phi_{\mathbf{x}_n}} \Big|_{\Phi=\bar{\Phi}} , \quad (5.22b)$$

where $n \geq 3$. Eq. (5.19) or more explicitly Eq. (5.22) directly show the relation between the 1PI correlation functions and the parameters of the microscopic (or more generally an effective) Hamiltonian. Together with the procedure to obtain the 1PI correlators, outlined below, they provide an experimental prescription for measuring a quantum many-body Hamiltonian.

5.2.5 Recipe to extract 1PI correlators

The extraction of 1PI correlators, which are the fundamental irreducible building blocks for the QFT description, from equal-time data proceeds in the following steps.

1. Identify the degrees of freedom of interest which constitute the elementary fields φ of the QFT.
2. Obtain many realisations ($i = 1, \dots, N$) of the desired field $\varphi_i(\mathbf{x})$ at the times t of interest.
3. Estimate the full correlators up to order n by calculating the ensemble average $G_{\mathbf{x}_1, \dots, \mathbf{x}_n}^{(n)} \approx \frac{1}{N} \sum_i \varphi_i(\mathbf{x}_1) \cdots \varphi_i(\mathbf{x}_n)$.
4. Obtain the connected correlators $G_c^{(n)}$ by subtracting the disconnected contributions according to Eq. (5.10).
5. Calculate the 1PI correlators $\Gamma^{(n)}$ by reducing the connected correlators according to Eq. (5.14).

This procedure corresponds to a shift of representation from the density operator $\hat{\rho}$ to Γ , the generating functional for 1PI correlators. In the following two sections we will illustrate and verify the method in the case of the sine-Gordon model with numerically simulated data (Section 5.3) and with experimental measurements (Section 5.4).

5.3 Example: Sine-Gordon model

As an explicit example, we consider the sine-Gordon model [199–202] in thermal equilibrium. It is an interacting relativistic scalar field theory described by

$$\beta \hat{H}_{\text{SG}} = \int_x \left\{ \beta g \hat{\Pi}_x^2 + \frac{\lambda_T}{4} \left[\frac{1}{2} (\partial_x \hat{\Phi}_x)^2 - \frac{1}{\ell_J^2} \cos(\hat{\Phi}_x) \right] \right\}, \quad (5.23)$$

where $\beta = (k_B T)^{-1}$ is the inverse temperature. The specific form of the Hamiltonian \hat{H}_{SG} given above is motivated by the recent progress to quantum simulate the SG model by two tunnel coupled 1D superfluids [38, 203]. See section 5.4 for the physical origin of the fields $\hat{\Phi}$ and $\hat{\Pi}$, the microscopic parameter g and the length scales λ_T and ℓ_J .

The semi-classical approximation Eq. (5.17) is valid for

$$\sqrt{4\gamma} \ll \min \left[1, \frac{4}{Q} \right], \quad (5.24)$$

where the dimensionless parameters are $\gamma = 16g\beta/\lambda_T$ and $Q = \lambda_T/\ell_J$. In the semi-classical limit the loop expansion is controlled by Q with the tree-level approximation

valid for $1/Q \ll 1$ (see appendix 5.A.7 and 5.A.10 for details). We therefore consider in the following $\lambda_T = 17.35 \mu\text{m}$ and vary ℓ_J such that $1 \lesssim Q \lesssim 20$.

Following the general discussion of the previous section, the tree-level vertices corresponding to Eq. (5.23) are

$$\Gamma_p^{(2),\text{tree}} = \frac{\lambda_T}{4} \left(p^2 + \frac{1}{\ell_J^2} \right), \quad (5.25a)$$

$$\Gamma_{p_1, \dots, p_{2n-1}}^{(2n),\text{tree}} = -\frac{\lambda_T}{4\ell_J^2} (-1)^n, \quad (5.25b)$$

$$\Gamma_{p_1, \dots, p_{2n-2}}^{(2n-1),\text{tree}} = 0, \quad (5.25c)$$

where $n > 2$ and we switched to momentum space correlators. Here and in the following we always consider a specific diagonal part in momentum space, namely $\Gamma_{p_1, \dots, p_n}^{(n)} = (2\pi) \delta(p_1 + \dots + p_n) \Gamma_{p_1, \dots, p_{n-1}}^{(n)}$ which removes the volume factors arising from translation invariance. Note that $\Gamma^{(2n-1)} = 0$ ($\forall n \geq 1$) remains valid beyond the tree-level approximation due to the symmetries of the SG Hamiltonian.

Employing a stochastic process based on a transfer matrix formalism [214], we numerically obtain thermal profiles of the field φ_x , corresponding to the operator $\hat{\Phi}_x$. These are exact solutions of the SG model within the semi-classical approximation and hence have contributions up to arbitrary order in the above loop expansion. With these statistical samples, we carry out the procedure described in section 5.2.5 and calculate the 1PI correlators up to fourth order.

So far, we have implicitly assumed in Eq. (5.25) that the correlations are obtained for an infinite system with periodic boundary conditions. The employed numerics, however, yield correlators from a finite subsystem, which is better described by open boundary conditions. We therefore employ a cosine transform and translate the results to momentum space, i.e., Fourier momenta (for details see appendix 5.A).

Figure 5.3 shows the calculated 1PI vertices in momentum space for a large value of $Q \approx 11.5$ and different volumes L . Note that due to the periodicity of the sine-Gordon potential³ the value of $p = 0$ is not defined for the correlations considered. Therefore the fact that the correlation function is diagonal is crucial to be able to perform the inversion of the connected second order correlation function in order to obtain $\Gamma^{(2)}$. The diagonal form allows to do the inversion for $p \neq 0$ without knowing the value for $p = 0$.

We find excellent agreement with the tree-level predictions for the momentum diagonal of the two and four vertex⁴. This demonstrates the possibility to carry out the procedure described in the previous section, which allows to directly measure the

³The SG model is invariant under the shift $\varphi \rightarrow \varphi + \mathbb{Z} \times 2\pi$. This leads to an undefined offset for the numerical profiles φ_x and hence an undefined value of the momentum correlators for $p = 0$.

⁴One might expect a better signal-to-noise ratio for larger system sizes due the larger number of data points. However, for a given correlator of order n the number of independent values to be estimated from the sample increases at the same time. This effect is more pronounced for larger n and we expect more noise at large momenta p (due to an effective volume average at low p), consistent with the observed behavior of the statistical errors. In view of experimental limitations, a detailed statistical survey of this point could be helpful.

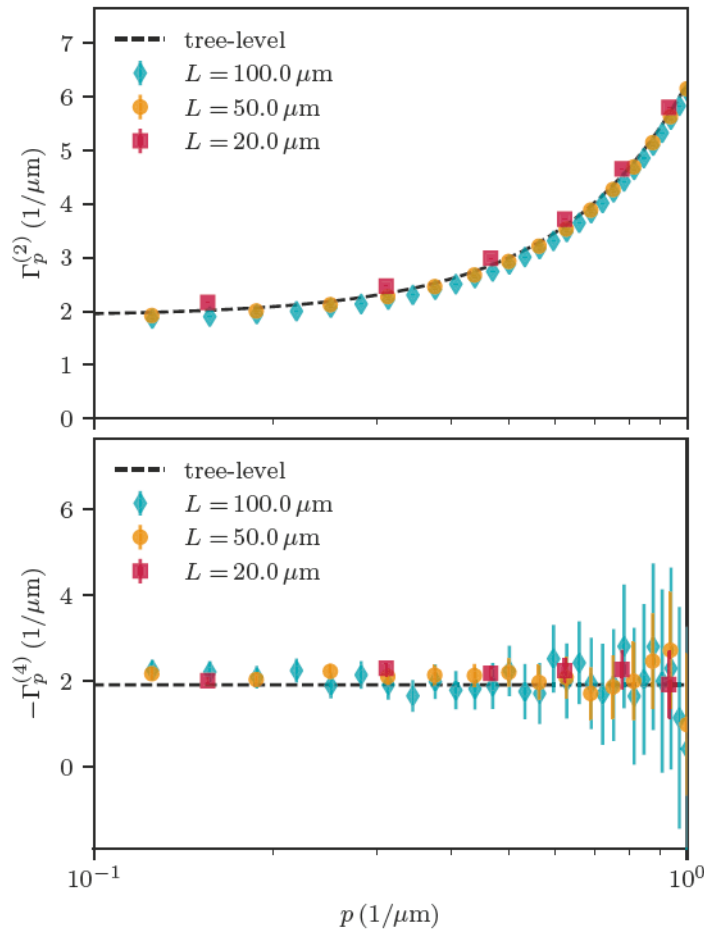


FIGURE 5.3: 1PI vertices in the weak coupling regime at $Q \approx 11.52$ calculated from the numerical data for different volumes $L = 20\mu\text{m}$ (■), $50\mu\text{m}$ (●), and $100\mu\text{m}$ (◆). The 1PI two-point function (upper panel) and 1PI four-vertex (lower panel) show excellent agreement with the tree-level prediction (dashed black line) for a wide range of momenta. The results have been obtained from 10^8 samples. The error bars indicate the standard error of the mean.

microscopic parameters through equal-time 1PI correlation functions if higher-order loop corrections can be neglected.

However, when the system becomes strongly correlated the microscopic details become irrelevant and replaced by effective, momentum-dependent (so-called running) couplings. This behavior is precisely captured by the 1PI correlation functions, which effectively replace the microscopic coupling parameters appearing in the Hamiltonian H_{SG} . We therefore adjust the parameters away from the weakly-coupled limit $Q \gg 1$. In general, we observe an increasing deviation from the tree-level approximation, which is expected because loop corrections due to increasing fluctuations modify the physics.

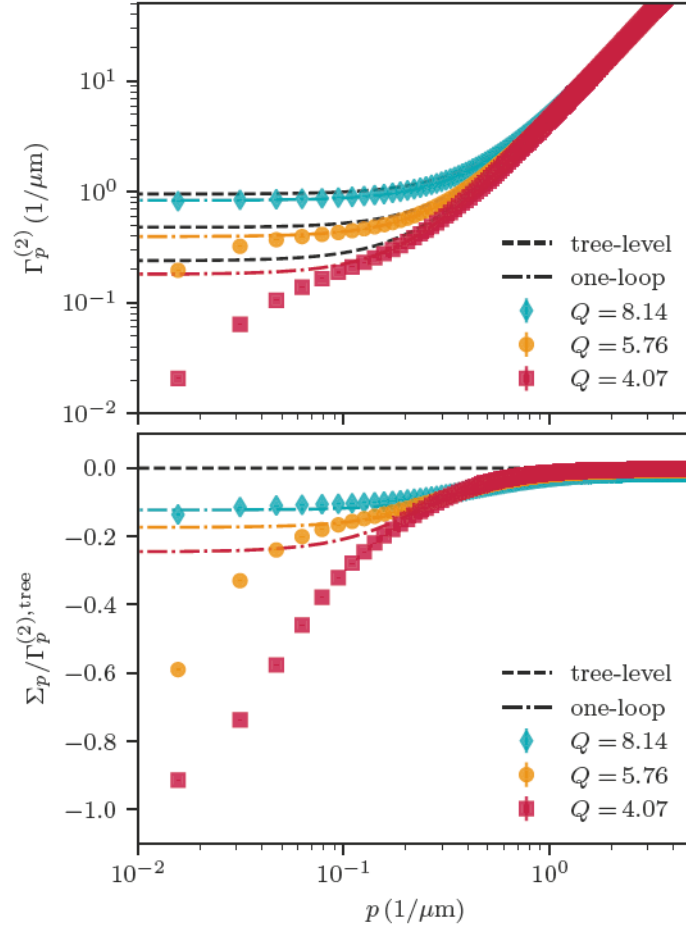


FIGURE 5.4: Loop corrections to the 1PI two-point function for different Q in the strong coupling regime, $Q = 8.14$ (\blacklozenge), 5.76 (\bullet), and 4.07 (\blacksquare). The calculated two-point function (upper panel) always approaches the corresponding tree-level predictions (black dashed lines) at high momenta, as expected. In the infrared, we observe deviations due to loop corrections. The corresponding colored dashed-dotted lines include the one-loop correction. The corresponding self-energy (lower panel) quantifies the deviations from the tree-level prediction. The corrections become more pronounced for smaller Q , as expected. Numerical results are calculated for $L = 200 \mu\text{m}$ and a sample size of 10^8 .

Quantitatively, the corrections to the 1PI two-point function are summarized in the “self-energy” Σ , defined via

$$\Gamma_p^{(2)} = \Gamma_p^{(2),\text{tree}} + \Sigma_p . \quad (5.26)$$

In the appendix 5.A.13, we calculate the leading correction,

$$\Sigma_p^{\text{one-loop}} = -1/(4\ell_J) . \quad (5.27)$$

In Fig. 5.4, the 1PI two-point function and the self-energy are plotted as a function of p . Generically, tree-level dominates in the UV (i.e., at high momenta), which we

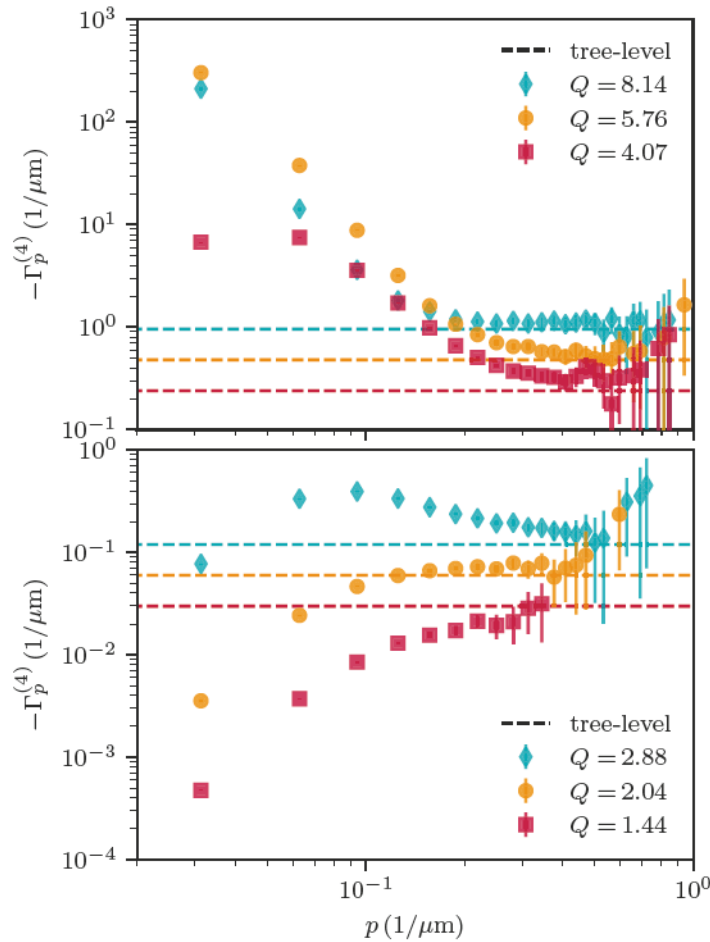


FIGURE 5.5: Loop corrections to the 1PI four-vertex for different values of Q . The (negative) four-vertex (\blacklozenge , \bullet , \blacksquare), shown for larger values of Q (upper panel, corresponding to Fig. 5.4), clearly approaches the corresponding tree-level predictions (colored dashed lines) at high momenta. In the infrared, we observe a strong momentum dependence, increasing the effective coupling. For decreasing values of Q (lower panel) the (negative) four-vertex is increasingly suppressed in the infrared. The results are consistent with the approach of the tree-level prediction (colored dashed lines) for high momenta. Numerical results are calculated for $L = 100 \mu\text{m}$ and a sample size of 10^8 . The error bars indicate the standard error of the mean. Note that we excluded data points at high momenta with errors larger than the mean from this plot.

also observe numerically. The 1PI two-point function approaches the power-law $\propto p^2$ in this limit and the (normalized) self-energy vanishes.

In the IR (low momenta), however, loop corrections are important. It is this regime where collective macroscopic phenomena emerge and the microscopic details are washed out. We observe a negative self-energy and hence a reduction of the 1PI two-point function, which agrees with the one-loop result over an intermediate range of momenta (and Q). Physically, this result implies stronger fluctuations as Q decreases, consistent with the expectation for a strongly correlated regime of the sine-Gordon model.

Similarly, the loop corrections to the 1PI vertices lead to the notion of running

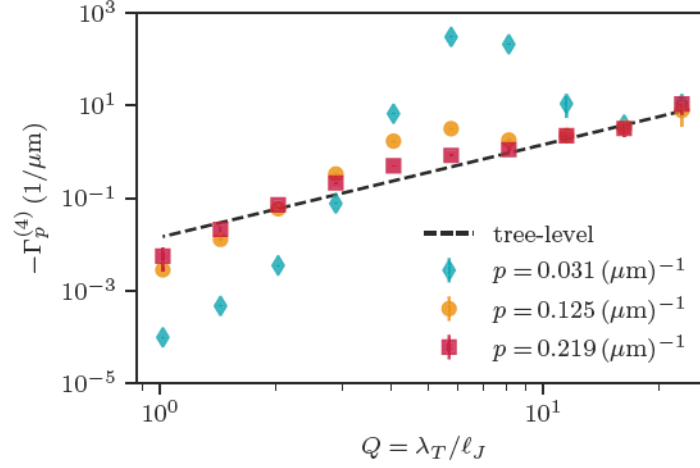


FIGURE 5.6: 1PI four-vertex as a function of Q for three different momenta $p = 0.031\mu\text{m}^{-1}$ (\blacklozenge), $0.125\mu\text{m}^{-1}$ (\bullet), and $0.219\mu\text{m}^{-1}$ (\blacksquare). At large momenta, the vertex approaches the tree-level prediction (black dashed-line). At low momenta, loop correction lead to a suppression or an enhancement depending on the values of Q and p (c.f. Fig. 5.5). Numerical results are calculated for $L = 100\mu\text{m}$ and a sample size of 10^8 .

couplings, i.e., momentum-dependent interaction vertices that deviate from the constant microscopic values. In the appendix 5.A.13. we calculate the one-loop vertex

$$\Gamma_p^{(4),\text{one-loop}} = -\frac{\lambda_T}{4\ell_J^2} - \frac{1}{8\ell_J^3} \frac{1}{p^2 + 1/\ell_J^2}. \quad (5.28)$$

Again, it is expected that loop corrections vanish for high momenta and the 1PI four-vertex converges to the tree-level result, i.e., the microscopic parameters of the Hamiltonian, which is confirmed by our numerical simulations.

This is demonstrated in Fig. 5.5, where the 1PI four-vertex is shown for the same values of Q as in Fig. 5.4. For very high momenta, we are again limited by finite statistics. In the infrared, we clearly observe the momentum-dependent, i.e., running, coupling. The increased values indicate stronger interactions, qualitatively consistent with the one-loop calculation. The effect is again more pronounced for smaller values of Q , as expected in the strongly correlated regime of the sine-Gordon model.

We observe a qualitative difference between large and small values of Q . For $Q \gtrsim 4$, the magnitude of the 1PI four-vertex is increased in the infrared and shows a running coupling towards the smaller tree-level value. For $Q \lesssim 3$, the magnitude of the vertex decreases in the infrared as compared to the tree-level value at higher momenta. This behavior is also clearly visible in Fig. 5.6, where we show the four-vertex as a function of Q for fixed momenta.

5.4 Experimental results: Proof of principle

As a proof of principle to extract the 1PI vertices from experimentally measured correlations we apply the formalism discussed above to the physical system of two tunnel-coupled one-dimensional superfluids in a double-well potential on an atomchip. Such a system can be seen as a quantum simulator of the sine-Gordon model [38, 203]. The relative phase φ_x between the superfluids corresponds to $\hat{\Phi}$ in Eq. (5.23) in section 5.3 while the relative density fluctuations correspond to the conjugate field $\hat{\Pi}$.

A schematic of the experimental system is given in Fig. 5.7. The parameters in H_{SG} (5.23) are related to the experimental parameters via $\lambda_T = 2\hbar^2 n_{1\text{D}} / (mk_B T)$, $\ell_J = \sqrt{\hbar / (4mJ)}$, and $g = g_{1\text{D}} + \hbar J / n_{1\text{D}}$. Here the 1D effective interaction strength $g_{1\text{D}} = 2\hbar a_s \omega_{\perp}$ is calculated from the s-wave scattering length a_s and the frequency ω_{\perp} of the radial confinement; $n_{1\text{D}}$ is the 1D density and m is the mass of the ^{87}Rb atoms which the superfluids consist of. The single particle tunneling rate between the wells is denoted by J .

In the experiment, the two superfluids are prepared by slow evaporative cooling in the double-well potential (the same way the slow-cooled data presented in [38] was prepared). However, in contrast to [38], the data used here was taken for a box-like longitudinal confinement [215] of $75\ \mu\text{m}$ length. Matter-wave interferometry [216] gives access to the spatially resolved relative phase fluctuations φ_x between the two superfluids. More details about the experimental procedure and the data analysis can be found in [38, 217].

Starting from the measured phase profiles, we can calculate the 1PI vertices in the same way as was done for the numerics (see section 5.3 and appendix 5.A). For box like potentials one naturally gets Neumann boundary conditions (BC) for the

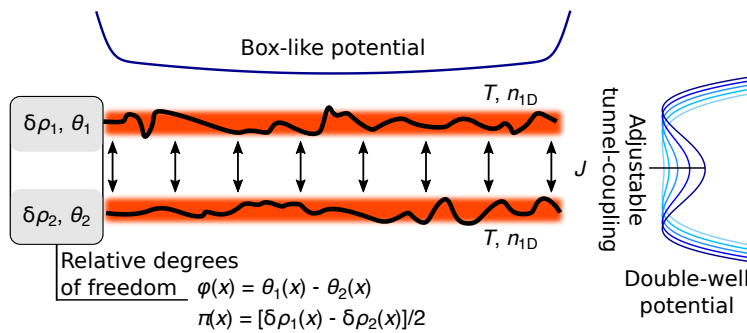


FIGURE 5.7: Schematics of the experimental setup. We consider two tunnel-coupled one-dimensional superfluids in a double-well potential at a common temperature T . Changing the barrier height of the potential (blue lines) allows for an adjustable tunnel-coupling J between the two superfluids. The superfluids are described in terms of density fluctuations $\delta\rho_{1,2}$ around their equal mean densities $n_{1\text{D}}$ and fluctuating phases $\theta_{1,2}$ (black lines). From these quantities we define the relative degrees of freedom π and φ which represent the conjugate fields in the sine-Gordon Hamiltonian. Figure adapted from [38].

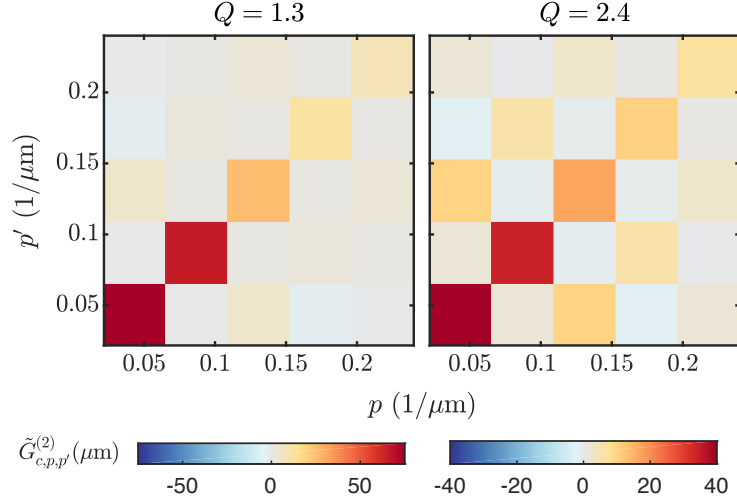


FIGURE 5.8: Cosine transformed second-order connected correlation function. Results for different phase-locking strength as indicated by the values of Q stated above the respective subplots. The color represents the values for cosine transformed second-order connected correlation function $\tilde{G}_{c,p,p'}^{(2)}$ as defined in (5.29). Note that the value (249.9 in the left subplot and 93.9 in the right subplot) for the lowest leftmost data point, lies outside the color-range. The color-range was chosen like this to get better visibility.

phase from the condition of vanishing particle current on the edges [215]. From the cosine transform (compatible with the Neumann BC) of the complete system we therefore get the 1PI vertices of the Hamiltonian with this BC. Acknowledging that our system is still too short to get results free from finite size effects, we nevertheless apply the conversion factors to Fourier momentum space given in (5.64) and (5.65) for consistency when presenting $\Gamma^{(n)}$.

Let us start the discussion of the experimental results with the cosine transformed second-order correlation function

$$\tilde{G}_{c,p,p'}^{(2)} = \frac{2}{L} (\langle \tilde{\varphi}_p \tilde{\varphi}_{p'} \rangle - \langle \tilde{\varphi}_p \rangle \langle \tilde{\varphi}_{p'} \rangle). \quad (5.29)$$

Here $\tilde{\varphi}_p$ represents the cosine transform (5.63b) over the finite interval with length L and we chose the prefactors for later convenience. The factor 2 comes from the identity (5.64) and the factor $1/L$ from the delta function. We see from Fig. 5.8 that the correlations are approximately diagonal. Further, note that density-phase two-point correlations, $\langle \pi\varphi \rangle_{W_t}$, vanish due to time-translation invariance of the thermal state, even beyond the semi-classical approximation Eq. (5.17). Together, this enables us to calculate the 1PI two-point correlator as

$$\Gamma_p^{(2)} = \frac{1}{\tilde{G}_{c,p,p}^{(2)}}, \quad (5.30)$$

where we neglected the small off-diagonal elements of $\tilde{G}_{c,p,p'}^{(2)}$. The results are presented in Fig. 5.9.

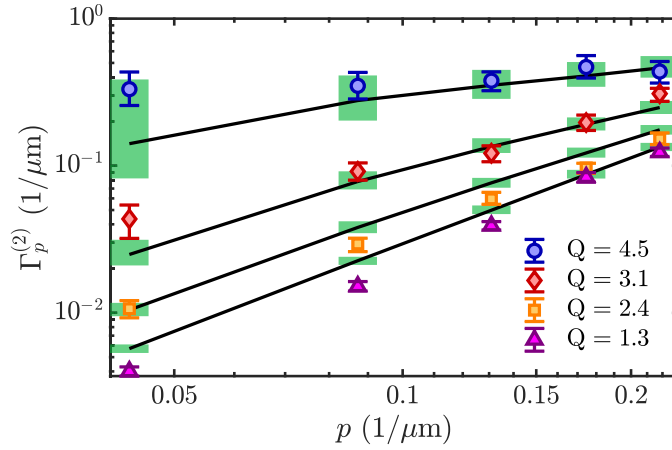


FIGURE 5.9: Experimental 1PI two-point function. The four different measurements correspond to $Q = 4.5$ (\bullet), 3.1 (\blacklozenge), 2.4 (\blacksquare), and 1.3 (\blacktriangle). The error bars represent the 80% confidence intervals obtained using bootstrapping. We see good agreement with the theory prediction from the sine-Gordon model in thermal equilibrium calculated for 10^6 numerical realizations (black solid lines). The height of the green bars indicates the 80% confidence interval for the numerical predictions considering the finite experimental sample size. Note that all uncertainty comes from the finite sample size, no uncertainty in the parameters λ_T and Q was assumed. The width of the bars was chosen arbitrarily.

All experimental results presented in this chapter are corrected for the expected influence of the finite imaging resolution. In our simple model, the imaging process leads to a convolution of the true phase profiles with a Gaussian function with $\sigma_{\text{psf}} = 3 \mu\text{m}$ [217]. In momentum space this leads to a multiplication with $\exp(-p^2 \sigma_{\text{psf}}^2 / 2)$, which can be corrected by dividing the cosine transformed relative phase $\tilde{\varphi}(p)$ by this factor.

In order to connect the experimental results to the theoretical model (section 5.3) we estimate $\lambda_T = 11 \mu\text{m}$ for all the different measurements. The values for $Q = \lambda_T / \ell_J$ are then self consistently fitted from $\langle \cos(\varphi) \rangle$ [217]. We see good agreement between experiment and thermal sine-Gordon theory for the 1PI two-point function in Fig. 5.9.

Having obtained the two-point function, and using that the third-order correlation functions vanish for symmetry reasons, we can calculate the diagonal part of the 4-vertex as

$$\Gamma_p^{(4)} = -\frac{8}{3} \frac{1}{L} \langle \tilde{\varphi}_p^4 \rangle_c \times \left(\Gamma_p^{(2)} \right)^4. \quad (5.31)$$

Here $\langle \tilde{\varphi}_p^4 \rangle_c$ stands for the diagonal elements of the cosine transformed fourth-order connected correlation function. The factor $8/3$ comes from the identity (5.65), the factor $1/L$ again comes from the delta function. The results for the three lowest lying momentum modes are presented in Fig. 5.10 as a function of Q . We find qualitative agreement between experiment and theory as well as the expected approach towards the tree-level result for higher momenta. The momentum dependence for the measurements with large experimental sample size (Fig. 5.11) reveal a running

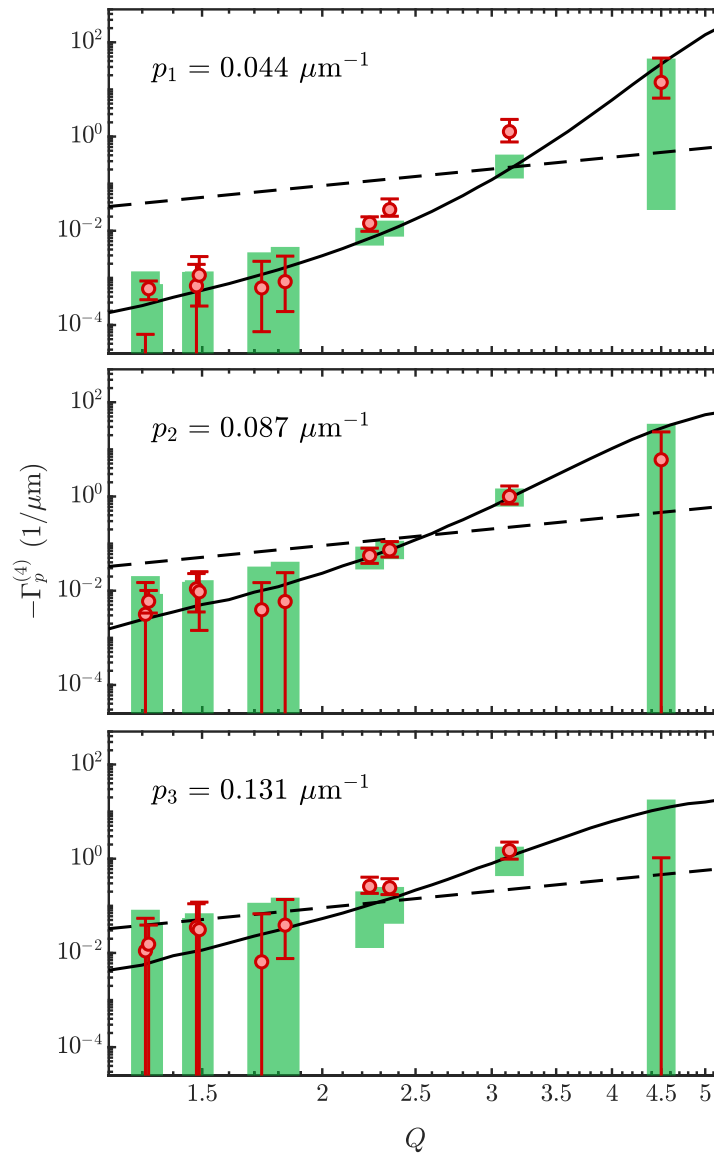


FIGURE 5.10: Experimental four-vertex. The red bullets represent the experimental results for the four-vertex as a function of $Q = \lambda_T/\ell_J$. The points in one particular subplot correspond to separate measurements with different tunneling strength. The different subplots show the results for the lowest three values of p indicated in the upper left corner of the subplots. The error bars represent 80% confidence intervals obtained using bootstrapping. The numerical prediction from the sine-Gordon model in thermal equilibrium is given by the green bars. The height of the bars indicates the 80% confidence interval for the theory predictions considering the finite experimental sample size. Note that all uncertainty comes from the finite sample size, no uncertainty in the parameters λ_T and Q was assumed. The width of the bars was chosen arbitrarily. The solid black line represents the theory prediction from 10^6 numerical realizations and the dashed black line the tree-level prediction (5.25).

coupling with a qualitative agreement between the experiment and thermal sine-Gordon theory.

5.5 Summary

The presented method provides a general framework to extract and test the effective or emergent quantum field theoretical description of generic quantum many-body systems from experiments. For the example of the sine-Gordon model, which is quantum simulated with two tunnel-coupled superfluids, we have demonstrated how to experimentally obtain the irreducible vertices in thermal equilibrium and compared to theoretical expectations. This represents an essential step in the verification of the approach, which opens a new pathway to study fundamental questions of QFT through large-scale (analog) quantum simulators.

This becomes especially interesting for strongly correlated systems and in non-equilibrium situations, where it is often not possible to solve the theory using classical computational techniques. Extracting the irreducible building blocks of quantum many-body systems, and how they change with time, promises to provide detailed insights into the dynamics for these cases. The next chapter – where we discuss a spin-1 Bose condensate far from equilibrium [65], which has been studied in parallel to the work presented in this chapter and employed similar methods – presents an example where currently no theoretical solution is available. In turn, the insight from experimental measurement can support theoretical developments in devising new approximation schemes and effective field theory descriptions.

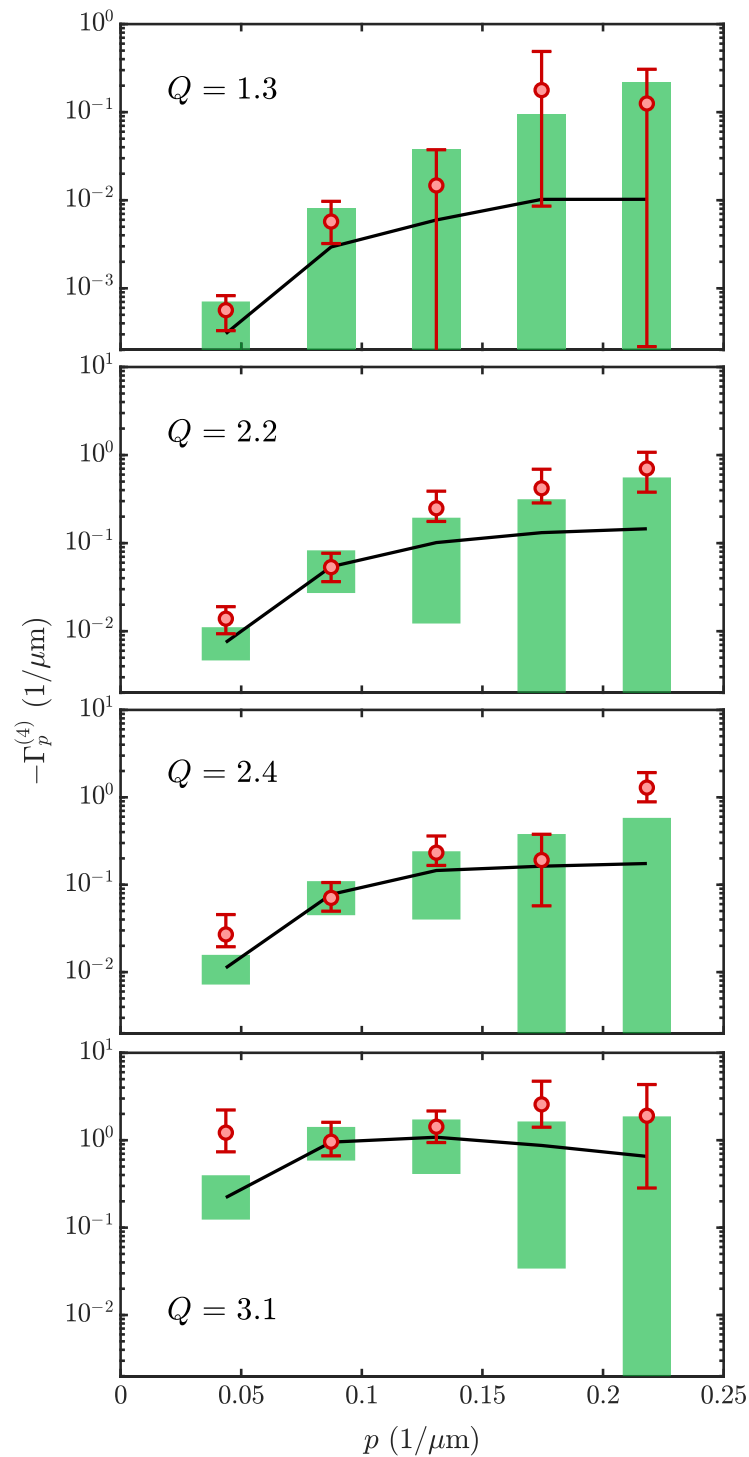


FIGURE 5.11: Running coupling. Like Fig. 5.10, but showing $\Gamma_p^{(4)}$ as a function of p for the four measurements with the biggest experimental sample size. Depending on the value of Q indicated in the different subplots one can see a clear momentum dependence, i.e., “running coupling”. Note that the vertical axis of the uppermost subplot is different from the rest. However, the logarithmic range is the same as in the other subplots.

$\hat{\rho}[\hat{\Phi}]$	density operator	$\hat{\Phi}$	field operator (non-commuting)
$W[\varphi]$	Wigner functional	φ	fluctuating (microscopic) field
$Z[J]$	g.f. for full correlators $G^{(n)}$	J	auxiliary source field
$E[J]$	g.f. for connected correlators $G_c^{(n)}$		
$\Gamma[\Phi]$	g.f. for 1PI correlators $\Gamma^{(n)}$	Φ	macroscopic field

TABLE 5.12: Overview over the different objects that appear in the general discussion. “g.f.” abbreviates “generating functional”.

Appendix: Details about the QFT analysis in equilibrium

In this appendix we show in section 5.A explicit calculations and detailed discussions that we left out in the discussion of equal-time correlation functions, as well as technical details concerning the example which is discussed in this chapter. Additionally, we briefly discuss quantum thermal equilibrium in section 5.B.

5.A Technical details

5.A.1 Notational conventions

In table 5.12, we have summarized the different generating functionals and the involved fields which appear throughout this chapter.

We use the following notations: Operators are always indicated by a hat. $\text{Tr}[\dots]$ indicates a trace over the full Hilbert space. The absence of a hat implies a c-number (i.e., commuting objects). In the whole formalism, the time t is treated as a label and often left out for brevity. Repeated spatial indices are integrated over, e.g., $J_{\mathbf{x}}^{\varphi} \hat{\Phi}_{\mathbf{x}} = \int d^d x J^{\varphi}(\mathbf{x}) \hat{\Phi}(\mathbf{x})$; we write explicit integrals if there is room for confusion.

In this appendix, we also use collective Latin indices, such as $a = (\varphi/\pi, \mathbf{x})$; then repeated indices are integrated or summed over as appropriate, e.g., $J_a \hat{\Phi}_a = \int d^d x [J^{\varphi}(\mathbf{x}) \hat{\Phi}(\mathbf{x}) + J^{\pi}(\mathbf{x}) \hat{\Pi}(\mathbf{x})]$. It is useful to think of correlation functions as tensors, e.g., $G_{c,ab}^{(2)}$ and its inverse $\Gamma_{ab}^{(2)}$ are the components of 2-tensors that fulfill $G_{c,ab}^{(2)} \Gamma_{bd}^{(2)} = \delta_{ad}$. Here δ_{ad} is the product of a discrete Kronecker delta and a continuous Dirac delta distribution.

5.A.2 Operator ordering at equal-time

There are three common choices of different orderings, often referred to as symmetric (Weyl), normal (P) and anti-normal (Q). In terms of creation and annihilation operators \hat{a}_p and \hat{a}_p^{\dagger} , which fulfill $[\hat{a}_p, \hat{a}_q^{\dagger}] \sim \delta_{pq}$, they can be realized by the definitions

$$Z_t^{(W)}[J] = \text{Tr} \left[\hat{\rho}_t \exp \left(J_p \hat{a}_p^\dagger - J_p^* \hat{a}_p \right) \right], \quad (5.32a)$$

$$Z_t^{(P)}[J] = \text{Tr} \left[\hat{\rho}_t \exp \left(J_p \hat{a}_p^\dagger \right) \exp \left(-J_p^* \hat{a}_p \right) \right], \quad (5.32b)$$

$$Z_t^{(Q)}[J] = \text{Tr} \left[\hat{\rho}_t \exp \left(-J_p^* \hat{a}_p \right) \exp \left(J_p \hat{a}_p^\dagger \right) \right]. \quad (5.32c)$$

In general, there is a continuum of other choices that smoothly connect these three cases. However, all different choices are fully equivalent in the sense that they contain all measurable information and the main difference lies in the associated quasi-probability distributions. For more details we refer to [206].

Explicitly, for our choice, the ordering is resolved as

$$\exp \left(J_{\mathbf{x}}^\varphi \hat{\Phi}_{\mathbf{x}} + J_{\mathbf{x}}^\pi \hat{\Pi}_{\mathbf{x}} \right) = e^{J_{\mathbf{x}}^\varphi \hat{\Phi}_{\mathbf{x}}} e^{J_{\mathbf{x}}^\pi \hat{\Pi}_{\mathbf{x}}} e^{-\frac{i}{2} J_{\mathbf{x}}^\varphi J_{\mathbf{x}}^\pi} = e^{J_{\mathbf{x}}^\pi \hat{\Pi}_{\mathbf{x}}} e^{J_{\mathbf{x}}^\varphi \hat{\Phi}_{\mathbf{x}}} e^{\frac{i}{2} J_{\mathbf{x}}^\varphi J_{\mathbf{x}}^\pi} \quad (5.33)$$

where we used the BCH formula in the form

$$e^{\hat{A}+\hat{B}} = e^{\hat{A}} e^{\hat{B}} e^{-\frac{1}{2}[\hat{A},\hat{B}]}, \quad (5.34)$$

which is valid for $[[\hat{A}, \hat{B}], \hat{B}] = [[\hat{A}, \hat{B}], \hat{A}] = 0$. Thus, derivatives acting on $\exp \left(J_{\mathbf{x}}^\varphi \hat{\Phi}_{\mathbf{x}} + J_{\mathbf{x}}^\pi \hat{\Pi}_{\mathbf{x}} \right)$ from the left result in operators and additional sources according to

$$\frac{\delta}{\delta J_{\mathbf{x}}^\varphi} \rightarrow \hat{\Phi}_{\mathbf{x}} - \frac{i J_{\mathbf{x}}^\pi}{2}, \quad \frac{\delta}{\delta J_{\mathbf{x}}^\pi} \rightarrow \hat{\Pi}_{\mathbf{x}} + \frac{i J_{\mathbf{x}}^\varphi}{2}. \quad (5.35)$$

Using this correspondence, it is straightforward to generate explicit expression for all correlators. For instance, at second order, we have

$$\frac{\delta}{\delta J_{\mathbf{x}}^\varphi} \frac{\delta}{\delta J_{\mathbf{y}}^\pi} \rightarrow \frac{\delta}{\delta J_{\mathbf{x}}^\varphi} \left(\hat{\Pi}_{\mathbf{y}} + \frac{i J_{\mathbf{y}}^\varphi}{2} \right) \rightarrow \left(\hat{\Pi}_{\mathbf{y}} + \frac{i J_{\mathbf{y}}^\varphi}{2} \right) \left(\hat{\Phi}_{\mathbf{x}} - \frac{i J_{\mathbf{x}}^\pi}{2} \right) + \frac{i}{2} \delta(\mathbf{x} - \mathbf{y}).$$

Setting the sources to zero proves that

$$\langle \varphi_{\mathbf{x}} \pi_{\mathbf{y}} \rangle_{W_t} = \text{Tr} \left[\hat{\rho}_t \hat{\Pi}_{\mathbf{y}} \hat{\Phi}_{\mathbf{x}} \right] + \frac{i}{2} \delta(\mathbf{x} - \mathbf{y}) = \frac{1}{2} \text{Tr} \left[\hat{\rho}_t \left(\hat{\Phi}_{\mathbf{x}} \hat{\Pi}_{\mathbf{y}} + \hat{\Pi}_{\mathbf{y}} \hat{\Phi}_{\mathbf{x}} \right) \right], \quad (5.36)$$

where we used the canonical commutation relations and the normalization of $\hat{\rho}_t$. In the following we drop the label t for brevity.

5.A.3 Correlations and the density operator

The density operator $\hat{\rho}$ can formally be recovered from Z as [206]

$$\hat{\rho} = \int \mathcal{D}J^\varphi \mathcal{D}J^\pi Z[J] \left[\exp \left(J_{\mathbf{x}}^\varphi \hat{\Phi}_{\mathbf{x}} + J_{\mathbf{x}}^\pi \hat{\Pi}_{\mathbf{x}} \right) \right]^{-1}. \quad (5.37)$$

Furthermore, the mappings between the different functionals are invertible (under appropriate mathematical assumptions): W and Z are related by Fourier transforms, Z and E by an exponential (or logarithmic) map, E and Γ by Legendre transforms. Thus, it is completely equivalent to work with the Wigner functional W or any of the generating functionals Z, E, Γ instead of the density operator $\hat{\rho}$.

5.A.4 Functional integral representation, Eq. (5.6)

We seek a representation of Z in terms of classical (commuting) instead of operator-valued fields. To this end, we evaluate the trace as

$$Z[J, \rho(t)] = \int \mathcal{D}\varphi^+ \mathcal{D}\varphi^- \langle \varphi^+ | \rho(t) | \varphi^- \rangle \langle \varphi^- | e^{J_x^\varphi \Phi_x + J_x^\pi \Pi_x} | \varphi^+ \rangle \quad (5.38a)$$

$$= \int \mathcal{D}\varphi^+ \mathcal{D}\varphi^- \mathcal{D}\tilde{\pi} \langle \varphi^+ | \rho(t) | \varphi^- \rangle \langle \varphi^- | e^{J_x^\varphi \Phi_x} | \tilde{\pi} \rangle \langle \tilde{\pi} | e^{J_x^\pi \Pi_x} | \varphi^+ \rangle e^{-\frac{i}{2} J_x^\varphi J_x^\pi} \quad (5.38b)$$

$$= \int \mathcal{D}\varphi \mathcal{D}\tilde{\varphi} \mathcal{D}\tilde{\pi} \left\langle \varphi + \frac{\tilde{\varphi}}{2} \middle| \rho(t) \middle| \varphi - \frac{\tilde{\varphi}}{2} \right\rangle \times e^{J_x^\varphi (\varphi_x - \frac{\tilde{\varphi}_x}{2}) + i(\varphi_x - \frac{\tilde{\varphi}_x}{2}) \tilde{\pi}_x + J_x^\pi \tilde{\pi}_x - i(\varphi_x + \frac{\tilde{\varphi}_x}{2}) \tilde{\pi}_x - \frac{i}{2} J_x^\varphi J_x^\pi} \quad (5.38c)$$

$$= \int \mathcal{D}\varphi \mathcal{D}\tilde{\varphi} \mathcal{D}\tilde{\pi} \mathcal{D}\pi W_t[\varphi, \pi] e^{i\pi_x \tilde{\varphi}_x + J_x^\varphi (\varphi_x - \frac{\tilde{\varphi}_x}{2}) + J_x^\pi \tilde{\pi}_x - i\tilde{\varphi}_x \tilde{\pi}_x - \frac{i}{2} J_x^\varphi J_x^\pi} \quad (5.38d)$$

$$= \int \mathcal{D}\varphi \mathcal{D}\pi W_t[\varphi, \pi] \exp[J_x^\varphi \varphi_x + J_x^\pi \pi_x] . \quad (5.38e)$$

In the above calculation, we have again used the BCH formula, performed a change of variables $\varphi^\pm \equiv \varphi \pm \tilde{\varphi}/2$, and employed the definition of the Wigner functional.

5.A.5 The connected correlators, Eq. (5.10)

To discuss the explicit form of the connected and 1PI correlators, we use the shorthand notation, where sources J_a have a single index indicating space \mathbf{x} , as well as any of the two fields φ and π . Repeated indices are summed and integrated over. Similarly, we abbreviate the fields as φ_a .

At first order, the connected correlators are directly related to the full Weyl-ordered one-point function,

$$\frac{\delta E}{\delta J_a} = \frac{\delta \log Z}{\delta J_a} = \frac{1}{Z} \frac{\delta Z}{\delta J_a} . \quad (5.39)$$

Setting the sources to zero, we have $Z[J = 0] = 1$, which proves Eq. (5.10a).

At second order, we calculate

$$\frac{\delta^2 E}{\delta J_a \delta J_b} = \frac{\delta}{\delta J_a} \left(\frac{1}{Z} \frac{\delta Z}{\delta J_b} \right) = \frac{1}{Z} \frac{\delta^2 Z}{\delta J_a \delta J_b} - \frac{1}{Z^2} \frac{\delta Z}{\delta J_a} \frac{\delta Z}{\delta J_b} , \quad (5.40)$$

which proves Eq. (5.10b).

The higher orders follow analogously by the combinatorics of the derivatives. E.g., the third order, Eq. (5.10c), is obtained by

$$\frac{\delta^3 E}{\delta J_a \delta J_b \delta J_c} = \frac{1}{Z} \frac{\delta^3 Z}{\delta J_a \delta J_b \delta J_c} - \left(\frac{1}{Z^2} \frac{\delta^2 Z}{\delta J_a \delta J_b} \frac{\delta Z}{\delta J_c} + 2 \text{ perm.} \right) + 2 \frac{1}{Z^3} \frac{\delta Z}{\delta J_a} \frac{\delta Z}{\delta J_b} \frac{\delta Z}{\delta J_c} \quad (5.41)$$

and using Eqs. (5.39) and (5.40).

5.A.6 The 1PI vertices, Eq. (5.14)

The expression for the 1PI two-point function is central for the construction of the higher orders. It follows by considering a derivative of the stationarity condition,

$$\frac{\delta^2 \Gamma}{\delta \Phi_a \delta \Phi_b} = \frac{\delta J_b}{\delta \Phi_a}. \quad (5.42)$$

This is the matrix inverse of the derivative of the one-point function (in the presence of sources), i.e.,

$$\frac{\delta \Phi_a(J)}{\delta J_b} = \frac{\delta}{\delta J_b} \left(\frac{1}{Z} \frac{\delta Z}{\delta J_a} \right) = \frac{\delta^2 E}{\delta J_a \delta J_b}. \quad (5.43)$$

Thus, we find Eq. (5.14b), or

$$\frac{\delta^2 \Gamma}{\delta \Phi_a \delta \Phi_b} = \left[\left(\frac{\delta^2 E}{\delta J \delta J} \right)^{-1} \right]_{ab}, \quad (5.44)$$

which also holds without setting the sources to zero.

The higher orders follow by taking derivatives of this equation (with non-zero sources). To this end, we replace a derivative by

$$\frac{\delta}{\delta \Phi_c} = \frac{\delta J_{c'}}{\delta \Phi_c} \frac{\delta}{\delta J_{c'}} = \frac{\delta^2 \Gamma}{\delta \Phi_c \delta \Phi_{c'}} \frac{\delta}{\delta J_{c'}} \quad (5.45)$$

and calculate the derivative of the inverse of a matrix $M(y)$ depending on a parameter y according to

$$\frac{d}{dy} (M^{-1}) = -M^{-1} \cdot \frac{dM}{dy} \cdot M^{-1}. \quad (5.46)$$

This results for the third order in

$$\frac{\delta^3 \Gamma}{\delta \Phi_a \delta \Phi_b \delta \Phi_c} = - \frac{\delta^2 \Gamma}{\delta \Phi_a \delta \Phi_{a'}} \frac{\delta^2 \Gamma}{\delta \Phi_b \delta \Phi_{b'}} \frac{\delta^2 \Gamma}{\delta \Phi_c \delta \Phi_{c'}} \frac{\delta^3 E}{\delta J_{a'} \delta J_{b'} \delta J_{c'}}, \quad (5.47)$$

which proves Eq. (5.14c).

Similarly, the fourth order, Eq. (5.14d), follows by the combinatorics of taking further derivatives,

$$\begin{aligned} \frac{\delta^4 \Gamma}{\delta \Phi_a \delta \Phi_b \delta \Phi_c \delta \Phi_d} = & - \frac{\delta^2 \Gamma}{\delta \Phi_a \delta \Phi_{a'}} \frac{\delta^2 \Gamma}{\delta \Phi_b \delta \Phi_{b'}} \frac{\delta^2 \Gamma}{\delta \Phi_c \delta \Phi_{c'}} \frac{\delta^2 \Gamma}{\delta \Phi_d \delta \Phi_{d'}} \frac{\delta^4 E}{\delta J_{a'} \delta J_{b'} \delta J_{c'} \delta J_{d'}} \\ & + \frac{\delta^2 \Gamma}{\delta \Phi_a \delta \Phi_{a'}} \frac{\delta^2 \Gamma}{\delta \Phi_b \delta \Phi_{b'}} \frac{\delta^2 \Gamma}{\delta \Phi_c \delta \Phi_{c'}} \frac{\delta^2 \Gamma}{\delta \Phi_d \delta \Phi_{d'}} \\ & \times \left(\frac{\delta^3 E}{\delta J_{a'} \delta J_{b'} \delta J_e} \frac{\delta^2 \Gamma}{\delta \Phi_e \delta \Phi_f} \frac{\delta^3 E}{\delta J_f \delta J_{c'} \delta J_{d'}} + 2 \text{ perm.} \right). \end{aligned} \quad (5.48)$$

5.A.7 The thermal case and the classical limit

In thermal equilibrium, the (unnormalized) canonical density operator $\hat{\rho}_\beta = e^{-\beta \hat{H}}$ fulfills the equation $\partial_\beta \hat{\rho}_\beta = -\frac{1}{2} (\hat{H} \hat{\rho}_\beta + \hat{\rho}_\beta \hat{H})$. Employing the quasi-probability formalism [208], one can show that this equation translates to an equation for W_β . It takes the form

$$\partial_\beta W_\beta = -\frac{1}{2} [H_W^+ + H_W^-] W_\beta, \quad (5.49)$$

where $H_W^\pm = H_W \left[\varphi \pm \frac{i\hbar}{2} \frac{\delta}{\delta \pi}, \pi \mp \frac{i\hbar}{2} \frac{\delta}{\delta \varphi} \right]$ is a functional differential operator obtained from the Weyl-transform $H_W[\varphi, \pi]$ of the Hamiltonian \hat{H} by replacing the arguments with the given operators [208]. With the initial condition $W_{\beta \rightarrow \infty} = \text{const.}$, which follows from the high-temperature limit, this functional flow equation can be solved perturbatively by expanding $W_\beta = \exp \left[\sum_{n=0}^{\infty} \hbar^n W_\beta^{(n)} \right]$ in powers of \hbar and comparing the coefficients⁵.

The first order in this expansion is the classical field theory limit, where $W_\beta \sim e^{-\beta H}$ with the classical Hamiltonian $H = H_W$. Parametrically, this is a valid approximation when \hbar is small. Since \hbar is a dimensionful quantity, the precise power-counting of this expansion has to be determined for each theory separately. In general, any quantum system in thermal equilibrium will be governed by (at least) two dimensionless parameters ϵ_q and ϵ_{th} that control the strength of quantum and classical fluctuations, respectively. A sufficient condition for the validity of the classical approximation is

$$\epsilon_q \ll \min[1, \epsilon_{\text{th}}]. \quad (5.50)$$

The parameters ϵ_q and ϵ_{th} are obtained by rescaling the Hamiltonian and the fundamental fields to dimensionless quantities. Explicitly, for the sine-Gordon model in the form of Eq. (5.23), we have

$$\beta \hat{H} = \frac{1}{\epsilon_{\text{th}}} \int_{x'} \left\{ \frac{1}{2} \left[\left(\hat{\Pi}' \right)_{x'}^2 + \left(\partial_{x'} \hat{\Phi}'_{x'} \right)^2 \right] - \cos \left(\hat{\Phi}'_{x'} \right) \right\}, \quad (5.51)$$

⁵See, however, our comment on this point for the example of a non-interacting theory in section 5.B.

together with the rescaled commutation relations

$$\left[\hat{\Phi}'_{x'}, \hat{\Pi}'_{y'} \right] = i\epsilon_q \delta(x' - y'), \quad (5.52)$$

such that we find

$$\epsilon_q = \sqrt{4\gamma}, \quad \epsilon_{\text{th}} = \frac{4\ell_J}{\lambda_T} = \frac{4}{Q}. \quad (5.53)$$

Here

$$\gamma = \frac{mg}{\hbar^2 n_{1D}} = \gamma_{\text{LL}} + \frac{1}{n_{1D}^2 \ell_J^2}, \quad (5.54)$$

is dominated by the 1D Lieb-Liniger parameter $\gamma_{\text{LL}} = mg_{1D}/(\hbar^2 n_{1D})$, such that the semi-classical approximation is valid in the weakly interacting regime $\gamma_{\text{LL}} \ll 1$, as expected.

5.A.8 Derivation of Eq. (5.18) and the Π -dependence

From Eq. (5.17), the generating functional separates into a product, i.e., $Z_\beta[J] = Z_\beta^\varphi[J^\varphi] Z_\beta^\pi[J^\pi]$, with

$$Z_\beta^\varphi[J^\varphi] \sim \int \mathcal{D}\varphi e^{-\beta \int_{\mathbf{x}} \left[\frac{1}{2} (\nabla_{\mathbf{x}} \varphi_{\mathbf{x}})^2 + V_{\mathbf{x}}(\varphi) \right] + \int_{\mathbf{x}} J_{\mathbf{x}}^\varphi \varphi_{\mathbf{x}}}, \quad (5.55a)$$

$$Z_\beta^\pi[J^\pi] \sim \int \mathcal{D}\pi \exp \left[-\frac{\beta}{2} \int_{\mathbf{x}} \pi_{\mathbf{x}}^2 + \int_{\mathbf{x}} J_{\mathbf{x}}^\pi \pi_{\mathbf{x}} \right] \sim \exp \left[\frac{1}{2\beta} \int_{\mathbf{x}} (J_{\mathbf{x}}^\pi)^2 \right]. \quad (5.55b)$$

This directly implies that $E[J] = \log Z_\beta^\varphi[J^\varphi] + \log Z_\beta^\pi[J^\pi] + \text{const.}$ and thus the effective action becomes $\Gamma[\Phi, \Pi] = \Gamma^\varphi[\Phi] + \Gamma^\pi[\Pi] + \text{const.}$, which proves Eq. (5.18).

Carrying out the Legendre transform in J^π , we solve

$$\Pi_{\mathbf{x}}(J^\pi) = \left. \frac{\delta Z^\pi[J^\pi]}{\delta J_{\mathbf{x}}^\pi} \right|_{J=0} = \frac{J_{\mathbf{x}}^\pi}{\beta} \Rightarrow J_{\mathbf{x}}^\pi(\Pi) = \beta \Pi_{\mathbf{x}}. \quad (5.56)$$

and finally obtain

$$\Gamma^\pi[\Pi] = -\log Z^\pi[J^\pi(\Pi)] + J_{\mathbf{x}}^\pi(\Pi) \Pi_{\mathbf{x}} = \frac{\beta}{2} \int_{\mathbf{x}} \Pi_{\mathbf{x}}^2. \quad (5.57)$$

5.A.9 Time translation invariance

For a stationary system, all observables are time-independent, $\partial_t \text{Tr} [\hat{\rho}_t \dots] = 0$. If additionally the Hamiltonian is of the form $\hat{H}[\hat{\Phi}, \hat{\Pi}] = \hat{H}[\hat{\Pi}] + \hat{H}[\hat{\Phi}]$ with $\hat{H}[\hat{\Pi}] = \frac{1}{2} \int_{\mathbf{x}} \Pi_{\mathbf{x}}^2$, then it follows that $0 = \text{Tr} \left[\hat{\rho}_t \left(\hat{\Phi}_x \hat{\Pi}_y + \hat{\Pi}_x \hat{\Phi}_y \right) \right] = \langle \varphi_x \pi_y \rangle_{W_t}$. As a consequence the two-point function becomes block diagonal, which simplifies the

inversion,

$$G_c^{(2)} = \begin{pmatrix} \langle \varphi \varphi \rangle & 0 \\ 0 & \langle \pi \pi \rangle \end{pmatrix} \Rightarrow \Gamma^{(2)} = \begin{pmatrix} \langle \varphi \varphi \rangle^{-1} & 0 \\ 0 & \langle \pi \pi \rangle^{-1} \end{pmatrix}. \quad (5.58)$$

5.A.10 Loop expansion of the effective action

Starting from Eq. (5.19), we calculate

$$e^{-\Gamma'_\beta[\Phi]} = e^{-\Gamma_\beta[\Phi] + \beta H[\Phi]} = e^{\log Z[J(\Phi) - J_x(\Phi)\Phi_x + \beta H[\Phi]]} \quad (5.59a)$$

$$= \int \mathcal{D}\varphi e^{-\beta H[\varphi] + J_x(\Phi)\varphi_x - J_x(\Phi)\Phi_x + \beta H[\Phi]} \quad (5.59b)$$

$$= \int \mathcal{D}\varphi e^{-\beta(H[\varphi + \Phi] - H[\Phi]) + J_x(\Phi)\varphi_x} \quad (5.59c)$$

$$= \int \mathcal{D}\varphi e^{-\beta\left(H[\varphi + \Phi] - H[\Phi] - \frac{\delta H[\Phi]}{\delta \Phi_x} \varphi_x\right) + \frac{\delta \Gamma'_\beta[\Phi]}{\delta \Phi_x} \varphi_x}. \quad (5.59d)$$

Here, we have used Eqs. (5.11) and (5.17), then performed a change of variables $\varphi \rightarrow \varphi + \Phi$ and finally expressed the sources as $J_x(\Phi) = (\delta \Gamma[\Phi]) / (\delta \Phi_x)$.

The first non-trivial correction (one-loop) is obtained by neglecting all terms beyond quadratic order in the fluctuating fields φ . The remaining Gaussian integral can then be performed analytically, which gives

$$e^{-\Gamma'_\beta{}^{\text{one-loop}}[\Phi]} = \int \mathcal{D}\varphi e^{-\frac{1}{2}\varphi_x G_{x,y}^{-1}[\Phi] \varphi_y} = (\det G^{-1}[\Phi])^{-1/2}. \quad (5.60)$$

The name ‘‘one-loop’’ stems from the expansion in terms of the tree-level two-point function G_0 . To see this, we rewrite

$$\Gamma'_\beta{}^{\text{one-loop}}[\Phi] = \frac{1}{2} \log \det G^{-1}[\Phi] = \frac{1}{2} \text{Tr} \log G^{-1}[\Phi] \quad (5.61a)$$

$$= \frac{1}{2} \text{Tr} \log (G_0 G^{-1}[\Phi]) + \frac{1}{2} \text{Tr} \log G_0^{-1} \quad (5.61b)$$

$$= \frac{1}{2} \sum_{n=1}^{\infty} \frac{(-1)^{n+1}}{n} \text{Tr} \{G_0 (G^{-1}[\Phi] - G_0^{-1})\}^n \quad (5.61c)$$

where we have used the identity $\log \det A = \text{Tr} \log A$, employed the series expansion of the logarithm and dropped the irrelevant constant. Graphically the result can be pictured as a sum of loops consisting of lines that stand for G_0 connected by field insertions coming from $(G^{-1}[\Phi] - G_0^{-1})$. For more details about the loop expansion, we refer to [50, 213].

Note that in the standard (unequal-time) formalism, the loop expansion is used as an expansion in weak quantum fluctuations. Here, in the context of the classical field theory limit in thermal equilibrium, it is employed as an expansion in weak thermal fluctuations. In terms of the dimensionless parameters introduced in section 5.A.7, the loop expansion is applicable for $\epsilon_{\text{th}} \ll 1$. Thus, the tree-level approximation (i.e., the leading order in the loop expansion), which we used to extract the microscopic

Hamiltonian parameters, is applicable when the following separation of scales holds:

$$\epsilon_q \ll \epsilon_{\text{th}} \ll 1 . \quad (5.62)$$

Colloquially speaking, this is the limit of weak thermal fluctuations and even weaker quantum fluctuations.

5.A.11 Cosine vs. Fourier transform and the boundary conditions

For an infinite system with translation invariance, the correlation functions in momentum (Fourier) space are directly related to the correlators obtained by a cosine transform. Explicitly, with the transforms

$$\varphi_p = \int dx e^{-ipx} \varphi_x , \quad (5.63a)$$

$$\tilde{\varphi}_p = \int dx \cos(px) \varphi_x = \frac{1}{2} (\varphi_p + \varphi_{-p}) , \quad (5.63b)$$

the two-point functions are related as

$$\langle \tilde{\varphi}_p^2 \rangle = \frac{1}{2} \langle \varphi_p \varphi_{-p} \rangle , \quad (5.64)$$

where we assumed translation invariance, thus $\langle \varphi_p^2 \rangle = 0$. Similarly, for the four-point functions, we have

$$\langle \tilde{\varphi}_p^4 \rangle = \frac{3}{8} \langle \varphi_p \varphi_p \varphi_{-p} \varphi_{-p} \rangle , \quad (5.65)$$

where the prefactors arises from the 6 non-vanishing contributions out of $2^4 = 16$ combinations.

In practice, we deal with a finite system without periodic boundary conditions. A discrete Fourier transform is then not appropriate as it yields numerical artifacts. Since the calculation of 1PI correlators simplifies tremendously in Fourier space, we still prefer to work in a Fourier basis. Therefore, we calculate the correlators with a discrete cosine transform, which reduces the artifacts from the boundary conditions. Then we translate the correlators using the factors of $1/2$ and $3/8$ to Fourier-space correlators and subsequently calculate the 1PI correlation functions. For sufficiently large system sizes, this procedure yields the desired results and reduces numerical artifacts in a controlled way.

5.A.12 The 1PI vertices from the numerical data

In practice, the numerical and experimental profiles live on a spatial lattice with lattice spacing Δx and a finite number of lattice sites N , i.e., we have φ_x for $\frac{x}{\Delta x} \in \{0, 1, \dots, N-1\}$. We employ a discrete cosine transform of the individual realizations to obtain profiles $\tilde{\varphi}_{p_{\text{lat}}}$ and later translate the results to the Fourier transform.

The lattice momentum takes the values $p_{\text{lat}} = j \frac{2\pi}{\Delta x N}$ with $j \in \{-\frac{N}{2}, \dots, \frac{N}{2} - 1\}$. We correct for some artifacts of the discrete transform at large momenta by considering physical momenta

$$p_{\text{phys}} = \frac{2}{\Delta x} \sin\left(\frac{p_{\text{lat}} \Delta x}{2}\right). \quad (5.66)$$

The two- and four-vertex densities (normalized to have units of $1/L$ with $L = N\Delta x$) from the main part of this chapter are obtained by

$$\Gamma_p^{(2)} = \frac{L}{\left\langle \left| \varphi_{p_{\text{phys}}} \right|^2 \right\rangle_c}, \quad \Gamma_p^{(4)} = -\frac{L^3 \left\langle \left| \varphi_{p_{\text{phys}}} \right|^4 \right\rangle_c}{\left\langle \left| \varphi_{p_{\text{phys}}} \right|^2 \right\rangle_c^4}. \quad (5.67)$$

Here, the expectation values are

$$\left\langle \left| \varphi_p \right|^2 \right\rangle_c = \langle \varphi_p \varphi_{-p} \rangle_c = 2 \langle \tilde{\varphi}_p^2 \rangle_c, \quad (5.68a)$$

$$\left\langle \left| \varphi_p \right|^4 \right\rangle_c = \langle \varphi_p \varphi_p \varphi_{-p} \varphi_{-p} \rangle_c = \frac{8}{3} \langle \tilde{\varphi}_p^2 \rangle_c, \quad (5.68b)$$

where the index c indicates connected correlators according to Eq. (5.10).

5.A.13 One-loop corrections

To obtain the one-loop correction to the effective action, we approximate

$$\beta K[\varphi, \Phi] = \beta \left(H[\varphi + \Phi] - H[\Phi] - \frac{\delta H[\Phi]}{\delta \Phi_x} \varphi_x \right) \quad (5.69a)$$

$$= \frac{\lambda_T}{4} \int_x \left\{ \frac{1}{2} (\partial_x \varphi_x)^2 - \frac{1}{\ell_J^2} \cos \Phi_x [-1 + \cos \varphi_x] - \frac{1}{\ell_J^2} \sin \Phi_x [\varphi_x - \sin \varphi_x] \right\} \quad (5.69b)$$

$$= \frac{1}{2} \varphi_{\mathbf{x}} G_{\mathbf{x}, \mathbf{y}}^{-1}[\Phi] \varphi_{\mathbf{y}} + \mathcal{O}(\varphi^3) \quad (5.69c)$$

with $G_{xy}^{-1}[\Phi] = \frac{\lambda_T}{4} \left[-\partial_x^2 + \frac{1}{\ell_J^2} \cos(\Phi_x) \right] \delta(x - y)$. From Eq. (5.61), we then have

$$\Gamma_\beta^{\prime, \text{one-loop}}[\Phi] = -\frac{1}{2} \sum_{n=1}^{\infty} \frac{1}{n} \left(\frac{\lambda_T}{4} \frac{2}{\ell_J^2} \right)^n \text{Tr} \left\{ G_0 \sin^2 \left(\frac{\Phi}{2} \right) \right\}^n, \quad (5.70)$$

where

$$G_{0,xy} = \int \frac{dp}{2\pi} e^{ip(x-y)} G_{0,p} \quad (5.71)$$

with $G_{0,p} = \frac{4}{\lambda_T} / (p^2 + 1/\ell_J^2)$.

The one-loop corrections to the 1PI vertices are now obtained by taking derivatives of Eq. (5.70), evaluated at $\Phi = 0$ in the symmetric case. Explicitly, we find at

second order

$$\Delta\Gamma_{xy}^{(2),\text{one-loop}} = -\frac{1}{2\ell_J^2} G_{0,xx} \delta(x-y) \quad (5.72)$$

and at fourth order

$$\begin{aligned} \Delta\Gamma_{xyzw}^{(4),\text{one-loop}} &= \frac{1}{2\ell_J^2} G_{0,xx} \delta(x-y) \delta(x-z) \delta(x-w) \\ &\quad - \frac{1}{2\ell_J^4} [G_{0,xy} G_{0,zw} \delta(x-z) \delta(y-w) + 2 \text{ perm.}] . \end{aligned} \quad (5.73)$$

The involved loop integrals are given by

$$\int_{-\infty}^{\infty} \frac{dq}{2\pi} \frac{1}{q^2 + 1/\ell_J^2} = \frac{\ell_J}{2} , \quad (5.74a)$$

$$\int_{-\infty}^{\infty} \frac{dq}{2\pi} \frac{1}{q^2 + 1/\ell_J^2} \frac{1}{(p-q)^2 + 1/\ell_J^2} = \frac{\ell_J}{(2/\ell_J)^2 + p^2} , \quad (5.74b)$$

which results in the expressions discussed in the main part of this chapter,

$$\Gamma_p^{(2),\text{one-loop}} = \frac{\lambda_T}{4} \left(p^2 + \frac{1}{\ell_J^2} \right) - \frac{1}{4\ell_J} , \quad (5.75a)$$

$$\Gamma_p^{(4),\text{one-loop}} = -\frac{\lambda_T}{4\ell_J^2} - \frac{1}{8\ell_J^3} \frac{1}{p^2 + 1/\ell_J^2} . \quad (5.75b)$$

Note that the one-loop correction is indeed of order $\mathcal{O}(\epsilon_{th}) = \mathcal{O}(1/Q) = \mathcal{O}(\ell_J/\lambda_T)$ compared to the tree-level approximation.

5.B Quantum thermal equilibrium

The main results of this chapter are obtained for a system in classical thermal equilibrium. We now briefly discuss how quantum fluctuations enter the presented formalism, which differs from the usual approach (see [218]). For simplicity, we restrict ourselves to a non-interacting real scalar field theory (in one spatial dimension), where the instantaneous effective action can be calculated analytically. Starting from the Hamiltonian

$$\hat{H} = \frac{1}{2} \int_x \left\{ \hat{\Pi}_x^2 + \left(\partial_x \hat{\Phi}_x \right)^2 + m^2 \hat{\Phi}_x^2 \right\} , \quad (5.76)$$

the β -flow equation for the Wigner functional W_β of the unnormalized density operator $\hat{\rho}_\beta = e^{-\beta\hat{H}}$, Eq. (5.49), becomes

$$\partial_\beta W_\beta = -\frac{1}{2} \int_x \left\{ \pi_x^2 + [(m^2 - \partial_x^2) \varphi_x^2] - \frac{\hbar^2}{4} \left(\frac{\delta^2}{\delta \varphi_x^2} + \left[(m^2 - \partial_x^2) \frac{\delta^2}{\delta \pi_x^2} \right] \right) \right\} W_\beta \quad (5.77a)$$

$$= - \int_{p>0} \left\{ \pi_p^* \pi_p + \omega_p^2 \varphi_p^* \varphi_p - \frac{\hbar^2}{4} \left[\frac{\delta}{\delta \varphi_p^*} \frac{\delta}{\delta \varphi_p} + \omega_p^2 \frac{\delta}{\delta \pi_p^*} \frac{\delta}{\delta \pi_p} \right] \right\}, \quad (5.77b)$$

where we switched to Fourier space⁶ in second the line, used $\varphi_{-p} = \varphi_p^*$ and the same for π and abbreviated $\omega_p^2 = p^2 + m^2$. The flow equation can be solved by the ansatz⁷

$$W_\beta[\varphi, \pi] = \exp \left\{ - \int_{p>0} [\Delta_{\beta,p} (\pi_p^* \pi_p + \omega_p^2 \varphi_p^* \varphi_p) + N_{\beta,p}] \right\}. \quad (5.78)$$

Then the functions Δ and N have to obey the equations

$$\partial_\beta \Delta_{\beta,p} = 1 - \frac{\hbar^2 \omega_p^2}{4} \Delta_{\beta,p}^2, \quad (5.79a)$$

$$\partial_\beta N_{\beta,p} = \frac{\hbar^2 \omega_p^2}{4} \Delta_{\beta,p} L, \quad (5.79b)$$

and the volume factor arises from functional derivatives like $(\delta \varphi_p) / (\delta \varphi_p) = L$. With the initial condition $\hat{\rho}_{\beta=0} = \hat{1}$, which translates to $W_{\beta=0} = 1$ and thus $\Delta_{\beta=0,p} = 0$ and $N_{\beta=0,p} = 0$, we obtain the solutions

$$\Delta_{\beta,p} = \frac{2}{\hbar \omega_p} \tanh \left(\frac{\beta \hbar \omega_p}{2} \right), \quad (5.80a)$$

$$N_{\beta,p} = L \log \left[\cosh \left(\frac{\beta \hbar \omega_p}{2} \right) \right]. \quad (5.80b)$$

As a consistency check we note that $\Delta_{\beta,p} \rightarrow \beta$ and $N_{\beta,p} \rightarrow 0$ in the limit $\hbar \rightarrow 0$, such that we recover the classical limit $W_\beta \rightarrow e^{-\beta H_W}$. From this simple example we also learn that a perturbative solution of the flow equation in powers of \hbar has to be considered very carefully. Here, the dimensionless expansion parameter would be $\beta \hbar \omega_p$ and thus the range of validity of the semi-classical expansion involves a certain temperature and momentum regime. Including interactions, the power counting will be more complicated in general.

Since the Wigner function (5.78) is Gaussian, we can directly read off the instantaneous effective action as

$$\Gamma_\beta[\Phi, \pi] = \int_{p>0} \Delta_{\beta,p} (\pi_p^* \pi_p + \omega_p^2 \Phi_p^* \Phi_p) + \Gamma_\beta[0, 0], \quad (5.81)$$

⁶We ignore the zero modes in the following.

⁷Here, we follow [208]. We refer to [207] for an alternative derivation in the context of a scalar field theory.

where the constant $\Gamma_\beta[0, 0]$ would be zero if we had normalized the Wigner functional. If we keep the density operator unnormalized, the constant is determined by the normalization and can be calculated by performing the Gaussian integration,

$$e^{-\Gamma_\beta[0,0]} = \int \mathcal{D}\varphi \mathcal{D}\pi W_\beta[\varphi, \pi] = \prod_p \left[\frac{e^{N_{\beta,p}/L}}{\hbar\omega_p \Delta_{\beta,p}} \right] = \prod_p \left[\frac{1}{2 \sinh\left(\frac{\beta\hbar\omega_p}{2}\right)} \right]. \quad (5.82)$$

In this way, we can recover the well-known result for the free energy density [218]

$$\begin{aligned} \frac{F}{L} &= -\frac{1}{\beta L} \log \text{Tr} \left[e^{-\beta \hat{H}} \right] = \frac{\Gamma_\beta[0, 0]}{\beta L} = \frac{1}{\beta} \int_p \log \left[2 \sinh\left(\frac{\beta\hbar\omega_p}{2}\right) \right] \\ &= \int_p \left\{ \frac{\hbar\omega_p}{2} + \frac{1}{\beta} \log \left[1 - e^{-\beta\hbar\omega_p} \right] \right\}. \end{aligned} \quad (5.83)$$

In the free theory, the only non-trivial equal-time correlation functions are

$$\Gamma_p^{\pi\pi} = \Delta_{\beta,p}, \quad \Gamma_p^{\varphi\varphi} = \omega_p^2 \Delta_{\beta,p}. \quad (5.84)$$

They determine the particle number distribution n_p as

$$\left(n_p + \frac{1}{2} \right)^{-1} = \Gamma_p^{a^*a} = \frac{\hbar}{2\omega_p} \Gamma_p^{\varphi\varphi} + \frac{\hbar\omega_p}{2} \Gamma_p^{\pi\pi} = \hbar\omega_p \Delta_{\beta,p}, \quad (5.85)$$

which follows from a change of variables to the modes a_p, a_p^* ,

$$\Phi_p = \sqrt{\frac{\hbar}{2\omega_p}} (a_p + a_{-p}^*), \quad \Phi_p = -i\sqrt{\frac{\hbar\omega_p}{2}} (a_p - a_{-p}^*), \quad (5.86)$$

As expected, we find the Bose-Einstein distribution

$$n_p = \frac{1}{2} \left(\frac{1}{\tanh\left(\frac{\beta\hbar\omega_p}{2}\right)} - 1 \right) = \frac{1}{e^{\beta\hbar\omega_p} - 1}, \quad (5.87)$$

which is characteristic for non-interacting bosons in thermal equilibrium.

Finally, by identifying $\Gamma_\beta = \beta H_{\text{eff}}$ with an effective ‘‘Hamiltonian’’, we can also identify an effective ‘‘mass’’ as

$$m_{\text{eff}}^2 = \frac{\Gamma_{p=0}^{\varphi\varphi}}{\beta} = \frac{2m}{\beta\hbar} \tanh\left(\frac{\beta\hbar m}{2}\right). \quad (5.88)$$

It reduces to the bare mass in the limit of weak fluctuations, i.e., $m_{\text{eff}}^2 \rightarrow m^2$ as $\beta\hbar m \rightarrow 0$. For large fluctuations (for instance increasing the temperature), the mass becomes irrelevant, $m_{\text{eff}}^2 \rightarrow 0$, as expected.

In conclusion, the equal-time formulation provides an alternative approach to study quantum field theory in thermal equilibrium. An extension to interacting theories may give a new perspective on thermal phase transitions and critical

phenomena. We plan to study this possibility in a future work.

Chapter 6

Extraction of the instantaneous effective action out of equilibrium

This chapter is based on the article [65] with the figures and large parts of the text taken from it. The authors of [65] contributed as follows: The experimental and theoretical concept was developed in discussions among all authors. M. Prüfer, P. Kunkel, S. Lannig, and A. Bonnin controlled the experimental apparatus. M. Prüfer and myself analyzed the data. M. Prüfer, P. Kunkel, H. Strobel, J. Berges, M. K. Oberthaler and myself discussed the measurement results. J. Berges and myself elaborated the equal-time formalism. All authors participated in the writing of the manuscript [65] and I made significant contributions to the wording and structuring of the text. In appendix 6.C, I include additional related material that was not printed in [65]. The article [65] is also covered in the experimental doctoral thesis by M. Prüfer [219].

6.1 Introduction

Understanding how macroscopic phenomena emerge from a given microscopic description is a formidable and often unsolvable theoretical task. On the fundamental level, quantum fluctuations or entanglement lead to novel forms of complex macroscopic dynamical behavior in many-body systems [220] for which a description as emergent phenomena can be found within the framework of quantum field theory. A central quantity in these efforts, containing all information about the measurable physical properties, is the quantum effective action [50]. Though the problem of non-equilibrium quantum dynamics can be exactly formulated in terms of the quantum effective action, the solution is in general beyond capabilities of classical computers when real-time or non-equilibrium questions are addressed [221]. In this chapter, we extend the strategy introduced in the previous chapter to determine the non-equilibrium quantum effective action [61] using analog quantum simulators, and demonstrate our method experimentally with a quasi one-dimensional spinor Bose gas out of equilibrium [122, 222]. Spatially resolved snapshots of the complex-valued transversal spin field [223] allow us to infer the quantum effective action up to fourth order in an expansion in one-particle irreducible correlation functions at equal times.

We uncover a strong suppression of the irreducible four-vertex emerging at low momenta, which solves the problem of dynamics in a highly occupied regime far from equilibrium where perturbative descriptions fail [224]. Similar behavior in this non-perturbative regime has been proposed in the context of early-universe cosmology [225]. Our results constitute a new realm of large-scale analog quantum computing [226], where the high level of control of synthetic quantum systems [227] provides the means for the solution of theoretical problems in high-energy and condensed matter physics with an experimental approach [8, 44, 45, 228].

6.2 Extraction of the effective action

In the many-body limit the measurable physical properties of an interacting quantum system are determined by only a small subset of all microscopic parameters. As a consequence of this effective loss of details, efficient descriptions of quantum many-body systems can be found using a concept known as the renormalization program of quantum field theory [50, 229]. Renormalization implies a scale-dependent description that links the physics on small characteristic distances with phenomena on macroscopic length scales. The scale dependence is encoded in “running” couplings, determined by momentum dependent expansion coefficients of the quantum effective action. Matching the experimental capabilities, we choose a formulation of quantum field theory based on equal-time correlation functions only [61] which has been exemplified in thermal equilibrium [39] but remains challenging far from equilibrium. Finding the time-dependent quantum effective action Γ_t , equivalent to solving the non-equilibrium dynamics, involves experimentally observable expectation values of the underlying quantum fields. Therefore, the problem is mapped onto the ability of synthetic quantum systems giving higher-order correlation functions [38, 198, 230, 231].

Our quantum simulation builds on a spinor Bose-Einstein condensate [122] and the spatially resolved detection of a complex-valued field $F_{\perp}(y) = F_x(y) + iF_y(y) = |F_{\perp}(y)|e^{i\varphi(y)}$ [223] (see appendix 6.A). We employ $\sim 100,000$ ^{87}Rb atoms in a quasi one-dimensional regime and quench the effective detuning of spin-mixing [62] by employing microwave dressing [232]. This leads to spin dynamics in the $F = 1$ hyperfine manifold (see Fig. 6.1a), building up excitations in the F_x - F_y -plane [233]. Here, F_x and F_y are the components of the hyperfine spin perpendicular to an applied external magnetic field. With an optimized optical trap we achieve coherence times, i.e., we find well defined phase relations of the three magnetic sublevels, up to ~ 50 s due to reduced heating and efficient evaporative cooling. We find that the dynamics leads to an approximately constant spin length $|F_{\perp}|$ and a fluctuating phase degree of freedom φ (see Fig. 6.1c), resembling the structure of a single-component Bose gas. By averaging over many realizations, we infer an estimator of the two- and four-point correlation functions (correlators) from the single-shot results of $F_{\perp}(y)$ (see Fig. 6.1b).

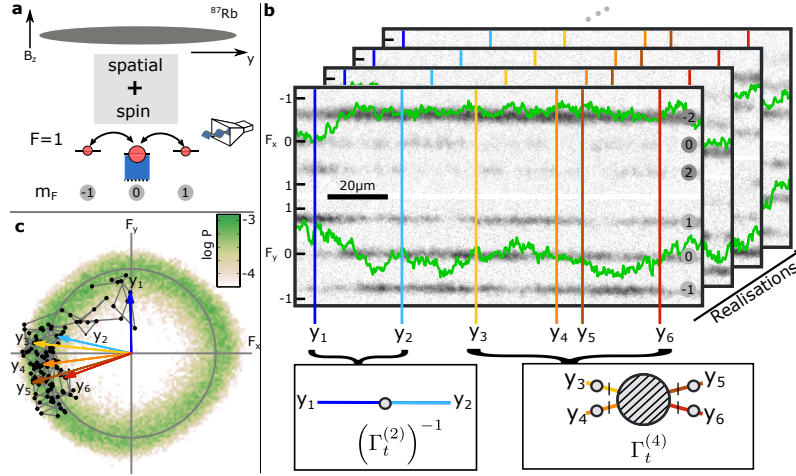


FIGURE 6.1: Experimental platform and extraction of correlation functions. **a**, The experimental system consists of an elongated, quasi one-dimensional ^{87}Rb Bose-Einstein condensate in a magnetic field B_z in z -direction. The spin dynamics takes place in the $F = 1$ hyperfine manifold and is controlled by employing microwave dressing (blue shading). **b**, In a single realization we access spatially resolved snapshots of the dynamics. We infer the transversal spin F_y and F_x (green lines) from atomic densities (gray shading) measured after a spin mapping sequence in the indicated magnetic substates in the $F = 1$ and $F = 2$ hyperfine manifolds, respectively (for details see appendix 6.A). Many realizations are used to determine the correlation functions of $F_\perp = F_x + iF_y$ to infer the proper vertices $\Gamma_t^{(n)}$. **c**, The distribution of F_\perp (all realizations and all spatial points) for 18 s evolution time. The black dots indicate the single realization shown in **b**, neighboring points are connected by a gray line. The colored arrows correspond to the spin inferred at the points y_1, \dots, y_6 .

At evolution time t , the corresponding instantaneous effective action Γ_t (see appendix 6.C for the connection to the Wigner distribution, e.g., used in quantum optics [208]) is a functional depending on the macroscopic field $\Phi^1(y)$ and its canonically conjugated field $\Phi^2(y) = (\Phi^1(y))^*$. Using a compact notation, the full quantum effective action may then be written as an expansion in the fields as (cf. Eq. (5.12) of the previous chapter)

$$\Gamma_t[\Phi] = \sum_{n=1}^{\infty} \frac{1}{n!} \Gamma_t^{\alpha_1, \dots, \alpha_n}(y_1, \dots, y_n) \Phi^{\alpha_1}(y_1) \dots \Phi^{\alpha_n}(y_n), \quad (6.1)$$

where we sum over repeated indices, $\alpha_j = 1, 2$ and integrate over all coordinates y_j with $j = 1, \dots, n$. The expansion coefficients $\Gamma_t^{\alpha_1, \dots, \alpha_n}(y_1, \dots, y_n)$ in (6.1), so-called proper vertices [50], are the one-particle irreducible (1PI) n -point correlation functions of $F_\perp(y)$. By assuming global $U(1)$ symmetry for our system, the only independent coefficients are $\Gamma_t^{1\dots 12\dots 2}(y_1, \dots, y_n) \equiv \Gamma_t^{(n)}(y_1, \dots, y_n)$ with n even and equally many field and conjugate field components. These quantities directly characterize the propagation ($\Gamma_t^{(2)}$) and interactions ($\Gamma_t^{(n>2)}$) of the field including all quantum-statistical fluctuations.

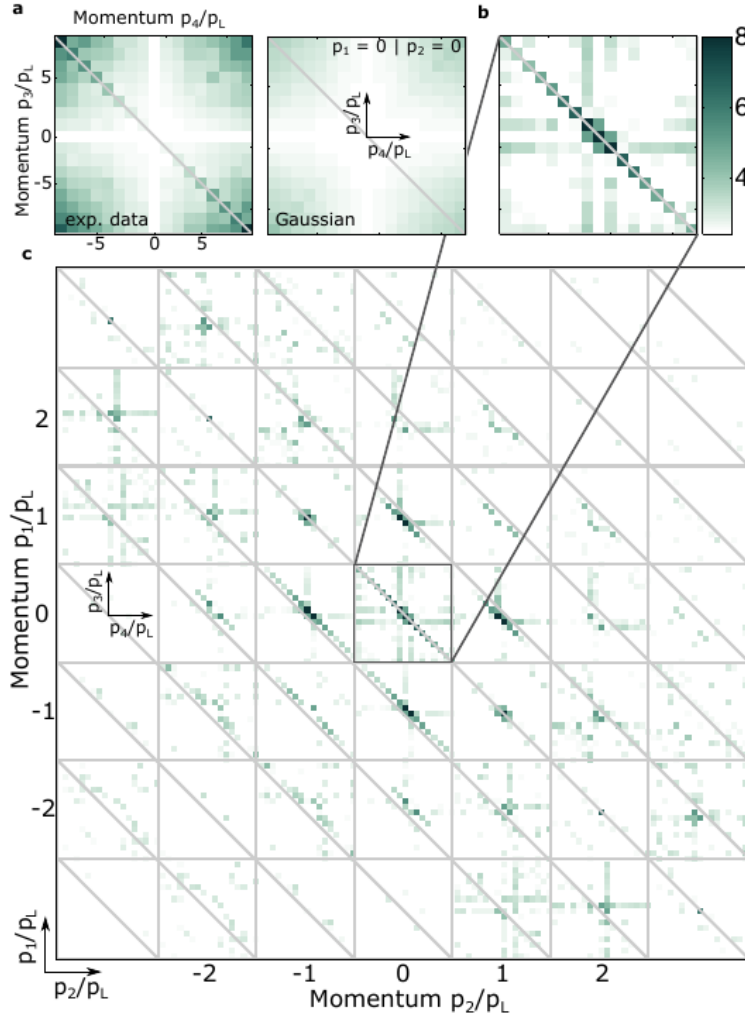


FIGURE 6.2: Statistical significance of the four-point 1PI correlator in momentum space. **a**, 1PI four-vertex $\Gamma_{t=18s}^{(4)}(0, 0, p_3, p_4)$ for experimental data (left panel); for Gaussian model with same statistics (right panel). $p_L = 1/L$ is the lowest momentum corresponding to the size L of the evaluation region. **b**, Ratio of experimental data and Gaussian model indicating the statistical significance of the inferred signal (see colorbar for scale). **c**, $\Gamma_{t=18s}^{(4)}(p_1, p_2, p_3, p_4)$ for different p_1 and p_2 (fixed in each gray square), divided by the Gaussian bias, revealing an overall momentum conserving structure (see colorbar in **b** for scale). We note that some values in **b** and **c** lie below the lower limit of the colorbar of 2.4, which was chosen for better visibility.

As discussed in the previous chapter 5, the equal-time 1PI effective action contains the same information as the density matrix but expressed in terms of observables (see also appendix 6.C for more details in the non-equilibrium case). While the entries of the density matrix are often inaccessible, the equal-time correlators can be extracted in experiments and are directly related to relevant observables, such as occupation number distributions. The 1PI vertices such as $\Gamma_t^{(4)}$ quantify the interactions between the excitations described by F_\perp in our system. These vertices are a generalization of the scattering amplitudes, which are often employed for the description of high-energy collider experiments. However, the scattering amplitudes

are typically based on the concept of asymptotic states in the infinite past and future [50], which is not adequate for strongly correlated many-body systems such as our cold Bose gas.

The proper vertices represent the irreducible building blocks for the description of the quantum many-body dynamics, and they can be related to the full correlation functions measured such as $\langle F_{\perp}(y_1)F_{\perp}^*(y_2) \rangle_t$ or $\langle F_{\perp}^*(y_1)F_{\perp}^*(y_2)F_{\perp}(y_3)F_{\perp}(y_4) \rangle_t$. Next, we obtain the connected correlation functions $C_t^{(2)}(y_1, y_2) = \langle F_{\perp}(y_1)F_{\perp}^*(y_2) \rangle_{t,c}$ and $C_t^{(4)}(y_1, y_2, y_3, y_4) = \langle F_{\perp}^*(y_1)F_{\perp}^*(y_2)F_{\perp}(y_3)F_{\perp}(y_4) \rangle_{t,c}$ [38] by subtracting the redundant disconnected parts (according to Eq. (5.10)) from the full correlators. The connected correlators are then decomposed into their irreducible parts representing the proper vertices (according to Eq. (5.14)). We obtain a momentum resolved picture by performing a discrete Fourier transform, which yields $|C_t^{(n)}(p_1, \dots, p_n)|$ with momenta p_j (see appendix 6.B). With that the macroscopic, long wavelength, behavior of the quantum system is encoded in the low-momentum or “infrared” properties of the 1PI correlation functions. More precisely, we extract $\Gamma_t^{(2)}(p, -p) \equiv \Gamma_t^{(2)}(p) = \left(C_t^{(2)}\right)^{-1}(p)$ from the inverse of the connected two-point correlator and with that the 1PI four-point correlation function for our $U(1)$ -symmetric case:

$$\Gamma_t^{(4)}(p_1, p_2, p_3, p_4) = -\Gamma_t^{(2)}(p_1) \Gamma_t^{(2)}(p_2) \Gamma_t^{(2)}(p_3) \Gamma_t^{(2)}(p_4) C_t^{(4)}(p_1, p_2, p_3, p_4). \quad (6.2)$$

Pictorially, acting with the inverse two-point correlators on the connected four-point function removes the “external legs” of the diagram (see Fig. 6.1b, and Fig. 5.2).

The experimental extraction of the 1PI four-point correlations requires sufficiently many experimental realizations to ensure the statistical significance of the results. In Fig. 6.2a we plot a slice of $|\Gamma_{t=18s}^{(4)}(p_1, p_2, p_3, p_4)|$ by fixing $p_1 = p_2 = 0$ and showing its dependence on p_3 and p_4 . Note that $\Gamma_t^{(4)}(p_1, p_2, p_3, p_4)$ is by construction symmetric under the exchange $p_1 \leftrightarrow p_2$ and $p_3 \leftrightarrow p_4$, however the symmetry $p_i \leftrightarrow -p_i$ is an experimental observation. The correlator exhibits an overall momentum dependence with a prominent contribution on the momentum conserving diagonal ($p_1 + p_2 + p_3 + p_4 = 0$). The values found are contrasted to a finite statistical bias obtained from a Gaussian model with the same number of realizations as in the experiment (see appendix 6.B). The momentum-conserving diagonal is shown to be statistically significant by dividing the values inferred from the experimental data by the finite statistical bias (see Fig. 6.2b). In Fig. 6.2c the same proper vertex divided by the Gaussian bias is shown for different p_1 and p_2 . This corroborates the overall momentum conserving structure.

6.3 Momentum and time dependence

For quantifying the renormalization effects, we investigate the momentum dependence of the proper vertices. Fig. 6.3a shows $\Gamma_{t=18s}^{(2)}(p)$ as a function of the spatial

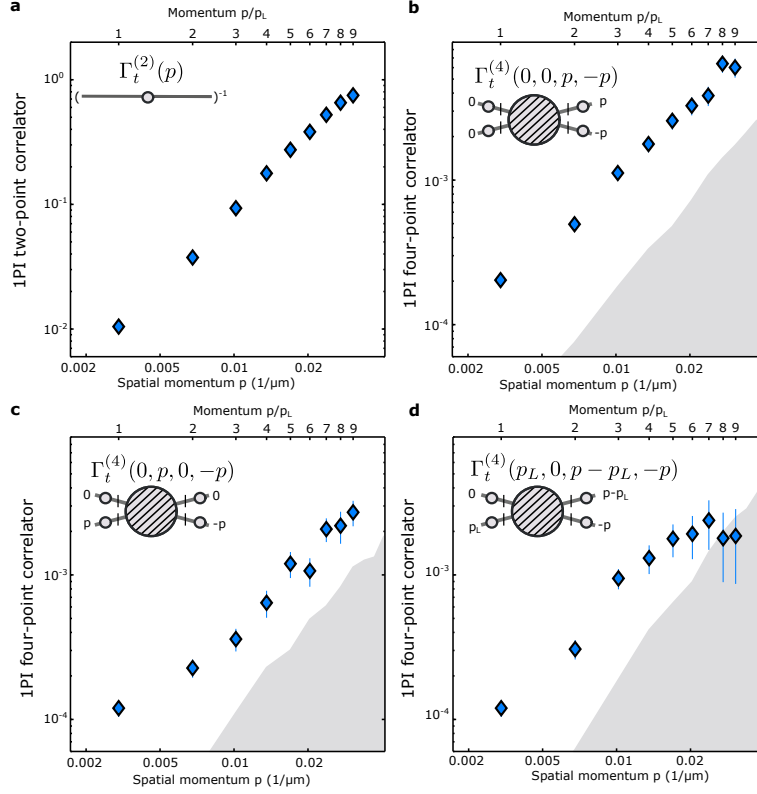


FIGURE 6.3: Momentum conserving diagonals of the 1PI correlators. **a**, Momentum conserving diagonal of $\Gamma_{t=18s}^{(2)}$. **b-d**, We show three different momentum conserving diagonals of the four point 1PI correlations (blue diamonds) for $t = 18$ s. They are statistically significant as quantified by the comparison to the finite statistics level for the Gaussian case (gray shaded region, see appendix 6.B). The complex-valued field allows the distinction between case **b** and **c**. The momentum dependence of these correlators over almost two orders of magnitude indicates the dramatic renormalization of the couplings. All error bars shown are 1 s.d. calculated from bootstrap resampling.

momentum p . We observe a suppression in the infrared [62, 187] up to a characteristic momentum set by the inverse of the length scale $l_s \sim 30 \mu\text{m}$. For the four-vertex $|\Gamma_{t=18s}^{(4)}(p_1, p_2, p_3, p_4)|$, we focus on statistically significant momentum conserving diagonals. As a representative example, the case of $p_1 = p_2 = 0$ and $p = p_3 = -p_4$ (Fig. 6.3b) shows strongly momentum-dependent values in the observed momentum regime; a similar behavior is also found for different diagonals as shown in Fig. 6.3c and 6.3d. This demonstrates that the infrared regime exhibits a strongly suppressed interaction vertex in this far-from-equilibrium situation [63, 64, 225, 234]. While quantitative theoretical predictions for this vertex are so far not possible, the observed qualitative behavior is expected from the large occupations in the infrared, as discussed below.

Motivated by the observed structure of the complex valued field, we derive an exact evolution equation for the two-point function $C_t^{(2)}(p)$ of a one-component Bose gas with interaction strength g (assuming spatial translational invariance; see

appendix 6.C for details):

$$\begin{aligned} \partial_t C_t^{(2)}(p) = g \int_{q,r,l} i \left[\Gamma_t^{(4)}(p, q, -r, -l) - \Gamma_t^{(4)}(l, r, -q, -p) \right] \\ \times C_t^{(2)}(p) C_t^{(2)}(q) C_t^{(2)}(r) C_t^{(2)}(l). \end{aligned} \quad (6.3)$$

Here, $C_t^{(2)}(p)$ has the interpretation of an occupation number distribution, where the total number $\int_p C_t^{(2)}(p)$ is conserved because of the $U(1)$ -symmetry assumed. Eq. (6.3) may be viewed as the full quantum field theoretical version of kinetic descriptions for the time evolution of $C_t^{(2)}(p)$. With our results we have determined the defining parameters $\Gamma_t^{(4)}(p_1, p_2, p_3, p_4)$ of this exact evolution equation¹, answering the question about the dynamics in the highly occupied regime, which cannot be captured by standard kinetic theory. Fig. 6.3 and 6.4 show that the momentum-dependent vertex $\Gamma_t^{(4)}$ drops by almost two orders of magnitude as the occupancy grows strongly towards lower momenta. The reduced effective interaction strength diminishes the rate of change of the distribution $C^{(2)}(p)$ according to (6.3), counteracting the Bose-enhancement from the high occupancies at low momenta.

Moreover, in our experiment we find self-similar dynamics for the statistically accessible diagonals of $\Gamma_t^{(4)}$ according to $\Gamma_t^{(4)}(0, 0, p, -p) = t^\gamma \Gamma_S(0, 0, t^{\beta_4} p, -t^{\beta_4} p)$ with scaling exponents γ and β_4 . In Fig. 6.4b we show the time evolution (inset) and the rescaled data with $\gamma = 0$ and $\beta_4 = 1/2$ revealing a scaling collapse on the function $\Gamma_S \propto 1 + (p/p_S)^{\zeta_4}$ with $\zeta_4 = 2.2 \pm 0.2$. We also find scaling of the two-point correlator $C_t^{(2)} = t^\alpha C_S(t^{\beta_2} p)$ with $C_S \propto (1 + (p/p_S)^{\zeta_2})^{-1}$ with $\zeta_2 = 2.3 \pm 0.1$ and the expected exponents $\alpha = \beta_2 \simeq 1/2$ [62, 234] (see Fig. 6.4a). The evolution equation (6.3) connects (α, β_2) to (γ, β_4) . Testing a relation of α and γ , implicitly given by the integration in Eq. (6.3), is currently hampered by the limited statistics. We anticipate that $C_t^{(2)}$ and $\Gamma_t^{(4)}$ have the same momentum scaling exponents, i.e., $\beta_2 = \beta_4$, which is consistent with our findings.

6.4 Summary

Our procedure provides a first application to extract the effective or emergent quantum field theoretical description of a far-from-equilibrium quantum many-body system from experiment. The approach is general with applications to a wide range of systems described by quantum field theory in and out of equilibrium. While our analog quantum simulator employs a specific setup with a spinor Bose gas, many of the results are insensitive to the detailed properties of the device on short-distance scales because of renormalization. Our methods are uniquely suitable to address such quantum simulations, where concepts of quantum field theory such as

¹To be precise, we have only determined the absolute value of the four-vertex. However, our derivation of the perturbative Boltzmann equation in section 6.C suggests that the four-vertex can exhibit a complex oscillating behavior as a function of time and momentum. We want to clarify this point in a future study.

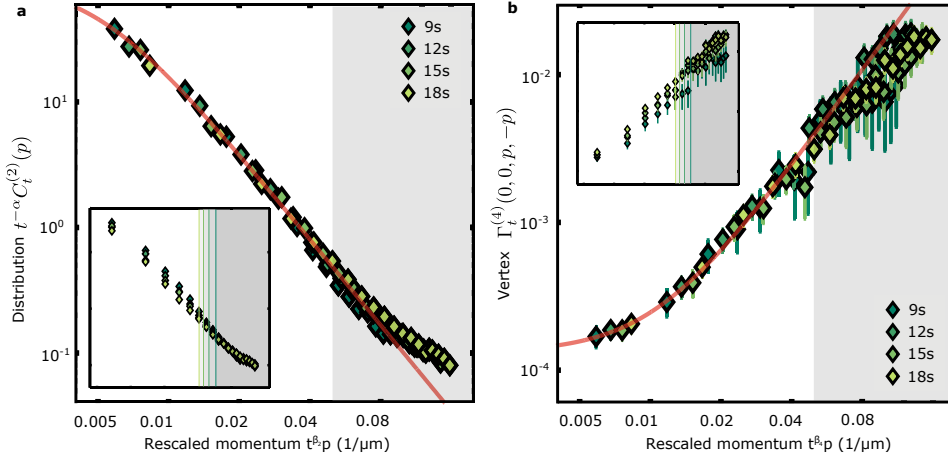


FIGURE 6.4: Observation of scaling in time of the distribution function as well as corresponding couplings. Rescaled distribution function $C_t^{(2)}(p)$ and 1PI four-point correlators $\Gamma_t^{(4)}(0, 0, p, -p)$ for times between 9 s and 18 s evolution time (the reference time for the rescaling is 12 s). We fit a universal function (red line; see text) with power law ζ and scale p_S up to the momentum scale indicated by the gray shading. The inset shows the unscaled data with same axis ticks as the main figure. The vertical lines indicate the unscaled momentum regions excluded for the fit shown in the main figure. **a**, We use $\alpha = \beta_2 = 1/2$ for rescaling and find $p_S = 1/199 \mu\text{m}^{-1}$ and $\zeta_2 = 2.3$. Here, error bars are smaller than the size of the plot markers. **b**, We use $\beta_4 = 1/2$ for rescaling and find $p_S = 1/93 \mu\text{m}^{-1}$ and $\zeta_4 = 2.2$. All error bars shown are 1 s.d. calculated from bootstrap resampling.

renormalization and the “running” of couplings become essential for a quantitative understanding. We are convinced that on the experimental side this will lead to a new class of continuous-variable quantum machines which operate in the regime of many degrees of freedom. On the theoretical side we foresee breakthroughs in understanding fundamental questions in quantum field theory inspired by results of this experimental approach.

Appendix: Details about the QFT analysis out of equilibrium

In this appendix we give more details about the experiment (section 6.A) and the data analysis (section 6.B). Additionally, we discuss in detail the real-time evolution of the instantaneous effective action for the example of a non-relativistic Bose gas in section 6.C. Within this formalism, we also provide an alternative derivation of Boltzmann's kinetic equation in a perturbative limit.

6.A Experimental details

In the experiment, we prepare $\sim 10^5$ atoms in the state $|F, m_F\rangle = |1, 0\rangle$ in a static magnetic field of 0.884 G in an optical dipole trap of 1030 nm light with trapping frequencies $(\omega_{\parallel}, \omega_{\perp}) \approx 2\pi \times (1.6, 167)$ Hz. We initiate dynamics by changing the experimental control parameter q , the second order Zeeman shift, by applying off-resonant microwave dressing. For details on the experiment and the parameter regime employed see [62].

We use a readout scheme to detect multiple spin projections in a single realization [223]. After the desired evolution time t we apply a first $\pi/2$ -rf rotation around the y -axis to map the spin projection F_x on the detectable population imbalance $N_{+1} - N_{-1}$. We store this projection in the initially empty $F = 2$ hyperfine manifold by splitting the populations of the three m_F states with three mw $\pi/2$ pulses. A second, hyperfine selective, rf rotation in $F = 1$ around the x -axis allows us to map the spin projection F_y onto the population imbalance in $F = 1$. Together with a single absorption image of the 8 hyperfine levels this procedure allows us to extract single shot snapshots of the complex valued order parameter $F_{\perp}(y) = F_x(y) + iF_y(y)$ with

$$F_x(y) = (N_{+2}^{F=2}(y) - N_{-2}^{F=2}(y)) / N_{\text{tot}}^{F=2}(y) \quad (6.4)$$

$$F_y(y) = (N_{+1}^{F=1}(y) - N_{-1}^{F=1}(y)) / N_{\text{tot}}^{F=1}(y), \quad (6.5)$$

where $N_{m_f}^{F=f}(y)$ is the atom number in the state $|f, m_f\rangle$ at position y and $N_{\text{tot}}^{F=f}(y)$ is the total atom number in the hyperfine manifold f after the readout sequence.

At evolution times of 18 s we observe no substantial loss of coherence of the different m_F states which would correspond to reductions of the transversal spin length. Optimizing the transversal confinement leads to coherence times up to ~ 50 s due to reduced heating and efficient evaporative cooling. Due to the harmonic confinement the atomic density is inhomogeneous and so is the transversal spin length profile. We choose to analyze the central 400 pixels corresponding to $\sim 168 \mu\text{m}$. The spatial resolution is $\sim 1.1 \mu\text{m}$ corresponding to three pixels (pixel size corresponds to 420 nm). As we are interested in the long wavelength (infrared) excitations we sum over 9 adjacent pixels to reduce the number of points and

Evolution Time (s)	Number of realizations
9	294
12	511
15	316
18	559

TABLE 6.5: Number of experimental realizations for the evolution times shown in this chapter.

the computation time. We use the number of realizations given in Table 6.5 for estimating the correlators.

For more details about the experiment, we refer to the doctoral thesis of M. Prüfer [219].

6.B Data analysis of correlation functions

In practice, we calculate the connected correlation functions in position space using the Julia package *Cumulants.jl* [235], which provides a very efficient implementation of Eq. (5.10). Assuming spatial translation invariance, we then calculate the 1PI correlators in momentum space where Eq. (5.14) becomes local.

6.B.1 Momentum resolved picture

We calculate all connected correlators in position space and find translation invariance. To obtain a momentum resolved picture we perform a discrete Fourier transform:

$$\begin{aligned}
 C_t^{\alpha_1, \dots, \alpha_n}(p_1, \dots, p_n) &= \text{DFT}_{y_j \rightarrow p_j} [C_t^{\alpha_1, \dots, \alpha_n}(y_1, \dots, y_n)] \\
 &\equiv \sum_{y_1=1}^N \dots \sum_{y_n=1}^N e^{-i2\pi y_1 p_1} \dots e^{-i2\pi y_n p_n} C_t^{\alpha_1, \dots, \alpha_n}(y_1, \dots, y_n),
 \end{aligned} \tag{6.6}$$

where $p_i \in [p_L, 2p_L, \dots, Np_L]$, with $p_L = 1/L$ and L the size of the evaluation region. Further, we compared the results obtained with this procedure with an evaluation based on calculating the correlator in momentum space by Fourier transforming the single shot profiles and find no qualitative differences.

6.B.2 Comparison with Gaussian fluctuations

Correlation functions of order > 2 will typically show non-vanishing values when inferred from finite statistics samples, even for the Gaussian case. In order to check for significance we compare the correlations obtained from the experimental data to samples drawn from a Gaussian distribution with a covariance matrix given by the experimentally estimated two-point correlations. We analyze the profiles obtained from this routine in the same way as the experimental data. The result of

this procedure is shown as the upper limit of the gray shaded areas in Fig. 6.3. Data points for which the 1 s.d. interval lies above this threshold are called significant. For non-significant points we cannot make a statement whether they are zero in the infinite statistics limit or just too small to resolve their value with the amount of experimental realizations employed here.

6.C Quantum field dynamics with equal-time correlations

In this section, we discuss a formulation of quantum field dynamics in terms of equal-time correlation functions. To be specific, we restrict ourselves to a single-component non-relativistic complex bosonic field, i.e., Schrödinger picture field operators $\hat{\psi}, \hat{\psi}^\dagger$ that fulfill $[\hat{\psi}_x, \hat{\psi}_y^\dagger] = \delta_{x,y}$. A generalization to multiple components, fermions, or relativistic fields is straightforward.

6.C.1 Instantaneous effective action

For completeness, we first repeat the constructions of chapter 5, but now with non-relativistic fields. An arbitrary state is determined by a density operator $\hat{\rho}_t$, or equivalently a generating functional Z_t , constructed as

$$Z_t[J, J^*] = \text{Tr} \left[\hat{\rho}_t e^{\int_x (J_x \hat{\psi}_x^\dagger + J_x^* \hat{\psi}_x)} \right] = \int \mathcal{D}\psi \mathcal{D}\psi^* W_t[\psi, \psi^*] e^{\int_x (J_x \psi_x^* + J_x^* \psi_x)}. \quad (6.7)$$

Z_t generates symmetrically ordered equal-time correlation functions and it is given by a functional integral with measure $\mathcal{D}\psi \mathcal{D}\psi^* = \prod_x \left[\frac{1}{\pi} d\text{Re}(\psi_x) d\text{Im}(\psi_x) \right]$ over W_t , the field theoretic version of the Wigner distribution which is extensively employed in quantum optics [208]. The Wigner functional W_t is given by the Wigner-Weyl transform of the density operator,

$$W_t[\psi, \psi^*] = \int \mathcal{D}\eta \mathcal{D}\eta^* \left\langle \psi - \frac{\eta}{2} \left| \hat{\rho}_t \right| \psi + \frac{\eta}{2} \right\rangle e^{-\int_x [\psi_x^* \psi_x + \frac{1}{4} \eta_x^* \eta_x + \frac{1}{2} (\psi_x^* \eta_x - \eta_x^* \psi_x)]}. \quad (6.8)$$

The instantaneous (equal-time) effective action is defined by the Legendre transform

$$\Gamma_t[\Psi, \Psi^*] = -\log Z_t[J(\Psi, \Psi^*), J^*(\Psi, \Psi^*)] + \int_x [J_x^*(\Psi, \Psi^*) \Psi_x + \Psi_x^* J_x(\Psi, \Psi^*)]. \quad (6.9)$$

It generates the 1PI correlation functions as discussed in chapter 5.

6.C.2 Evolution equation

Given a Hamiltonian \hat{H} , the von-Neumann equation,

$$i\partial_t \hat{\rho}_t = [\hat{H}, \hat{\rho}_t], \quad (6.10)$$

dictates the quantum dynamics. It translates to an evolution equation for the instantaneous effective action according to

$$i\partial_t \Gamma_t[\Psi, \Psi^*] = - \frac{i\partial_t Z_t[J, J^*]}{Z_t[J, J^*]} \Bigg|_{J=J(\Psi, \Psi^*), J^*=J^*(\Psi, \Psi^*)} \quad (6.11)$$

$$= - \frac{1}{Z_t[J, J^*]} \text{Tr} \left\{ \hat{\rho}_t \left[\hat{H}, e^{\int_x (J_x \hat{\psi}_x^\dagger + J_x^* \hat{\psi}_x)} \right] \right\} \Bigg|_{J=J(\Psi, \Psi^*), J^*=J^*(\Psi, \Psi^*)} . \quad (6.12)$$

We can evaluate the trace in terms of phase-space averages over W_t as follows. For a general operator \hat{O} , the expectation value w.r.t. $\hat{\rho}_t$ is given by

$$\text{Tr}[\hat{\rho}_t \hat{O}] = \int \mathcal{D}\psi \mathcal{D}\psi^* W_t[\psi, \psi^*] O_W[\psi, \psi^*] , \quad (6.13)$$

where O_W is the Weyl symbol corresponding to \hat{O} [208, 209]. The Weyl symbol of a product of two operators can be expressed as [208, 209]

$$\left(\hat{A} \hat{B} \right)_W = A_W e^{\frac{\Lambda}{2}} B_W = B_W e^{-\frac{\Lambda}{2}} A_W , \quad (6.14)$$

where we introduced the symplectic operator

$$\Lambda = \int_x \left(\frac{\overleftarrow{\delta}}{\delta\psi_x} \frac{\overrightarrow{\delta}}{\delta\psi_x^*} - \frac{\overleftarrow{\delta}}{\delta\psi_x^*} \frac{\overrightarrow{\delta}}{\delta\psi_x} \right) . \quad (6.15)$$

Therefore the trace in (6.11) becomes

$$\text{Tr} \left\{ \hat{\rho}_t \left[\hat{H}, e^{\int_x (J_x \hat{\psi}_x^\dagger + J_x^* \hat{\psi}_x)} \right] \right\} = 2 \int \mathcal{D}\psi \mathcal{D}\psi^* W_t H_W \sinh \left(\frac{\Lambda}{2} \right) e^{\int_x (J_x \psi_x^* + J_x^* \psi_x)} , \quad (6.16)$$

where H_W is the Weyl symbol of the Hamiltonian \hat{H} . Given an explicit form of H_W , it is straightforward to calculate the right-hand side. Plugging the result back into (6.11), the sources are evaluated at

$$J_x = J_x(\Psi, \Psi^*) = \frac{\delta \Gamma_t[\Psi, \Psi^*]}{\delta \Psi_x} . \quad (6.17)$$

Then, by construction of the effective action, the resulting expression involves symmetrically ordered equal-time correlation functions which have to be expressed in terms of 1PI correlators. Since the latter are generated by Γ_t , this procedure yields a closed evolution equation.

6.C.3 Evolution of the Bose gas

As an explicit example, relevant for the experiment discussed in this chapter, we consider a non-relativistic Bose gas described by the quantum many-body Hamiltonian

$$\hat{H} = \int_x \left[\frac{1}{2m} \left(\nabla_x \hat{\psi}_x^\dagger \right) \left(\nabla_x \hat{\psi}_x \right) + \frac{g}{2} \hat{\psi}_x^\dagger \hat{\psi}_x^\dagger \hat{\psi}_x \hat{\psi}_x - \mu \hat{\psi}_x^\dagger \hat{\psi}_x \right]. \quad (6.18)$$

Here, m , g and μ denote the mass, interaction constant and chemical potential, respectively. Direct computation yields the Weyl symbol

$$H_W = \int_x \left[\frac{|\nabla_x \psi_x|^2}{2m} - (\mu + g\delta(0)) |\psi_x|^2 + \frac{g}{2} |\psi_x|^4 + \frac{g}{4} \delta^2(0) \right], \quad (6.19)$$

where $\delta(0) = [\hat{\psi}_x, \hat{\psi}_x^\dagger]$ arises from the commutation relations. The last term is a constant and does not affect the evolution. The remaining term involving $\delta(0)$ can be removed by adding the constant² term $g\delta(0) \int_x \hat{\psi}_x^\dagger \hat{\psi}_x$ to the Hamiltonian, which renormalizes the chemical potential.

Since H_W involves at most four powers of fields, only the first two terms of $2 \sinh(\Lambda/2) = \Lambda + \Lambda^3/4! + \dots$ contribute to (6.16). Explicitly, the quadratic terms contribute as

$$\int_x \psi_x^* \psi_x 2 \sinh\left(\frac{\Lambda}{2}\right) e^{\int_y (J_y \psi_y^* + J_y^* \psi_y)} = \int_x (\psi_x^* J_x - J_x^* \psi_x) e^{\int_y (J_y \psi_y^* + J_y^* \psi_y)} \quad (6.20)$$

and the quartic term gives

$$\begin{aligned} & \int_x \psi_x^* \psi_x^* \psi_x \psi_x 2 \sinh\left(\frac{\Lambda}{2}\right) e^{\int_y (J_y \psi_y^* + J_y^* \psi_y)} \\ &= \int_x \left[\psi_x^* \left(2\psi_x^* \psi_x - \frac{1}{2} J_x^* J_x \right) J_x - J_x^* \left(2\psi_x^* \psi_x - \frac{1}{2} J_x^* J_x \right) \psi_x \right] e^{\int_y (J_y \psi_y^* + J_y^* \psi_y)}. \end{aligned} \quad (6.21)$$

Taking the phase space average w.r.t. W_t and replacing the sources by derivatives, we find

$$i\partial_t \Gamma_t[\Psi, \Psi^*] = \mathcal{L}_{\text{cl}} \Gamma_t[\Psi, \Psi^*] + \mathcal{L}_{\text{q}}[\Gamma_t], \quad (6.22)$$

where the ‘‘classical’’ part \mathcal{L}_{cl} resp. ‘‘quantum’’ part \mathcal{L}_{q} are linear resp. nonlinear in derivatives,

$$\mathcal{L}_{\text{cl}} = \int_x \left\{ \left[\left(-\frac{\nabla_x^2}{2m} - \mu \right) \Psi_x + g G_{xxx}^{\psi^* \psi} \right] \frac{\delta}{\delta \Psi_x} - \left[\left(-\frac{\nabla_x^2}{2m} - \mu \right) \Psi_x^* + g G_{xxx}^{\psi \psi^*} \right] \frac{\delta}{\delta \Psi_x^*} \right\}, \quad (6.23a)$$

$$\mathcal{L}_{\text{q}} = \frac{g}{4} \int_x \left(\Psi_x^* \frac{\delta \Gamma_t}{\delta \Psi_x^*} \frac{\delta \Gamma_t}{\delta \Psi_x^*} \frac{\delta \Gamma_t}{\delta \Psi_x} - \Psi_x \frac{\delta \Gamma_t}{\delta \Psi_x} \frac{\delta \Gamma_t}{\delta \Psi_x} \frac{\delta \Gamma_t}{\delta \Psi_x^*} \right). \quad (6.23b)$$

²It is proportional to the total number of particles, which is conserved.

Here, the full three-point functions have to be expressed in terms of 1PI correlators,

$$G_{xxx}^{\psi^* \psi \psi} = G_{c,xxx}^{\psi^* \psi \psi} + 2G_{c,xx}^{\psi^* \psi} \Psi_x + G_{c,xx}^{\psi \psi} \Psi_x^* + \Psi_x^* \Psi_x \Psi_x, \quad (6.24a)$$

$$G_{xxx}^{\psi \psi^* \psi} = G_{c,xxx}^{\psi \psi^* \psi} + 2G_{c,xx}^{\psi \psi^*} \Psi_x^* + G_{c,xx}^{\psi^* \psi} \Psi_x + \Psi_x^* \Psi_x^* \Psi_x, \quad (6.24b)$$

with the connected two- and three-point functions given by

$$G_{c,xy}^{\alpha\beta} = \left[\left(\frac{\delta^2 \Gamma_t}{\delta \Psi \delta \Psi} \right)^{-1} \right]_{xy}^{\alpha\beta}, \quad (6.25a)$$

$$G_{c,xyz}^{\alpha\beta\gamma} = - \sum_{\alpha', \beta', \gamma'} \int_{x' y' z'} G_{c,xx'}^{\alpha\alpha'} G_{c,yy'}^{\beta\beta'} G_{c,zz'}^{\gamma\gamma'} \frac{\delta^3 \Gamma_t}{\delta \Psi_{x'}^{\alpha'} \delta \Psi_{y'}^{\beta'} \delta \Psi_{z'}^{\gamma'}}. \quad (6.25b)$$

6.C.4 Symmetric case

Since the Hamiltonian is $U(1)$ symmetric, an initially $U(1)$ symmetric state will remain so. For simplicity, we now focus on this symmetric phase, where all correlation functions are invariant under global $U(1)$ transformations. This symmetry simplifies the structure of the effective action,

$$\Gamma_t[\Psi, \Psi^*] = \bar{\Gamma}_t[|\Psi|^2], \quad (6.26)$$

where we denote $|\Psi|_{xy}^2 = \Psi_x^* \Psi_y$. With this assumption, the evolution equation reduces to

$$\begin{aligned} i\partial_t \bar{\Gamma}_t[|\Psi|^2] &= \int_{xy} \left[\frac{-\nabla_y^2 + \nabla_x^2}{2m} |\Psi|_{xy}^2 + g \left(G_{yyy}^{\psi^* \psi \psi} \Psi_x^* - G_{xxx}^{\psi \psi^* \psi} \Psi_y \right) \right] \frac{\delta \bar{\Gamma}_t}{\delta |\Psi|_{xy}^2} \\ &+ \frac{g}{4} \int_{xyzw} |\Psi|_{xy}^2 |\Psi|_{zw}^2 \left(\frac{\delta \bar{\Gamma}_t}{\delta |\Psi|_{zx}^2} \frac{\delta \bar{\Gamma}_t}{\delta |\Psi|_{xw}^2} - \frac{\delta \bar{\Gamma}_t}{\delta |\Psi|_{zy}^2} \frac{\delta \bar{\Gamma}_t}{\delta |\Psi|_{yw}^2} \right) \frac{\delta \bar{\Gamma}_t}{\delta |\Psi|_{xy}^2}. \end{aligned} \quad (6.27)$$

In order to obtain explicit expressions for the evolution equations of correlation functions, we need to express the terms involving $G^{(3)}$ with 1PI correlators. To reveal the dependence of these terms on $|\Psi|^2$, we first split the 1PI two-point function as $\Gamma^{(2)} = \bar{\Gamma}^{(2)} + \tilde{\Gamma}^{(2)}$ with

$$\Gamma_{xy}^{(2)} = \begin{pmatrix} \frac{\delta \bar{\Gamma}_t}{\delta \Psi_x \delta \Psi_y} & \frac{\delta \bar{\Gamma}_t}{\delta \Psi_x \delta \Psi_y^*} \\ \frac{\delta \bar{\Gamma}_t}{\delta \Psi_x^* \delta \Psi_y} & \frac{\delta \bar{\Gamma}_t}{\delta \Psi_x^* \delta \Psi_y^*} \end{pmatrix}, \quad (6.28a)$$

$$\bar{\Gamma}_{xy}^{(2)} = \begin{pmatrix} 0 & \frac{\delta \bar{\Gamma}_t}{\delta |\Psi|_{yx}^2} \\ \frac{\delta \bar{\Gamma}_t}{\delta |\Psi|_{xy}^2} & 0 \end{pmatrix}, \quad (6.28b)$$

$$\tilde{\Gamma}_{xy}^{(2)} = \int_{zw} \begin{pmatrix} \Psi_z^* \Psi_w^* \frac{\delta^2 \bar{\Gamma}_t}{\delta |\Psi|_{zx}^2 \delta |\Psi|_{wy}^2} & \Psi_z^* \Psi_w \frac{\delta^2 \bar{\Gamma}_t}{\delta |\Psi|_{zx}^2 \delta |\Psi|_{yw}^2} \\ \Psi_z \Psi_w^* \frac{\delta^2 \bar{\Gamma}_t}{\delta |\Psi|_{xz}^2 \delta |\Psi|_{wy}^2} & \Psi_z \Psi_w \frac{\delta^2 \bar{\Gamma}_t}{\delta |\Psi|_{xz}^2 \delta |\Psi|_{yw}^2} \end{pmatrix}. \quad (6.28c)$$

Analogously, we write the connected two-point function as $G_c^{(2)} = \bar{G}_c^{(2)} + \tilde{G}_c^{(2)}$ with $\bar{G}_c^{(2)} = (\bar{\Gamma}^{(2)})^{-1}$, which implies the geometric (Dyson-type) series

$$G_c^{(2)} = \bar{G}_c^{(2)} - \bar{G}_c^{(2)} \tilde{\Gamma}^{(2)} \bar{G}_c^{(2)} + \bar{G}_c^{(2)} \tilde{\Gamma}^{(2)} \bar{G}_c^{(2)} \tilde{\Gamma}^{(2)} \bar{G}_c^{(2)} \mp \dots \quad (6.29)$$

In the following, we will further restrict our attention to the 1PI two- and four-point functions,

$$\bar{\Gamma}_{xy} = \frac{\delta \Gamma_t}{\delta |\Psi|_{xy}^2} \Big|_{\Psi=\Psi^*=0} = \bar{\Gamma}_{xy}^{(2)} \Big|_{\Psi=\Psi^*=0}, \quad (6.30a)$$

$$\bar{\Gamma}_{xy,zw} = \frac{\delta^2 \Gamma_t}{\delta |\Psi|_{xy}^2 \delta |\Psi|_{zw}^2} \Big|_{\Psi=\Psi^*=0}. \quad (6.30b)$$

Since we need to take at most two $|\Psi|^2$ derivatives of equation (6.27), only the first two terms of the Dyson series contribute to the evolution of these correlators.

6.C.5 Evolution of the two-point and four-point functions

Explicitly, the two-point function evolves according to

$$i\partial_t \bar{\Gamma}_{xy} = \frac{-\nabla_y^2 + \nabla_x^2}{2m} \bar{\Gamma}_{xy} + g \int_{zw} \frac{\delta \left(G_{www}^{\psi^* \psi \psi} \Psi_z^* - G_{zzz}^{\psi^* \psi^* \psi} \Psi_w \right)}{\delta |\Psi|_{xy}^2} \Big|_{\Psi=\Psi^*=0} \bar{\Gamma}_{zw}. \quad (6.31)$$

The evolution equation for the four-point function reads

$$\begin{aligned} i\partial_t \bar{\Gamma}_{xy,zw} &= \frac{-\nabla_x^2 + \nabla_y^2 - \nabla_z^2 + \nabla_w^2}{2m} \bar{\Gamma}_{xy,zw} \\ &+ g \int_{ab} \frac{\delta \left(G_{bbb}^{\psi^* \psi \psi} \Psi_a^* - G_{aaa}^{\psi^* \psi^* \psi} \Psi_b \right)}{\delta |\Psi|_{xy}^2} \Big|_{\Psi=\Psi^*=0} \bar{\Gamma}_{ab,zw} + (xy \leftrightarrow zw) \\ &+ g \int_{ab} \frac{\delta^2 \left(G_{bbb}^{\psi^* \psi \psi} \Psi_a^* - G_{aaa}^{\psi^* \psi^* \psi} \Psi_b \right)}{\delta |\Psi|_{xy}^2 \delta |\Psi|_{zw}^2} \Big|_{\Psi=\Psi^*=0} \bar{\Gamma}_{ab} \\ &+ \frac{g}{4} [(\bar{\Gamma}_{zw} \bar{\Gamma}_{xw} - \bar{\Gamma}_{zy} \bar{\Gamma}_{yw}) \bar{\Gamma}_{xy} + (\bar{\Gamma}_{xz} \bar{\Gamma}_{zy} - \bar{\Gamma}_{xw} \bar{\Gamma}_{wy}) \bar{\Gamma}_{zw}], \quad (6.32) \end{aligned}$$

where $(xy \leftrightarrow zw)$ denotes the permutation of the expression in the same line with the indicated replacement. Evaluating the remaining derivatives is tedious, but straightforward. For future reference, we sketch how to perform this calculation.

Consider

$$\begin{aligned} \frac{\delta \left(G_{www}^{\psi^* \psi \psi} \Psi_z^* \right)}{\delta |\Psi|_{xy}^2} &= \frac{\delta \left(G_{c,www}^{\psi^* \psi \psi} \Psi_z^* \right)}{\delta |\Psi|_{xy}^2} + |\Psi|_{zw}^2 \frac{\delta G_{c,www}^{\psi^* \psi \psi}}{\delta |\Psi|_{xy}^2} + \frac{\delta \left(G_{c,w}^{\psi \psi} \Psi_w^* \Psi_z^* \right)}{\delta |\Psi|_{xy}^2} \\ &+ 2\delta_{xz} \delta_{yw} G_{c,www}^{\psi^* \psi \psi} + \delta_{xw} \delta_{yw} |\Psi|_{zw}^2 + \delta_{xz} \delta_{yw} |\Psi|_{wz}^2. \quad (6.33) \end{aligned}$$

Using the geometric series for the two-point functions, we obtain

$$\frac{\delta G_{c,ww}^{\psi^*\psi}}{\delta |\Psi|_{xy}^2} = \frac{\delta \bar{G}_{c,ww}^{\psi^*\psi}}{\delta |\Psi|_{xy}^2} - \int_{w'w''} \frac{\delta \left(\bar{G}_{c,ww'}^{\psi^*\psi} \tilde{\Gamma}_{w'w''}^{\psi^*\psi} \bar{G}_{c,ww'}^{\psi^*\psi} \right)}{\delta |\Psi|_{xy}^2} \pm \dots \quad (6.34)$$

The first term is given by

$$\frac{\delta \bar{G}_{c,ww}^{\psi^*\psi}}{\delta |\Psi|_{xy}^2} = - \int_{w'w''} \frac{\delta \bar{\Gamma}}{\delta |\Psi|_{ww'}^2} \frac{\delta^2 \bar{\Gamma}}{\delta |\Psi|_{w'w''}^2 \delta |\Psi|_{xy}^2} \frac{\delta \bar{\Gamma}}{\delta |\Psi|_{w''w}^2}, \quad (6.35)$$

and the second term does not contribute to the evolution of the two- and four-point functions. Similarly, we have

$$\frac{\delta \left(G_{c,ww}^{\psi\psi} \Psi_w^* \Psi_z^* \right)}{\delta |\Psi|_{xy}^2} = - \int_{w'w''} \frac{\delta \left(\bar{G}_{c,ww'}^{\psi\psi} \tilde{\Gamma}_{w'w''}^{\psi\psi} \bar{G}_{c,ww'}^{\psi\psi} \Psi_w^* \Psi_z^* \right)}{\delta |\Psi|_{xy}^2} \pm \dots \quad (6.36)$$

and only the leading term contributes as

$$\begin{aligned} & \frac{\delta \left(\bar{G}_{c,ww'}^{\psi\psi} \tilde{\Gamma}_{w'w''}^{\psi\psi} \bar{G}_{c,ww'}^{\psi\psi} \Psi_w^* \Psi_z^* \right)}{\delta |\Psi|_{xy}^2} \\ &= \int_{\tilde{w}'\tilde{w}''} \left[\left(\frac{\delta \bar{\Gamma}}{\delta |\Psi|^2} \right)^{-1} \right]_{w'w} \frac{\delta^2 \bar{\Gamma}}{\delta |\Psi|_{w'\tilde{w}'}^2 \delta |\Psi|_{w''\tilde{w}''}^2} \left[\left(\frac{\delta \bar{\Gamma}}{\delta |\Psi|^2} \right)^{-1} \right]_{w''w} \\ & \quad \times \left(\delta_{xz} \delta_{y\tilde{w}''} |\Psi|_{w\tilde{w}'}^2 + \delta_{xw} \delta_{y\tilde{w}'} |\Psi|_{z\tilde{w}''}^2 \right) + \dots, \end{aligned} \quad (6.37)$$

where we have not written out terms involving higher powers of $|\Psi|^2$. The connected three-point function contributes

$$\frac{\delta \left(G_{c,ww}^{\psi^*\psi} \Psi_z^* \right)}{\delta |\Psi|_{xy}^2} = - \sum_{\alpha,\beta,\gamma} \int_{w'w''w'''} \frac{\delta}{\delta |\Psi|_{xy}^2} \left\{ G_{c,ww'}^{\psi^*\alpha} G_{c,ww''}^{\psi\beta} G_{c,ww'''}^{\psi\gamma} \frac{\delta^3 \bar{\Gamma}_t}{\delta \Psi_w^\alpha \delta \Psi_{w''}^\beta \delta \Psi_{w'''}^\gamma} \Psi_z^* \right\}. \quad (6.38)$$

Again, we do not need the full expression, but just the terms up to $|\Psi|^2$. The leading term in the series of the “diagonal” two-point functions $G_c^{\psi\psi}$ and $G_c^{\psi^*\psi^*}$ involves two powers of the fields Ψ or Ψ^* . The same is true for the third derivative of $\bar{\Gamma}_t$ times one field Ψ . Thus only the following four (out of the total eight) terms of the

sum can contribute,

$$(1) = G_{c,ww'}^{*\psi\psi} G_{c,ww''}^{*\psi\psi} G_{c,ww'''}^{*\psi\psi} \frac{\delta^3 \bar{\Gamma}_t}{\delta \Psi_{w'} \delta \Psi_{w''}^* \delta \Psi_{w'''}^*} \Psi_z^*, \quad (6.39a)$$

$$(2) = G_{c,ww'}^{*\psi\psi} G_{c,ww''}^{*\psi\psi} G_{c,ww'''}^{*\psi\psi} \frac{\delta^3 \bar{\Gamma}_t}{\delta \Psi_{w'}^* \delta \Psi_{w''}^* \delta \Psi_{w'''}^*} \Psi_z^*, \quad (6.39b)$$

$$(3) = G_{c,ww'}^{*\psi\psi} G_{c,ww''}^{*\psi\psi} G_{c,ww'''}^{*\psi\psi} \frac{\delta^3 \bar{\Gamma}_t}{\delta \Psi_{w'} \delta \Psi_{w''} \delta \Psi_{w'''}^*} \Psi_z^*, \quad (6.39c)$$

$$(4) = G_{c,ww'}^{*\psi\psi} G_{c,ww''}^{*\psi\psi} G_{c,ww'''}^{*\psi\psi} \frac{\delta^3 \bar{\Gamma}_t}{\delta \Psi_{w'} \delta \Psi_{w''}^* \delta \Psi_{w'''}^*} \Psi_z^*. \quad (6.39d)$$

For example, the term (1) involves the third-order derivative

$$\begin{aligned} \frac{\delta^3 \bar{\Gamma}_t}{\delta \Psi_{w'} \delta \Psi_{w''}^* \delta \Psi_{w'''}^*} \Psi_z^* &= \int_{\tilde{w}'' \tilde{w}'''} \left[(|\Psi|_{z\tilde{w}''}^2 \delta_{\tilde{w}'' w'} + |\Psi|_{z\tilde{w}'''}^2 \delta_{\tilde{w}''' w'}) \frac{\delta^2 \bar{\Gamma}_t}{\delta |\Psi|_{w'''}^2 \delta |\Psi|_{w'' \tilde{w}'}^2} \right. \\ &\quad \left. + |\Psi|_{z\tilde{w}'}^2 |\Psi|_{\tilde{w}''}^2 \frac{\delta^3 \bar{\Gamma}_t}{\delta |\Psi|_{w'''}^2 \delta |\Psi|_{w'' \tilde{w}'}^2 \delta |\Psi|_{w' \tilde{w}''}^2} \right]. \quad (6.40) \end{aligned}$$

Collecting all relevant terms, the evolution equation of the 1PI two-point function reads

$$\begin{aligned} i\partial_t \bar{\Gamma}_{xy} &= \left[\frac{-\nabla_y^2 + \nabla_x^2}{2m} + 2g (\bar{\Gamma}_{yy}^{-1} - \bar{\Gamma}_{xx}^{-1}) \right] \bar{\Gamma}_{xy} \\ &\quad + 2g \int_{zabc} \bar{\Gamma}_{za}^{-1} \bar{\Gamma}_{bz}^{-1} (\bar{\Gamma}_{zc}^{-1} \bar{\Gamma}_{cy,ab} \bar{\Gamma}_{xz} - \bar{\Gamma}_{cz}^{-1} \bar{\Gamma}_{xc,ab} \bar{\Gamma}_{zy}) , \quad (6.41) \end{aligned}$$

where we denote the inverse of $\bar{\Gamma}_{xy}$ as $\bar{\Gamma}_{xy}^{-1}$. We emphasize that this equation holds exactly (assuming only $U(1)$ invariance). Given the 1PI four-point function $\bar{\Gamma}_{xy,zw}$, it determines the real-time evolution of $\bar{\Gamma}_{xy}$.

The evaluation of the terms for the evolution equation of the four-point function proceeds analogously. For brevity, we just state a part of the full result,

$$\begin{aligned} i\partial_t \bar{\Gamma}_{xy,zw} &= \left[\frac{-\nabla_y^2 + \nabla_x^2 - \nabla_z^2 + \nabla_w^2}{2m} + 2g (\bar{\Gamma}_{yy}^{-1} - \bar{\Gamma}_{xx}^{-1} + \bar{\Gamma}_{ww}^{-1} - \bar{\Gamma}_{zz}^{-1}) \right] \bar{\Gamma}_{xy,zw} \\ &\quad + g [\delta_{xy} \delta_{xw} \bar{\Gamma}_{zx} + \delta_{zy} \delta_{zw} \bar{\Gamma}_{xz} - \delta_{yx} \delta_{yz} \bar{\Gamma}_{yw} - \delta_{wx} \delta_{wz} \bar{\Gamma}_{wy}] \\ &\quad + \frac{g}{4} [(\bar{\Gamma}_{zw} \bar{\Gamma}_{xw} - \bar{\Gamma}_{zy} \bar{\Gamma}_{yw}) \bar{\Gamma}_{xy} + (\bar{\Gamma}_{xz} \bar{\Gamma}_{zy} - \bar{\Gamma}_{xw} \bar{\Gamma}_{wy}) \bar{\Gamma}_{zw}] \\ &\quad + \dots \quad (6.42) \end{aligned}$$

The dots indicate several terms that we omitted. They are all proportional to the coupling g and involve at least one power of $\bar{\Gamma}_{xy,zw}$ or they depend on the 1PI six-point function $\bar{\Gamma}_{xy,zw,uv}$. Neglecting the six-point function closes the set of coupled evolution equations. If we further assume that the four-point function is of order g , then the omitted terms above do not contribute to leading order in g . In the remainder of this section, we will demonstrate analytically that this perturbative truncation can be reduced to a standard kinetic description. We plan to solve the full

system (neglecting only, e.g., the six-point function) numerically in a future work.

6.C.6 Definition of the particle number distribution

Out of equilibrium, the concept of a particle is not uniquely defined. For a physical interpretation, it is nevertheless useful to define a particle number distribution. In the following we assume spatial translation invariance and then define the number density f_p according to

$$f_p + \frac{1}{2} = \int_{x-y} e^{-ip(x-y)} \frac{1}{2} \text{Tr} \left[\hat{\rho}_t \left(\hat{\psi}_x^\dagger \hat{\psi}_y + \hat{\psi}_y \hat{\psi}_x^\dagger \right) \right]. \quad (6.43)$$

To motivate that this definition makes sense, we consider $\hat{\rho}_t = |\Omega_t\rangle\langle\Omega_t|$ with a $U(1)$ symmetric pure and spatially translation invariant state $|\Omega_t\rangle$. In this case, equation (6.43) becomes

$$f_p = \frac{1}{V} \langle \Omega_t | \hat{\psi}_p^\dagger \hat{\psi}_p | \Omega_t \rangle \quad (6.44)$$

with the momentum space operators

$$\hat{\psi}_p = \int_x e^{-ipx} \hat{\psi}_x, \quad \hat{\psi}_p^\dagger = \int_x e^{ipx} \hat{\psi}_x^\dagger \quad (6.45)$$

that fulfill $[\hat{\psi}_p, \hat{\psi}_q^\dagger] = (2\pi)^d \delta(p-q)$, resulting in the volume factor $V = (2\pi)^d \delta(0)$. In the non-interacting case f_p therefore coincides with the usual definition. In the interacting case the definition remains sensible because

$$f_p \geq 0. \quad (6.46)$$

This follows from the Cauchy-Schwartz inequality

$$\langle u|u\rangle\langle v|v\rangle \geq |\langle u|v\rangle|^2 \Rightarrow f_p(f_p + 1) \geq 0 \quad (6.47)$$

with $|u\rangle = \hat{\psi}_p|\Omega_t\rangle$ and $|v\rangle = \hat{\psi}_p^\dagger|\Omega_t\rangle$, where we used the commutation relations and $U(1)$ invariance.

The definition (6.43) is equivalent to

$$f_p + \frac{1}{2} = \int_{x-y} e^{-ip(x-y)} \bar{\Gamma}_{yx}^{-1} = \bar{\Gamma}_{-p}^{-1}, \quad f_{-p} + \frac{1}{2} = \int_{x-y} e^{-ip(x-y)} \bar{\Gamma}_{xy}^{-1} = \bar{\Gamma}_p^{-1}, \quad (6.48)$$

such that the equation (6.41) becomes an exact Boltzmann-type evolution equation,

$$\partial_t f_p = C_p[f, \Gamma^{(4)}]. \quad (6.49)$$

Here the ‘‘collision integral’’ $C_p[f, \Gamma^{(4)}]$ explicitly depends on the two-point functions (or according to (6.48) equivalently on f) and on the 1PI four-vertices as

$$C_p[f, \Gamma^{(4)}] = -ig \int_{qrl} \left(f_p + \frac{1}{2}\right) \left(f_q + \frac{1}{2}\right) \left(f_r + \frac{1}{2}\right) \left(f_l + \frac{1}{2}\right) \times \left[\Gamma_{l,r,-q,-p}^{\psi\psi\psi^*\psi^*} - \Gamma_{p,q,-r,-l}^{\psi\psi\psi^*\psi^*} \right], \quad (6.50)$$

where we relabeled the 1PI four-vertex in accordance with the presentation in section 6.3,

$$\Gamma_{l,r,-q,-p}^{\psi\psi\psi^*\psi^*} = \frac{\delta^4 \bar{\Gamma}_t}{\delta \Psi_l \delta \Psi_r \delta \Psi_{-q}^* \delta \Psi_{-p}^*} \Big|_{\Psi=\Psi^*=0} = \int_{xyzw} e^{-i(l y - r w - q x - p z)} \frac{\bar{\Gamma}_{xy,zw}}{2}. \quad (6.51)$$

Of course the Boltzmann-type equation (6.49) can be obtained with much less effort, e.g., by directly calculating the Heisenberg equations of motion for the product of two field operators, taking the average w.r.t. the density operator and expressing the appearing four-point functions in terms of 1PI correlators. The advantage of the approach presented here is that it generates equations for the full hierarchy of 1PI correlators. We use this to discuss the evolution of the 1PI four-vertex next.

6.C.7 Perturbative four-vertex and Boltzmann equation

To leading order in g , the evolution of the four-vertex [Eq. (6.42)] can be written in momentum space as

$$i\partial_t \Gamma_{pqrl}^{\psi\psi\psi^*\psi^*} = -\Delta\omega_{pqrl} \Gamma_{pqrl}^{\psi\psi\psi^*\psi^*} - \frac{g}{2} \delta(p+q+r+l) \bar{g}_{pqrl} \quad (6.52)$$

with $\Delta\omega_{pqrl} = (p^2 + q^2 - r^2 - l^2)/(2m)$ and the abbreviation

$$\bar{g}_{pqrl}[f] = 4(\bar{\Gamma}_p + \bar{\Gamma}_q - \bar{\Gamma}_{-r} - \bar{\Gamma}_{-l}) - \bar{\Gamma}_p \bar{\Gamma}_q (\bar{\Gamma}_{-r} + \bar{\Gamma}_{-l}) + \bar{\Gamma}_{-r} \bar{\Gamma}_{-l} (\bar{\Gamma}_p + \bar{\Gamma}_q). \quad (6.53)$$

The general solution of (6.52) with initial condition $\Gamma_{pqrl}^{\psi\psi\psi^*\psi^*}(t_0)$ is given by

$$\Gamma_{pqrl}^{\psi\psi\psi^*\psi^*}(t) = \Gamma_{pqrl}^{\psi\psi\psi^*\psi^*}(t_0) e^{i\Delta\omega_{pqrl}(t-t_0)} + \frac{ig}{2} \delta(p+q+r+l) \int_{t_0}^t d\tau e^{-i\Delta\omega_{pqrl}(\tau-t)} \bar{g}_{pqrl}[f](\tau). \quad (6.54)$$

Without the initial condition (for, e.g., a Gaussian initial state) the contribution to the collision integral (6.50) becomes

$$\begin{aligned}
\Gamma_{l,r,-q,-p}^{\psi\psi\psi^*\psi^*} - \Gamma_{p,q,-r,-l}^{\psi\psi\psi^*\psi^*} &= 2ig \delta(p+q-r-l) \int_{t_0}^t d\tau \cos[\Delta\omega_{pqrl}(\tau-t)] \bar{g}_{p,q,-r,-l}[f](\tau) \\
&\approx 2ig \delta(p+q-r-l) \bar{g}_{p,q,-r,-l}[f](t) \int_{t_0}^t d\tau \cos[\Delta\omega_{pqrl}(\tau-t)] , \\
&= 2ig \delta(p+q-r-l) \bar{g}_{p,q,-r,-l}[f](t) \frac{\sin[\Delta\omega_{pqrl}(t-t_0)]}{\Delta\omega_{pqrl}(\tau-t)} \\
&\rightarrow 2ig\delta(p+q-r-l) \pi\delta(\Delta\omega_{pqrl}) \bar{g}_{p,q,-r,-l}[f](t) , \tag{6.55}
\end{aligned}$$

where the approximation of the second line holds for slowly varying f and we have taken the limit of late times ($t-t_0 \rightarrow \infty$) in the last line. Inserting this result into (6.50) gives

$$C_p[f] \approx \frac{g^2}{2} \int_{qrl} d\Omega_{pqrl} \left(f_p + \frac{1}{2}\right) \left(f_q + \frac{1}{2}\right) \left(f_r + \frac{1}{2}\right) \left(f_l + \frac{1}{2}\right) \bar{g}_{p,q,-r,-l}[f] \tag{6.56}$$

with the integration constrained by momentum and energy conservation,

$$\int_{qrl} d\Omega_{pqrl} = \int \frac{d^d q}{(2\pi)^d} \frac{d^d r}{(2\pi)^d} \frac{d^d l}{(2\pi)^d} (2\pi)^d \delta^{(d)}(p+q-r-l) (2\pi) \delta(\Delta\omega_{pqrl}) . \tag{6.57}$$

Rewriting the integrand in terms of the distribution f ,

$$\begin{aligned}
&\left(f_p + \frac{1}{2}\right) \left(f_q + \frac{1}{2}\right) \left(f_r + \frac{1}{2}\right) \left(f_l + \frac{1}{2}\right) \bar{g}_{p,q,-r,-l}[f] \\
&= 4[(f_p+1)(f_q+1)f_r f_l - (f_r+1)(f_l+1)f_p f_q] , \tag{6.58}
\end{aligned}$$

we finally arrive at the standard perturbative Boltzmann equation (see, e.g., [234])

$$\partial_t f_p \approx 2g^2 \int_{qrl} d\Omega_{pqrl} [(f_p+1)(f_q+1)f_r f_l - (f_r+1)(f_l+1)f_p f_q] . \tag{6.59}$$

In the approach presented here, the Boltzmann equation relies on several assumptions. It is valid in the spatially translation invariant and $U(1)$ symmetric case. Additionally, we solved the evolution of the 1PI four-vertex by neglecting the effect all 1PI correlators of order six or higher, assuming Gaussian initial conditions and a perturbative expansion in the coupling. Finally, we approximated the resulting integral for a slowly evolving two-point function at sufficiently late times.

Chapter 7

Conclusion

The work presented in this thesis includes several results relevant for the quantum simulation of high-energy physics. In this chapter, we briefly discuss the relevance of the different results before closing with an outlook on possible future research directions.

7.1 Discussion

Our proposal to implement a quantum simulation of QED in one spatial dimension with Wilson fermions (chapter 2) illustrates the importance of taking into account equivalent formulations of the same physics for finding experimentally feasible schemes. Here we exploited the possibility to choose different representations of the Clifford algebra together with the fundamental non-uniqueness of discretizing Dirac fermions. From a more general point of view, it is sufficient to realize an experimental system that has the right continuum limit. In principle this opens up the possibility to consider a multitude of different Hamiltonians, only constrained by relevant couplings (in the sense of the renormalization group), which share the same universal properties.

In a similar spirit, it is only necessary to retain the mathematical equivalence between the target system of the quantum simulation and the experimental platform. By giving up the direct correspondence between the lattice sites of the simulated gauge theory and the lattice wells of the trapped quantum gas, we have also exploited this fact (chapter 3). Our improved proposal combines these advances and can be scaled to large system sizes by connecting elementary gauge-invariant building blocks. Together with the experimental demonstration of the building block, this moved the quantum simulation of continuous $U(1)$ gauge theories in one spatial dimension within immediate reach.

Motivated by the prospect of an experimental realization of QED, we identified dynamical topological transitions (chapter 4) as an ideal target phenomenon for a quantum simulation. Here we take into account experimental imperfections since this physical phenomenon is robustly accessible within relatively short time-scales and small lattice sizes. In this context, we also re-interpreted the physics of DQPTs in terms of correlation functions, which allowed us to obtain a dynamical topological order parameter that remains well-defined in the interacting theory.

Since correlation functions completely determine any quantum field theory, a correlator-based description of quantum simulators is highly desirable for the simulation of high-energy physics. We presented such a formulation based on equal-time correlation functions (chapter 5), which allows for the extraction of irreducible vertices directly from experimental data. We verified this novel approach to analyze quantum simulators for the example of the sine-Gordon model in thermal equilibrium, both numerically and in a proof-of-principle experiment.

The application of this approach to the dynamics of a strongly correlated Bose gas (chapter 6) shed some new light on the interaction vertices in a far-from-equilibrium regime associated to a non-thermal fixed point. In this way, the analysis in terms of the instantaneous effective action can provide new input for developing effective models for situations that have otherwise eluded an efficient description.

7.2 Outlook

While our results significantly advance the quantum simulation of high-energy physics – specifically the simulation of $U(1)$ LGTs and the analysis of quantum simulators from a QFT perspective – many important questions remain to be tackled in the future.

One of the most pressing tasks is the extension of LGT implementations to spatial dimensions larger than one, where qualitatively different phenomena emerge. The drastic simplification of our approach based on Wilson fermions is unique to one spatial dimension. However, by relaxing the requirement to recover Lorentz covariance in the continuum limit and by allowing, e.g., for bosonic matter, an extension of the matter-gauge coupling to higher dimensions appears to be feasible.

The implementation of non-abelian theories, which has not been addressed within this thesis, is of equal importance. Since the formulation of non-abelian gauge invariance differs significantly from the abelian case, we believe that this step requires a careful re-examination of the available mathematically equivalent descriptions [56, 236, 237]. For the $U(1)$ case, it was the combination [18] of a suitable formulation, together with the atomic symmetry underlying SCCs that allowed for an efficient scalable implementation. We expect a similar approach to be successful in the case of non-abelian gauge groups, such as $SU(N)$. Promising examples are the combination of a quantum link formulation with the approximate $SU(N)$ symmetry present in alkaline-earth atoms [23], and dual formulations of LGTs combined with atomic constraints arising in Rydberg systems [30].

For both higher dimensions and non-abelian theories, it is conceivable that the dynamical topological transitions discovered in this work persist. Moreover, it is straightforward to apply the dynamical topological order parameter introduced here to these situations and other models as well. It will be exciting to study this possibility, for instance in QED in two spatial dimensions [32] and related condensed matter models, arising in the context of topological insulators [238], in the future.

The demonstrated equal-time formulation of QFT offers unique complementary perspectives. It provides an equivalent, but yet unexplored description of thermal field theory that requires further development. If successful, this approach might provide an alternative picture for thermal phase transitions and critical phenomena. With the directly experimentally accessible 1PI vertices, this possibility becomes particularly appealing in the vicinity of a quantum critical point, which could lead to new experimental signatures of the quantum critical region in terms of renormalization effects.

Out of equilibrium, extracting the instantaneous effective action can provide previously unavailable information of the physics emerging in the real-time dynamics of quantum fields. To elevate this method from diagnostics to a theoretical tool with predictive power, it is crucial to develop controlled approximation schemes. Although this has not been achieved yet [239], the fact that it is possible to recover perturbative kinetic descriptions gives hope that this endeavor is not in vain. A starting point can be non-thermal fixed points [234], which simplify the dynamics due to self-similarity. If possible, an approximate numerical solution of the evolution of the instantaneous effective action, which is local in time and scales only polynomially with increasing order of the employed correlation functions, could even shed new light on the late-time dynamics of quantum fields and the eventual thermalization [240].

Finally, we plan to apply the equal-time formulation also to LGTs. To this end, it is necessary to extend the formalism from scalars to fermions [241], spins and gauge fields [242]. Since the instantaneous effective action captures the same information as the density matrix, it is in principle possible to study intriguing quantum effects such as entanglement in real-time dynamics in terms of 1PI correlation functions. Moreover, it is possible to translate unitary transformations, in particular those corresponding to symmetries, to the correlators. Concerning gauge invariance, this translation will yield a set of constraints among the correlators, similar to Ward identities [50], which in turn may provide the means to test gauge invariance experimentally. In this way, analyzing quantum simulators of LGTs with QFT methods may facilitate the controlled quantum simulation of the non-equilibrium dynamics of gauge theories.

Declaration of authorship and publications

I, Torsten Victor ZACHE, declare that this thesis titled, “*Quantum simulation of high-energy physics with ultracold atoms*” and the work presented in it are my own. I confirm that:

- Where any part of this thesis has previously been submitted for a degree or any other qualification at this University or any other institution, this has been clearly stated.
- Where I have consulted the published work of others, this is always clearly attributed.
- Where I have quoted from the work of others, the source is always given. With the exception of such quotations, this thesis is entirely my own work.
- Parts of this dissertation have been published in the following articles:
 1. Zache, T. V., Hebenstreit, F., Jendrzejewski, F., Oberthaler, M. K., Berges, J., and Hauke, P., “Quantum simulation of lattice gauge theories using Wilson fermions”, *Quantum Science and Technology* **3**, 034010 (2018)
 2. Mil, A., Zache, T. V., Hegde, A., Xia, A., Bhatt, R. P., Oberthaler, M. K., Hauke, P., Berges, J., and Jendrzejewski, F., “A scalable realization of local U(1) gauge invariance in cold atomic mixtures”, *Science* **367**, 1128–1130 (2020)
 3. Zache, T. V., Mueller, N., Schneider, J. T., Jendrzejewski, F., Berges, J., and Hauke, P., “Dynamical Topological Transitions in the Massive Schwinger Model with a θ Term”, *Physical Review Letters* **122**, 50403 (2019)
 4. Zache, T. V., Schweigler, T., Erne, S., Schmiedmayer, J., and Berges, J., “Extracting the Field Theory Description of a Quantum Many-Body System from Experimental Data”, *Physical Review X* **10**, 11020 (2020)
 5. Prüfer, M., Zache, T. V., Kunkel, P., Lannig, S., Bonnín, A., Strobel, H., Berges, J., and Oberthaler, M. K., “Experimental extraction of the quantum effective action for a non-equilibrium many-body system”, arXiv:1909.05120 (2019)
- During my doctoral studies I was involved in the following publications that are not part of this dissertation:
 6. Zache, T. V., Kasper, V., and Berges, J., “Inflationary preheating dynamics with two-species condensates”, *Physical Review A* **95**, 063629 (2017)
 7. Ott, R., Zache, T. V., Mueller, N., and Berges, J., “Non-cancellation of the parity anomaly in the strong-field regime of QED₂₊₁”, arXiv:1903.11109 (2019)
 8. Yang, B., Sun, H., Ott, R., Wang, H.-Y., Zache, T. V., Halimeh, J. C., Yuan, Z.-S., Hauke, P., and Pan, J.-W., “Observation of gauge invariance in a 71-site quantum simulator”, arXiv:2003.08945 (2020)

Signed:

Date:

Bibliography

- ¹Feynman, R. P., “Simulating physics with computers”, *International Journal of Theoretical Physics* **21**, 467–488 (1982).
- ²Manin, Y., “Computable and Uncomputable (in Russian)”, *Sovetskoye Radio Press, Moscow* **128** (1980).
- ³Cirac, J. I. and Zoller, P., “Goals and opportunities in quantum simulation”, *Nature Physics* **8**, 264–266 (2012).
- ⁴Georgescu, I. M., Ashhab, S., and Nori, F., “Quantum simulation”, *Reviews of Modern Physics* **86**, 153–185 (2014).
- ⁵Jaksch, D., Bruder, C., Cirac, J. I., Gardiner, C. W., and Zoller, P., “Cold Bosonic Atoms in Optical Lattices”, *Physical Review Letters* **81**, 3108–3111 (1998).
- ⁶Greiner, M., Mandel, O., Esslinger, T., Hänsch, T. W., and Bloch, I., “Quantum phase transition from a superfluid to a Mott insulator in a gas of ultracold atoms”, *Nature* **415**, 39–44 (2002).
- ⁷Wiese, U.-J. U. J., “Ultracold quantum gases and lattice systems: Quantum simulation of lattice gauge theories”, *Annalen der Physik* **525**, 777–796 (2013).
- ⁸Zohar, E., Cirac, J. I., and Reznik, B., “Quantum simulations of lattice gauge theories using ultracold atoms in optical lattices”, *Reports on Progress in Physics* **79**, 14401 (2015).
- ⁹Bañuls, M. C., Blatt, R., Catani, J., Celi, A., Cirac, J. I., Dalmonte, M., Fallani, L., Jansen, K., Lewenstein, M., Montangero, S., Muschik, C. A., Reznik, B., Rico, E., Tagliacozzo, L., Van Acoleyen, K., Verstraete, F., Wiese, U. J., Wingate, M., Zakrzewski, J., and Zoller, P., “Simulating Lattice Gauge Theories within Quantum Technologies”, arXiv:1911.00003 (2019).
- ¹⁰Kasper, V., Hebenstreit, F., Oberthaler, M., and Berges, J., “Schwinger pair production with ultracold atoms”, *Physics Letters B* **760**, 742–746 (2016).
- ¹¹Banerjee, D., Dalmonte, M., Müller, M., Rico, E., Stebler, P., Wiese, U.-J. J., and Zoller, P., “Atomic Quantum Simulation of Dynamical Gauge Fields Coupled to Fermionic Matter: From String Breaking to Evolution after a Quench”, *Physical Review Letters* **109**, 175302 (2012).
- ¹²Preskill, J., “Quantum Computing in the NISQ era and beyond”, *Quantum* **2**, 79 (2018).

- ¹³Martinez, E. A., Muschik, C. A., Schindler, P., Nigg, D., Erhard, A., Heyl, M., Hauke, P., Dalmonte, M., Monz, T., Zoller, P., Blatt, R., and Others, “Real-time dynamics of lattice gauge theories with a few-qubit quantum computer”, *Nature* **534**, 516–519 (2016).
- ¹⁴Klco, N., Dumitrescu, E. F., McCaskey, A. J., Morris, T. D., Pooser, R. C., Sanz, M., Solano, E., Lougovski, P., and Savage, M. J., “Quantum-classical computation of Schwinger model dynamics using quantum computers”, *Physical Review A* **98**, 032331 (2018).
- ¹⁵Schweizer, C., Grusdt, F., Berngruber, M., Barbiero, L., Demler, E., Goldman, N., Bloch, I., and Aidelsburger, M., “Floquet approach to Z₂ lattice gauge theories with ultracold atoms in optical lattices”, *Nature Physics* **15**, 1168–1173 (2019).
- ¹⁶Mil, A., Zache, T. V., Hegde, A., Xia, A., Bhatt, R. P., Oberthaler, M. K., Hauke, P., Berges, J., and Jendrzejewski, F., “A scalable realization of local U(1) gauge invariance in cold atomic mixtures”, *Science* **367**, 1128–1130 (2020).
- ¹⁷Wiese, U. J., “Towards quantum simulating QCD”, *Nuclear Physics A* **931**, 246–256 (2014).
- ¹⁸Zohar, E., Cirac, J. I., and Reznik, B., “Quantum simulations of gauge theories with ultracold atoms: Local gauge invariance from angular-momentum conservation”, *Physical Review A* **88**, 023617 (2013).
- ¹⁹Zohar, E., Cirac, J. I., and Reznik, B., “Cold-atom quantum simulator for SU(2) yang-mills lattice gauge theory”, *Physical Review Letters* **110**, 125304 (2013).
- ²⁰Zohar, E., Cirac, J. I., and Reznik, B., “Simulating (2+1)-dimensional lattice QED with dynamical matter using ultracold atoms”, *Physical Review Letters* **110**, 55302 (2013).
- ²¹Marcos, D., Rabl, P., Rico, E., and Zoller, P., “Superconducting circuits for quantum simulation of dynamical gauge fields”, *Physical Review Letters* **111**, 110504 (2013).
- ²²Stannigel, K., Hauke, P., Marcos, D., Hafezi, M., Diehl, S., Dalmonte, M., and Zoller, P., “Constrained dynamics via the zeno effect in quantum simulation: Implementing non-abelian lattice gauge theories with cold atoms”, *Physical Review Letters* **112**, 120406 (2013).
- ²³Banerjee, D., Bögli, M., Dalmonte, M., Rico, E., Stebler, P., Wiese, U. J., and Zoller, P., “Atomic quantum simulation of U(N) and SU(N) Non-abelian lattice gauge theories”, *Physical Review Letters* **110**, 125303 (2013).
- ²⁴Rico, E., Dalmonte, M., Zoller, P., Banerjee, D., Bögli, M., Stebler, P., and Wiese, U. J., “SO(3) ‘Nuclear Physics’ with ultracold Gases”, *Annals of Physics* **393**, 466–483 (2018).
- ²⁵Surace, F. M., Mazza, P. P., Giudici, G., Lerose, A., Gambassi, A., and Dalmonte, M., “Lattice gauge theories and string dynamics in Rydberg atom quantum simulators”, arXiv:1902.09551 (2019).

- ²⁶Dalmonte, M. and Montangero, S., “Lattice gauge theory simulations in the quantum information era”, *Contemporary Physics* **57**, 388–412 (2016).
- ²⁷Yang, D., Giri, G. S., Johanning, M., Wunderlich, C., Zoller, P., and Hauke, P., “Analog quantum simulation of (1+1) -dimensional lattice QED with trapped ions”, *Physical Review A* **94**, 52321 (2016).
- ²⁸González-Cuadra, D., Zohar, E., and Cirac, J. I., “Quantum simulation of the Abelian-Higgs lattice gauge theory with ultracold atoms”, *New Journal of Physics* **19**, 063038 (2017).
- ²⁹Zache, T. V., Hebenstreit, F., Jendrzejewski, F., Oberthaler, M. K., Berges, J., and Hauke, P., “Quantum simulation of lattice gauge theories using Wilson fermions”, *Quantum Science and Technology* **3**, 034010 (2018).
- ³⁰Celi, A., Vermersch, B., Viyuela, O., Pichler, H., Lukin, M. D., and Zoller, P., “Emerging 2D Gauge theories in Rydberg configurable arrays”, arXiv:1907.03311 (2019).
- ³¹Berges, J., “Scaling up quantum simulations”, *Nature* **569**, 339–340 (2019).
- ³²Ott, R., Zache, T. V., Mueller, N., and Berges, J., “Non-cancellation of the parity anomaly in the strong-field regime of QED₂₊₁”, arXiv:1903.11109 (2019).
- ³³Zache, T. V., Mueller, N., Schneider, J. T., Jendrzejewski, F., Berges, J., and Hauke, P., “Dynamical Topological Transitions in the Massive Schwinger Model with a θ Term”, *Physical Review Letters* **122**, 50403 (2019).
- ³⁴Hauke, P., Cucchietti, F. M., Tagliacozzo, L., Deutsch, I., and Lewenstein, M., “Can one trust quantum simulators?”, *Reports on Progress in Physics* **75**, 82401 (2012).
- ³⁵Kokail, C., Maier, C., Bijnen, R. van, Brydges, T., Joshi, M. K., Jurcevic, P., Muschik, C. A., Silvi, P., Blatt, R., Roos, C. F., and Zoller, P., “Self-verifying variational quantum simulation of lattice models”, *Nature* **569**, 355–360 (2019).
- ³⁶Halimeh, J. C. and Hauke, P., “Reliability of lattice gauge theories”, arXiv:2001.00024 (2019).
- ³⁷Yang, B., Sun, H., Ott, R., Wang, H.-Y., Zache, T. V., Halimeh, J. C., Yuan, Z.-S., Hauke, P., and Pan, J.-W., “Observation of gauge invariance in a 71-site quantum simulator”, arXiv:2003.08945 (2020).
- ³⁸Schweigler, T., Kasper, V., Erne, S., Mazets, I., Rauer, B., Cataldini, F., Langen, T., Gasenzer, T., Berges, J., and Schmiedmayer, J., “Experimental characterization of a quantum many-body system via higher-order correlations”, *Nature* **545**, 323–326 (2017).
- ³⁹Zache, T. V., Schweigler, T., Erne, S., Schmiedmayer, J., and Berges, J., “Extracting the Field Theory Description of a Quantum Many-Body System from Experimental Data”, *Physical Review X* **10**, 11020 (2020).
- ⁴⁰Nielsen, M. A. and Chuang, I. L., *Quantum Computation and Quantum Information* (2010).

- ⁴¹Lloyd, S., “Universal Quantum Simulators”, *Science* **273**, 1073–1078 (1996).
- ⁴²Ceperley, D. and Alder, B., “Quantum Monte Carlo”, *Science* **231**, 555–560 (1986).
- ⁴³Sokal, A., “Monte Carlo Methods in Statistical Mechanics: Foundations and New Algorithms”, in *Functional integration* (Springer, 1997), pp. 131–192.
- ⁴⁴Loh, E. Y., Gubernatis, J. E., Scalettar, R. T., White, S. R., Scalapino, D. J., and Sugar, R. L., “Sign problem in the numerical simulation of many-electron systems”, *Physical Review B* **41**, 9301–9307 (1990).
- ⁴⁵Troyer, M. and Wiese, U. J., “Computational complexity and fundamental limitations to fermionic quantum Monte Carlo simulations”, *Physical Review Letters* **94**, 170201 (2005).
- ⁴⁶Blatt, R. and Roos, C. F., “Quantum simulations with trapped ions”, *Nature Physics* **8**, 277–284 (2012).
- ⁴⁷Aspuru-Guzik, A. and Walther, P., “Photonic quantum simulators”, *Nature Physics* **8**, 285–291 (2012).
- ⁴⁸Houck, A. A., Türeci, H. E., and Koch, J., “On-chip quantum simulation with superconducting circuits”, *Nature Physics* **8**, 292–299 (2012).
- ⁴⁹Gross, C. and Bloch, I., “Quantum simulations with ultracold atoms in optical lattices”, *Science* **357**, 995–1001 (2017).
- ⁵⁰Weinberg, S., *The quantum theory of fields* (Cambridge University Press, 1995).
- ⁵¹Zinn-Justin, J., *Quantum Field Theory and Critical Phenomena* (2010).
- ⁵²Montvay, I. and Münster, G., *Quantum Fields on a Lattice* (1994).
- ⁵³Landau, L. D. and Lifshitz, E. M., “Course of Theoretical Physics Volume 1: Mechanics”, in *Course of theoretical physics* (1982).
- ⁵⁴Jackson, J. D. and Fox, R. F., *Classical Electrodynamics* (1999).
- ⁵⁵Rothe, H. J., *Lattice Gauge Theories: An Introduction* (World Scientific Publishing Company, 2005).
- ⁵⁶Kogut, J. and Susskind, L., “Hamiltonian formulation of Wilson’s lattice gauge theories”, *Physical Review D* **11**, 395–408 (1975).
- ⁵⁷Coleman, S., Jackiw, R., and Susskind, L., “Charge shielding and quark confinement in the massive schwinger model”, *Annals of Physics* **93**, 267–275 (1975).
- ⁵⁸Chupp, T. E., Fierlinger, P., Ramsey-Musolf, M. J., and Singh, J. T., “Electric dipole moments of atoms, molecules, nuclei, and particles”, *Reviews of Modern Physics* **91**, 015001 (2019).
- ⁵⁹Peccei, R. D. and Quinn, H. R., “CP conservation in the presence of pseudoparticles”, *Physical Review Letters* **38**, 1440–1443 (1977).
- ⁶⁰Heyl, M., Polkovnikov, A., and Kehrein, S., “Dynamical Quantum Phase Transitions in the Transverse-Field Ising Model”, *Physical Review Letters* **110**, 135704 (2013).

- ⁶¹Wetterich, C., “Nonequilibrium time evolution in quantum field theory”, *Physical Review E* **56**, 2687–2690 (1997).
- ⁶²Prüfer, M., Kunkel, P., Strobel, H., Lannig, S., Linnemann, D., Schmied, C. M., Berges, J., Gasenzer, T., and Oberthaler, M. K., “Observation of universal dynamics in a spinor Bose gas far from equilibrium”, *Nature* **563**, 217–220 (2018).
- ⁶³Walz, R., Boguslavski, K., and Berges, J., “Large- N kinetic theory for highly occupied systems”, *Physical Review D* **97**, 116011 (2018).
- ⁶⁴Chantesana, I., Orioli, A. P., and Gasenzer, T., “Kinetic theory of nonthermal fixed points in a Bose gas”, *Physical Review A* **99**, 043620 (2019).
- ⁶⁵Prüfer, M., Zache, T. V., Kunkel, P., Lannig, S., Bonnin, A., Strobel, H., Berges, J., and Oberthaler, M. K., “Experimental extraction of the quantum effective action for a non-equilibrium many-body system”, arXiv:1909.05120 (2019).
- ⁶⁶Sauter, F., “Über das Verhalten eines Elektrons im homogenen elektrischen Feld nach der relativistischen Theorie Diracs”, *Zeitschrift für Physik* **69**, 742–764 (1931).
- ⁶⁷Schwinger, J., “On gauge invariance and vacuum polarization”, *Physical Review* **82**, 664–679 (1951).
- ⁶⁸Philipsen, O. and Wittig, H., “String breaking in non-abelian gauge theories with fundamental matter fields”, *Physical Review Letters* **81**, 4056–4059 (1998).
- ⁶⁹Prkacin, Z., Bali, G. S., Düssel, T., Lippert, T., Neff, H., and Schilling, K., “Anatomy of string breaking in QCD”, *Proceedings of Science* **20**, 114513 (2005).
- ⁷⁰Hebenstreit, F., Berges, J., and Gelfand, D., “Real-time dynamics of string breaking”, *Physical Review Letters* **111**, 201601 (2013).
- ⁷¹Nielsen, H. B. and Ninomiya, M., “Absence of neutrinos on a lattice. (I). Proof by homotopy theory”, *Nuclear Physics B* **185**, 20–40 (1981).
- ⁷²Wilczek, F., “Lattice fermions”, *Physical Review Letters* **59**, 2397–2400 (1987).
- ⁷³Wilson, K. G., “Quarks and Strings on a Lattice”, in *New phenomena in subnuclear physics* (Springer, 1977), pp. 69–142.
- ⁷⁴Bermudez, A., Mazza, L., Rizzi, M., Goldman, N., Lewenstein, M., and Martin-Delgado, M. A., “Wilson fermions and axion electrodynamics in optical lattices”, *Physical Review Letters* **105**, 190404 (2010).
- ⁷⁵Mazza, L., Bermudez, A., Goldman, N., Rizzi, M., Martin-Delgado, M. A., and Lewenstein, M., “An optical-lattice-based quantum simulator for relativistic field theories and topological insulators”, *New Journal of Physics* **14**, 015007 (2012).
- ⁷⁶Kuno, Y., Ichinose, I., and Takahashi, Y., “Generalized lattice Wilson–Dirac fermions in $(1 + 1)$ dimensions for atomic quantum simulation and topological phases”, *Scientific Reports* **8**, 10699 (2018).
- ⁷⁷Sernelius, B. E., “Polaron in n dimensions”, *Physical Review B* **36**, 9059–9067 (1987).

- ⁷⁸Karsten, L. H. and Smith, J., "Lattice fermions: Species doubling, chiral invariance and the triangle anomaly", *Nuclear Physics B* **183**, 103–140 (1981).
- ⁷⁹Irving, A. C. and Thomas, A., "Finite lattice fermions and gauge fields in 1+1 dimensions", *Nuclear Physics B* **215**, 23–44 (1983).
- ⁸⁰Wilson, K. G., "Confinement of quarks", *Physical Review D* **10**, 2445–2459 (1974).
- ⁸¹Mace, M., Mueller, N., Schlichting, S., and Sharma, S., "Nonequilibrium study of the chiral magnetic effect from real-time simulations with dynamical fermions", *Physical Review D* **95**, 36023 (2017).
- ⁸²Banks, T., Susskind, L., and Kogut, J., "Strong-coupling calculations of lattice gauge theories: (1 + 1)-dimensional exercises", *Physical Review D* **13**, 1043–1053 (1976).
- ⁸³Mueller, N., Hebenstreit, F., and Berges, J., "Anomaly-Induced Dynamical Refractive Index in Strong-Field QED", *Physical Review Letters* **117**, 61601 (2016).
- ⁸⁴Müller, N., Schlichting, S., and Sharma, S., "Chiral Magnetic Effect and Anomalous Transport from Real-Time Lattice Simulations", *Physical Review Letters* **117**, 142301 (2016).
- ⁸⁵Mace, M., Mueller, N., Schlichting, S., and Sharma, S., "Simulating chiral magnetic effect and anomalous transport phenomena in the pre-equilibrium stages of heavy-ion collisions", *Nuclear Physics A* **967**, 752–755 (2017).
- ⁸⁶Coleman, S., "More about the massive Schwinger model", *Annals of Physics* **101**, 239–267 (1976).
- ⁸⁷Kasper, V., Hebenstreit, F., Jendrzejewski, F., Oberthaler, M. K., and Berges, J., "Implementing quantum electrodynamics with ultracold atomic systems", *New Journal of Physics* **19**, 023030 (2017).
- ⁸⁸Chandrasekharan, S. and Wiese, U. J. J., "Quantum link models: A discrete approach to gauge theories", *Nuclear Physics B* **492**, 455–471 (1997).
- ⁸⁹Kühn, S., Cirac, J. I., and Bañuls, M.-C., "Quantum simulation of the Schwinger model: A study of feasibility", *Physical Review A* **90**, 042305 (2014).
- ⁹⁰Macomber, J. D. and Lynch, R., "Squeezed spin states", *The Journal of Chemical Physics* **83**, 6514–6519 (1985).
- ⁹¹Gelis, F. and Tanji, N., "Schwinger mechanism revisited", *Progress in Particle and Nuclear Physics* **87**, 1–49 (2016).
- ⁹²Pethick, C. J. and Smith, H., *Bose–Einstein condensation in dilute gases* (Cambridge university press, 2008).
- ⁹³Glück, M., Kolovsky, A. R., Korsch, H. J., and Zimmer, F., "Wannier-Stark resonances in semiconductor superlattices", *Physical Review B* **65**, 115302 (2002).
- ⁹⁴Houbiers, M., Stoof, H. T., McAlexander, W. I., and Hulet, R. G., "Elastic and inelastic collisions of 6-Li atoms in magnetic and optical traps", *Physical Review A* **57**, R1497–R1500 (1998).

- ⁹⁵Kasper, V., Hebenstreit, F., and Berges, J., “Fermion production from real-time lattice gauge theory in the classical-statistical regime”, *Physical Review D* **90**, 025016 (2014).
- ⁹⁶Buyens, B., Haegeman, J., Hebenstreit, F., Verstraete, F., and Van Acoleyen, K., “Real-time simulation of the Schwinger effect with matrix product states”, *Physical Review D* **96**, 114501 (2017).
- ⁹⁷Hauke, P., Lewenstein, M., and Eckardt, A., “Tomography of band insulators from quench dynamics”, *Physical Review Letters* **113**, 45303 (2014).
- ⁹⁸Fläschner, N., Rem, B. S., Tarnowski, M., Vogel, D., Lühmann, D. S., Sengstock, K., and Weitenberg, C., “Experimental reconstruction of the Berry curvature in a Floquet Bloch band”, *Science* **352**, 1091–1094 (2016).
- ⁹⁹Parsons, M. F., Mazurenko, A., Chiu, C. S., Ji, G., Greif, D., and Greiner, M., “Site-resolved measurement of the spin-correlation function in the Fermi-Hubbard model”, *Science* **353**, 1253–1256 (2016).
- ¹⁰⁰Boll, M., Hilker, T. A., Salomon, G., Omran, A., Nespolo, J., Pollet, L., Bloch, I., and Gross, C., “Spin- and density-resolved microscopy of antiferromagnetic correlations in Fermi-Hubbard chains”, *Science* **353**, 1257–1260 (2016).
- ¹⁰¹Cheuk, L. W., Nichols, M. A., Lawrence, K. R., Okan, M., Zhang, H., Khatami, E., Trivedi, N., Paiva, T., Rigol, M., and Zwierlein, M. W., “Observation of spatial charge and spin correlations in the 2D Fermi-Hubbard model”, *Science* **353**, 1260–1264 (2016).
- ¹⁰²Bañuls, M., Cichy, K., Cirac, J., and Jansen, K., “The mass spectrum of the Schwinger model with matrix product states”, *Journal of High Energy Physics* **2013**, 158 (2013).
- ¹⁰³Pichler, T., Dalmonte, M., Rico, E., Zoller, P., and Montangero, S., “Real-time dynamics in U(1) lattice gauge theories with tensor networks”, *Physical Review X* **6**, 11023 (2016).
- ¹⁰⁴Kühn, S., Zohar, E., Cirac, J. I., and Bañuls, M. C., “Non-Abelian string breaking phenomena with matrix product states”, *Journal of High Energy Physics* **2015**, 130 (2015).
- ¹⁰⁵Su, W. P., Schrieffer, J. R., and Heeger, A. J., “Solitons in polyacetylene”, *Physical Review Letters* **42**, 1698–1701 (1979).
- ¹⁰⁶Zwerger, W., “Mott Hubbard transition of cold atoms in optical lattices”, *Journal of Optics B: Quantum and Semiclassical Optics* **5**, S9–S16 (2003).
- ¹⁰⁷Ho, L. T. A. and Chibotaru, L. F., “A simple derivation of the Landau-Zener formula”, *Physical Chemistry Chemical Physics* **16**, 6942–6945 (2014).
- ¹⁰⁸Mil, A., “Experimental realization of U(1) gauge invariance in ultracold atomic mixtures”, PhD thesis (2020).

- ¹⁰⁹Kogut, J. B., “An introduction to lattice gauge theory and spin systems”, *Reviews of Modern Physics* **51**, 659–713 (1979).
- ¹¹⁰Horn, D., “Finite matrix models with continuous local gauge invariance”, *Physics Letters B* **100**, 149–151 (1981).
- ¹¹¹Jaksch, D. and Zoller, P., “Creation of effective magnetic fields in optical lattices: the Hofstadter butterfly for cold neutral atoms”, *New Journal of Physics* **5**, 56–56 (2003).
- ¹¹²Aidelsburger, M., Atala, M., Nascimbène, S., Trotzky, S., Chen, Y. A., and Bloch, I., “Experimental realization of strong effective magnetic fields in optical superlattice potentials”, *Applied Physics B* **113**, 1–11 (2013).
- ¹¹³Gross, C., Zibold, T., Nicklas, E., Estève, J., and Oberthaler, M. K., “Nonlinear atom interferometer surpasses classical precision limit”, *Nature* **464**, 1165–1169 (2010).
- ¹¹⁴Riedel, M. F., Böhi, P., Li, Y., Hänsch Signnsch, T. W., Sinatra, A., and Treutlein, P., “Atom-chip-based generation of entanglement for quantum metrology”, *Nature* **464**, 1170–1173 (2010).
- ¹¹⁵Li, X., Zhu, B., He, X., Wang, F., Guo, M., Xu, Z. F., Zhang, S., and Wang, D., “Coherent Heteronuclear Spin Dynamics in an Ultracold Spinor Mixture”, *Physical Review Letters* **114**, 255301 (2015).
- ¹¹⁶Nicklas, E., Strobel, H., Zibold, T., Gross, C., Malomed, B. A., Kevrekidis, P. G., and Oberthaler, M. K., “Rabi flopping induces spatial demixing dynamics”, *Physical Review Letters* **107**, 193001 (2011).
- ¹¹⁷Preskill, J., “Lecture Notes for Physics 229: Quantum Information and Computation”, *California Institute of Technology* **16** (1998).
- ¹¹⁸Bloch, I., Dalibard, J., and Zwirger, W., “Many-body physics with ultracold gases”, *Reviews of Modern Physics* **80**, 885–964 (2008).
- ¹¹⁹Bernien, H., Schwartz, S., Keesling, A., Levine, H., Omran, A., Pichler, H., Choi, S., Zibrov, A. S., Endres, M., Greiner, M., Vuletic, V., and Lukin, M. D., “Probing many-body dynamics on a 51-atom quantum simulator”, *Nature* **551**, 579–584 (2017).
- ¹²⁰Ockeloen, C. F., Tauschinsky, A. F., Spreeuw, R. J. C., and Whitlock, S., “Detection of small atom numbers through image processing”, *Physical Review A* **82**, 061606 (2010).
- ¹²¹Reinaudi, G., Lahaye, T., Wang, Z., and Guéry-Odelin, D., “Strong saturation absorption imaging of dense clouds of ultracold atoms”, *Optics Letters* **32**, 3143 (2007).
- ¹²²Stamper-Kurn, D. M. and Ueda, M., “Spinor Bose gases: Symmetries, magnetism, and quantum dynamics”, *Reviews of Modern Physics* **85**, 1191–1244 (2013).

- ¹²³Luo, M., Li, Z., and Bao, C., "Bose-Einstein condensate of a mixture of two species of spin-1 atoms", *Physical Review A* **75**, 043609 (2007).
- ¹²⁴Tiemann, E., *Private communication*.
- ¹²⁵Dao, T.-L., Carusotto, I., and Georges, A., "Probing quasiparticle states in strongly interacting atomic gases by momentum-resolved Raman photoemission spectroscopy", *Physical Review A* **80**, 023627 (2009).
- ¹²⁶Weideman, J. A. and Herbst, B. M., "Split-Step Methods for the Solution of the Nonlinear Schroedinger Equation.", *SIAM Journal on Numerical Analysis* **23**, 485–507 (1986).
- ¹²⁷Bao, W., Jaksch, D., and Markowich, P. A., "Numerical solution of the Gross-Pitaevskii equation for Bose-Einstein condensation", *Journal of Computational Physics* **187**, 318–342 (2003).
- ¹²⁸McLachlan, R. I. and Atela, P., "The accuracy of symplectic integrators", *Nonlinearity* **5**, 541–562 (1992).
- ¹²⁹Chiofalo, M. L., Succi, S., and Tosi, M. P., "Ground state of trapped interacting Bose-Einstein condensates by an explicit imaginary-time algorithm", *Physical Review E* **62**, 7438–7444 (2000).
- ¹³⁰Stenger, J., Inouye, S., Stamper-Kurn, D. M., Miesner, H. J., Chikkatur, A. P., and Ketterle, W., "Spin domains in ground-state Bose-Einstein condensates", *Nature* **396**, 345–348 (1998).
- ¹³¹Klinkhamer, F. R. and Manton, N. S., "A saddle-point solution in the Weinberg-Salam theory", *Physical Review D* **30**, 2212–2220 (1984).
- ¹³²Dashen, R. F., Hasslacher, B., and Neveu, A., "Nonperturbative methods and extended-hadron models in field theory. III. Four-dimensional non-Abelian models", *Physical Review D* **10**, 4138–4142 (1974).
- ¹³³Soni, V., "Possible classical solutions in the Weinberg-Salam model", *Physics Letters B* **93**, 101–106 (1980).
- ¹³⁴Boguta, J., "Can nuclear interactions be long ranged?", *Physical Review Letters* **50**, 148–152 (1983).
- ¹³⁵Forgács, P. and Horváth, Z., "Topology and saddle points in field theories", *Physics Letters B* **138**, 397–401 (1984).
- ¹³⁶’t Hooft, G., "Computation of the quantum effects due to a four-dimensional pseudoparticle", *Physical Review D* **14**, 3432–3450 (1976).
- ¹³⁷Jackiw, R. and Rebbi, C., "Vacuum periodicity in a Yang-Mills quantum theory", *Physical Review Letters* **37**, 172–175 (1976).
- ¹³⁸Callan, C. G., Dashen, R. F., and Gross, D. J., "Instantons as a bridge between weak and strong coupling in quantum chromodynamics", *Physical Review D* **20**, 3279–3291 (1979).

- ¹³⁹Weinberg, S., "A new light boson?", *Physical Review Letters* **40**, 223–226 (1978).
- ¹⁴⁰Wilczek, F., "Problem of strong P and T invariance in the presence of instantons", *Physical Review Letters* **40**, 279–282 (1978).
- ¹⁴¹Graham, P. W., Irastorza, I. G., Lamoreaux, S. K., Lindner, A., and Bibber, K. A. van, "Experimental Searches for the Axion and Axion-Like Particles", *Annual Review of Nuclear and Particle Science* **65**, 485–514 (2015).
- ¹⁴²Mace, M., Schlichting, S., and Venugopalan, R., "Off-equilibrium sphaleron transitions in the glasma", *Physical Review D* **93**, 74036 (2016).
- ¹⁴³Petreczky, P., "Lattice QCD at non-zero temperature", *Journal of Physics G: Nuclear and Particle Physics* **39**, 093002 (2012).
- ¹⁴⁴Fläschner, N., Vogel, D., Tarnowski, M., Rem, B. S., Lühmann, D. S., Heyl, M., Budich, J. C., Mathey, L., Sengstock, K., and Weitenberg, C., "Observation of dynamical vortices after quenches in a system with topology", *Nature Physics* **14**, 265–268 (2018).
- ¹⁴⁵Jurcevic, P., Shen, H., Hauke, P., Maier, C., Brydges, T., Hempel, C., Lanyon, B. P., Heyl, M., Blatt, R., and Roos, C. F., "Direct Observation of Dynamical Quantum Phase Transitions in an Interacting Many-Body System", *Physical Review Letters* **119**, 80501 (2017).
- ¹⁴⁶Heyl, M., "Dynamical quantum phase transitions: A review", *Reports on Progress in Physics* **81**, 54001 (2018).
- ¹⁴⁷Budich, J. C. and Heyl, M., "Dynamical topological order parameters far from equilibrium", *Physical Review B* **93**, 085416 (2016).
- ¹⁴⁸Tian, T., Ke, Y., Zhang, L., Lin, S., Shi, Z., Huang, P., Lee, C., and Du, J., "Observation of dynamical phase transitions in a topological nanomechanical system", *Physical Review B* **100**, 024310 (2019).
- ¹⁴⁹Xu, X.-Y., Wang, Q.-Q., Heyl, M., Budich, J. C., Pan, W.-W., Chen, Z., Jan, M., Sun, K., Xu, J.-S., Han, Y.-J., Li, C.-F., and Guo, G.-C., "Measuring a dynamical topological order parameter in quantum walks", *Light: Science & Applications* **9**, 7 (2020).
- ¹⁵⁰Shimizu, Y. and Kuramashi, Y., "Critical behavior of the lattice Schwinger model with a topological term at $\theta=\pi$ using the Grassmann tensor renormalization group", *Physical Review D* **90**, 74503 (2014).
- ¹⁵¹Gorin, T., Prosen, T., Seligman, T. H., and Žnidarič, M., "Dynamics of Loschmidt echoes and fidelity decay", *Physics Reports* **435**, 33–156 (2006).
- ¹⁵²Weinberg, P. and Bukov, M., "QuSpin: a Python package for dynamics and exact diagonalisation of quantum many body systems. Part II: bosons, fermions and higher spins", *SciPost Physics* **7**, 020 (2019).

- ¹⁵³Hamer, C. J., Weihong, Z., and Oitmaa, J., “Series expansions for the massive Schwinger model in Hamiltonian lattice theory”, *Physical Review D* **56**, 55–67 (1997).
- ¹⁵⁴Fukui, T., Hatsugai, Y., and Suzuki, H., “Chern numbers in discretized Brillouin zone: Efficient method of computing (spin) Hall conductances”, *Journal of the Physical Society of Japan* **74**, 1674–1677 (2005).
- ¹⁵⁵Abdalla, E., Abdalla, M. C. B., and Rothe, K. D., *Non-perturbative methods in 2 dimensional quantum field theory* (World Scientific, 1991).
- ¹⁵⁶Monz, T., Nigg, D., Martinez, E. A., Brandl, M. F., Schindler, P., Rines, R., Wang, S. X., Chuang, I. L., and Blatt, R., “Realization of a scalable Shor algorithm”, *Science* **351**, 1068–1070 (2016).
- ¹⁵⁷Barends, R., Shabani, A., Lamata, L., Kelly, J., Mezzacapo, A., Heras, U. L., Babush, R., Fowler, A. G., Campbell, B., Chen, Y., Chen, Z., Chiaro, B., Dunsworth, A., Jeffrey, E., Lucero, E., Megrant, A., Mutus, J. Y., Neeley, M., Neill, C., O’Malley, P. J., Quintana, C., Roushan, P., Sank, D., Vainsencher, A., Wenner, J., White, T. C., Solano, E., Neven, H., and Martinis, J. M., “Digitized adiabatic quantum computing with a superconducting circuit”, *Nature* **534**, 222–226 (2016).
- ¹⁵⁸Kandala, A., Mezzacapo, A., Temme, K., Takita, M., Brink, M., Chow, J. M., and Gambetta, J. M., “Hardware-efficient variational quantum eigensolver for small molecules and quantum magnets”, *Nature* **549**, 242–246 (2017).
- ¹⁵⁹Landsman, K. A., Figgatt, C., Schuster, T., Linke, N. M., Yoshida, B., Yao, N. Y., and Monroe, C., “Verified quantum information scrambling”, *Nature* **567**, 61–65 (2019).
- ¹⁶⁰Lu, H.-H., Klco, N., Lukens, J. M., Morris, T. D., Bansal, A., Ekström, A., Hagen, G., Papenbrock, T., Weiner, A. M., Savage, M. J., and Lougovski, P., “Simulations of subatomic many-body physics on a quantum frequency processor”, *Physical Review A* **100**, 012320 (2019).
- ¹⁶¹Muschik, C., Heyl, M., Martinez, E., Monz, T., Schindler, P., Vogell, B., Dalmonte, M., Hauke, P., Blatt, R., and Zoller, P., “U(1) Wilson lattice gauge theories in digital quantum simulators”, *New Journal of Physics* **19**, 103020 (2017).
- ¹⁶²Magnifico, G., Vodola, D., Ercolessi, E., Kumar, S. P., Müller, M., and Bermudez, A., “Symmetry-protected topological phases in lattice gauge theories: Topological QED2”, *Physical Review D* **99**, 014503 (2019).
- ¹⁶³Knap, M., Kantian, A., Giamarchi, T., Bloch, I., Lukin, M. D., and Demler, E., “Probing real-space and time-resolved correlation functions with many-body Ramsey interferometry”, *Physical Review Letters* **111**, 147205 (2013).
- ¹⁶⁴Uhrich, P., Gross, C., and Kastner, M., “Probing unitary two-time correlations in a neutral atom quantum simulator”, *Quantum Science and Technology* **4**, 024005 (2019).

- ¹⁶⁵Gurarie, V., “Single-particle Green’s functions and interacting topological insulators”, *Physical Review B* **83**, 085426 (2011).
- ¹⁶⁶Goldman, N., Budich, J. C., and Zoller, P., “Topological quantum matter with ultracold gases in optical lattices”, *Nature Physics* **12**, 639–645 (2016).
- ¹⁶⁷Rachel, S., “Interacting topological insulators: a review”, *Reports on Progress in Physics* **81**, 116501 (2018).
- ¹⁶⁸Kharzeev, D. E., McLerran, L. D., and Warringa, H. J., “The effects of topological charge change in heavy ion collisions: ‘Event by event P and CP violation’”, *Nuclear Physics A* **803**, 227–253 (2008).
- ¹⁶⁹Fukushima, K., Kharzeev, D. E., and Warringa, H. J., “Chiral magnetic effect”, *Physical Review D* **78**, 74033 (2008).
- ¹⁷⁰Kharzeev, D., Liao, J., Voloshin, S., and Wang, G., “Chiral magnetic and vortical effects in high-energy nuclear collisions—A status report”, *Progress in Particle and Nuclear Physics* **88**, 1–28 (2016).
- ¹⁷¹Koch, V., Schlichting, S., Skokov, V., Sorensen, P., Thomas, J., Voloshin, S., Wang, G., and Yee, H.-U., “Status of the chiral magnetic effect and collisions of isobars”, *Chinese Physics C* **41**, 072001 (2017).
- ¹⁷²Son, D. T. and Surówka, P., “Hydrodynamics with Triangle Anomalies”, *Physical Review Letters* **103**, 191601 (2009).
- ¹⁷³Yee, H.-U., “Holographic Chiral magnetic conductivity”, *Journal of High Energy Physics* **2009**, 085–085 (2009).
- ¹⁷⁴Son, D. T. and Yamamoto, N., “Berry curvature, triangle anomalies, and the chiral magnetic effect in fermi liquids”, *Physical Review Letters* **109**, 181602 (2012).
- ¹⁷⁵Stephanov, M. A. and Yin, Y., “Chiral kinetic theory”, *Physical Review Letters* **109**, 162001 (2012).
- ¹⁷⁶Chen, J. W., Pang, J. Y., Pu, S., and Wang, Q., “Kinetic equations for massive Dirac fermions in electromagnetic field with non-Abelian Berry phase”, *Physical Review D* **89**, 94003 (2014).
- ¹⁷⁷Mueller, N. and Venugopalan, R., “Chiral anomaly, Berry phase, and chiral kinetic theory from worldlines in quantum field theory”, *Physical Review D* **97**, 051901 (2018).
- ¹⁷⁸Mueller, N. and Venugopalan, R., “Worldline construction of a covariant chiral kinetic theory”, *Physical Review D* **D96**, 16023 (2017).
- ¹⁷⁹Tuchin, K., “Impact of domain walls on the chiral magnetic effect in hot QCD matter”, *Physical Review C* **97**, 064914 (2018).
- ¹⁸⁰Rosales-Zárata, L. E. C. and Drummond, P. D., “Linear entropy in quantum phase space”, *Physical Review A* **84**, 042114 (2011).

- ¹⁸¹Haller, E., Hart, R., Mark, M. J., Danzl, J. G., Reichsöllner, L., Gustavsson, M., Dalmonte, M., Pupillo, G., and Nägerl, H.-C., “Pinning quantum phase transition for a Luttinger liquid of strongly interacting bosons”, *Nature* **466**, 597–600 (2010).
- ¹⁸²Gring, M., Kuhnert, M., Langen, T., Kitagawa, T., Rauer, B., Schreitl, M., Mazets, I., Smith, D. A., Demler, E., and Schmiedmayer, J., “Relaxation and Prethermalization in an Isolated Quantum System”, *Science* **337**, 1318–1322 (2012).
- ¹⁸³Hung, C.-L., Gurarie, V., and Chin, C., “From Cosmology to Cold Atoms: Observation of Sakharov Oscillations in a Quenched Atomic Superfluid”, *Science* **341**, 1213–1215 (2013).
- ¹⁸⁴Langen, T., Erne, S., Geiger, R., Rauer, B., Schweigler, T., Kuhnert, M., Rohringer, W., Mazets, I. E., Gasenzer, T., and Schmiedmayer, J., “Experimental observation of a generalized Gibbs ensemble”, *Science* **348**, 207–211 (2015).
- ¹⁸⁵Navon, N., Gaunt, A. L., Smith, R. P., and Hadzibabic, Z., “Critical dynamics of spontaneous symmetry breaking in a homogeneous Bose gas”, *Science* **347**, 167–170 (2015).
- ¹⁸⁶Navon, N., Gaunt, A. L., Smith, R. P., and Hadzibabic, Z., “Emergence of a turbulent cascade in a quantum gas”, *Nature* **539**, 72–75 (2016).
- ¹⁸⁷Erne, S., Bücker, R., Gasenzer, T., Berges, J., and Schmiedmayer, J., “Universal dynamics in an isolated one-dimensional Bose gas far from equilibrium”, *Nature* **563**, 225–229 (2018).
- ¹⁸⁸Eckel, S., Kumar, A., Jacobson, T., Spielman, I. B., and Campbell, G. K., “A Rapidly Expanding Bose-Einstein Condensate: An Expanding Universe in the Lab”, *Physical Review X* **8**, 021021 (2018).
- ¹⁸⁹Hu, J., Feng, L., Zhang, Z., and Chin, C., “Quantum simulation of Unruh radiation”, *Nature Physics* **15**, 785–789 (2019).
- ¹⁹⁰Feng, L., Hu, J., Clark, L. W., and Chin, C., “Correlations in high-harmonic generation of matter-wave jets revealed by pattern recognition”, *Science* **363**, 521–524 (2019).
- ¹⁹¹Murthy, P. A., Defenu, N., Bayha, L., Holten, M., Preiss, P. M., Enss, T., and Jochim, S., “Quantum scale anomaly and spatial coherence in a 2D Fermi superfluid”, *Science* **365**, 268–272 (2019).
- ¹⁹²Keesling, A., Omran, A., Levine, H., Bernien, H., Pichler, H., Choi, S., Samajdar, R., Schwartz, S., Silvi, P., Sachdev, S., Zoller, P., Endres, M., Greiner, M., Vuletić, V., and Lukin, M. D., “Quantum Kibble–Zurek mechanism and critical dynamics on a programmable Rydberg simulator”, *Nature* **568**, 207–211 (2019).
- ¹⁹³Flammia, S. T., Gross, D., Liu, Y.-K., and Eisert, J., “Quantum tomography via compressed sensing: error bounds, sample complexity and efficient estimators”, *New Journal of Physics* **14**, 095022 (2012).

- ¹⁹⁴Bücker, R., Perrin, A., Manz, S., Betz, T., Koller, C., Plisson, T., Rottmann, J., Schumm, T., and Schmiedmayer, J., “Single-particle-sensitive imaging of freely propagating ultracold atoms”, *New Journal of Physics* **11**, 103039 (2009).
- ¹⁹⁵Bakr, W. S., Gillen, J. I., Peng, A., Fölling, S., and Greiner, M., “A quantum gas microscope for detecting single atoms in a Hubbard-regime optical lattice”, *Nature* **462**, 74–77 (2009).
- ¹⁹⁶Sherson, J. F., Weitenberg, C., Endres, M., Cheneau, M., Bloch, I., and Kuhr, S., “Single-atom-resolved fluorescence imaging of an atomic Mott insulator”, *Nature* **467**, 68–72 (2010).
- ¹⁹⁷Nachbagauer, H., “Wigner Functionals and their Dynamics in Quantum-Field-Theory”, arXiv:hep-th/9703105 (1997).
- ¹⁹⁸Rispoli, M., Lukin, A., Schittko, R., Kim, S., Tai, M. E., Léonard, J., and Greiner, M., “Quantum critical behaviour at the many-body localization transition”, *Nature* **573**, 385–389 (2019).
- ¹⁹⁹Coleman, S., “Quantum sine-Gordon equation as the massive Thirring model”, *Physical Review D* **11**, 2088–2097 (1975).
- ²⁰⁰Mandelstam, S., “Soliton operators for the quantized sine-Gordon equation”, *Physical Review D* **11**, 3026–3030 (1975).
- ²⁰¹Faddeev, L. and Korepin, V., “Quantum theory of solitons”, *Physics Reports* **42**, 1–87 (1978).
- ²⁰²Sklyanin, E. K., Takhtadzhyan, L. A., and Faddeev, L. D., “Quantum inverse problem method. I”, *Theoretical and Mathematical Physics* **40**, 688–706 (1979).
- ²⁰³Gritsev, V., Polkovnikov, A., and Demler, E., “Linear response theory for a pair of coupled one-dimensional condensates of interacting atoms”, *Physical Review B* **75**, 174511 (2007).
- ²⁰⁴Schwinger, J., “The Theory of Quantized Fields. I”, *Physical Review* **82**, 914–927 (1951).
- ²⁰⁵Schwinger, J., “On the Green’s functions of quantized fields. II”, *Proceedings of the National Academy of Sciences* **37**, 455–459 (1951).
- ²⁰⁶Cahill, K. E. and Glauber, R. J., “Density Operators and Quasiprobability Distributions”, *Physical Review* **177**, 1882–1902 (1969).
- ²⁰⁷Mrówczyński, S. and Müller, B., “Wigner functional approach to quantum field dynamics”, *Physical Review D* **50**, 7542–7552 (1994).
- ²⁰⁸Hillery, M., O’Connell, R. F., Scully, M. O., and Wigner, E. P., “Distribution functions in physics: Fundamentals”, *Physics Reports* **106**, 121–167 (1984).
- ²⁰⁹Polkovnikov, A., “Phase space representation of quantum dynamics”, *Annals of Physics* **325**, 1790–1852 (2010).

- ²¹⁰Aarts, G. and Berges, J., “Classical aspects of quantum fields far from equilibrium”, *Physical Review Letters* **88**, 416031–416034 (2002).
- ²¹¹Shiryaev, A. N., *Probability - 1* (Springer, New York, 2016).
- ²¹²Coleman, S., “Erratum: Fate of the false vacuum: semiclassical theory”, *Physical Review D* **16**, 1248–1248 (1977).
- ²¹³Kleinert, H., *Particles and quantum fields* (World Scientific Singapore, 2016).
- ²¹⁴Beck, S., Mazets, I. E., and Schweigler, T., “Nonperturbative method to compute thermal correlations in one-dimensional systems”, *Physical Review A* **98**, 023613 (2018).
- ²¹⁵Rauer, B., Erne, S., Schweigler, T., Cataldini, F., Tajik, M., and Schmiedmayer, J., “Recurrences in an isolated quantum many-body system”, *Science* **360**, 307–310 (2018).
- ²¹⁶Schumm, T., Hofferberth, S., Andersson, L. M., Wildermuth, S., Groth, S., Bar-Joseph, I., Schmiedmayer, J., and Krüger, P., “Matter-wave interferometry in a double well on an atom chip”, *Nature Physics* **1**, 57–62 (2005).
- ²¹⁷Schweigler, T., “Correlations and dynamics of tunnel - coupled one - dimensional Bose gases”, PhD thesis (TU Wien, 2019).
- ²¹⁸Laine, M., “Basics of Thermal Field Theory 1”, *Lecture Notes in Physics* **925** (2008).
- ²¹⁹Prüfer, M., “Experimentally testing quantum field theory concepts with spinor Bose gases far from equilibrium”, PhD thesis (2020).
- ²²⁰Polkovnikov, A., Sengupta, K., Silva, A., and Vengalattore, M., “Colloquium: Nonequilibrium dynamics of closed interacting quantum systems”, *Reviews of Modern Physics* **83**, 863–883 (2011).
- ²²¹Jordan, S. P., Lee, K. S., and Preskill, J., “Quantum algorithms for quantum field theories”, *Science* **336**, 1130–1133 (2012).
- ²²²Sadler, L. E., Higbie, J. M., Leslie, S. R., Vengalattore, M., and Stamper-Kurn, D. M., “Coherence-Enhanced Imaging of a Degenerate Bose-Einstein Gas”, *Physical Review Letters* **98**, 110401 (2007).
- ²²³Kunkel, P., Prüfer, M., Lannig, S., Rosa-Medina, R., Bonnin, A., Gärttner, M., Strobel, H., and Oberthaler, M. K., “Simultaneous Readout of Noncommuting Collective Spin Observables beyond the Standard Quantum Limit”, *Physical Review Letters* **123**, 63603 (2019).
- ²²⁴Lifshitz, E. M. and Pitaevskii, L. P., *Physical kinetics* (Butterworth-Heinemann, 1981).
- ²²⁵Berges, J., Rothkopf, A., and Schmidt, J., “Nonthermal fixed points: Effective weak coupling for strongly correlated systems far from equilibrium”, *Physical Review Letters* **101**, 41603 (2008).

- ²²⁶Horsman, C., Stepney, S., Wagner, R. C., and Kendon, V., “When does a physical system compute?”, *Proceedings of the Royal Society A* **470**, 20140182 (2014).
- ²²⁷Bloch, I., Dalibard, J., and Nascimbène, S., “Quantum simulations with ultracold quantum gases”, *Nature Physics* **8**, 267–276 (2012).
- ²²⁸Lewenstein, M., Sanpera, A., Ahufinger, V., Damski, B., Sen(De), A., and Sen, U., “Ultracold atomic gases in optical lattices: mimicking condensed matter physics and beyond”, *Advances in Physics* **56**, 243–379 (2007).
- ²²⁹Wilson, K. G., “The renormalization group: Critical phenomena and the Kondo problem”, *Reviews of Modern Physics* **47**, 773–840 (1975).
- ²³⁰Hodgman, S. S., Khakimov, R. I., Lewis-Swan, R. J., Truscott, A. G., and Kheruntsyan, K. V., “Solving the Quantum Many-Body Problem via Correlations Measured with a Momentum Microscope”, *Physical Review Letters* **118**, 240402 (2017).
- ²³¹Preiss, P. M., Becher, J. H., Klemt, R., Klinkhamer, V., Bergschneider, A., Jochim, S., Defenu, N., and Jochim, S., “High-Contrast Interference of Ultracold Fermions”, *Physical Review Letters* **122**, 143602 (2019).
- ²³²Gerbier, F., Widera, A., Fölling, S., Mandel, O., and Bloch, I., “Resonant control of spin dynamics in ultracold quantum gases by microwave dressing”, *Physical Review A* **73**, 041602 (2006).
- ²³³Kawaguchia, Y. and Uedaa, M., “Spinor Bose-Einstein condensates”, *Physics Reports* **520**, 253–381 (2012).
- ²³⁴Piñeiro Orioli, A., Boguslavski, K., and Berges, J., “Universal self-similar dynamics of relativistic and nonrelativistic field theories near nonthermal fixed points”, *Physical Review D* **92**, 25041 (2015).
- ²³⁵Domino, K., Gawron, P., and Pawela, Ł., “Efficient Computation of Higher-Order Cumulant Tensors”, *SIAM Journal on Scientific Computing* **40**, A1590–A1610 (2018).
- ²³⁶Zohar, E. and Burrello, M., “Formulation of lattice gauge theories for quantum simulations”, *Physical Review D* **054506**, 1–15 (2015).
- ²³⁷Anishetty, R., Mathur, M., and Raychowdhury, I., “Prepotential formulation of SU(3) lattice gauge theory”, *Journal of Physics A: Mathematical and Theoretical* **43**, 035403 (2010).
- ²³⁸Asboth, J. K., Oroszlany, L., and Palyi, A., *A Short Course on Topological Insulators* (2016).
- ²³⁹Bettencourt, L. M. and Wetterich, C., “Time evolution of correlation functions in non-equilibrium field theories”, *Physics Letters B* **430**, 140–150 (1998).
- ²⁴⁰Berges, J. and Cox, J., “Thermalization of quantum fields from time-reversal invariant evolution equations”, *Physics Letters B* **517**, 369–374 (2001).
- ²⁴¹Mrówczyński, S., “Wigner functional of fermionic fields”, *Physical Review D* **87**, 065026 (2013).

²⁴²Bialynicki-Birula, I., “The Wigner functional of the electromagnetic field”, *Optics Communications* **179**, 237–246 (2000).

²⁴³Zache, T. V., Kasper, V., and Berges, J., “Inflationary preheating dynamics with two-species condensates”, *Physical Review A* **95**, 063629 (2017).